Republic of Iraq
Ministry of Higher Education
and Scientific Research
University of Misan
College of Science
Department of Physics

Nanosensors-based microfluidics devices for detection of narcotic drugs and heavy metals in blood plasma

A Thesis Submitted to
The College of Science / University of Misan as Partial Fulfillment
of the Requirements for the Master Degree of Science in Physics

By

Baheya Abdulbaqi Dhahi

B.Sc. Physics / Basrah University (2015)

Supervisors

Asst.Prof. Dr **Asst.Prof. Dr**

Mundher Abd Al Hasan Al-Shakban **Zaidon Tarik Al-aqbi**

2025 AD **1447 AH**

بِسْمِ اللَّهِ الرَّحْمَٰنِ الرَّحِيمِ

﴿يَرْفَعِ اللَّهُ الَّذِينَ آمَنُوا مِنكُمْ وَالَّذِينَ أُوتُوا الْعِلْمَ دَرَجَاتٍ وَاللَّهُ بِمَا تَعْمَلُونَ خَبِيرٌ﴾

صدق الله العظيم

سورة المجادلة/الأية (11)

Supervisors Certification

We, the supervisors of **Ms. Baheya Abdulbaqi Dhahi**, certify that the thesis **(Design and Performance Study on Nanofiltration Membrane for Blood Purification)** has been completed and written under our supervision as part of the requirements for obtaining a Master of Science degree in Physics.

Signature:

Asst.Prof. Dr

Mundher Abd Al Hasan Al-Shakban
Physics Department
College of Science

Misan University

Date: / /2025

Signature:

Asst.Prof. Dr

Zaidon Tarik Al-aqbi
Chemical Department
College of Science

Misan University

Date: / /2025

Head of Physics Department Recommendation

According to the recommendation of the supervisors, this thesis is forwarded to the examination committee for approval.

Signature:
Asst.Prof. Dr. Ahmed Khalaf
Head of Physics Department
College of Science
Misan University
Date: / /2025

Dedication

To the soul of my dear mother who departed this world, her presence remains in my heart, and her prayers support me in my steps. May God make Paradise your resting place and abode.

To the soul of my martyr brother, who ascended with honor and dignity, immortalizing the meaning of sacrifice with his blood. Your memory will remain a beacon illuminating my path and an endless source of pride... Refaq

To my dear father, the constant support and the never-ending giver, you lived to grant me strength and sacrificed to pave my path to success.

To my dear brother, companion on the journey, and helping hand who has never hesitated to offer support and assistance... Ahmed

To my dear sister, the heart that has been our comfort and the spirit that has been our support and refuge in the toughest moments... Rasha

To all of you, I dedicate the harvest of my work and my life, as a symbol of my eternal gratitude and devotion.

Baheya

Acknowledgement

I thank God Almighty who guided me to complete this work and directed my steps toward what is good. Based on the principle that "he who does not thank the created does not thank the Creator," I am pleased to express my gratitude and appreciation to my esteemed supervisors, **Assistant Professor Dr. Munther Abdul Hassan Al-Shakban** and **Assistant Professor Dr. Zaidon Tariq Al aqbi**, for their valuable advice, sound observations, and continuous follow-up. I would also like to extend my sincere thanks and appreciation to the Deanship of the College of Science at Maysan University and the Department of Physics, especially for providing the opportunity to present this work and for their scientific and academic support.

I would like to extend my sincere thanks and appreciation to the government departments and official entities that provided the necessary facilities, including the Presidency of the Basra Court of Appeals for facilitating the acquisition of statistics on prohibited pharmaceutical substances, as well as the Basra Health Directorate / Al-Fayhaa Teaching Hospital / Addiction Treatment Department and its director, **Dr. Ameen Al-Zamil**, for facilitating the acquisition of pharmaceutical substances to complete the research. My heartfelt gratitude and appreciation also go to the administration of Ibn Al-Bitar Hospital and **Dr. Raed Jassim Al-Dawl** for providing us with medical information on the misuse and handling of medications.

Sincere thanks and appreciation to the Deanship of the College of Science at the University of Basra for facilitating the task of conducting some measurements in the Departments of Physics and Chemistry.

I would also like to thank my dear colleagues for their cooperation and continuous support. And finally, I extend my highest expressions of gratitude to my esteemed family for their support and encouragement, which had the greatest impact on the completion of this thesis.

Baheya

Summary

The rapid increase in the illegal use of narcotic pharmaceuticals and the growing exposure to heavy metals in biological samples have created an urgent need for fast, sensitive, and cost-effective detection methods. Conventional analytical techniques, although accurate, often require complex instrumentation, long analysis times, and skilled operators. In this context, nanomaterials synthesized through environmentally friendly routes have emerged as promising alternatives for colorimetric sensing applications.

In this work, various nanomaterials were prepared using green synthesis methods. CoO NPs, Ag NPs, NiO NPs, and FeO NPs were synthesized using green tea extract as a reducing agent, while Cu NPs and ZnO NPs were prepared using *Boswellia sacra* extract. Furthermore, bimetallic nanomaterials were synthesized using the same plant extracts in molar ratios of 1:1 and 3:1, where Ag:NiO BNPs were prepared using green tea extract, and Cu: NiO BNPs, Cu:CoO BNPs, and Cu:ZnO BNPs were synthesized using *Boswellia sacra* extract.

The prepared nanomaterials were characterized using FESEM and TEM to evaluate particle size and morphology, confirming that all materials were within the nanoscale range. EDX analysis verified elemental composition and purity, while FTIR spectroscopy confirmed the effective role of plant extracts through the presence of characteristic vibrational bands. The crystalline structure was investigated using X-ray diffraction, and the obtained patterns matched standard reference data. UV–Vis spectroscopy was employed to determine the optical absorption characteristics.

Additionally, a microfluidic device was designed using SOLIDWORKS 2022 and fabricated via 3D printing, resulting in two models a quadrilateral device for pharmaceutical detection and a bilayer device for heavy-metal detection in blood samples.

The synthesized mono- and bimetallic nanoparticles demonstrated high efficiency in detecting narcotic pharmaceutical substances through rapid and

visible color changes. Ag NPs showed excellent sensitivity toward Fentanyl Citrate ($C_{22}H_{28}N_2O \cdot C_6H_8O_7$), while CoO NPs effectively detected Tramadol Hydrochloride ($C_{16}H_{25}NO_2 \cdot HCl$). Bimetallic nanomaterials also played a significant role in detecting Pethidine Hydrochloride ($C_{15}H_{21}NO_2 \cdot HCl$). Moreover, Cu NPs successfully detected mercury at very low concentrations in blood plasma, where as ZnO NPs exhibited high sensitivity toward cadmium. Overall, the results confirm the potential of green-synthesized nanomaterials combined with microfluidic platforms as rapid, low-cost, and effective sensing systems for pharmaceutical and heavy metal detection.

Table of Contents

Table of Contents

Table of Contents

List of Tables

List of Figures

List of Figures

List of Figures

List of Figures

List of Abbreviations

Abbreviations	Key
NPs	Nano Particles
BNPs	Bimetallic nano particles
PVD	physical vapor deposition
IGC	Inert Gas Condensation
IONPs	iron oxide nanoparticles
ST	Solvothermal
HT	Hydrothermal
CFF	cell-free filtrate
EOF	Electroosmotic flow
EWOD	Electrowetting-on-Dielectric
TDM	Therapeutic drug monitoring
GC-MS	gas chromatography-mass spectrometry
LIF	Laser Induced Fluorescence
WHO	World Health Organization
EPA	Environmental Protection Agency
OSHA	Occupational Safety and Health Administration
AAS	atomic absorption spectroscopy
ICP-MS	Inductively coupled plasma mass spectrometry
LOD	limit of detection
RSD	relative standard deviation
SD	standard deviation
BS	Boswell sacra
Ag NPs	Silver nano particles
Ni O NPs	Nickel oxide nano particles
Co NPs	Cobalt nano particles
Fe NPs	Iron nano particle
Zn O NPs	Zinc oxide nano particles
Cu NPs	Cupper nano particles
UV-Vis	Ultraviolet-Visible Spectrophotometry
XRD	X-Ray diffraction
FESEM	The field emission scanning electron microscope

List of Abbreviations

EDX	Energy Dispersive x-ray spectroscopy
TEM	Transmission electron microscopy
FTIR	Fourier Transform Infrared Spectroscopic
DLS	Dynamic light scattering
PDI	Particle distribution length
D	Particle size
Ph	Potential of Hydrogen
LOC	Lab on a chip
Hg^{+2}	Mercury ion
Cd^{2+}	cadmium ion
R^2	correlation coefficient
HPLC	High performance Liquid chromatography
SERS	Surface Enhanced Raman
LC-MS/MS	Liquid Chromatography -Tandem Mass Spectrometry
SPCE	screen-printed carbon electrode
DPASV	Differential Pulse Anodic Stripping Voltammetry
PCD	paper-based colorimetric device

Chapter one

Introduction

1.1 Nanomaterials

Nanomaterial is a particle of matter with a diameter of one to one hundred nanometers (nm) and is commonly referred to as a nanoparticle or ultrafine particle. Nanoparticles frequently exhibit distinctive size-dependent features, mostly due to their tiny size [1]. The nanostructure can be one-dimensional, two-dimensional, or three-dimensional within the nanoscale range. At these scales, the surface-to-volume ratio becomes extremely high, resulting in dramatic changes in mechanical, optical, electrical, and magnetic properties compared to the bulk state [2, 3].

The very small size of nanomaterials and shape-related properties have made them useful materials in various fields and industries [4].

Scientists assume that nanoparticles and nanomaterials that were designed first occurred during the Big Bang through meteors, which resulted in the formation of the universe and Earth, where the application of nanotechnology rose in the 1980s due to the convergence of experimental developments that occurred over the years, including the invention of the scanning tunneling microscope in 1981 and the discovery of fullerenes during the year 1985 [5].Among the metallic nanoparticles, silver nanoparticles are regarded as one of the primary types used in biological and medical applications. Among the particles primarily used in biological applications, in the nineteenth century, silver particles were used as antibacterial agents [6, 7].

In 1990, nanoparticles were identified using a transmission electron microscope, where scientists analyzed a cup with two colors to explain the phenomenon of dichroism. It was observed that this was due to the presence of nanoparticles with a diameter ranging from 50 to 100 nanometers. Nanotechnology became a very common term since the year 1990 owing to the development in the field of imaging technology that led to specialized applications in the industrial sector [8]. The word "nanomedicine" was coined in 1991 as the usage of nanotechnology in

medicine to diagnose, monitor, prevent, and treat different diseases that attack humans [9].

Today, the scale of production of nanoparticles and nanomaterials is large, and such objects are irreplaceable in numerous increasingly large industries. This optimizes and assists studies in such areas as applications of biochemistry, biophysics, and biochemical engineering. In the recent past, nanotechnology has been incorporated with other sciences in order to come up with novel forms of nanomaterial that are, perhaps, applicable in areas such as diagnostic tools, the delivery of drugs, the generation/storage of energy, or even the removal of environmental pollution, areas of agriculture, and food processing. Intra-facilities may be added to nanoparticles, nanostructures, and nano systems in comparison to traditional materials because it is easier to alter the scale rather than the shape and composition [10].

Nanotechnology is revolutionizing manufacturing methods of materials and production of devices. Nanotechnology and nanoscience depend crucially on the synthesis of nanomaterials. The various aspects that affect the crystallization and the subsequent formation of stable nanoparticles during the process of synthesis of nanomaterials are temperature, concentration of the reactants, time of reaction and pH. Nanoparticles take a number of varieties, such as hexagonal, circular, triangular, and chain-like shapes. Conventionally, nanoparticle synthesis occurs in two ways as shown in the figure (1-1) that could be categorized depending on how they are assembled, i.e., top-down begins with large materials and reduces to the nanoscale, it can be likened to sculpting since it starts with a block of marble, and one chips away and chisels on top of another [11].

The bottom-up method is a visualization in which nanomaterials are compartmented atom by atom or molecule by molecule. These methods exploit physical and chemical forces that incline atoms and molecules to organize by themselves in a predetermined manner [12].

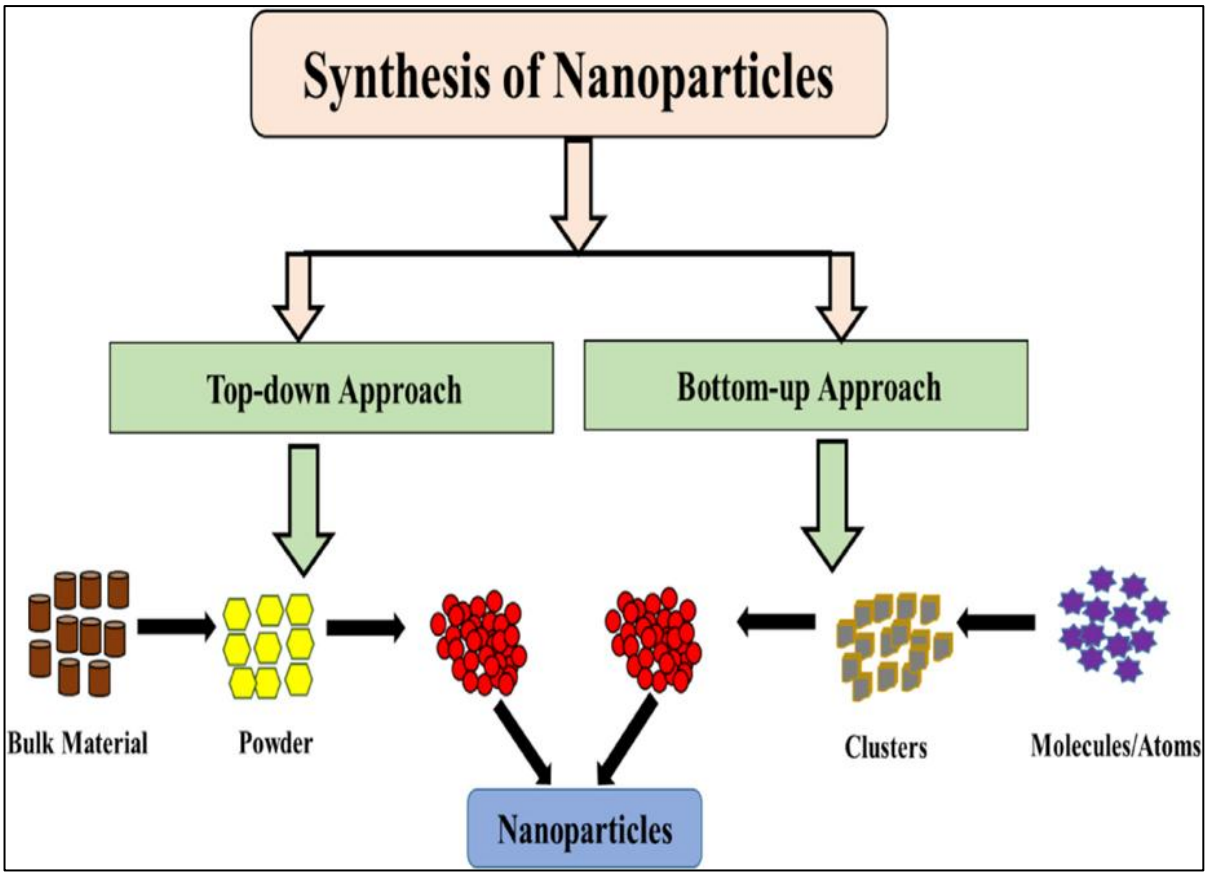

Figure (1-1) **:**Schematic representation of 'top-down approach' and 'bottom-up approach' for synthesis of nanoparticles [13].

1.2 Methods of nanomaterials synthesis

Nanomaterials can be synthesized through several major approaches, which commonly categorized into three main methods: physical, chemical, and biological. Each method differs in its principles, processing conditions, and the characteristics of the resulting nanoparticles [14].

1.2.1 Physical Methodes

The physical approach to creating nanomaterials involves the principle of using mechanical pressure forces and thermal energy where the material condenses, melts, evaporates, or erodes. Environmental friendliness and lack of pollution distinguish the physical method from the chemical method. In addition, it produces homogeneous nanoparticles, and this method is also free of chemical solvents.

It is common to obtain nanomaterials by physical processes involving the fragmentation of bulk materials in a top-down process [15]. The physical methods for preparing nanomaterials include the following:

1.2.1.1 Mechanical milling

The first ball mill was created by the German physicist and chemist Friedrich Fischer in the late 19th century. In 1970, John Benjamin developed the synthesis of oxide-dispersed strengthened alloys that could withstand high temperatures and pressures [16].

The ball milling strategy is a mechanical approach to reduce the particle size of materials, such as powders and suspensions. This simple technique involves grinding bulk materials in rotating cylinders containing solid balls (usually made of steel or ceramic). When the balls collide with the material, they generate enough force to break it down into nanoparticles. One of the critical parameters in the ball milling process is the milling time, which determines the extent of particle size reduction and the level of homogeneity in general, longer milling times lead to smaller particle sizes, but there is a limit beyond which the particles can become too fine and unstable. The duration of milling affects the degree of mechanical activation, particle size and distribution, as well as the final structure and product properties.

Longer milling times usually lead to smaller particle sizes, larger surface areas, and an increase in defects. This method is characterized by its simplicity, effectiveness, and low cost. The old method is widely used to produce metal nanoparticles and metal oxides used in food packaging applications [17, 18]. Naaman Salah and others used this method to prepare zinc oxide nanoparticles with antibacterial activity [19]. figure (1-2) explains the mechanism of ball milling.

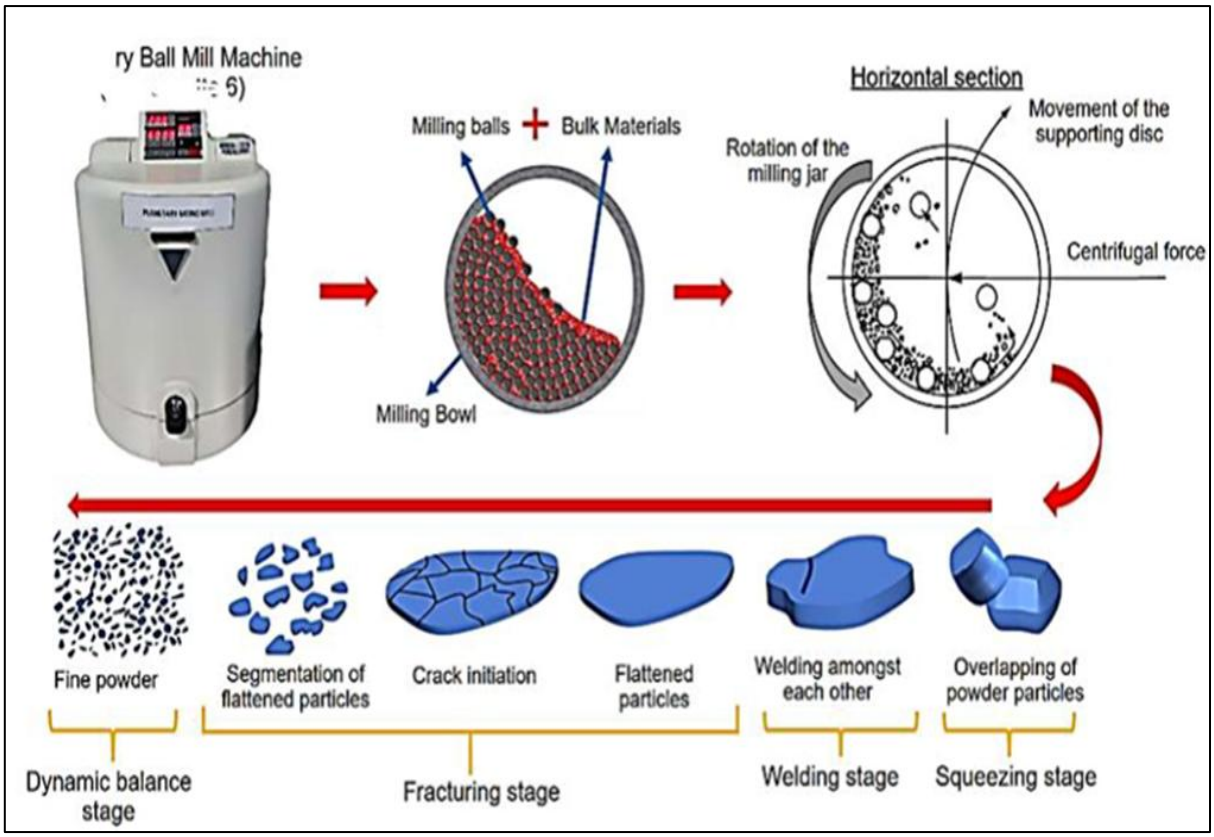

Figure (1-2)**:** Principles of the ball milling method for reducing powder particle size [18].

1.2.1.2 Laser Ablation

One of the physicochemical processes for generating nanostructures based on material removal through the interaction of a laser with the material from the solid target in the liquid. The final structure and other properties of nanomaterials depend not only on the interaction of the laser with the material but also on subsequent evaporation parameters such as laser irradiation duration, pulse width, solid target background, solvent nature, and laser beam optics. The laser ablation process of solid targets in a liquid environment allows for the generation of nanoparticles with various valuable properties, such as high purity, easily deployable surfaces, thermally stable compositions, or complex structures, including doped nanocrystals [20] and for the core shells, hollow spheres, nanofibers, or nano fluorescents, the laser ablation process is carried out by directing a powerful laser onto a metallic target placed in a liquid. Part of the laser

pulse interacts with the surface of the target to form the plasma generated by the laser in the liquid, while most of the energy is spent on heating the electrons during the interaction. This means that the material reaches the plasma phase during the initial interaction of part of the laser pulse with the material.

This means that the material transitions to the plasma phase during the initial interaction of a part of the laser pulse. The plasma cloud is mainly composed of a large amount of atoms, ions, and electrons that are ejected from the solid target through multiphoton absorption. If the pulse duration is greater than a few tens of picoseconds to a few nanoseconds, the lateral part of the laser pulse stimulates a temperature gradient in the plasma cloud by reheating the laser-emitted materials, i.e., the plasma cloud. While the targeted solid species absorb the lateral part of the laser pulse, they generate a constant amount of evaporated species. Thus, the plasma column expands unevenly due to the shock wave, leading to an increase in pressure and additional temperature in the plasma generated by the laser. The temperature of the plasma cloud generated by the laser increases rapidly because it arises from the pressure generated by the plasma[21]. The shock wave resulting from the expansion the plasma cloud drives the plasma produced by the laser into a unique thermal state with extremely high pressure and temperature. The plasma cloud plays an important role in the formation of nanoparticles, as nanoparticles are formed within the mass of the plasma cloud. There is a rapid exchange of energy from the plasma cloud to the surrounding liquid, leading to various types of chemical reactions within the liquid and plasma. The energy transferred to the surroundings causes the formation of a thin layer of vapor figure (1-3) explain this process.

This vapor layer transforms into the initial stage of cavitation bubbles and expands until equilibrium is reached. To achieve equilibrium in the surrounding liquid, the cavitation bubbles begin to collapse when the bubble pressure reaches its minimum at the maximum expansion of their volume. The subsequent stage of

plasma cloud development, the sudden cooling and contraction of the plasma cloud accompanied by a decrease in temperature, leads to the release of nanoparticles.

Despite the significant success of this method in manufacturing colloidal nanostructures, some aspects of the laser ablation process limit its use in industrial nanostructure fabrication, such as low colloidal stability and phenomena resulting from agglomeration. It is also considered a bond-free synthesis. This process has been used to produce silver nanoparticles applicable in water treatment from organic compounds. A composite nanostructure was created using the pulsed laser method by making a silver plate [22].

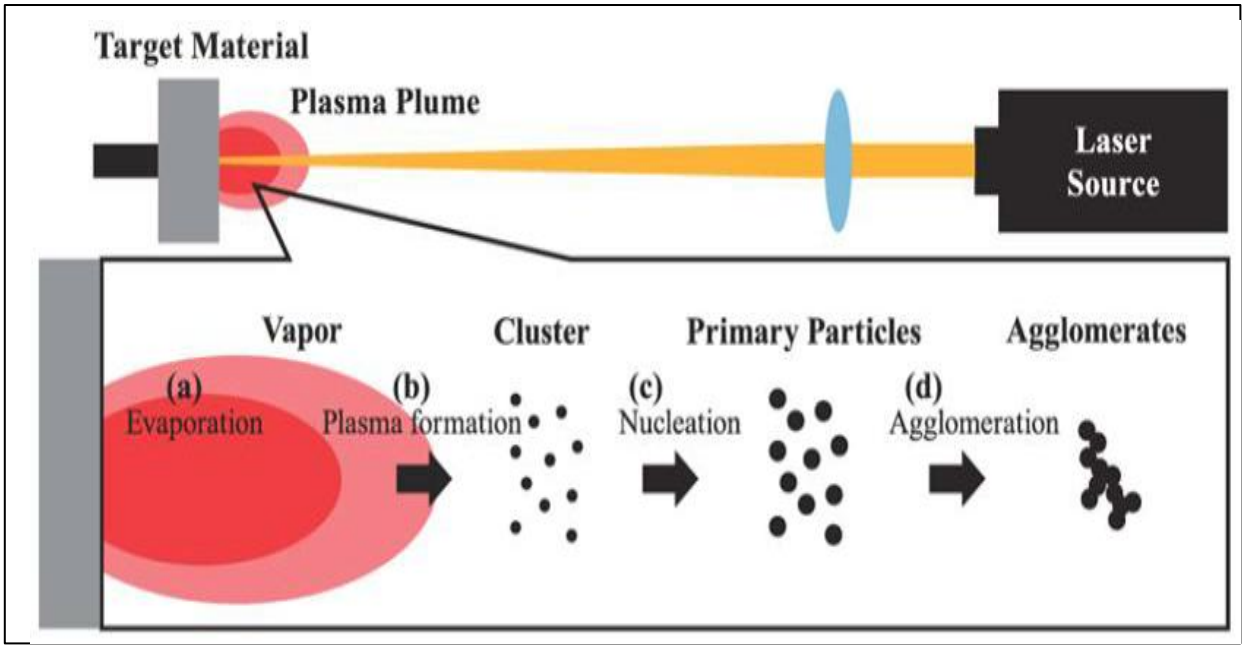

Figure (1-3)**:** Laser ablation process [23]**.**

1.2.1.3 The physical vapor deposition (PVD)

It was discovered in the early twentieth century, but most of its development occurred in the 1960s and 1970s, and it became widely used in industrial applications. The table (1-1) shows the physical vapor deposition techniques.
The coating material is deposited onto a substrate by directing a beam of ions and electrons towards the target. In the magnetic deposition process, which is a plasma-based coating process, negatively charged source materials are shattered by positively charged particles from magnetically confined plasma. When two bodies collide, the atoms in each are pushed away from each other and eventually settle onto the substrate. Vapor deposition, or physical vapor deposition (PVD), is a versatile and popular method for applying thin films of materials onto surfaces across a range of industries. Due to their numerous functional and aesthetic benefits, PVD coatings are useful in various applications, from electronics and optics to automotive and medical equipment [24].

PVD coating technology significantly improves the effectiveness and quality of medical implants. PVD-coated medical implants improve osseointegration, reduce wear and friction, increase corrosion resistance, and possess antibacterial properties, leading to better patient outcomes, reduced complications, and an overall higher quality of life for individuals who require implantable medical devices [25].

This technique is widely used to prepare nano-layers and particles using ion sputtering or evaporation. This process is ideal for preparing nano-metals such as Cu, Ag, and Au. It is characterized by its ability to control the thickness and composition of the layer and produce nano-materials free from chemical contaminants, making it suitable for use in medicine, industry, and precision sensors [26].

The results from previous studies show the success of the materials prepared in this manner as sensors, and they are also used in sensor devices [27] . Through

this technique, High-quality zinc oxide nanowires on n-type silicon substrates using the physical vapor deposition method[28] , Different types of zinc oxide nanocrystals were also synthesized through the physical vapor deposition of zinc powders without the presence of catalysts and subsequent exposure to air at high temperatures. It was found that these crystals are composed of zinc oxide nanowires [29].

Table (1-1): shows the different technologies of PVD coating

<table>
<tr><th colspan="2">Sputtering</th><th>Evaporation</th></tr>
<tr><td>Ion Beam Sputtering</td><td>Magnetron Sputtering</td><td>Electron Beam (E-Beam) Evaporation</td></tr>
<tr><td>Ion Beam Sputtering (IBS) / Ion Beam (Sputter) Deposition (IBD)

An ion beam is focused on a target. Subsequent ion bombardment physically erodes the deposited material on the substrate. By introducing reactive
 
gases like oxygen, materials like dielectrics can be sputtered using a focused ion beam.</td><td>Sputtering with a Single Magnetron
 
The processing chamber has just one magnetron, and its target diameter is larger than the substrate's. The setup allows for high-output thin films to be produced.</td><td> 
When current is passed through a tungsten filament, an electron emission is created; this emission is then combined and accelerated to generate an electron beam using high voltage. A magnetic field deflects the e-beam, directing it into the crucible. The substance in the crucible is subjected to intense bombardment from the e-beam, turning into a gas and deposited onto the substrate.</td></tr>
<tr><td>Dual Ion Beam Sputtering (DIBS) / Dual Ion Beam (Sputter) Deposition (DIBD)
 
Additional ion bombardment of the substrate can be introduced with the help of an assist ion beam source. The film's development can be tweaked, and the substrate can be cleaned.</td><td>Confocal Sputtering
 
Each magnetron in the sputter setup has an intended diameter less than the substrate's. Bipolar sputtering (using the same target material) and co-sputtering of alloys (using separate target materials) possess a combination of magnetrons. Rapid substrate rotation is required to maintain a consistent surface material mixture.
Dynamic Sputter Deposition
 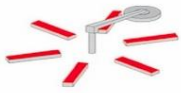
A rotating substrate is rotated linearly or orbitally over rectangular magnetrons to create multilayer coatings. By calculating the movement profiles in advance, we can counteract the magnetrons' unique emission profiles and adjust the layer thickness by changing the rotational velocity.</td><td>E-Beam Evaporation with Ion Beam Assistance
 
The substrate is pre-cleaned using an ion beam source built into the electron beam evaporator.
The finest quality PVD coating is created using ion beam sputtering. Evaporation production is no longer viable because of increased accuracy and layer density demands in industries like microelectronics and precision optics.</td></tr>
</table>

1.2.1.4 Inert Gas Condensation (IGC)

In the gas-phase condensation method, a system that uses a circular magnet to create a lot of metal vapor is employed. Iron nanoparticles of selected size are deposited through four main processes: evaporation, aggregation, filtration, and deposition. In the gas-phase condensation technique, a cathodic erosion system with a circular magnet is used to generate excessively saturated metal vapor.

The size of the nanoparticles can be adjusted by three parameters: the length of the condensation zone (which can range from 30 to 150 mm), the magnetron power (which ranges from 25 to 100 W), and the gas flow (Ar and He, partial pressure 1-2 × 10^{-1} Torr). The condensation zone is defined as the distance between the magnetron head (erosion zone) and the first expansion orifice; this condensation zone can be adjusted by a linear motor, which reduces or increases the distance between the magnetron head and the first expansion orifice. Similarly, accumulation the size of the nanoparticles can change over time once the saturated metal vapor is collected, due to the increase or decrease in the residence time of the nanoparticles in the aggregation zone [30].

Another factor that modifies the size of the nanoparticles is the magnetron power; as the magnetron power increases, the density of the evaporated atoms from the target increases, leading to an increase in the size of the nanoparticles. This relationship increases linearly upon reaching a saturation system, where increasing energy slightly reduces the size of the nanoparticles. The final parameter for modifying the size of the nanoparticles is the gas flow (Ar and He), where Ar is used as an etching gas. With the increase in Ar flow, the metal vapor pressure increases. When He gas was introduced into the chamber (which was used as a carrier gas) and its flow was increased, the size of the nanoparticles was reduced; this reduction is related to the collisions between the nanoparticles and He particles; thus, the mean free path of the nanoparticles is reduced which decreases their size[31].

IGC is a powerful tool for measuring the surface energy and acid-base properties of solid materials, which helps in understanding the behavior of powders, fibers, and nanoparticles in different environments.

The basic tools for IGC technique are inexpensive, widely available, and perfectly suitable for routine laboratory applications. Using standard gas chromatography devices or slightly modified gas chromatography devices enables the collection of retention data for the tested materials over a wide range of temperatures [32]. prepared Fe_3O_4 and study of using targets for the discharge and Ver Hemben deposition of magnetic nanoparticles on thin silicon substrates coated with PEG Gen Trio system. He emphasized using the IGC technique by the Mantis Nano that. The produced nanoparticles do not require further purification and are ready for use; for example, in biomedical applications [33].

1.2.2 Chemical Methods

Chemical synthesis refers to the process by which nanomaterials are produced through chemical reactions occurring in either a single-phase solution or a multiphase system. In contrast to mechanical fabrication methods (top-down approaches) and physical methods such as gas-phase synthesis, chemical synthesis methods are generally classified as wet or liquid-phase synthesis techniques. In these methods, soluble precursor species are converted into insoluble or slightly soluble products, leading to nucleation and precipitation of nanomaterials [35,34].

Chemical synthesis of nanomaterials typically follows a bottom-up approach, which enables precise control over particle size, morphology, and composition. Additionally, this approach facilitates surface modification and functionalization of nanostructures with relative ease. One of the main advantages of chemical methods over physical approaches is that they do not require large-scale or expensive equipment, unlike many physical synthesis techniques [36].

Wet chemical synthesis allows for accurate control of reaction parameters, including temperature, precursor concentration, additives, and pH, which is essential for obtaining nanomaterials with desired properties. However, the formation and deposition of toxic reaction by-products on the surface of nanoparticles during synthesis may limit their application in biomedical fields and pose potential environmental risks. Consequently, non-toxic and environmentally friendly biosynthesis methods have been developed to overcome these limitations [37]. Chemical synthesis methods can be further classified into several main techniques, including:

1.2.2.1 Chemical Reduction Method

The chemical reduction method is one of the most widely employed techniques for the synthesis of metallic nanoparticles. This method is based on the reduction of metal ions dissolved in an aqueous or organic medium using a suitable reducing agent, leading to the formation of zero-valent metal atoms. Historically, the earliest systematic studies on colloidal metal nanoparticles prepared by chemical reduction date back to 1857, when Michael Faraday reported the synthesis of colloidal gold [38].

The reduction process can be carried out in either aqueous or organic solvents. However, organic solvents are often preferred due to the high susceptibility of metal nanoparticles to oxidation in aqueous environments. Proper control of the reaction conditions enables the production of metal nanoparticles with tailored particle size, shape, and size distribution. Parameters such as temperature, metal salt concentration, reduction potential, surfactant type and concentration, solvent viscosity, and surface tension play a crucial role in determining the final physicochemical properties of the nanoparticles, including size, morphology, stability, and degree of agglomeration.

The synthesis of metallic nanoparticles via the chemical reduction method generally proceeds through three fundamental steps, The first step involves a

redox reaction, during which electrons are transferred from the reducing agent to the metal ions, resulting in the formation of free metal atoms. The second step is the nucleation stage, where these free metal atoms collide and combine to form stable nuclei. Once a critical nucleus size is reached, the nuclei become thermodynamically stable and persist in the solution. The third step consists of particle growth and stabilization, in which additional metal atoms deposit onto the existing nuclei, leading to the formation of nanoparticles at the nanoscale [39,40].

To prevent excessive particle growth and agglomeration, stabilizing agents (capping agents or surfactants) are introduced to adsorb onto the nanoparticle surface and provide steric or electrostatic repulsion. One of the major advantages of the chemical reduction method is the precise control it offers over nanoparticle size and morphology. In addition, it is a cost-effective and easily scalable technique that does not require high pressure, extreme temperatures, or excessive energy input, making it suitable for large-scale nanoparticle production. Several studies have demonstrated the effectiveness of this method in synthesizing various metallic nanoparticles. For example, Alexandra Pricop and co-workers successfully prepared spherical copper nanoparticles using the chemical reduction method and reported their potential applications in biomedical fields, noting that the observed cellular toxicity was dose-dependent. Furthermore, copper nanoparticles synthesized by this approach have been utilized in 2D and 3D printing technologies. Similarly, Landage S.M. reported the preparation of silver nanoparticles via chemical reduction and confirmed that this method remains one of the most commonly applied techniques for silver nanoparticle synthesis [41].

1.2.2.2 Sol-Gel Method

The earliest work on sol-gel synthesis dates back to the mid-19th century when there were studies on the production of silica gel. Interest in the gel grew rapidly, and prominent researchers contributed their work in this field. A large

variety of ceramics were manufactured over the years, and in the 1970s, researchers introduced new methods for synthesizing multi-component glasses from oxides. The sol-gel method became a popular route for producing glasses and ceramics in large quantities [42].

Wet chemical procedures Sol-gel is a common technique of manufacturing nanomaterials. This technique forms different nanomaterials of high quality whose compositions are metal oxides. This process is referred to as the sol-gel process, where the initial liquid is converted to a colloidal liquid, which later on is turned into a networked structure known as the gel [43].

Metal alkoxides are the traditional raw materials used in the creation of nanomaterials with the sol-gel process. Using the sol-gel method, nanoparticles can be synthesized in the course of multiple steps. The first step involves the hydrolysis of the metal oxide in water or through the help of alcohol to make a solution. Thereafter, condensation takes place where the viscosity of the solvent is raised to create porous structures that subsequently are allowed to age. Even when condensed or multiply condensed, metal-hydroxy or metal-oxo polymers are obtained in the solution. The extreme polymerization persists during the aging process, which is accompanied by the shift in structure, properties, and porosity. Porosity becomes less.

Separation between the colloidal particles becomes more during the aging process. An aging process is followed by drying, wherein the water and organic solvents are evaporated in the gel. At last, the nanoparticles are obtained through the process of calcination. The determinants of the end product of the sol-gel process are the sol nature, rate of hydrolysis, aging period, pH, and molar ratio of H_2O with the sol. The sol-gel technique is cost-effective and possesses numerous other benefits, which include the homogeneous nature of the produced material, the low temperature of the process, and the technique's simple use to obtain

complex compounds and nanostructures, and the technique being a convenient route to fabricate multifaceted nanocomposites and designs [23, 44].

Ergas Abdurakhman examined manufacturing thin film samples at the composition of TEOS/75TiO_2 + CdO with the assistance of the sol-gel process That is sensitive to Co gas. Carbon monoxide (II) selective sensors were also developed [45].

1.2.2.3 Chemical Precipitation Method

The co-precipitation method is the most efficient and effective in the chemical synthesis approach, with a wide size distribution and high yield. However, the products of the co-precipitation method are characterized by poor size distribution, low crystallinity, and significant polydispersity. The chemical reaction of the co-precipitation method for preparing nano-sized iron particles, for example, is as follows:

$Fe^{2+} + 2\ Fe_3 + 8OH^- \rightarrow Fe_3\ O_4 + 4\ H_2O$……. (1)

$Fe_3O_4 + 2H^+ \rightarrow \gamma\ Fe_2O_3 + Fe^{2+} + H_2O$ …… (2)

Microemulsions consist of two immiscible liquids: oil in water and water in oil. The main strength of the microemulsion method is that it allows for the control of the size, formation, and aggregation of iron nanoparticles. However, the crystallinity and yield of magnetic iron oxide nanoparticles (IONPs) are relatively low [46] Additionally, the remaining surfactants may affect the properties of the iron nanoparticles. is worth mentioning that experimental factors, including pH value, types of iron salts, ionic strength in the medium, and the Fe(II)/Fe (III) ratio, significantly affect the properties of nanoscale iron oxide Like shape and size control [47].

in addition to the success of the chemical deposition method in preparing iron and lead, Bahari Molla Mahaleh succeeded in the preparation of NiO with an average particle size of less than 50 nm[48] .

1.2.2.4 Thermal Decomposition Method

Pyrolysis is a widely used method for preparing nanoparticles, especially metallic nanoparticles and metal oxides. Pyrolysis involves the decomposition of compounds at high temperatures to produce nanoparticles. The pyrolysis reaction often begins by heating the material to a temperature where it undergoes pyrolysis, resulting in the formation of nanoparticles as byproducts of the decomposition. The selection of the sulfide compound is crucial and depends on the desired composition of the nanoparticles. Common precursors include metal salts, metal complexes, organometallic compounds, and metal-containing polymers for nanometer-sized metal oxide particles, metal alkoxides or metal acetates are often used as precursors. The sulfide compound is dissolved or dispersed. In this method, organic-inorganic precursors are used to produce monodisperse nanoparticles at high temperatures. The magnetic nanoparticles prepared in this way possess high crystallinity, controlled size, and well-defined shape. The process of decomposing organic-inorganic precursors is carried out in the presence of organic surfactants to produce magnetic nanoparticles of the desired size and shape. The stabilizing agents used in the synthesis of magnetic nanoparticles include fatty acids, hexadecyl amine, and oleic acid. The stabilizers used in the decomposition process can slow down the nucleation of the nanoparticles, which controls the growth of the magnetic nanoparticles and helps produce a spherical shape and a desired size of less than 30 nm [49].

This method is considered one of the best ways to produce magnetic nanoparticles on a large scale with uniform size and homogeneous shape. The associated risk with this method is the production of soluble toxic organic solvents, which limits its application in the biomedical field. Thermal decomposition is more advantageous compared to co-precipitation for synthesizing smaller-sized magnetic particles[50].

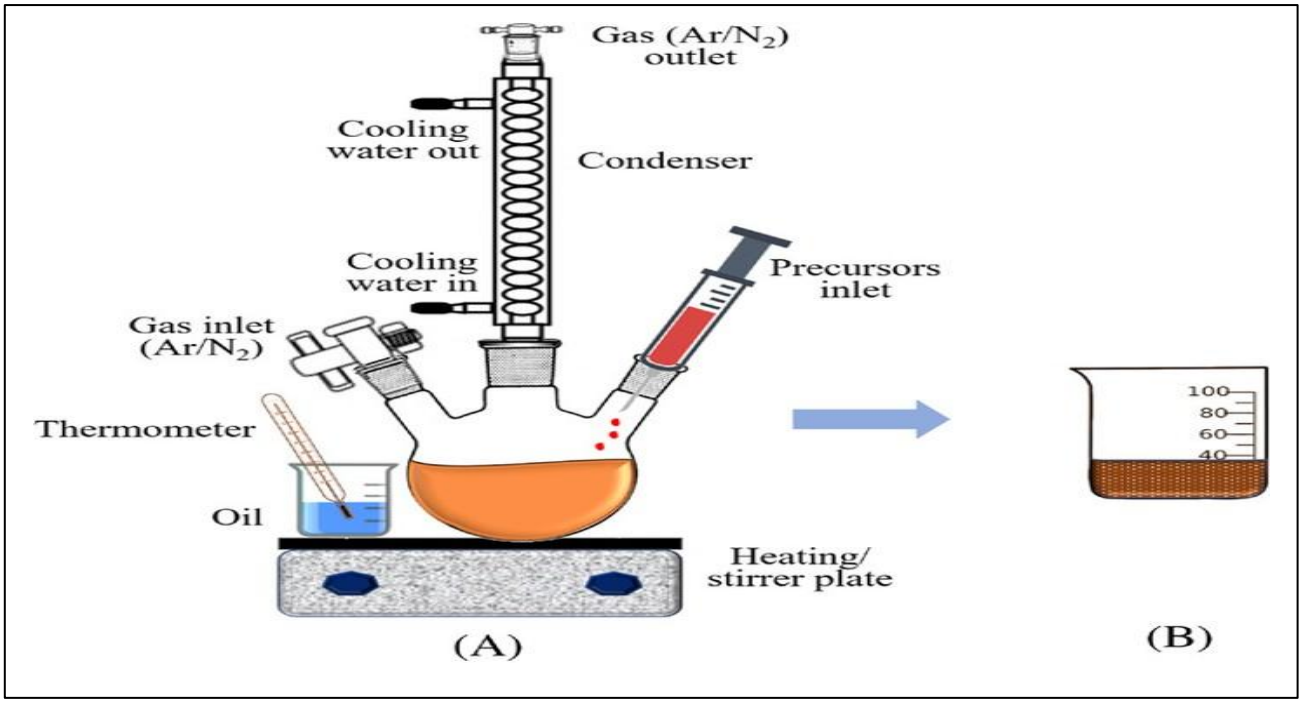

Figure (1-4) **:** Experimental setup for nanoparticle synthesis following the thermal decomposition method [51].

1.2.2.5 Solvothermal and Hydrothermal Method

This method is defined as any heterogeneous chemical reaction in the presence of a solvent (aqueous or non-aqueous) above ambient temperature, and at a pressure exceedin1 atmosphere in a closed system. Chemists prefer the term "thermochemical state," which refers to any chemical reaction occurring in the presence of a non-aqueous solvent or a solvent under supercritical or near-supercritical conditions. Similar to Solvothermal (ST)and Hydrothermal (HT), there are several other terms such as glycthermy (in the presence of glycol), alcthermy (in the presence of alcohol), and ammoniothermy (in the presence of ammonia). However, the supercritical fluid technique is considered an extension of the HT technique [52]. Therefore, the term hydrothermal is used in many literatures to describe all heterogeneous chemical reactions that occur in solutions. Aqueous Processing materials using the ST technique requires low energy, shorter reaction times, and most importantly, scalability.

The raw materials or precursors used in most inorganic material synthesis by the

liquid method are metal salts and appropriate solvents. Additionally, by changing the synthesis parameters: temperature, pressure, or reactant concentration, the properties of the particles can be easily controlled. HT/ST synthesis and its applications are not limited to thermoelectric materials. This synthesis technique has been successful in preparing important solid materials: chemical sensors, luminescent phosphors, mesoporous crystals, superionic conductors, electronically conductive solids, ceramics, complex oxides and fluorides, and magnetic materials. Although HT/ST techniques can provide excellent control over shape and particle size distribution, adjusting the chemical ratios and obtaining dense materials can be challenging, which may negatively affect the electrical transport properties [53].

1.2.3 Biological Methods

Although physical and chemical methods are effective in creating well-defined nanoparticles, they have some drawbacks, including long synthesis times, high production costs, difficulty in purification, and the disposal of hazardous and harmful by-products. Chemical synthesis techniques can also contribute to the emergence. The hazardous chemical species that have been absorbed, which can have negative consequences in medical applications[54].

Green synthesis methods have advantages over traditional methods that use environmentally toxic chemical agents. Nanoparticles were synthesized by biological entities both inside and outside the cells. The ability of living systems to reshape inorganic metal ions into nanoparticles using their intrinsic organic chemical processes has revealed an previously unknown field in biochemical analysis [55].It combines nanotechnology and biology to form nanobiotechnology, an advanced field that involves living organisms of both eukaryotic and prokaryotic origin. The technique of nanoparticle synthesis follows bottom-up approach that involves an initial reaction (oxidation/reduction). To create nanoparticles of metals and metal oxides, these

methods use biological systems such as fungi, actinomycetes, bacteria, viruses, yeast, biological molecules, various plant extracts, etc. [13].

Nanomaterials manufactured using environmentally friendly methods contribute to developing sustainable electronic devices with improved performance and reduced waste. In the biomedical field, nanotechnology offers unique opportunities to study and manage a wide range of technologies at the nanoscale, with the potential to create a revolutionary impact on biology, medicine, and other health-related fields. Nano-carriers have unique advantages for targeted drug delivery systems, diagnostics, anti-cancer activity, and anti-microbial activity. Different types of nanoparticles (NPs), such as solid lipid nanoparticles, metal nanoparticles, polymeric nanoparticles, carbon nanotubes, nanogel-based compounds, nano capsules, nanofluids, nanowires, and liposomes, are just a few examples of the diverse range of nanomaterials of biomedical importance the potential for their use in therapeutic applications has been examined, with a focus on their suitability and biocompatibility, drug management, drug delivery, cancer diagnosis and treatment, and antimicrobial applications[56].

Nanoparticles can be produced using a variety of techniques, including hydrothermal reaction, conventional heating, anodic oxidation, evaporation deposition, wet oxidation, electrochemical deposition, and sonication. However, these production techniques are often expensive, require a significant amount of manual labor, and harm the environment and living organisms. Green synthesis offers a highly desirable alternative by using bacteria, fungi, yeast, algae, and plants to produce nanoparticles.

Green synthesis has numerous advantages, as it allows for rapid large-scale synthesis, is cost-effective, environmentally friendly, and does not require the use of hazardous chemicals, high temperatures, or excessive energy. For drug delivery, there are two different types of nanoparticles. The first group includes

natural or synthetic polymers, while the second group contains metallic nanoparticles Ag, Zn, Fe, Cu, etc. [57].

1.2.3.1 Biological resources for the green synthesis of nanoparticles

Bacteria, fungi, algae, and types of plants are among the most commonly used biological resources in the green synthesis of nanoparticles. This biological approach has provided a reliable, simple, non-harmful, and environmentally friendly method [58, 59].

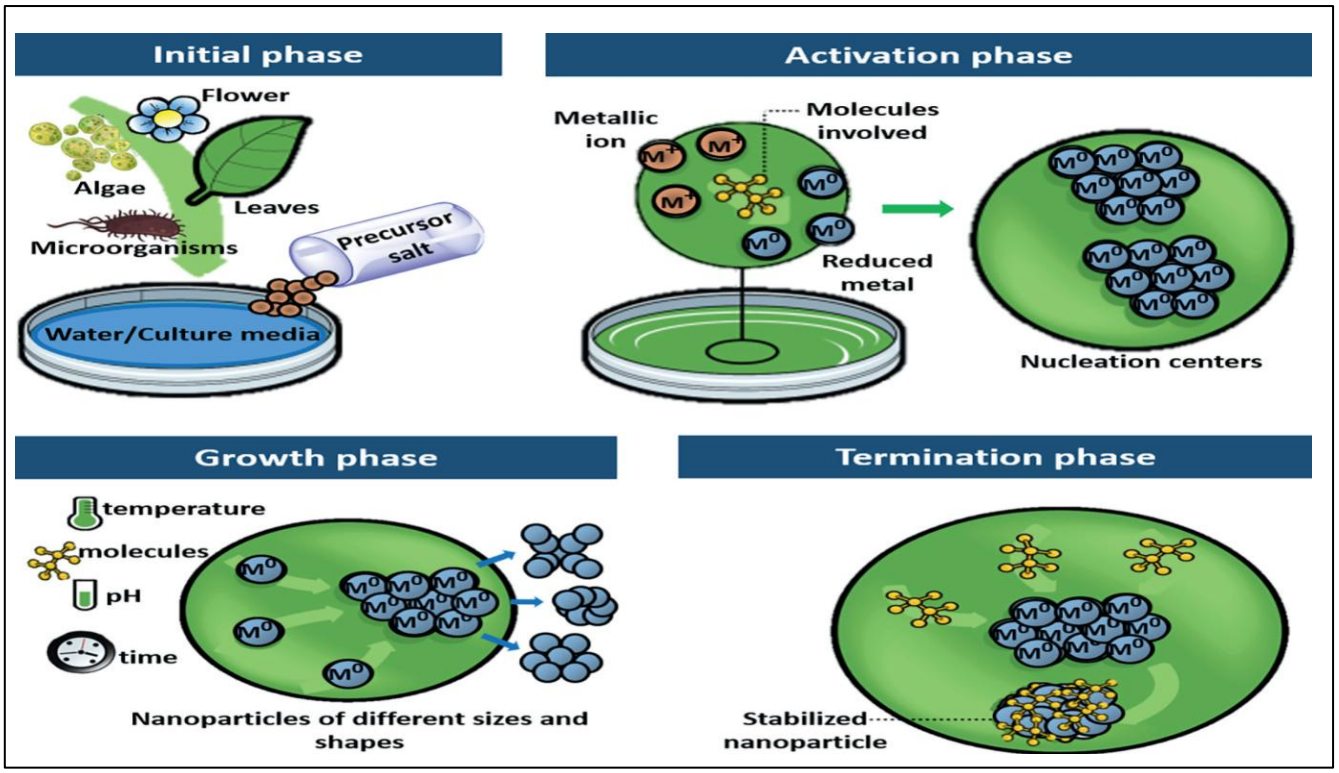

Figure (1-5): Phases involved in the green synthesis of nanoparticles [60].

Bacteria: Nanoparticle synthesis with the help of bacteria occurs in two ways, the extracellular approach and the intracellular approach. The extracellular synthesis of nanoparticles has an advantage over the intracellular method in that it is less time-consuming, as it does not require any subsequent process to collect the nanoparticles from the living organisms.

Bacteria contain an intracellular reductive enzyme that catalyzes the reduction of metal ions to metallic nanoparticles.

Bacterial species such as (D. radio Urans) are characterized by high antioxidant activity and high resistance to radiation and oxidative stress. It makes it suitable for use in the green synthesis of gold nanoparticles from its ionic form. The synthesized gold nanoparticles Au NPs were more stable for a longer period and exhibited better antimicrobial activity [61].

Fungi: A large group of fungi is used in various applications across multiple sciences, such as bioremediation, enzyme production, and nanotechnology[62]. Fungi have garnered significant interest in the production of metallic nanoparticles due to their several advantages over bacteria when it comes to nanoparticle synthesis. The simplicity of the expansion process and subsequent treatment, as well as the economic feasibility and the presence of fungi, which provide a larger surface area, are all significant advantages. The mechanism of biomineralization is used in the production of fungal-based nanomaterials, which involve internal and external enzymes and bioactive particles by reducing various metal ions. Additionally, Au, Ti, Se, Cu, and Zn were identified as the most important metal ions used by fungi in the production of nanoparticles. Further research has been conducted on the synthesis of nanomaterials using the fungal species Fusarium, Aspergillus, Trichoderma, Verticillium, Rhizopus, and Penicillium [63] .

The fungus Fusarium oxysporum can produce nanomaterials from zinc sulfide, for example, by incorporating ZnO nanoparticles using A. Niger and F. keratoplasty, resulting in the development of ZnO NPs with a consistent diameter ranging from 8-38 nanometers and 10-42 nm for Z particles Hexagonal and vertical nanostructures, respectively, with high monodispersed (evenly distributed) and free from any agglomerations. Additionally, the authors recommended that the protein buried by the fungi was associated and reduced. ZnO NPs were spherical in shape and prevented the nanoparticles from

agglomerating. Additionally, a cell-free filtrate (CFF) from the Aspergillus Tereus alternative was used in the incorporation of ZnO NPs [64, 65].

Plant: The plant-assisted synthesis of nanoparticles is more efficient in terms of achieving a higher yield compared to microbial synthesis. Plants have various natural substances and chemicals like (polyphenols) that can help stabilize and reduce materials in the creation of nanoparticles. The synthesis of nanoparticles by plants is environmentally friendly (avoiding the use of toxic chemicals) and economical. It was found that the nanoparticles manufactured from plant sources were much more stable than those formed by microbes and fungi. The synthesis of nanoparticles by plants can be classified into three groups: extracellular, intracellular, and through phytochemicals. The extracellular method is used when the plant extract is employed as a raw material for nanoparticle synthesis. The synthesis of nanoparticles occurs intracellularly within the plant tissue cells using cellular enzymes. After synthesis, the nanoparticles are recovered by rupturing the cell wall of the plant cells. The synthesis of nanoparticles from plant extracts is a relatively cheaper method and leads to a higher yield due to the presence of larger amounts of phytochemicals in plant extracts that can stabilize or reduce metal ions to metallic nanoparticles [61].

The most important advantages of the green synthesis method are that it is environmentally friendly, meaning it reduces the use of chemicals and toxic substances. It operates under mild conditions, and plant chemicals act as both reducing and capping agents simultaneously. They are renewable materials. However, the limitations include difficulty in controlling the shape, making it hard to achieve a uniform shape, and the inability to expand indefinitely without standardizing the specifications. Additionally, there is variation in the composition of plant extracts from batch to batch [66].

Previous researchers have counted various nanomaterials from several plant extracts. They used basil extract [67]. To prepare ZnO, while olive leaf extract

(A. M. Mohammed) for the preparation of Fe_2O_3 [68] . Additionally, silver was prepared using mint leaves Spherical silver nanoparticles were synthesized from the leaf extract of A. indica. FTIR analysis showed that the flavonoids and phytochemicals in the plant extract act as reducing and stabilizing agents during the synthesis of the nanoparticles. These nanoparticles exhibited strong antimicrobial activity , There are many other plant extracts as well[69] .

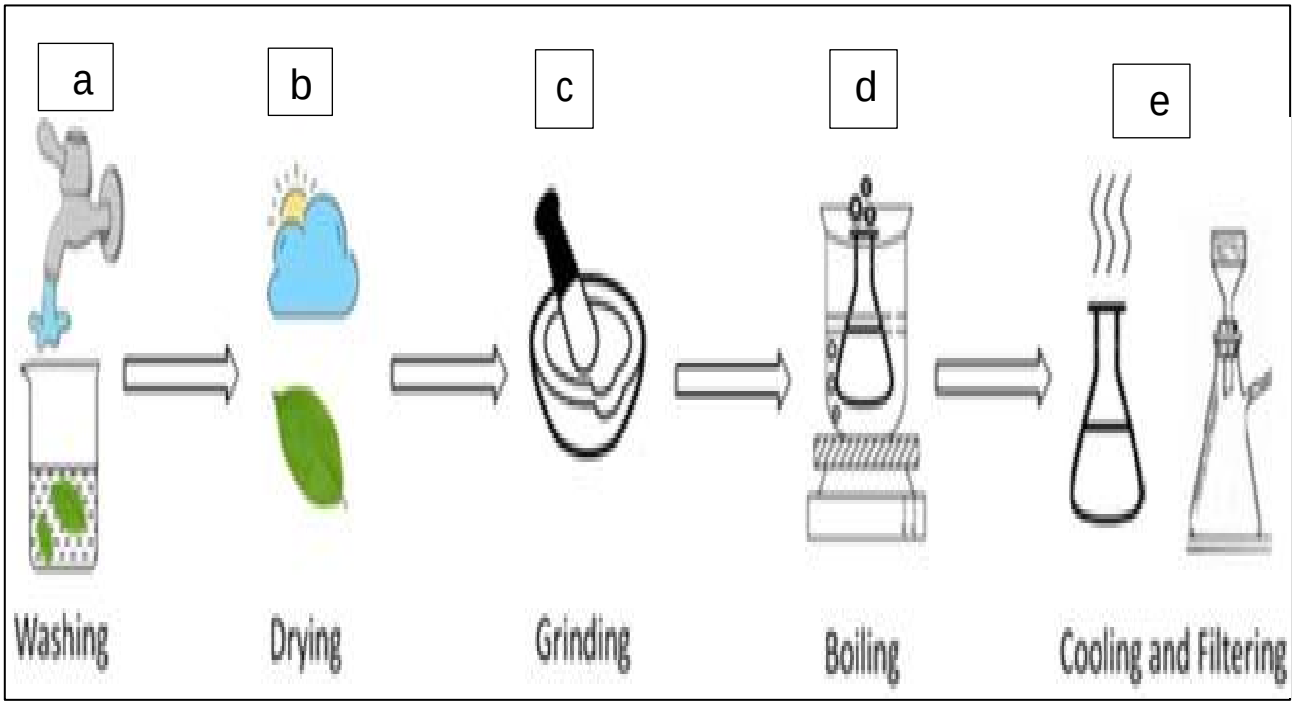

Figure (1-6): explains the steps to prepare the plant extract. The first step is to prepare the plant extract by washing the fresh or dried leaves or roots(a). Then, dry it well(b) And grinding it (c). After that, it is boiled in distilled water, deionized water, or a mixture of ethanol and water to extract the bioactive compounds(d). The final step, after it is left to settle, is to filter the extract(e), and it becomes ready for use [66, 70].

Algae: they are renowned for concentrating heavy metal ions and molding them into easier forms. Consequently, algae have been cited as biosynthetic models to manufacture biogenic nanomaterials, fats, unsaturated fatty acids, and biologically active compounds such as chlorophyll, phycobiliproteins, pigments such as carotenoids (carotene and zeaxanthin), and antioxidants (polyphenols and

tocopherols). These all occur in algal extracts (phycoerythrin and phycocyanin) in different concentrations according to the type and age of algae.

Such active compounds have been predicted to be reducing and stabilizing agents towards nanoparticle synthesis [71].

Nanoparticle synthesis using algal resources in a broad range has proved to be among the most modern and renewable areas in the field of biochemical research because they have the capacity to reduce metal ions. Depending on both the algae type and the method of preparing, nanoparticles may be produced either intracellularly or extracellularly. In order to synthesize metal nanoparticles with algae, then, in most of the experiments carried out, the first step is heating/boiling the algal extract in water or an organic medium over a certain duration. Then ionic metal compounds in the form of molar solutions are prepared, after which the algae and the ionic metal compound solution are incubated under specific conditions either with or without stirring [72].

The synthesis of nanoparticles can happen in a very particular (and quantitative) way either extracellularly or intracellularly, depending on the properties of the algae. Polysaccharides, reduced carbohydrates, proteins, peptides, or other reducing species within the algal cultures may have reduced metal ions to nanoparticles using the carbon formed during the process in reducing states according to a theory that suggests the synthesis of extracellular metal nanoparticles.

Nanomachines made of Cyanophycean (blue-green algae), Chlorophyceae (green algae), Phaeophyceae (brown algae), and Rhodophyceae (red algae) through intracellular and extracellular synthesis of Au, Ag, and other metal nanoparticles have been utilized. The effective constituent compounds in the cellular extracts, including pigments and antioxidants from algae, have bioactive properties that make them a potential processing medium for numerous nanomaterials, as they are biocompatible and capable of acting as reducing agents. The nanoparticle

silver was synthesized; they can efficiently avoid bacteria growth in an environmentally friendly way [73].

promoting the bactericidal effect on the pathogens growing into Gram-negative and Gram-positive biofilms. Consequently, the silver nanoparticles that are formed by the brown algae can serve as an anti-Pollutants coating for many biomedical and environmental uses. In the form of anti-fouling coatings for a wide range of biomedical and environmental uses. The algae-produced nanoparticles can rival conventional drugs and have already proven to be antibacterial/anticancer [74]. However, the issue with current methods supports the safer and appropriate selection of solvents during the green synthesis process, the appropriate parameters of the process itself, the toxicity of nanomaterials to the cells exposed to these materials, mass production and manipulation of nanomaterial morphology, the burdensome preservation, and ignorance. Consequently, the development of the use of nanomaterials through green synthesis is mainly held at the laboratory level. Nevertheless, environmental friendliness, biocompatibility, and sensitivities of the resultant nanoparticles are more general in biomedical sciences, elimination of environmental pollution, and consumer markets. To popularize the use of nano biological materials in the future, it is desirable to study the mechanisms of the synthesis process, identify more biological and chemical parameters that are applicable in synthesis, promote the viability of green synthesis at the industrial level, and enhance the variables that will influence the synthesis process [75].

1.3 Bimetallic Nanoparticles

Bimetallic nanoparticles are nanostructures that contain two different metallic elements within a single particle in a core-shell or alloy structure. This combination produces synergistic effects that enhance the catalytic activity and chemical stability of the material, which improves overall performance [76]. This is different from the properties of each pure metal alone, as these effects can

enhance catalytic activity, chemical stability, electronic properties, and selectivity. These features make bimetallic nanoparticles highly desirable for heterogeneous catalysis, electrocatalysis, environmental remediation, biosensing, and energy storage [77,78].

Chemical stability, electronic properties, and selectivity of these formations significantly enhance electrochemical activity, making bimetallic nanoparticles highly desirable for heterogeneous catalytic reactions, electrocatalysis, environmental remediation, biosensing, and energy storage. Their adsorption capacity and catalytic properties make them suitable for environmental detection, energy storage, and biological sensing [79,80].

They also exhibit unique behaviors in gas sensing and biology applications. During the formation of bimetallic nanoparticles, the distribution of both metals can be random, leading to a single-phase crystalline structure if the components are solid solutions. It can be in the form of a core-shell, where one metal forms the core and the other metal covers it with a thin shell, known as the shell. This type of formation enhances surface interaction while preserving precious metals [81].

It is also possible for them to be in the form of small clusters of one metal embedded in other clusters, in addition to being in the form of semi-nuclei (Janus particles) or distinctly arranged atoms that differ from random alloys [82, 83]. It has been mentioned that BNPs with core-shell structures can offer unique physical and optical properties that cannot be achieved in single-metal systems after preparing bimetallic particles composed of gold and silver with different optical properties and applications, including catalysis, signal enhancement devices, and biomedical purposes [84]. Many researchers have studied the preparation of nanomaterials in different ratios, including the 1:1 or 3:1 ratio. In 2008, Jahangeer Ahmed and others prepared Cu: Ni particles and found that increasing the copper ratio enhances the surface effects that counteract the magnetism experienced by

the surface before the two metals are combined [85,86]. Similarly, Pan prepared Co: Pt particles and found that among the prepared ratios, the 3:1 ratio was more effective than the 1:1 ratio, as it exhibited high stability and catalytic activity [87]. The figure (1-8) illustrates the variation in ratios for bimetallic nanomaterials.

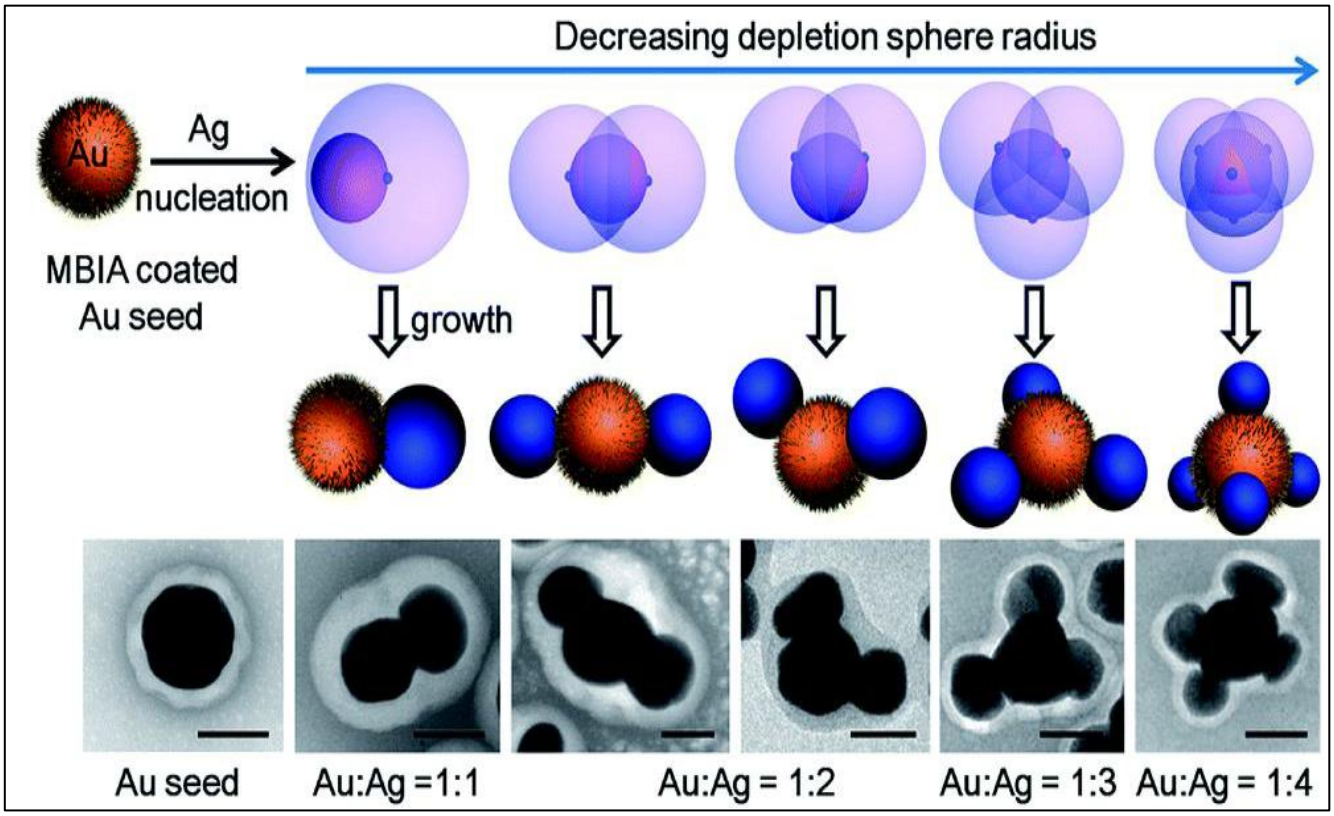

Figure (1-7): Schematics illustrating the effects of controlling the Ag nucleation on Au seeds and their later growth into Au: Ag Janus/core: satellite structures with different Au: Ag Island ratio: 1: 1; 1: 2; 1: 3; and 1: 4. New nucleation sites can start when the depletion sphere does not fully cover the seed surface [88].

As for the preparation methods of bimetallic nanomaterials, they are prepared using the same methods as the monometallic materials shown in figure (1-9).

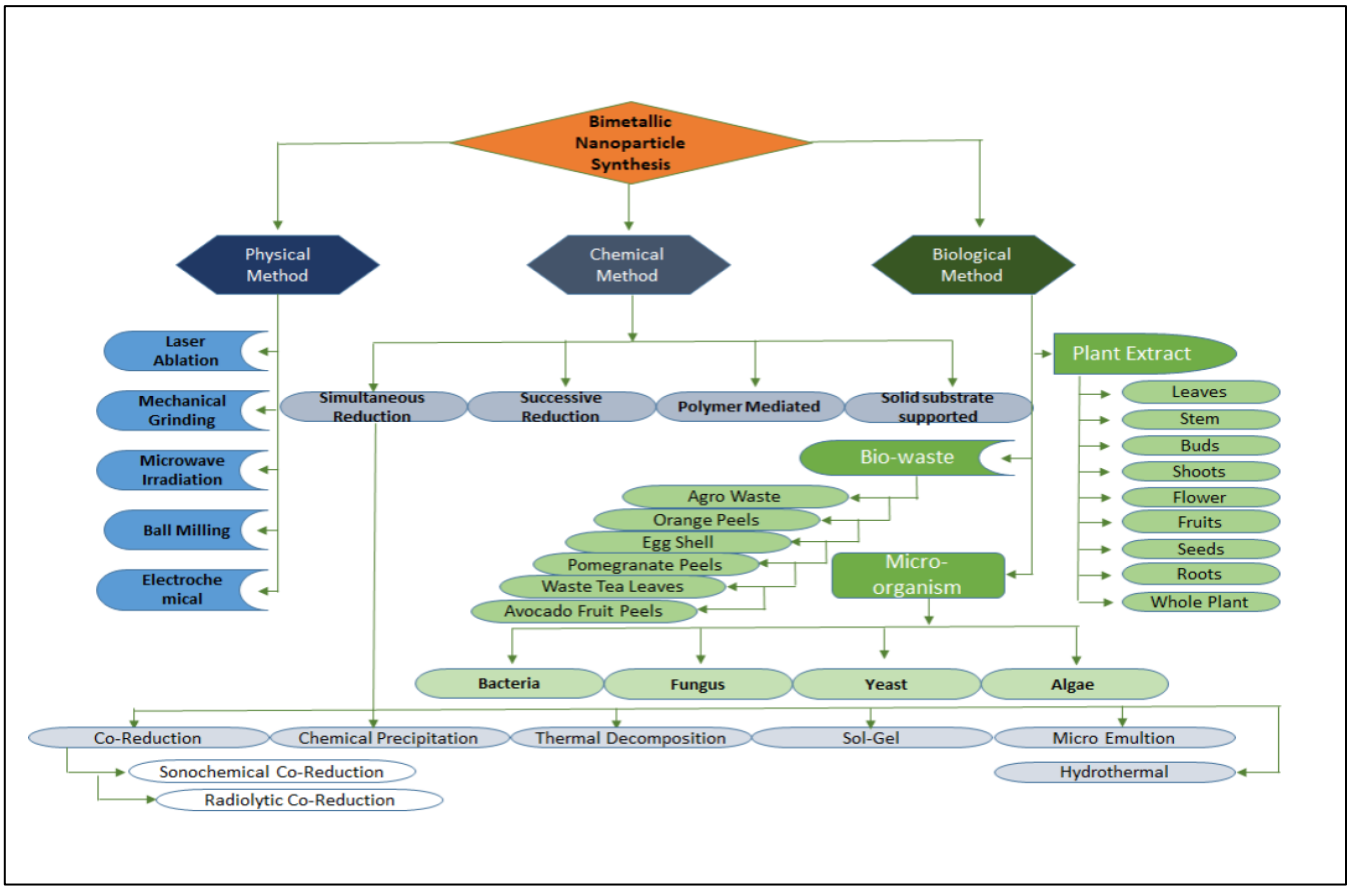

Figure (1-8): Methods of synthesizing bimetallic nanoparticles [89].

1.4 Applications of Nanomaterials

Metallic and bimetallic nanoparticles and metal oxides have been widely used in various applications, including biomedical, industrial, and many other fields. Nanoparticles have become a major focus of interest, especially when using elements in their monometallic or bimetallic forms. These materials exhibit exceptional performance due to their high surface-to-volume ratio and high reactivity, in addition to the ability to control their crystalline structure and molecular shape [90,91].

Nanoparticles, which consist of a mixture of two metallic elements, possess enhanced properties compared to their monometallic counterparts [92,93]. This is due to the synergistic effect between the two elements, which improves functional

performance in chemical reactions, biological activity, or catalytic properties [94]. The applications of these materials are highly diverse, such as in medicine as anticancer or antimicrobial agents and in the environment for pollutant removal or water treatment [95,96]. Medicine as anti-cancer or antimicrobial agents, the environment in pollutant removal or water treatment. And industry, such as their use in solar cells, catalysis, and sensors [97,98]. Below is a table that includes the most widely applied nanomaterials in various fields.

Table (1-2): The table includes the nanomaterial, application

Nanomaterial	**Application**
Ag NPs	Water purification, Antimicrobial and cancer treatment.
ZnO NPs	Antioxidant, anticancer, drug delivery, Sensors, electronic devices.
NiO NPs	Used as catalyst In energy strong devices, biomedical applications, dye degradation.
Co NPs	Pollutant treatment biocide. Catalysis, magnetism, gas sensors
Fe_3O_4 NPs	Treatment of water and soil pollutants
Cu NPs	Antimicrobial and potential cancer treatment, wound healing Removing artificial dyes

Ag: ZnO BNPs 1:1	Anti-bacterial, Anticancer Antioxidant and dye degradation in environmental application
Cu: Zn BNPs 2:1 Cu: Zn BNPs 1:1	Solar cells, tumor treatment, stimulation
Cu: Co BNPs1:1 Cu: Co BNPs3:1	Cancer treatment stimulation, high efficiency stimulants

1.5 Microfluidics

Microfluidic systems emerged in the early 1980s as an extension of the technologies used in the fabrication of microelectronic circuits, particularly photolithography. The first experiments in fluid transport through microchannels using microelectronics techniques took place in 1980. With the beginning of the nineties, specifically in 1990, these systems began to receive increasing attention in the field of analytical chemistry, where the first lab-on-a-chip platforms were developed, aiming to miniaturize chemical and biological analysis processes within small-sized chips.

The credit for establishing the concept of microfluidics goes to pioneering works published in the early 1990s, including the research of scientist George M. Whitesides and his team at Harvard University, who played a crucial role in 1998 in developing new materials (such as PDMS) and low-cost manufacturing techniques. In the period from 2000 to 2007, the technology of paper-based microfluidics emerged, culminating in the innovation of 2D using paper as the primary substrate without pumps. However, in 2010, the development of Organs-on-a-Chip technology to simulate human organ functions on microfluidic chips was witnessed, reducing the need for animal testing [99]. Since then, the field has

expanded to include many applications such as rapid medical diagnostics, DNA analysis, water quality monitoring, and environmental sensing [100, 101].

Microfluidic systems are promising technologies that have brought about a radical transformation in the fields of analytical chemistry, biomedicine, and engineering by controlling very small amounts of fluids in channels with micrometer dimensions.

This technology relies on the design and development of small-scale analytical systems capable of performing complex processes such as mixing, separation, reaction, and detection on a single platform known as a "lab-on-a-chip." These systems are characterized by several advantages, including reduced reagent and sample consumption, shortened analysis time, and lower operational costs, as well as ease of mobility and integration with other technologies such as nano sensing and electrochemical sensing.

This technology also allows for the simultaneous analysis of multiple samples using minimal amounts of samples, making it very suitable for clinical applications, toxin detection, environmental monitoring, and even single-cell research [102, 103]. .

Interest in using microfluidic systems has increased in recent years within the field of biochemical sensing, where nanomaterials, such as metallic nanoparticles (such as silver, copper, and gold), are integrated to enhance the efficiency of sensitive and precise analysis. These platforms enable the design of portable and rapid-response sensors for detecting various compounds, including drugs, toxins, and environmental factors [104].

1.5.1 Types of microfluidic systems

With the evolution of designs and materials, different types of microfluidic systems have emerged, each relying on a specific driving mechanism and design features suitable for certain applications, making them a central focus in the development of biotechnology and precision medicine [105]. Among these systems:

1.5.1.1 Pressure-driven systems

In these systems, fluids are moved within microchannels using a pressure difference applied through a compressed gas such as nitrogen or air. This pressure creates a smooth and pulse-free flow, allowing for precise control of the flow towards the chips [106, 107]. These systems are characterized by high precision and stability, with a rapid response time of less than 20 ms, and the flow is free of vibrations. This type is capable of handling large sample volumes, making it suitable for cases that require large inputs [108, 109].

These systems are usually used in the manufacturing of microcells due to their precise pressure execution. Despite its widespread use, it has some drawbacks, as it requires an external gas source with pressure regulators that can be expensive, and it is sensitive to air leaks [110].

1.5.1.2 Electroosmotic flow(EOF)

One of the main mechanisms used in microfluidic systems, characterized by its ability to drive fluids within microchannels through the application of a direct electric field. This flow occurs as a result of the interaction between the applied electric field and the electrical double layer formed at the inner surface of the channels, especially those made of negatively charged materials such as glass or silica. When a voltage difference is applied across the channel, the positively charged ions accumulated near the wall move towards the negative electrode, dragging along liquid molecules with them, resulting in a uniform flow known as

"plug-like flow" due to the homogeneous velocity distribution across the cross-section of the channel [111, 112].

The characteristics are already defined by the low flow control tolerance and the nonavailability of moving mechanical components, which makes them be used in sensitive biological tasks like capillary electrophoresis and analyses of DNA and proteins in lab-on-a-chip systems. The systems, however, have limitations, such as their inability to work effectively under low-ion liquids, sensitivity to changes in pH and viscosity, and the likelihood of having bubbles form due to electrolysis reactions at the electrodes, which might impair the flow [113].One of its most important applications is in the development of a device that relies on this type of flow, achieving a separation rate of up to 83% at 650 volts, which can be used for bacterial separation [114].

Although EOF provides an accurate and mechanical-free system for fluid transport, electrolysis bubbles, pH sensitivity, reduced flow rate, and low-frequency oscillations are the main challenges that must be addressed in the design of micro-systems, especially in sensitive biological applications [115, 116].

1.5.1.3 Capillary Driven Microfluidic systems

These systems rely on the automatic movement of fluids due to surface tension within fine channels (or porous materials like paper) without the need for pumps or electrical electrodes, known as the "capillarity" effect [117, 118]. When the channel has a nanoscale or microscale dimension, the surface tension force becomes stronger than gravity, causing the liquid to move inside it spontaneously. The flow rate depends on. The properties of the liquid, such as surface tension and viscosity. The flow rate also depends on the channel structure, length, width, and surface properties.

This type of system is characterized by being ideal for portable uses and remote areas, as well as being economical and simple; they can be easily and quickly manufactured through printing or engraving [119, 120]. They operate as portable "mobile laboratories" for point-of-care (POC) diagnostics, including glucose analysis and the detection of water contaminants [121]. Among its practical applications, paper μ PAD systems are used to analyze urine and blood to detect malaria and HIV in the field, and lateral-flow tests – such as home COVID-19 tests that rely on self-flow through the paper One of the obstacles to its use is poor control over fluid flow. The flow rate cannot be precisely adjusted as in driven systems, and there are difficulties in integrating with electronic systems or applications that require precise and complex preparation [122, 123].

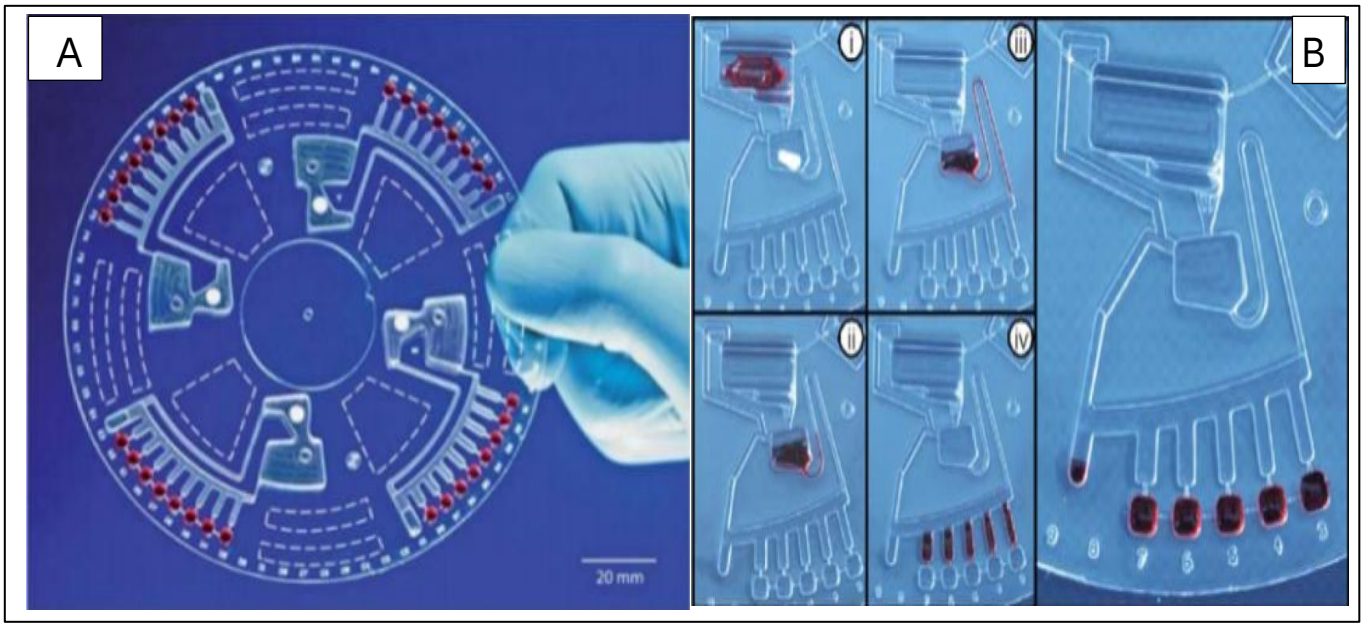

Figure(1-9):Application of Capillary Driven Microfluidic in different microfluidic scenarios(A) A panoramic view of the lab on disk chip. Reprinted with permission from(B) The process of working in a lab on a disk chip. Reprinted with permission from [119].

1.5.1.4 Digital microfluidic systems(DMF)

This technique is used to control separate droplets of liquids (instead of continuous streams), and these droplets are moved on a flat surface by applying an electric voltage. This effect is known as Electrowetting-on-Dielectric (EWOD), where the voltage changes the contact angle of the droplet, causing it to move on the surface. Programmable plates are used, and the droplets are manipulated separately for interaction, splitting, merging, heating, or transport. The system generally consists of two parallel plates [124,125] .

The lower one contains small electrical electrodes and the upper part is a ground conductor, with an oil separator layer sometimes placed between the plates where liquid droplets are positioned. The system is insulated with a dielectric layer and a hydrophobic layer to facilitate the movement of droplets [126].

These systems are characterized by very precise control over the size and location of droplets (pL to μL) and the possibility of full automation. In addition to the ease of reprogramming to change the type of analysis or interaction flow [127].Also, very low sample consumption – ideal for sensitive biological applications. And it is possible to perform multiple steps on the same chip (such as merging, splitting, heating).Many researchers have used these systems in various applications, including DNA and RNA analysis such as PCR reactions in separate droplets and rapid medical diagnostics such as testing blood and saliva samples in portable devices Also, protein analysis via ELISA [128, 129].Among the obstacles of this type of system Complex architectural manufacturing, the high sensitivity to liquid and contaminants, Also, its manufacturing cost is relatively high [130, 131].

1.6 Narcotic drugs in the blood

Narcotic drugs are chemical substances that primarily depress the central nervous system, producing effects such as analgesia, sedation, and euphoria. Traditionally, the term “narcotic” refers to opioids, natural, semi-synthetic, or synthetic compounds. that bind to specific opioid receptors in the brain and spinal cord to modulate pain perception and emotional response.

While some narcotics have legitimate medical uses in pain management and anesthesia, many are also highly addictive and subject to abuse. Regulatory classifications often distinguish between controlled prescription opioids and illicit narcotics such as heroin, reflecting their differing medical value and abuse potential. The diversion of drug use to illegal use was widely commented upon. In the 1970s, many studies documented the misuse and diversion of barbiturates, sedatives, and methaqualone. By the 1980s, media and government attention shifted away from drug use and diversion to the newer "epidemics" of cocaine and crack use. In the 1990s, the focus shifted to other emerging drug issues [132].

Narcotic drugs exert their primary effects by binding to opioid receptors (μ, δ, κ) in the central nervous system, inhibiting pain transmission and altering emotional states.

Therapeutic doses result in analgesia, mild sedation, and euphoria, making these drugs essential for managing moderate to severe pain, particularly in surgical or palliative settings. However, higher doses cause profound central nervous system depression, respiratory suppression, and potential coma or death. For example, fentanyl is approximately 50–100 times more potent than morphine, with lethal doses measured in micrograms.

Beyond analgesia, opioids slow gastrointestinal motility (leading to constipation), suppress the cough reflex, and cause miosis (pupil constriction). It was mentioned that fentanyl is a synthetic opioid and can cause death when an excessive dose is

taken illicitly [128]. Alexander R. Bazazi and others conducted a survey study in which he mentioned the percentage of those who obtained buprenorphine naloxone illegally and the reasons that led to this use, causing this group to suffer from misuse or addiction [133, 134]. SS Boun also examined the non-medical use of tramadol and described this use as a multi-dimensional issue with far-reaching economic, social, and security implications [135]. The illegal use of tramadol has become a threat to public health, and it is important to curb this phenomenon and necessary to expose it [136].

1.6.1 Detection of Narcotic drugs in Blood Samples

Therapeutic drug monitoring (TDM) the narcotic drugs has become an urgent necessity and an essential part of the work of health and security institutions due to the increase in drug use and production worldwide. This increase in drug use is attributed to the misuse of psychoactive and mental effect medications or non-compliance with prescribed dosages. Therefore, it has become necessary to find easy and quick methods to detect these substances [137].

Several techniques were used to detect the suspected materials, including the use of gas chromatography-mass spectrometry (GC-MS). This method was unsuccessful because it is expensive, requires experienced operators, and is not portable, meaning it operates in dedicated laboratories instead of on-site testing [138].Later, many portable technologies were developed, including handheld Raman devices, which were also expensive and had low sensitivity [139], they used Laser Induced Fluorescence (LIF), but it is difficult to use it locally because it requires a laser source and other components.

Because of their special qualities, which include strong chemical reactivity, a huge surface area, and the capacity for surface modification, nanomaterials can be used in a variety of sectors. Including nanomaterial-based assays. Such advanced methods aim to identify trace concentrations of narcotics rapidly and accurately, supporting efforts to mitigate opioid abuse and improve patient safety [140]. Ag,

Cu, and ZnO nanoparticles have been extensively studied for their role in drug-sensing applications. Their surface properties can be modified with functional groups, aptamers, or antibodies to selectively bind drugs such as morphine, cocaine, methadone, and heroin [141].

1.7 Heavy Metals in Blood

Heavy metals are a group of elements with high atomic weights and densities that can be toxic even at low concentrations. In human blood, heavy metals include both essential trace elements necessary for physiological function and toxic elements that pose significant health risks when accumulated beyond safe thresholds. Monitoring heavy metal concentrations in blood is crucial for assessing environmental and occupational exposures, diagnosing poisoning, and preventing long-term health effects [142].

Vita V. McCabe, M.D., presented a study linking the increased levels of cadmium and lead to alcoholic liver disease (ALD) due to their neurotoxic properties [143]. Shenghua Yao analyzed through his study the relationship between blood concentrations of mercury, lead, and cadmium and proved that increased levels of Cadmium and lead in the blood are associated with the occurrence of chronic kidney disease, as studies have indicated, exposure to heavy metals limits the neurological development of children [144, 145]. has been found that exposure to heavy metals affects embryos. In a study conducted in a country with a rapidly growing economy, it was found that the levels of most heavy metals in pregnant women were higher. The study presented by Yu-Mi Kim indicates that total mercury and methylmercury are capable of accumulating in embryos as shown in table (1-3) [146].

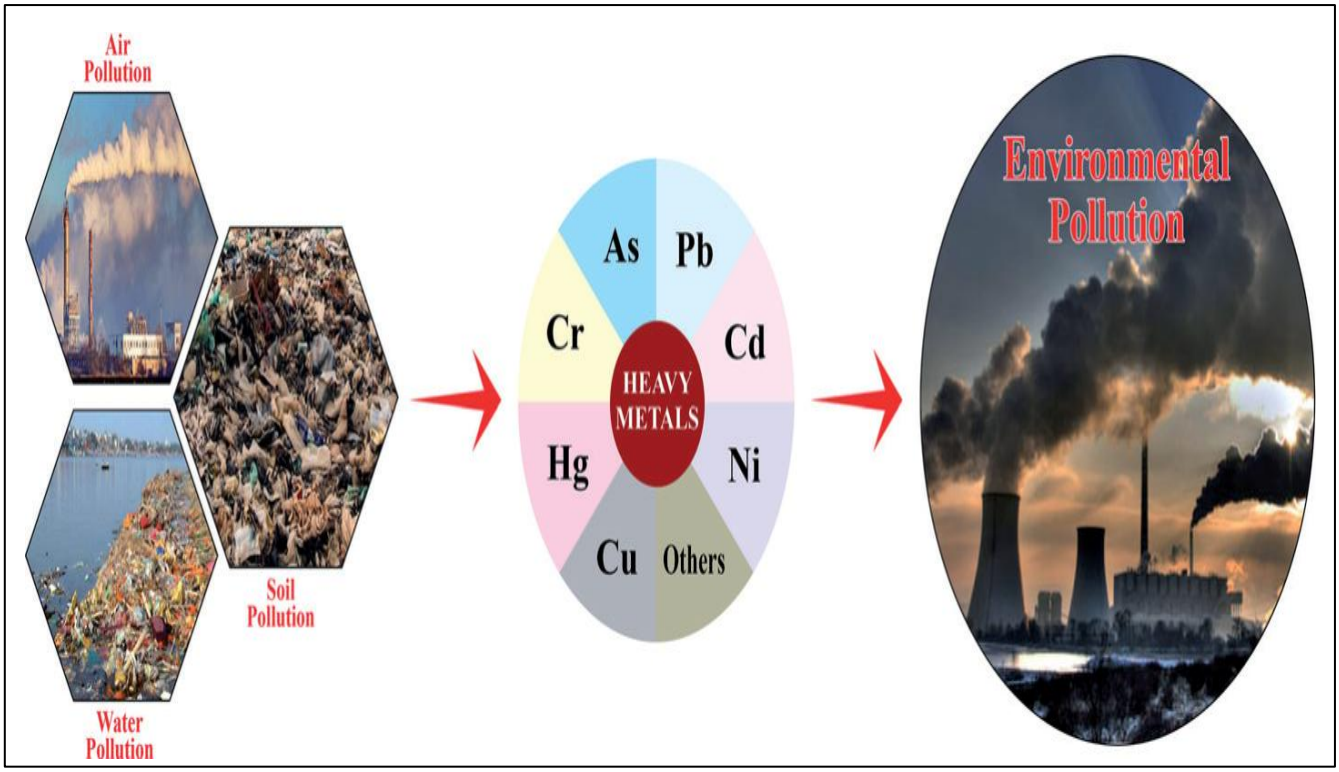

Figure (1-10): Sources, metals and the environmental degradation[147].

There are two categories of heavy elements; the first one is essential heavy metal. are less toxic when they are in low concentration and are required in the metabolic process. Such as vitamin B12, which is composed of cobalt, as well as iron. [149, 150]. Therefore, vitamin B12 and iron are essential nutrients for the human body, although they must be consumed in certain amounts. The second category includes elements like lead, chromium, cadmium, arsenic, and mercury, as well as copper, zinc, and selenium, which are extremely poisonous even at low concentrations and have long-lasting effects on living things [148].

.

Table (1-3): sources and health effects of Essential and Non-Essential heavy metals.

Heavy metal	Sources	Health Effects	Types of heavy metal
Zinc (Zn)	Oil Refining Plumbing Brass manufacturing	Gastrointestinal disorders, abnormal kidney and liver functioning	Essential heavy metals
Copper (Cu)	Copper polishing Plating Printing	Abnormalities in metabolic activity	Essential heavy metals
Iron (Fe)	High intake of iron supplement & oral consumption	Lethargy, diarrhea, vomiting, and abdominal pain	Essential heavy metals
Cobalt (Co)	Hip alloy replacement case	Cardiovascular Hepatic Endocrine Hematological	Essential heavy metals
Chromium (Cr)	Steel fabrication Electroplating Textile	Lung disorders (bronchitis, cancer), The renal and reproductive system	Non-Essential heavy metals
Lead (Pb)	Batteries Coal combustion Paint industry	Serious effect on mental health (Alzheimer's disease), Nervous system	Non-Essential heavy metals
Arsenic (As)	Atmospheric deposition Mining Pesticides	Highly effects dermal region (Cancer), Brain &	Non-Essential heavy metals

		Cardiac problems	
Mercury (Hg)	Coal combustion Fish Mining Paint industry Paper industry Volcanic eruption	Sclerosis Blindness Minamata disease Deafness Gastric problems Renal disorders	Non-Essential heavy metals
Cadmium (Cd)	Plastic Fertilizers pesticides	Osteo related problems Prostate cancer Lung diseases Renal issues	Non-Essential heavy metals

Such chronic exposure, even at moderate levels, may cause accumulation in the body, so that sensitive and reliable blood tests are important [151]. Blood carries essential minerals, which are very essential micronutrients in the human body and are most common in low concentrations in the blood.

The acceptable maximum limits of lead, cadmium, arsenic, and mercury in other environmental matrices have been taken into consideration, as indicated in table (1-4), and have been suggested by reputable international organizations such as the Occupational Safety and Health Administration (OSHA), the World Health Organization (WHO), and the U.S. Environmental Protection Agency (EPA) [150].

Table (1-4): Permissible limits of different toxic elements in environmental matrices.

	US EPA			WHO			OSHA
	Ambient Air	**Drinking Water**	**Soil**	**Ambient Air**	**Drinking Water**	**Soil**	**Air at work place**
pb	0.151µg/m³	15 µ g/L	400 ppm[1] (play areas); 1200 ppm non-play areas	___	152 µg/L	___	30 µg/m³
Cd	6.5–130 µg/m³	0.0053 mg/L	854 mg/kg	___	0.0033 mg/L	___	5 µg/m³
As	50 µg/m³	0.01 mg/L	___	___	0.01mg/L	___	10 µg/m³
Hg	5 µg/m³	0.0022 mg/L	4–16 mg/kg	___	0.0012 mg/L	___	___

1.7.1 Detection of Heavy Metals in Blood

The concentration of heavy metals in blood is one of the common bios monitored practices applied to determine personal and community exposure, inform clinical action, and guide policy. Accommodated analytical methods, which include atomic absorption spectroscopy (AAS), mass spectrometry inductively coupled plasma The new nanomaterial-based sensors and ICP-MS provide accurate quantification of the low concentrations of the tumor cells at the

trace levels, which favor early detection and prevention of the exposure to toxic metals [152].

Toxic elements of extreme toxicity like cadmium (Cd) and mercury (Hg) are heavy metals with severe repercussions on human health when present in minute quantities. Prolonged exposure to these metals causing environmental pollution and occupational hazards may lead to impairment of the nervous system, impaired kidney functioning, and so on, and developmental disorders. Therefore, it has been accurately detected in biological fluids, e.g., blood, which is most important in clinical toxicology and occupational health. and surveillance of the environment [153].

The pollution caused by heavy metal ions has attracted a lot of attention, and it is very important to develop a sensitive and simultaneous method for detecting them using common techniques without the need for highly sensitive devices. Many researchers have found various means to detect this type of ion. For instance, the researcher Le Ma and Wen-Yuan Pei prepared a new and practical magnetic nanomaterial with a core-shell structure.

Fe:Ag@ dimer cap to benzene (Fe:Ag@DMB), using sodium borohydride as a reducing agent in a one-step method. His study demonstrated that the functional thiol groups on the newly synthesized magnetic nanoparticles can interact with Cd^{2+}, Pb^{2+}, and Hg^{2+} ions in water samples, thus achieving effective extraction of Cd^{2+}, Pb^{2+}, and Hg^{2+} ions [154].

In the sensitive and stable detection of the heavy metals in the air. The FIFS system performed optimally when optimization of the trade between the thread length and the detection distance was run, and the limit of detecting lead in the heavy metals was found to be at 0.3 picograms/m^3, and the minimum detectable concentration at 10 m was 0.47 pgm/m^3.A narrow range of concentrations ensured the high stability of the system since the relative standard deviation (RSD) did not exceed 7%. Besides Pb, the system also managed to determine Cd, Hg, and Co in the air with measurable detection limits [155].

Additionally, a portable microfluidic device with optical display screens resembling a thermometer has been developed for real-time quantitative estimation of water contamination with cadmium, enabling quantitative detection through the naked eye. It uses the DNA enzyme based on Cd2þ (Cd16). The proposed device exhibited a detection limit of 11.3 nm for Cd^{2+}, with selectivity over 200 times against other metal ions [156].

In a study conducted by Ahmed Radwan and others, it examines Daily used cosmetics, as it was found that they contain high levels of Heavy metals are added to improve the quality and shine of cosmetics, but they pose a threat to human health. Optical nano sensors based on powder and paper were designed using porous silica beads as carriers to detect Co^{2+} and Cd^{2+} in commonly used cosmetics. It was found that they possess selective sensing and low detection limits down to parts per billion, a wide detection range, and a fast response within seconds [155].

A fast and environmentally friendly colorimetric sensor was also prepared from silver nanoparticles Ag NPs using *Boswellia sacra* extract as a stabilizing and reducing agent to selectively detect mercury ions. Several techniques were used to characterize the morphology of the nano semiconductor sensor prepared from Ag NPs, as well as its optical properties [157].

Nanomaterials such as ZnO, NiO, and Co_3O_4 have shown exceptional potential in sensing applications due to their tunable surface properties, high surface area, and ability to facilitate electron transfer reactions. These metal oxide nanoparticles can be functionalized with specific chelating agents or ligands to enhance the selective binding of Cd^{2+} and Hg^{2+} ions. When used as modifiers on electrode surfaces, they improve signal response, reduce background noise, and enhance the sensitivity of electrochemical detection systems [158, 159].

Huang et al. reported that the Ag: Fe bimetallic nanoparticle was produced simply by the 2-step method. The nanoparticle was characterized by high-resolution environmental scanning electron microscopy, transmission electron microscopy,

X-ray diffraction, Fourier transform infrared spectroscopy, and energy dispersive spectrometry.

Co (II) ions were removed using Fe nanoparticles, as well as Ag: Fe bimetallic nanoparticles found in aqueous solution. It was found out in the experiments that the Bimetallic nanoparticle Ag: Fe was able to clear Co (II) ions rapidly in the water solutions in less than 5 min, and the elimination percentage was as large as 99%. The adsorption capacity and reaction rate of the as-prepared Ag:Fe bimetallic nanoparticles are greater than that of Fe nanoparticles, since the numerous nanoscale

Ag: Fe primary batteries are identified, and therefore, the bimetallic nanoparticles are greatly promising in the context of the research on primary batteries, water treatment applications [160].

1. 8 The Aims of This Study

This study aims to:

1. Prepare Single-metal nanomaterial (Ag, Cu, NiO FeO, and Zn O using a green synthesis method.
2. Synthesize bimetallic nanomaterials in different ratios (1:1 and 3:1), Such as Ag:NiO,Cu:NiO , Cu:CoO and Cu:ZnO , inorder to enhance the crystalline Structure and monometallic materials.

3. Design and printing of precision liquid devices in small sizes and new shapes.

4. Investigate the applicability of the prepared nanomaterials in the detection of narcotic drugs in blood plasma.

5. Evaluate the efficiency at the prepared nanomaterials in the detection of Cadmium and Mercury in blood plasma.

Chapter Two

Experimental

2.1 Instruments and Chemicals

The chemicals listed in Table (2-1), the instruments used in the present study and their models, companies and origin are listed in Table (2-2).

Table (2-1): Chemicals used, chemical formula, company, origin and purity

Ser.	Chemicals	Chemical Formula	Company	Origin	Purity
1	Silver Nitrate	$AgNO_3$	LOBA Chemi	India	99.9%
2	Zinc Acetate	$Zn(CH_3CO_2)_2(H_2O)$	Fengcheng	Chaina	99%
3	Copper Sulfate	$CuSO_4.5H_2O$	LOBA Chemi	India	98% to 99.5%
4	Mercuric Chloride	$Hg\ Cl_2$	Thomas Baker	India	99%
5	Cadmium Sulfate	$Cd\ SO_4$	LOBA Chemi	India	98.%
6	Cobalt Nitrate	$Co\ (NO_3)_2.6H_2O$	Sigma-Aldrich	UK	99.9%
7	Nickel Nitrate	$Ni\ (NO_3)_2.6H_2O$	Sigma-Aldrich	UK	99%
8	Sodium Hydroxide	$Na\ OH$	LOBA Chemi	India	98%
9	Pethidine100mg (aldine)	$C_{15}H_{21}NO_2 \cdot HCl$	Nexus global pharmaceutical company	Turkey	50mg/ml
10	Fentanyl	$C_{22}H_{28}N_2OC_6H_8O_7$	Verve human care laboratories	India	15mg/10ml
11	Verdol	$C_{16}H_{25}NO_2 \cdot HCl$	Haver pharmaceuticals	Turkey	5mg/10ml
12	Hydrazine hydrate	$N_2H_5.H_2O$	LOBA Chemi	India	85%
13	Iron (II)Chloride	$Fe\ Cl_2.4H_2O$	LOBA Chemi	India	99%

14	green tea leaves	—	Basrah Governorate	Iraq	—
15	Boswellia sacra grains	—	Basrah Governorate	Iraq	—

Table (2-2): Instruments used in study, models, companies, origin and laboratory

Ser.	Device	Company	Origin	Laboratory
1	Centrifuge	Hettich-D-78532	Germany	Misan University/College of Science
2	Hotplate Magnetic Stirrer	LK Co.	Korea	Misan University/College of Science
3	Field Emission Scanning Electronic Microscope (FESEM), 5 KV	Zeiss	Germany	Tehran University/Advanced Materials Characterization Institute
4	Transmission electron microscope (TEM)	Horiba	Japan	Tehran University
5	X-Rey Diffraction (XRD), XRD-6000	Shimadzu	Japan	Basrah University/College of Science
6	FT-IR Spectrophotometer FT-IR-Alpha ii	Bruker	Germany	Basrah University/College of Science
7	UV-Vis Spectrophotometer UV-1800	Shimadzu	Japan	Misan University/College of Science
8	pH, pH7110 Meter	Inolab	Germany	Misan University/College of Science
9	Oven DZ-2BC	Tianjin City Taisite Instrument Co., Ltd	Chaina	Misan University/College of Science

10	Ultrasonic Bath Sonicator, WHC-A10H	Daihan Scientific	Chaina	Misan University/College of Science
11	Zeta Potential Analyzer, Zeta Plus	Horiba	Japan	Tehran University
12	Dynamic Light Scattering (DLS)	Horiba	Japan	Tehran University
13	Micropipette	Dragon Med	China	Misan University/College of Science

2.2 Preparation of Nanomaterials

2.2.1 Preparation of the *Boswell sacra* (BS) Extract Solution

The *Boswellia sacra* extract solution of 1% was prepared using a method by [157] with some modifications. Firstly, the *Boswell sacra* solid particles were crushed by a mill to get a fine powder. Then, 1 g of the Boswellia sacra powder was moved to a conical flask and left dissolving and stirring with 100 mL of distilled water for 30 min at 70°C. Finally, the mixture was filtered by centrifuge machine at a speed of 500 RPM for 2 min each time using plastic containers with a capacity of 15 ml and stored in a refrigerator at 5°C to be used for later.

2.2.2 Green synthesis of copper nanoparticles

The copper nanoparticles were prepared using the method [168] by adding 5 ml of (0.1 M) copper sulfate, 8 ml of (0.01 M) NaOH, and 8 ml of 1% BS in a beaker, and for 5 min, the mixture was heated to 75°C and stirred at a speed of 500. After that, 3 ml of 88% N_2H_5OH (hydrazine) was added to the reactor solution gradually, and it was continuously stirred until the pH reached 10 after 30 min. When hydrazine was added, the color gradually changed from light blue to blue to green to yellow until it reached dark red. Then the solution is filtered by a centrifuge machine at a speed of 500 RPM for 2 min each time using plastic containers with a capacity of 15 ml. The material was collected, distilled water

was added to it, and it was placed again in the centrifuge. The separation process was repeated 3 times, and then the result was placed in a Petri dish covered with perforated foil at laboratory temperature for two days until it dried. Then the material was collected, and it was in the form of a reddish-brown powder.

2.2.3 Green synthesis of zinc oxide nanoparticles

Zinc oxide nanoparticles were prepared using the method in the preparation of copper nanoparticles with some modifications. 5 ml of 0.1 M and 8 ml of 0.1 NaOH were added, then 8 ml of 1% BS extract were added, where the solution gradually changed from transparent to white. After 5 minutes, 3 ml of 88% N_2H_5OH (hydrazine) was added, and white precipitates began to appear, making the solution whiter. The reaction continued for 45 min at a temperature of 70°C and was stirred at a speed of 350 RPM. Then the solution is filtered by a centrifuge machine at a speed of 500 RPM for 2 min each time using plastic containers with a capacity of 15 ml. The material was collected, distilled water was added to it, and it was placed again in the centrifuge. The separation process was repeated three times, and then the result was placed in a Petri dish covered with perforated foil at laboratory temperature for 24 h until it dried. Then the material was collected, and it was in the form of a white powder.

2.2.4 Preparation of green tea extract

100 ml of deionized water at 100°C is mixed with 5 gm of green tea leaves, and the mixture is agitated at 500 rpm for fifteen minutes until it reaches the boiling point. After settling for 45 min, it is centrifuged for 2 min at a speed of 500 RPM for each time using plastic containers with a capacity of 15 ml to produce a dark green solution, which is then kept in a refrigerator at 5°C until it is needed. This method is as mentioned by [169], with some modifications.

2.2.5 Green synthesis of silver nanoparticles

Silver nano particles were prepared using the method [170] with some modifications by dissolving 5.096 gm of silver nitrate in 100 ml of deionized water to obtain 0.6 M for 10 min at a temperature of 50°C and stirring at 300 RPM until fully dissolved. Then, 50 ml of green tea was added slowly, and the color of the solution gradually changed to dark brown. To reach a pH of 8, gradually add 50 drops of 1 M NaOH at a rate of one drop per second, and black precipitates will be observed. The reaction continued for 120 min, and finally, a very dark brown solution was obtained. The solution was left to settle for 15 minutes and then filtered using a centrifuge at a speed of 500 RPM for 2 minutes each time using plastic containers with a capacity of 15 ml. The material was collected, deionized water was added to it, and it was placed again in the centrifuge. The separation process was repeated 3 times, and then the result was placed in a Petri dish. And wrapping it in perforated foil and leaving it for 4 h at laboratory temperature, after which silver nanoparticles were obtained in the form of a shiny gray powder.

2.2.6 Green synthesis of nickel oxide nanoparticles

In a glass beaker, 4.76 gm of nickel nitrate were dissolved in 100 ml of deionized water for 5 minutes at a temperature of 60°C and a stirring speed of 300 RPM. On the other hand, 50 ml of previously prepared green tea extract was heated for 5 min at a temperature of 75°C and a speed of 300 RPM and was slowly added to the nickel nitrate solution. The color of the solution gradually changed to green and then to dark green. After that, we started adding drops of 1.0 M NaOH, and from the fourth drop, white precipitates were observed. The slow addition continued until reaching pH 8 after 40 drops, and the reaction continued for 120 min under the same conditions. Then the solution is filtered by a centrifuge machine at a speed of 500 RPM for 2 min each time using plastic containers with a capacity of 15 ml. The material was collected, deionized water was added to it,

and it was placed again in the centrifuge. The separation process was repeated three times, and then the result was placed in a Petri dish covered with perforated foil and dried in an oven at 45°C for 8 hours. Then the material was collected, and it was in the form of a gray-colored powder. method, as mentioned by [171], with some modifications.

2.2.7 Green synthesis of cobalt oxide nanoparticles

In a conical flask, 3.65 gm of cobalt nitrate was dissolved in 100 ml of deionized water. After heating 50 ml of the previously prepared green tea for 5 min at 60°C and a speed of 350 RPM, the extract was gradually added to the pink cobalt solution, which gradually turned reddish-brown. Then, 10 drops of 1 M NaOH were added at a rate of one drop per second until the pH reached 10, and precipitates were observed during the addition. The reaction continued for two hours at a temperature of 60°C and a speed of 350 RPM. Then the solution is filtered by a centrifuge machine at a speed of 500 rpm for two minutes each time using plastic containers with a capacity of 15 ml. The material was collected, deionized water was added to it, and it was placed again in the centrifuge. The separation process was repeated three times, and then the result was placed in a Petri dish covered with perforated foil at laboratory temperature for 24 h until it dried. Then the material was collected, and it was in the form of a brown powder.

2.2.8 Green synthesis of iron oxide nanoparticles

The synthesis of iron oxide nanoparticles using green tea extracts was described previously [172]. In this work, a solution of 0.1 M ($Fe\ Cl_2 \cdot 4H_2O$) was prepared by adding 19.9 gm of solid $Fe\ Cl_2 \cdot 4H_2O$ in 1 L of deionized water. Subsequently, 0.1 M ($Fe\ Cl_2 \cdot 4H_2O$) solution was added slowly to 60 gm L^{-1} green tea at 75°C and stirred at 500 RPM. After 9 min, start adding 15 ml of 1M NaOH until the pH of the solution reaches 7.1, and the formation of FeO NPs was marked by the appearance of intense black suspension. The suspension continued to appear until the 50th min.

Then the solution is filtered by centrifuge machine at a speed of 500 RPM for 2 min each time using plastic containers with a capacity of 15 ml; the material was collected, deionized water was added to it, and it was placed again in the centrifuge. The separation process was repeated three times, and then the result was placed in a Petri dish covered with perforated foil and dried in an oven at 50°C for 6 h. the material was collected, and it was in the form of a brown powder.

2.3 Preparation of bimetallic nanoparticles

2.3.1 Synthesis of bimetallic nanoparticles of copper and zinc oxide

The bimetallic Cu:ZnO nanoparticles were prepared using the green synthesis method. To obtain 0.1 M of bimetallic nanoparticles, the two materials were mixed in ratios of 1:1 and 3:1 Cu:ZnO, respectively method, as mentioned by [173] with some modifications.

To obtain a 1:1 ratio Cu:ZnO of bimetallic particles after preparing 0.05 M zinc acetate at a temperature of 20°C and shaking at 350 RPM for 5 min, then adding 0.05 M copper sulfate, resulting in 50 ml of blue solution. Gradually add 80 ml of 1% BS extract, then add NaOH drops until reaching 80 ml. White precipitates appeared, and the pH of the mixture became 10. After 5 min, the gradual addition of 30 ml of 88% N_2H_5OH (hydrazine) began, and the solution turned brown, with the color gradually changing to reddish-brown. The reaction continued for two hours at a temperature of 70°C and shaking at 300 RPM. And after the solution stabilized,

It was filtered using a centrifuge for 2 min at a rate of 500 revolutions per minute in a 15 ml test tube. Then, we washed the resulting nanomaterial by adding distilled water and returning it to the centrifuge, repeating the process three times. The resulting material was placed in a thermal oven at a temperature not exceeding 45°C for 6 h, resulting in bimetallic nanoparticles of Cu: ZnO with a brown color.

To obtain a 3:1 ratio Cu:ZnO of bimetallic particles after preparing 0.015 M zinc acetate at a temperature of 20°C and shaking at RPM for 5 min, 0.075 M copper sulfate was added, resulting in 50 ml of dark blue solution. Gradually, 80 ml of 1% BS extract was added, followed by NaOH drops until reaching 80 ml. brownish precipitates appeared, and the pH of the mixture became 10. After 5 minutes, 30 ml of 88% N_2H_5OH (hydrazine) was added gradually, turning the solution brown. The color change continued until reaching reddish-brown. The reaction lasted for two hours at 70°C and 300 RPM. After the solution stabilized, it was centrifuged for 2 min at 500 RPM in a 15 ml test tube. Then, the resulting nanomaterial was washed by adding distilled water and returning it to the centrifuge, and this process was repeated three times. The resulting material was placed in a thermal oven at a temperature not exceeding 45°C for 4 h, resulting in bimetallic nanoparticles of Cu:ZnO with a brownish color.

2.3.2 Synthesis of bimetallic nanoparticles of copper and nickel oxide

The bimetallic nanoparticles Cu: NiO were prepared using the green synthesis method. To obtain 0.1 M of the bimetallic nanoparticles, the two materials were mixed in ratios of 1:1 and 3:1 Cu: NiO.

To prepare a 1:1 ratio Cu: NiO of bimetallic nanoparticles, after dissolving 0.05 M nickel nitrate and 0.05 M copper sulfate and mixing, a 50 ml green solution was obtained to which 80 ml of 1% BS extract was added. Then, 80 ml of 0.01 M NaOH was added. In the fifth min of the reaction, 30 ml of 88% N_2H_5OH (hydrazine) was added, and the color turned brown and gradually became darker. Upon measurement, the pH was found to be 7. The reaction continued for 140 min at 70 °C and a speed of 350 RPM. Then the solution is filtered by a centrifuge machine at a speed of 500 RPM for 2 min each time using plastic containers with a capacity of 15 ml. The material was collected, distilled water was added to it, and it was placed again in the centrifuge. The separation process was repeated

three times, and then the result was placed in a Petri dish covered with perforated foil at laboratory temperature for 24 h until it dried. Then the material was collected, and it was in the form of a shiny reddish-brown powder.

To prepare a 3:1 ratio (Cu:NiO) of bimetallic nanoparticles, after dissolving 0.075 M copper sulfate and 0.015M nickel nitrate and mixing, a 50 ml green solution was obtained to which 80 ml of 1% BS extract was added. Then, 80 ml of 0.01 M NaOH was added. In the fifth min of the reaction, 30 ml of 88% N_2H_5OH (hydrazine) was added, and the color turned brown and gradually became darker. Upon measurement, the pH was found to be 7. The reaction continued for 140 min at 70 °C and a speed of 350 RPM. Then the solution is filtered by a centrifuge machine at a speed of 500 RPM for 2 minutes each time using plastic containers with a capacity of 15 ml. The material was collected, distilled water was added to it, and it was placed again in the centrifuge. The separation process was repeated three times, and then the result was placed in a Petri dish covered with perforated foil at laboratory temperature for 24 h until it dried. Then the material was collected, and it was in the form of a reddish-brown powder.

2.3.3 Synthesis of bimetallic nanoparticles of copper and cobalt oxide

The bimetallic Cu: CoO nanoparticles were prepared using the green synthesis method. To obtain 0.1 M of bimetallic nanoparticles, the two materials were mixed in ratios of 1:1 and 3:1 Cu: CoO, respectively.

To prepare a 1:1 ratio Cu:CoO mixture of bimetallic nanoparticles at a concentration of 0.1 M, 0.399 gm of copper sulfate and 0.387 gm of cobalt nitrate were dissolved in 50 mL of distilled water in a glass beaker. After dissolution, 80 ml of 1% BS extract and 80 ml of 0.01 M NaOH solution were gradually added dropwise until reaching a pH of 10. In the sixth min, the slow addition of 88 % N_2H_5OH (hydrazine)at a concentration began.

The reaction continued for 40 min at a temperature of 75°C and a speed of 500

RPM. During this period, the color of the solution changed from pink to dark green and eventually settled to a dark reddish-brown color.

After the solution stabilized, it was centrifuged for 2 min at 500 RPM in a 15 ml test tube. Then, the resulting solution was washed by adding distilled water and returning it to the centrifuge; this process was repeated three times. The resulting material was placed in a thermal oven at a temperature not exceeding 45°C for 6 hours, resulting in bimetallic nanoparticles of Cu: CoO with a brownish color.

To prepare a 1:1 ratio Cu:CoO mixture of bimetallic nanoparticles at a concentration of 0.1 M, 0.399 gm of copper sulfate and 0.387 gm of cobalt nitrate were dissolved in 50 mL of distilled water in a glass beaker. After dissolution, 80 ml of 1% BS extract and 80 ml of 0.01M NaOH solution were gradually added dropwise until reaching a pH of 10. In the sixth minute, the slow addition of 88% N_2H_5OH (hydrazine) at a concentration began.

The reaction continued for 40 min at a temperature of 75°C and a speed of 500 RPM. During this period, the color of the solution changed from pink to dark green and eventually settled to a dark reddish-brown color.

After the solution stabilized, it was centrifuged for 2 min at 500 RPM in a 15 ml test tube. Then, the resulting solution was washed by adding distilled water and returning it to the centrifuge; this process was repeated three times. The resulting material was placed in a thermal oven at a temperature not exceeding 45°C for 6 hours, resulting in bimetallic nanoparticles of Cu:CoO with a brownish color.

To prepare a 3:1 mixture of bimetallic nanoparticles with a concentration of 0.1 M, 0.598 gm of copper sulfate and 0.025 gm of cobalt nitrate were dissolved in 50 mL of distilled water in a glass beaker. After dissolution, 80 ml of 1% BS extract and 80 ml of 0.01M NaOH solution were gradually added dropwise until reaching pH 10. In the sixth min, the slow addition of 88% N_2H_5OH (hydrazine)began.

The reaction lasted for 60 min at a temperature of 70°C and a speed of 350 RPM.

During this period, the color of the solution changed from purple to dark blue and eventually settled to a reddish-brown color .

After the solution stabilized, it was centrifuged for 2 min at 500 RPM in a 15 ml test tube. Then, the product was washed by adding distilled water and returned to the centrifuge, and this process was repeated three times. The resulting material was placed in a thermal oven at a temperature not exceeding 45°C for 6 h, resulting in brown bimetallic Cu:CoO nanoparticles.

2.3.4 Synthesis of bimetallic nanoparticles of silver and nickel oxide

To prepare the bimetallic nanoparticles Ag:NiO in a 1:1 ratio. 2.54 gm of silver nitrate is dissolved in 50 ml of deionized water in an opaque beaker for 5 min at a temperature of 25°C and a speed of 350 RPM. After dissolving, 5.4 gm of nickel nitrate is added, and the solution is left to homogenize for 5 min. Then, 25 ml of pre-prepared and heated green tea extract is added. 25 drops of 0.01M NaOH are added at a rate of one drop per second until reaching pH 9, and brownish precipitates were observed.

The reaction continued for 104 min under the same conditions. After the reaction is complete, the brown solution is left to settle for 1 h, then filtered using a centrifuge at a speed of 500 RPM for two min each time using plastic containers with a capacity of 15 ml. The material was collected, deionized water was added to it, and it was placed again in the centrifuge. The separation process was repeated three times, and then the result was placed in a Petri dish. And wrapping it in perforated foil and leaving it for 4 h at laboratory temperature, after which Ag: NiO nanoparticles were obtained in the form of a shiny gray powder.

To prepare the bimetallic nanoparticles Ag:NiO in a 3:1 ratio, 2.54 gm of silver nitrate is dissolved in 50 ml of deionized water in an opaque beaker for 5 min at a temperature of 25°C and a speed of 350 RPM. After dissolving, 5.4 gm of nickel nitrate is added, and the solution is left to homogenize

for 7 min. Then, 25 ml of pre-prepared and heated green tea extract is added. 25 drops of 0.01 M NaOH are added at a rate of one drop per second until reaching pH 10, and brownish precipitates were observed. The reaction continued for 104 min under the same conditions.

After the reaction is complete, the dark brown solution is left to settle for 1 h, then filtered using a centrifuge at a speed of 500 RPM for 2 min each time using plastic containers with a capacity of 15 ml. The material was collected, deionized water was added to it, and it was placed again in the centrifuge. The separation process was repeated three times, and then the result was placed in a Petri dish. And wrapping it in perforated foil and leaving it for 4 h at laboratory temperature, after which Ag:NiO nanoparticles were obtained in the form of a shiny gray powder.

2.4 Detection of narcotic drugs

2.4.1 Preparing blood plasma sample

The traditional rapid method involves using a 15 ml special glass tube containing anticoagulants to prevent blood clotting. The drawn blood sample is placed in the tube. It is left for 10-15 minutes, then the tube is gently inverted three times and placed in a centrifuge for 10 min at 5000 RPM. After the separation process is complete, the plasma is carefully drawn using a plastic pipette and stored in a 10 ml test tube at a temperature of 5 °C until use After a few minutes.

2.4.2 Detection of Fentanyl Citrate by silver nanoparticles

The pharmaceutical substance Fentanyl Citrate ($C_{22}H_{28}N_2O \cdot C_6H_8O_7$) is classified as a narcotic if misused, according to the Iraqi Health Report. To detect the presence of the lowest concentration of it in blood plasma, we take the concentrations (0.5, 1, 1.5, 2, 2.5) mg/L using a pipette and place each in a 10 ml test tube. We add 0.1 ml of the silver nanoparticle filtrate diluted with distilled

water to 2 ml. When measuring the absorbance with a UV device for each concentration, a difference in absorbance was observed with the addition of the reagent and before the addition. Therefore, 25 μL of the previously prepared blood plasma is taken, and the lowest concentration of the narcotic substance, 0.5 mg/L, is added to it, along with 2 ml of the diluted silver nanoparticle filtrate. We observe a color change in the mixture, in addition to a difference in absorbance of 1.362.

2.4.3 Detection of Tramadol Hydrochloride by cobalt oxide nanoparticles

Tramadol Hydrochloride ($C_{16}H_{25}NO_2 \cdot HCl$) is considered a narcotic substance as mentioned in the list of drugs prohibited for illegal use. To detect this type of pharmaceutical substance, the absorbance for the concentrations (0.5, 1.0, 1.5, 2.0, 2.5) mg/L of drug is measured, and then it is measured again by adding 0.5 nano cobalt oxide diluted in distilled water to 2 ml. The detection is conducted at the lowest possible concentration of the narcotic substance in the blood (0.5 mg/L) by adding it to 25 μL of previously prepared blood plasma and 2 ml of Cobalt oxide solution is added to it. A clear color change in the mixture and an absorbance difference of 0.107 were observed.

2.4.4 Detection of Pethidine Hydrochloride by Cu: NiO BNPs

Pethidine Hydrochloride ($C_{15}H_{21}NO_2 \cdot HCl$) is one of the classified narcotic drugs. To detect its presence in blood plasma, after study and experimentation, it was found that this narcotic drug can be detected using bimetallic Cu:NiO nanoparticles prepared previously by the green synthesis method in a 3:1 ratio. By taking concentrations of 0.5, 1.0, 1.5, 2.0, and 2.5 mg/L of the narcotic drug and adding 0.2 ml of the diluted Cu:NiO BNPs leachate solution to 2 ml of distilled water, the absorbance for each concentration was measured before and after the addition. Then, the detection was applied to the lowest concentration of

the drug in blood plasma (0.5 mg/L added to 25 µL of plasma), and 2 ml of the diluted Cu:NiO BNPs leachate solution was added, resulting in a color change and an absorbance difference of 0.008.

2.5 Detection of heavy metal

2.5.1 Preparation of cadmium solution

To obtain (0.1m M) cadmium, dissolve 0.00104 g from cadmium sulfate in 50 ml of distilled water at a temperature of 50 °C and a speed of 500 RPM for 18 minutes [174].

2.5.2 Preparation of mercury solution

To obtain a 0.1 molar solution of mercury, dissolve 0.000368 g of mercuric chloride in 50 ml of distilled water at a temperature of 50 °C and a speed of 500RPM [174].

2.5.3 Detection of cadmium by zinc oxide nanoparticles

Cadmium is considered a heavy metal, and if its concentration exceeds 5 micrograms/liter, it becomes toxic, according to the American Conference of Governmental and Industrial Hygienists [175]. To detect the presence of the lowest concentration of it in blood plasma, we take the concentrations (0.5, 1, 1.5, 2, 2.5) mg/L using a pipette and place each in a 5 mL test tube. We add 0.2 mL of the zinc oxide nanoparticle filtrate diluted with distilled water to 2 mL. When measuring the absorbance with a UV device for each concentration, a difference in absorbance was observed with the addition of the reagent and before the addition. Therefore, 25 µL of the previously prepared blood plasma is taken, and the lowest concentration of cadmium substance, 0.5 mg/L, is added to it, along with 2 mL of the diluted zinc oxide nanoparticle filtrate.

2.5.4 Detection of mercury by copper nanoparticles

Mercury is one of the toxic elements, and exceeding the normal levels in the blood leads to numerous health risks for humans**.** To detect the presence of the lowest concentration of it in blood plasma, we take the concentrations (0.5, 1, 1.5, 2, 2.5) mg/L using a pipette and place each in a 5 mL test tube. We add 0.2 mL of the copper nanoparticle filtrate diluted with distilled water to 2 mL. When measuring the absorbance with a UV device for each concentration, a difference in absorbance was observed with the addition of the reagent and before the addition. Therefore, 25 µL of the previously prepared blood plasma is taken, and the lowest concentration of mercury substance, 0.5 mg/L, is added to it, along with 2 mL of the diluted copper nanoparticle filtrate.

2.6 Microfluidic device

2.6.1 Design of microfluidic device

The microfluidic device was drawn and designed using the SolidWorks 2022 design software, where a three-dimensional model with four channels (60 × 40 × 1.5) mm and a central channel was designed as shown in Figure 2-1A. Additionally, a two-channel device (30 × 13 × 10) mm was designed along with the main central channel, as shown in figure (2-1B). After printing the designed models with a 3D printer, and before using them, they are placed in a 0.1M sodium hydroxide solution for 40 min, washed with water, and left to dry completely to be ready for use.

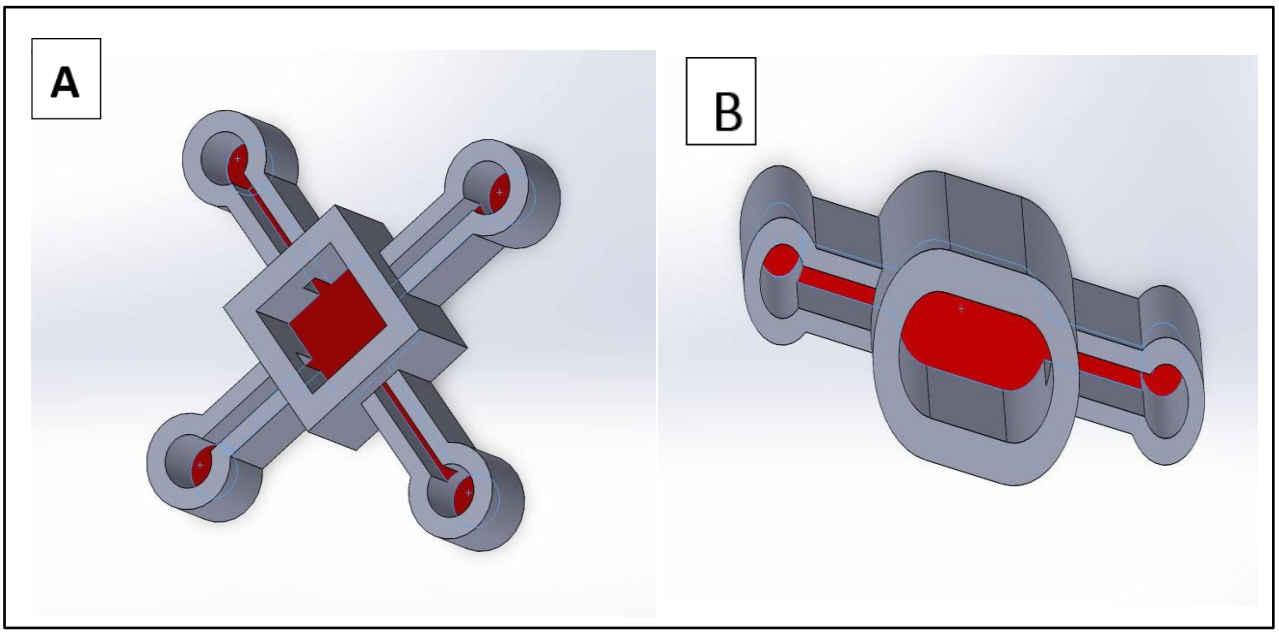

Figure (2-1): A microfluidic device designed using SolidWorks software (A) a three-dimensional model with four channels and dimensions of (60 × 40 × 1.5) mm and a central channel, (B) a three-dimensional model with two-channel device (30 × 13 × 10) mm.

2.6.2Microfluidic device operation

Due to its many advantages, including those related to cost, time, and design, we decided to use a 3D printer for our wafer. Rapid design and production, quick prototyping, on-demand printing, durable and lightweight components, economic feasibility, ease of use, waste reduction, and environmental friendliness are some of these advantages. The 3D microdevice, sized (60 × 40 × 1.5) mm, is specifically designed to detect drugs in blood plasma samples simultaneously. And the other device, designed with dimensions of (30 × 13 × 10) mm, is for determining heavy metals in plasma. We chose to use these designs for the reservoirs containing the reagent and sample components because, as we previously reported in our research [157, 168], it is very easy to inject both the reagent and sample components into the channels using an automatic injector. After injecting the substance, the developed color is examined, the data is interpreted, and the quantification step is performed using the ImageJ software.

In order to analyze narcotic compounds and heavy metals in blood plasma samples, we introduced the synthesized nano-probes into the reservoirs after adjusting the settings. This made it possible for the sensors to selectively identify drugs and heavy metals. The sample will be pumped into the sample reservoir(medium).

2.7 Characterization Devices

Several diagnostic techniques have been employed to characterize the produced nanoparticles, including UV, XRD, FESEM, TEM, FTIR, and zeta potential.

2.7.1 Ultraviolet-Visible Spectrophotometry (UV)

UV-Vis spectroscopic studies are a primary choice to confirm the presence of most NPs, as they provide a quick and accurate method for understanding the physical and chemical properties of materials. They are considered one of the essential analytical tools widely used in various scientific fields [161]**.** The visible spectrum of ultraviolet rays was measured using the device UV-Vis spectrophotometer within the wavelength range of 200-800 nm.

2.7.2 X-Ray Diffraction (XRD)

X-ray diffraction technology is one of the most important techniques in determining the crystalline structure of a material. The XRD spectrum was measured by using the X-ray diffraction (XRD) machine with a single-color beam from copper that has a wavelength of K-Alpha1 [Å] 1.54060, a voltage of 40 kV, and a current of 30 mA, with an angular range (2Theta=20-80).

2.7.3 The field emission scanning electron microscope (FESEM)

FESEM is a technique that helps determine the nanoscale dimensions of particles, such as diameters and lengths, and also allows for the analysis of the distribution of nanoscale particles on the surface.

2.7.4 Transmission electron microscope (TEM)

Transmission electron microscopy (TEM) is often used to characterize the physical characteristics of NPs. TEM provided a clear picture of the particles' sizes and shapes at a very high resolution. To characterize NPs, TEM is a valuable technique [162].

2.7.5 Energy Dispersive X-ray Spectroscopy (EDX)

An analytical technique used to determine the elemental composition of materials, revealing impurities or unexpected elements, and is usually used with electron microscopy or transmission electron microscopy.

2.7.6 Zeta potential and Dynamic Light Scattering (DLS)

The surface potential of nanoparticles is the potential difference between the medium where the nanoparticles are dispersed and the surface that can be reached by the dispersed nanoparticles, which can be analyzed using the zeta size [163]. On the other hand, zeta potential is considered a measure of the magnitude of electrostatic repulsion or attraction between particles in a liquid suspension, making it one of the fundamental criteria for describing particle stability in an aqueous environment. Particles with zeta potentials greater than +30 mV and less than -30 mV are considered stable [164,165]. The zeta potential was measured at a carrier dispersion temperature of 25.2°C with an average viscosity of 0.891 m Pa·s in addition to the electrical potential of 3.3 V. As for particle distribution length (PDL), it is a number calculated from the ratio of two parameters of the correlation data, meaning it is dimensionless [166]. The Dynamic Light Scattering (DLS) technique is used to verify the hydrodynamic size and measure, And DLS was measured at scattering angle 90°, dispersion medium viscosity 0.893 m Pa·s, and count rate 237 k CPS.

2.7.7 Fourier Transform Infrared Spectroscopic (FTIR)

FTIR is a spectroscopic method for identifying potential functional groups in the reduction of metal ions and the stabilization of composite nanoparticles; FTIR operates within the wavelength range of 400 to 4000 [167].

Chapter Three

Results and Discussion

3.1 Spectroscopic characterization of synthesized nanoparticles

3.1.1 Ultraviolet-Visible Spectrophotometry

The visible spectrum of ultraviolet rays was measured using the device UV-Vis spectrophotometer within the wavelength range of 200-800 nm. Figure (3-1A) illustrates the visible spectrum of ultraviolet rays for silver nanoparticles, showing the maximum absorption peak at 420 nm, as reported [176] with slight differences. Figure (3-1B) shows the visible spectrum of ultraviolet rays for nickel oxide nanoparticles prepared by the green synthesis method. It is observed in the figure that there are two absorption peaks within the range of 300-400 nm. The absorption peak at 302.5 nm represents NiO, while the peak at 396.5 nm is due to the transfer of non-bonding electrons from the absorbed phytochemicals towards the nickel void, as mentioned [177], with slight variation. Figure (3-1C) represents Ag: NiO BNPs in a 1:1 ratio; a very shift in the absorption peaks of nickel oxide and silver is observed. Also, regarding the figure (3-1D), there is a change in the position of the silver absorption peak and a change in the nickel oxide absorption peak.

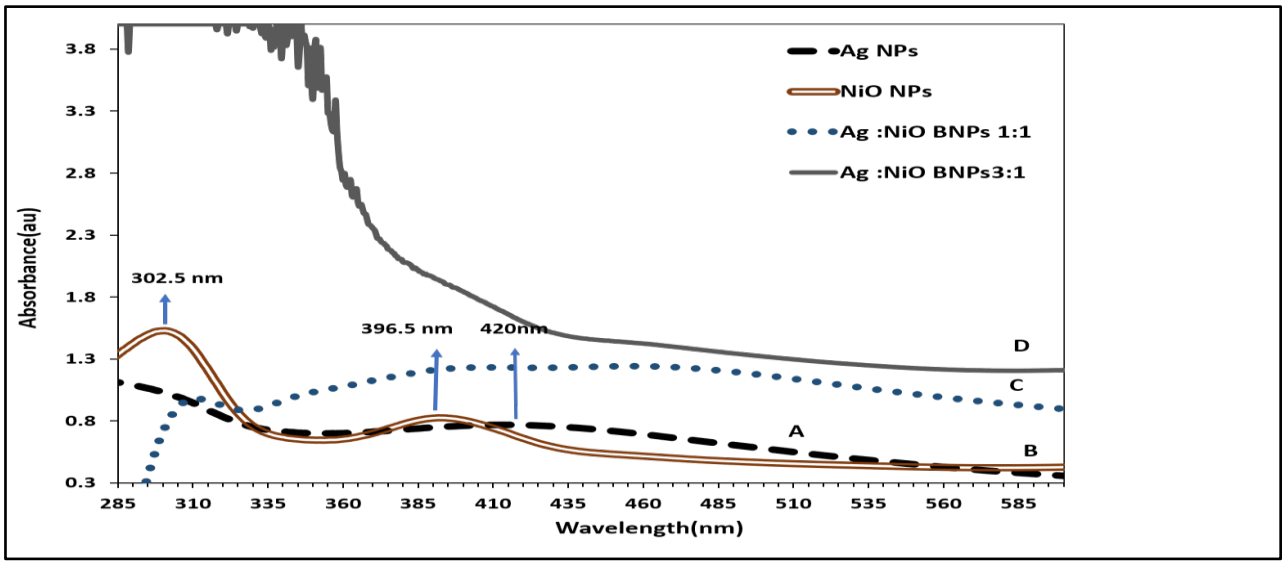

Figure (3-1): UV-Visible spectrum of green synthesized (A) for silver nanoparticles (B) nickel oxide nanoparticles (C) Ag: NiO bimetallic particles prepared in a 1:1 ratio (D) Ag: NiO bimetallic particles prepared in a 3:1 ratio.

Figure (3-2A) illustrates the visible spectrum of ultraviolet rays for copper nanoparticles prepared by the green synthesis method. The maximum absorption peak appears at 579 nm, as mentioned in [178]. with slight variation. Figure (3-2B) shows the visible spectrum of ultraviolet rays for cobalt oxide nanoparticles prepared by the green synthesis method. The maximum absorption peak appears at 303.5 nm. Additionally, a small peak is observed at the wavelength 515.5 nm, representing the absorption peak of cobalt oxide nanoparticles, as mentioned in [179] with slight variation, the appearance of more than one peak can be attributed to the difference in the sizes of the nanoparticles. The curve (C) in the figure represents the absorption spectrum of the bimetallic Cu: CoO particles prepared in a 1:1 ratio. We observe a shift of the cobalt oxide peak to the region below 300 nm, while the peak of the copper nanoparticles shifts to the right, becoming approximately 580 nm and showing a lower peak. The curve (D) also shown in the figure represents the absorption spectrum of the bimetallic Cu:CoO particles prepared in a 3:1 ratio .

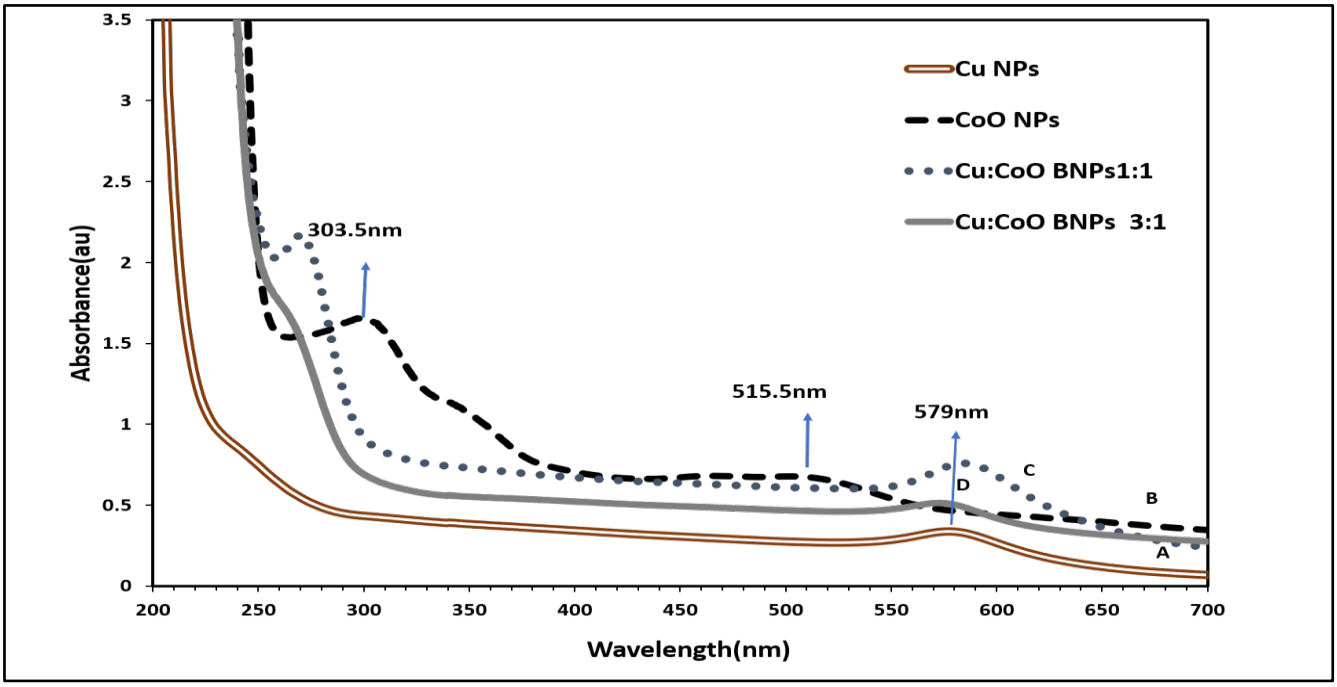

Figure (3-2): UV–Visible spectrum of green synthesized (A) for copper nanoparticles (B) for cobalt oxide nanoparticles (C) Cu: CoO bimetallic particles prepared in a 1:1 ratio (D) Cu: CoO bimetallic particles are prepared in a 3:1 ratio.

Figure (3-3A) illustrates the visible spectrum of ultraviolet rays for green-synthesized copper nanoparticles. The curve (B) illustrates the visible spectrum of ultraviolet rays for green-synthesized zinc oxide nanoparticles. The maximum absorption peak appears at 369.5 nm, as mentioned in [180]. Curve (C) represents the absorption spectrum of the Cu: ZnO bimetallic particles prepared in a 1:1 ratio, where we observe the peak associated with zinc oxide fading. However, in the copper wavelength range of 579 nm, there is a slight increase resembling a broad peak. Similarly, at the 3:1 ratio, we observe a peak shifting to the right, i.e., to the 800 nm wavelength range, as shown in the curve (D).

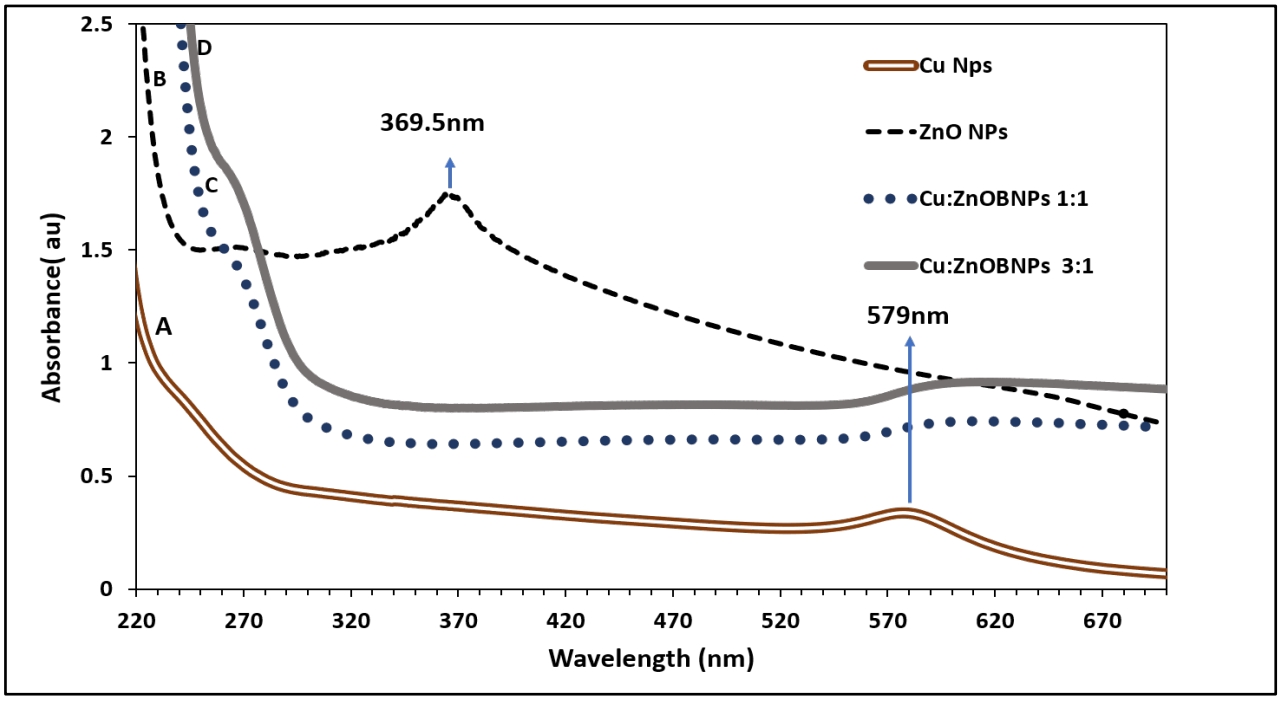

Figure (3-3): UV-Visible spectrum of green synthesized (A) for copper nanoparticles (B) for zinc oxide nanoparticles (C) Cu: Zn O bimetallic particles prepared in a 1:1 ratio (D) Cu: ZnO bimetallic particles prepared in a 3:1 ratio.

Figure (3-4A) illustrates the visible spectrum of ultraviolet rays for copper nanoparticles prepared by the green synthesis method. The maximum absorption peak appears at 579 nm, as mentioned in [178], with slight variation, figure (3-4B) shows the visible spectrum of ultraviolet rays for nickel oxide nanoparticles prepared by the green synthesis method. It is observed in the figure that there are

two absorption peaks within the range of 300-400 nm. The absorption peak at 302.5 nm represents NiO, while the peak at 396.5 nm is due to the transfer of non-bonding electrons from the absorbed phytochemicals towards the nickel void, as mentioned [177], with slight variation. Furthermore, figure (3-4C) represents the absorption spectrum of the Cu:NiO bimetallic particles prepared in a 1:1 ratio, where the absorption peak shifts to the region beyond the copper absorption peak range, figure (3-4 D) represents the absorption spectrum of the Cu: NiO bimetallic particles prepared in a 3:1 ratio. Where a weak absorption peak is observed in the area very close to the nickel oxide absorption peak.

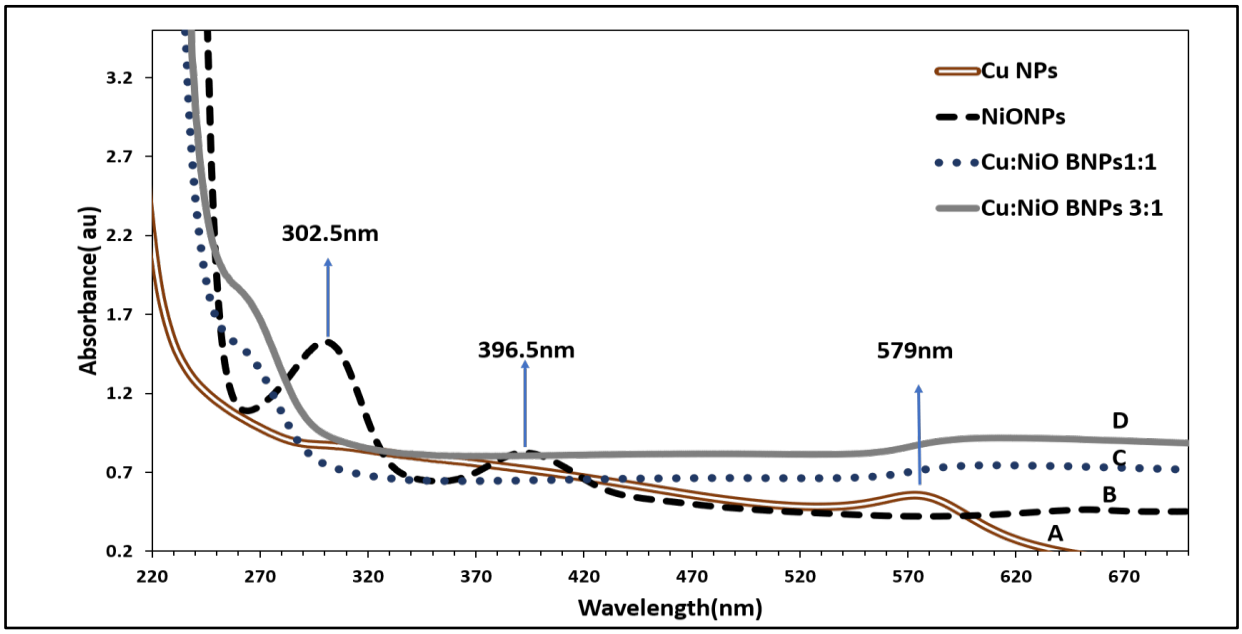

Figure (3-4): UV-visible spectrum of green synthesized (A) for copper nanoparticles (B) for nickel oxide nanoparticles (C) of the Cu:NiO bimetallic particles prepared in a 1:1 ratio (D) of the Cu:NiO bimetallic particles prepared in a 3:1 ratio.

3.1.2 X-Ray diffraction Analysis

The crystalline structure of the prepared nanomaterials was characterized using an X-ray diffraction device. Figure (3-5) shows X-ray diffraction of silver nanoparticles prepared by the green synthesis method. We observe from the figure that the compound exhibited four characteristic peaks at the positions (2Theta =

38.3°, 44.1°, 64.3°, and 77.6°). The X-ray diffraction pattern indicates that the crystal structure of the sample is (111, 200, 220, and 311), respectively, which corresponds to the standard card lanes of the face-centered cubic (FCC) geometry of Ag nanocrystals (JCPDS NO 04-0783) [181].Likewise, X-ray diffraction of nickel and nickel oxide nanoparticles, where distinct peaks (111, 220, 311) appear at angles (2Theta = 37.6°, 62.1°, 75.6°) for nickel oxide, corresponding to the FCC structure and indicating good crystallinity of the nickel oxide nanoparticles. The common reference number for nickel oxide is JCPDS Card No. 04-1049. Additional peaks (111, 200) appeared at angles (2Theta = 44.1°, 52.1°), with the common reference number for nickel (JCPDS No. 04-0850) [182]. X-ray diffraction of Ag: NiO bimetallic particles in 1:1 and 3:1 ratio. Through the figure, the diffraction peaks were recorded in the X-ray diffraction pattern, which represents the characteristic crystalline peaks of the (FCC) structure. A slight difference in the peak positions is observed compared to individual NiO and Ag particles. The difference in positions is due to the interference between the crystal lattices of silver and nickel oxide .

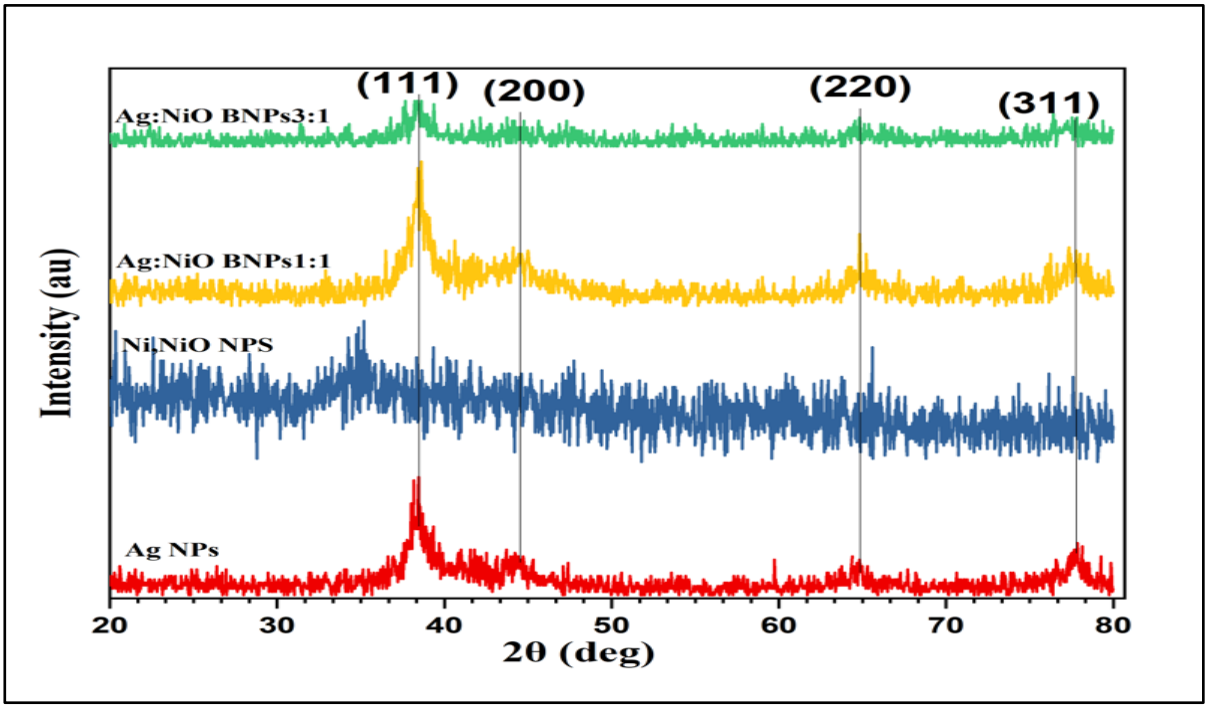

Figure (3-5): XRD powder pattern of the crystalline Ag NPs, NiO NPs, and bimetallic Ag: NiO BNPs 1:1 and 3:1.

Figure (3-6) shows X-ray diffraction to determine the crystalline structure of Cu: CoO bimetallic particles in ratios of 1:1 and 3:1. As shown through the figure, the diffraction peaks in the X-ray diffraction pattern representing the characteristic crystalline peaks of the (FCC) structure were recorded. A slight difference in the positions of the peaks is observed compared to the individual particles of Cu and CoO. The difference in positions is due to the interference between the crystalline lattices of copper, cobalt oxide. It can be observed that the diffraction peaks of copper, cobalt, and cobalt oxide at 1:1 and 3:1 are higher compared to their peaks in the individual particles of the same elements. The distinctive peak of the copper, which is located at (43.58° = 2Theta), was also found to have no change in position at 1:1 with a very slight change at3:1.

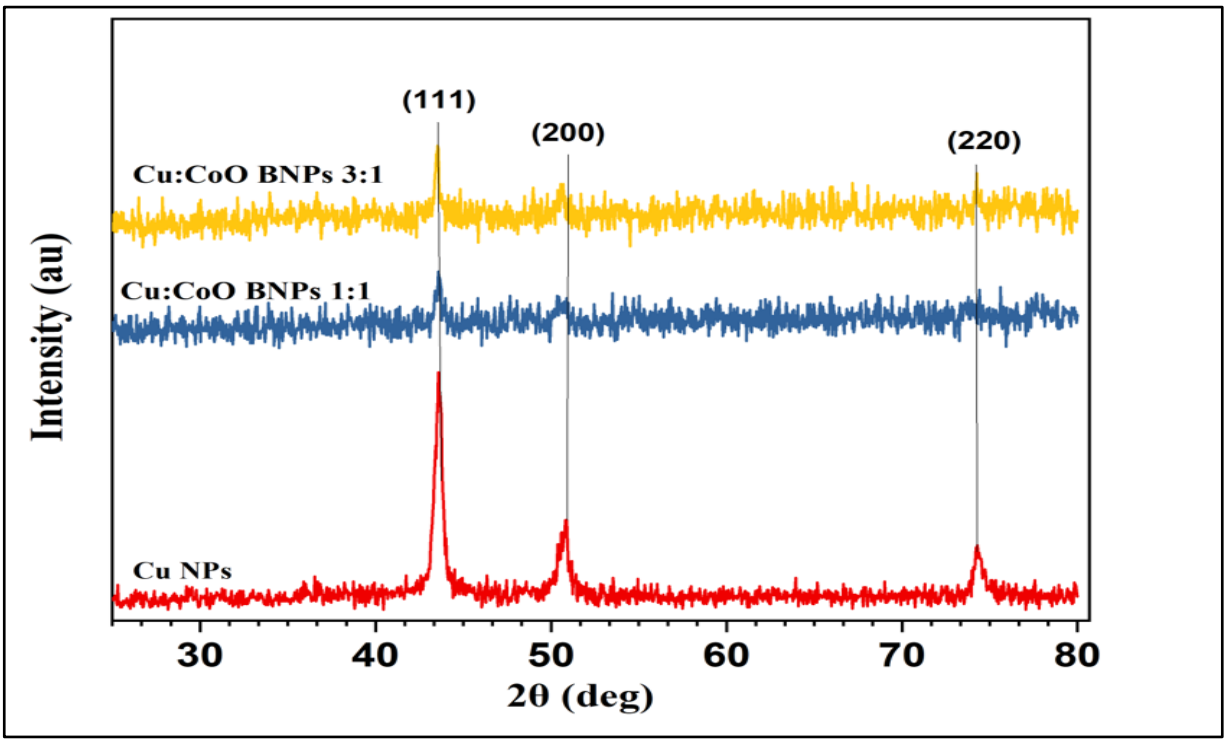

Figure (3-6): XRD powder pattern of the crystalline Cu NPs, bimetallic Cu:CoO BNPs 1:1, 3:1.

Figure (3-7) shows X-ray diffraction was used to determine the crystalline structure of the prepared copper nanoparticles, and the measurement showed the presence of pure copper, known for its face-centered cubic FCC crystalline structure, The results in the figure showed clear peaks at the angles (2Theta =

43.5°, 50.8°, 74.3°), which correspond to the crystal planes (111, 200, 220) according to the reference data (JCPDS No. 04-0836) [183] .

X-ray diffraction of nickel and nickel oxide nanoparticles in the figure (3-7), where distinct peaks (111, 220, 311) appear at angles (2Theta = 37.6°, 62.1°, 75.6°) for nickel oxide, corresponding to the FCC structure and indicating good crystallinity of the nickel oxide nanoparticles. The common reference number for nickel oxide is (JCPDS Card No. 04-1049). Additional peaks (111, 200) appeared at angles (2Theta = 44.1°, 52.1°), and the weak peaks of the nickel indicate incomplete crystallization, with the common reference number for nickel (JCPDS No. 04-0850) [182]. Also, X-ray diffraction of Cu: Ni and NiO bimetallic particles in ratios of 1:1 and 3:1. Through the figure, the diffraction peaks in the X-ray diffraction pattern representing the characteristic crystal peaks of the FCC structure were recorded. A slight difference in the positions of the peaks is observed compared to the individual Cu, Ni, and NiO particles. The difference in positions is due to the interference between the crystal lattices of copper, nickel, or nickel oxide. It can be observed that the diffraction peaks of copper, nickel, and nickel oxide at a 1:1 and 3:1 ratio are higher compared to their peaks in the individual particles of the same elements.

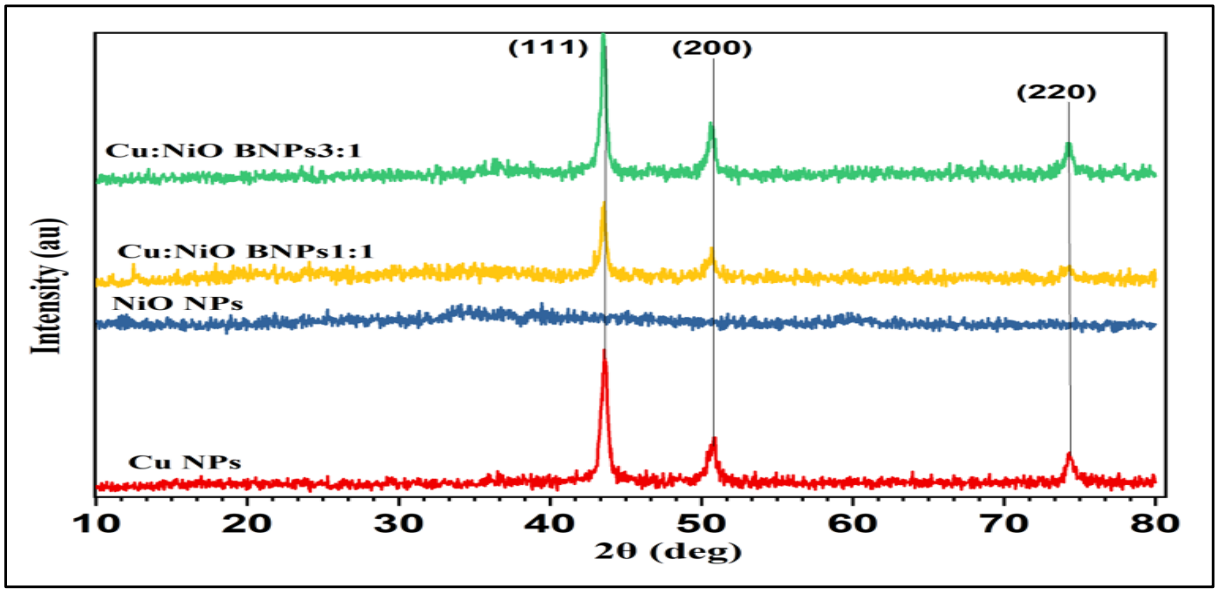

Figure (3-7): XRD powder pattern of the crystalline Cu NPs, Ni, NiO NPs, and bimetallic Cu: NiO BNPs 1:1 and 3:1.

Figure (3-8) illustrates the X-ray diffraction patterns used to determine the crystal structure of nanostructured zinc oxide. The diffraction patterns were recorded in the angular range of (20 to 80 °). The results showed conformity with the standards of hexagonal wurtzite zinc oxide, which corresponds to the International Card (JCPDS No. 00-036-1451). The main crystalline levels were identified (2Theta = 31.74°, 34.62°, 36.34°, 47.64°, 56.9°, 62.9°, and 67.86°) corresponding to the levels (111), (002), (101), (102), (110), (103), and (112), respectively [184]. The X-ray diffraction of Cu: ZnO bimetallic particles in ratios of 1:1 and 3:1. Through the figure, the diffraction peaks in the X-ray diffraction pattern representing the characteristic crystalline peaks of the FCC structure were recorded. It is observed that there is a slight difference in the peak positions compared to individual Cu and ZnO particles. The difference in positions is due to the interference between the crystalline lattices of copper and zinc oxide. It can be observed that the diffraction peaks of the Nano copper at a 3:1 ratio are higher compared to their height at a 1:1 ratio, while the peaks of Nano nickel and nickel oxide are clearer at a 1:1 ratio than at a 3:1 ratio. In addition to the X-ray diffraction of copper, it is also shown in the figure (3-8)

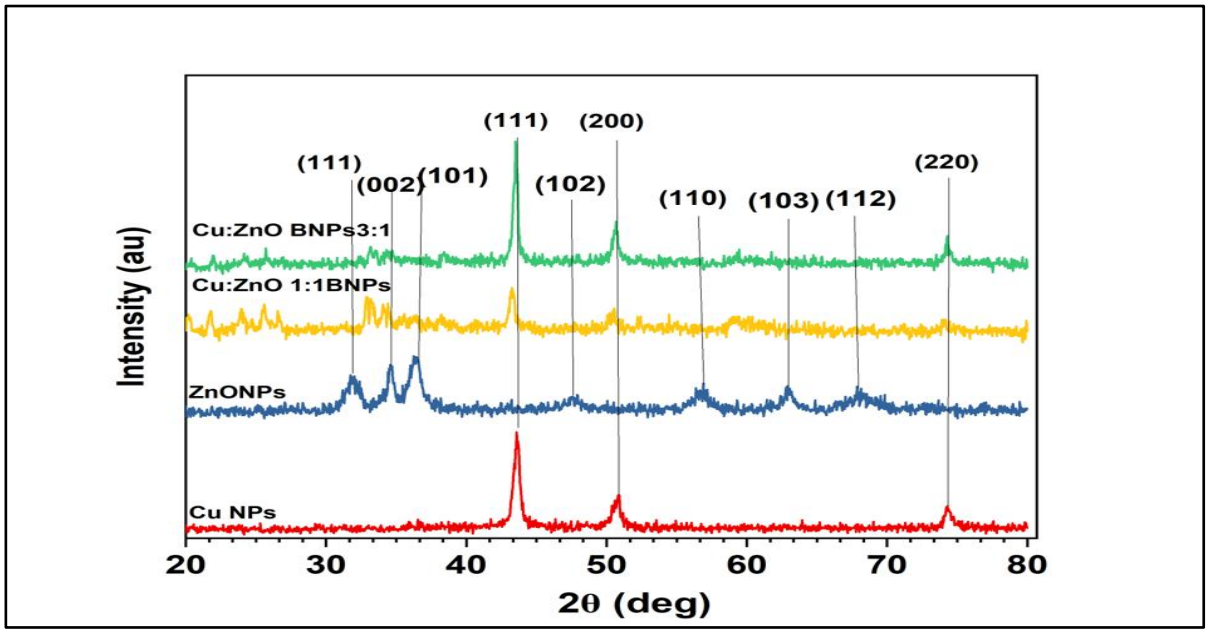

Figure (3-8): XRD powder pattern of the crystalline Cu NPs, ZnO NPs, and bimetallic Cu:ZnO BNPs 1:1, 3:1.

3.1.3 Field Emission Scanning Electron Microscopic Results

To determine the nanoscale dimensions of particles used (FESEM) and used (EDX) to measure the purity of the material, The figure (3-9A, B) shows an FESEM image of the green-synthesized silver nanoparticles. It appears that the formed particles are in the form of nanofibers with an average size of D1=64.86 nm and D2=74.54 nm. Where D = crystallite size, and these dimensions were measured at a magnification of 200 nm. This result is very close to the study presented by [185]. The EDX is presented in figure (3-9 C), measured at 15 kV, which indicates a very high presence of silver and a small amount of C and O, attributed to the presence of organic compounds on the surface of the nanoparticles. These results are similar to what was mentioned by Mohammad Amin Taleb Safa with others [176] .

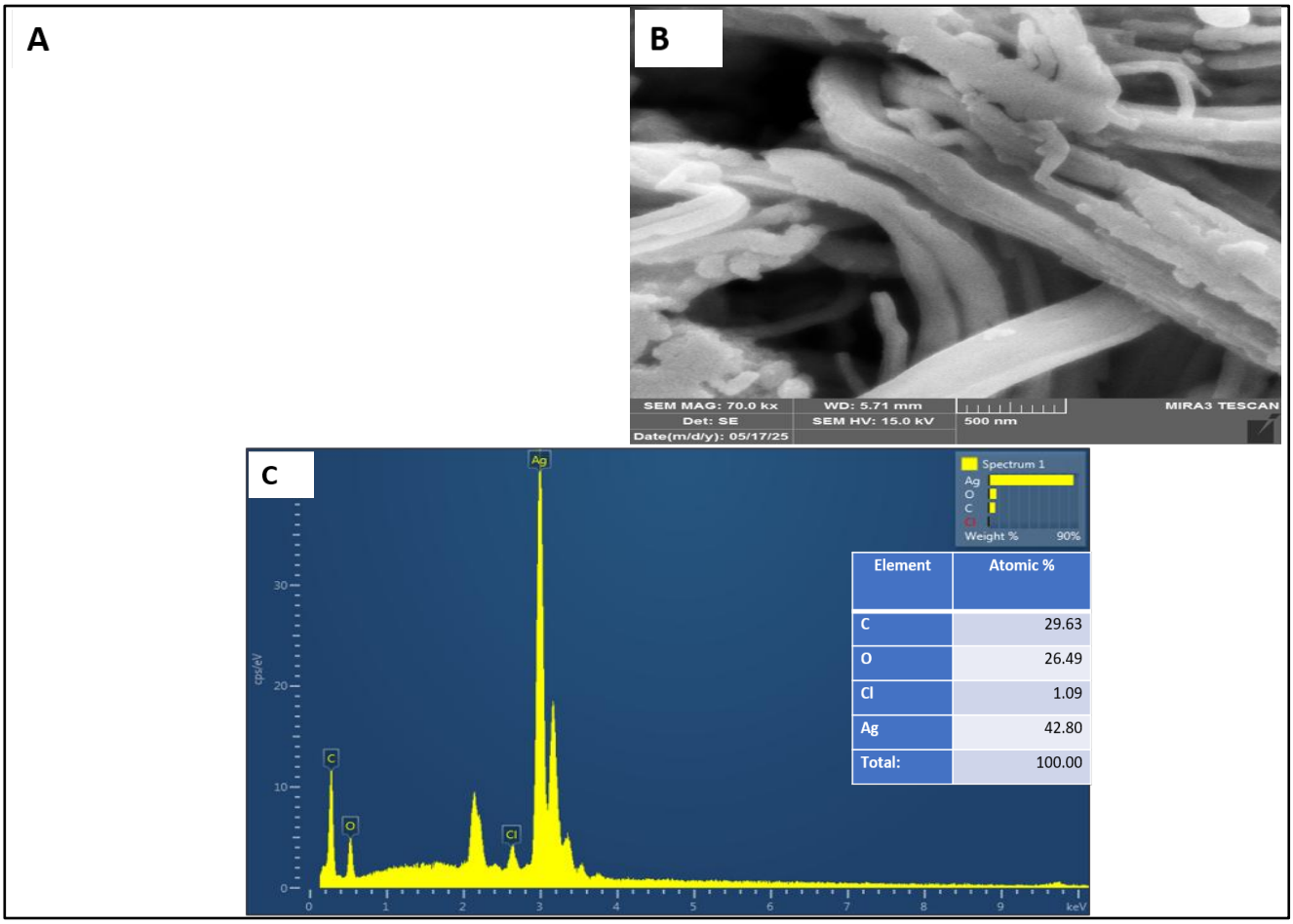

Figure (3-9): FESEM images of the green-synthesized silver nanoparticles (A) at 200 nm and (B) at 500 nm. (C) EDX spectroscopy of silver nanoparticles.

Figure (3-10 A, B) shows an FESEM image of the nanostructured nickel oxide that reveals a semi-spherical structure with an average diameter of 28.41 nm. This result is very close to what was previously mentioned [186]. The EDX spectrum of nano nickel oxide in figure (3-10 C) shows clear peaks for O and Ni, with small amounts of C, which is a result of reaction residues. [187].

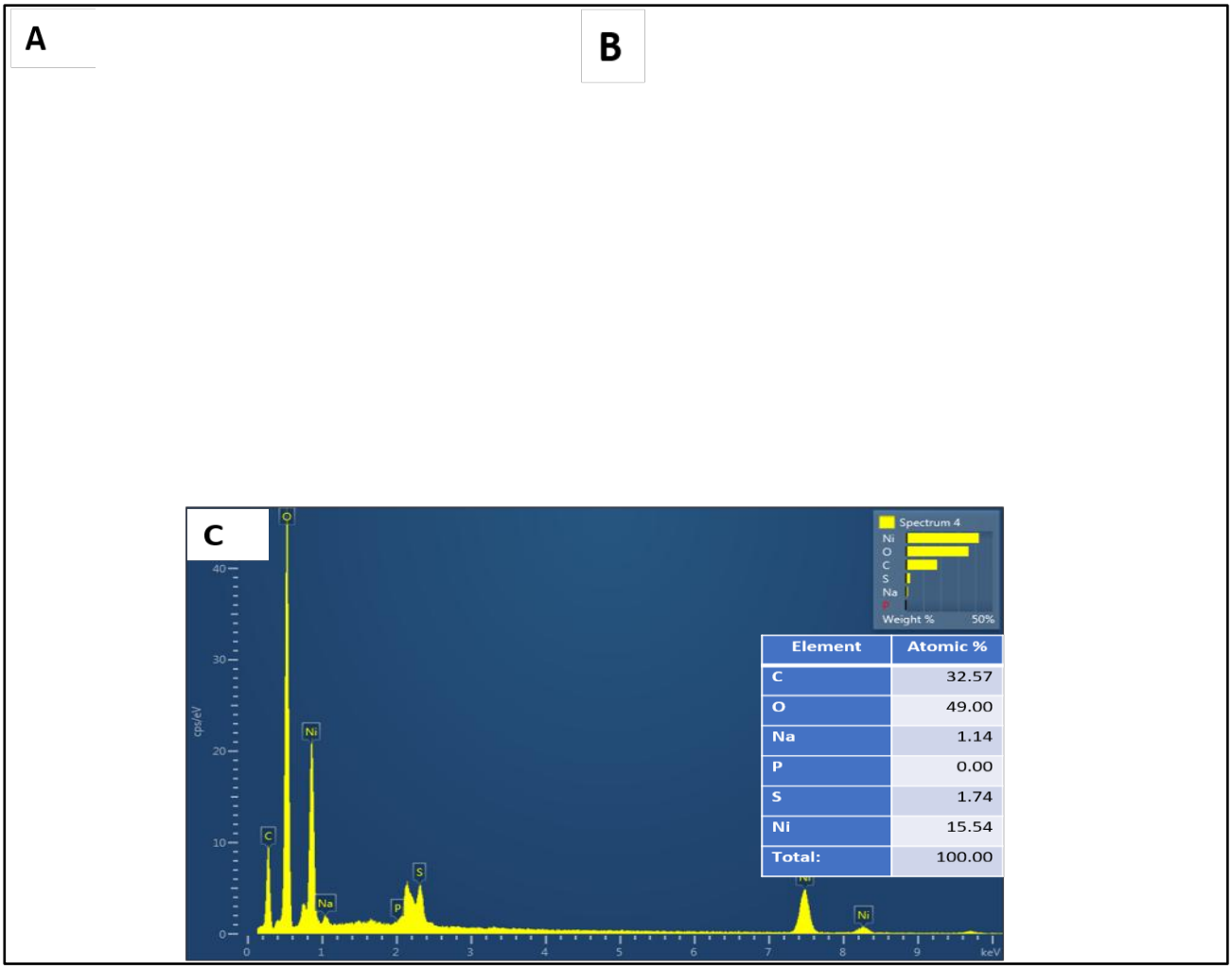

Figure (3-10): FESEM images of the green-synthesized nickel oxide nanoparticles (A) at 200 nm and (B) at 500 nm. (C) EDX spectroscopy of nickel oxide nanoparticles.

Through the FESEM electron microscopy scan shown in figure (3-11 A, B), for Ag nanoparticles prepared in a 1:1 ratio, the image reveals uniformly spherical particles with an average size of 43.24 nm. The figure (3-11C) illustrates the EDX spectrum of Ag: NiO BNP particles prepared using a plant extract (green tea) in

the ratio 1:1. The figure (3-11 C) indicates the presence of Ag and NiO elements, confirming the formation of bimetallic nanoparticles in a 1:1 ratio. The EDX provides quantitative data on the composition of nickel and silver, and it is clear from the figure that some parts of Ag: NiO BNPs exist as oxides due to an excess of oxygen, which may be due to the open reaction system. And there is also a very small percentage of Cl, C, and S resulting from the plant extract.

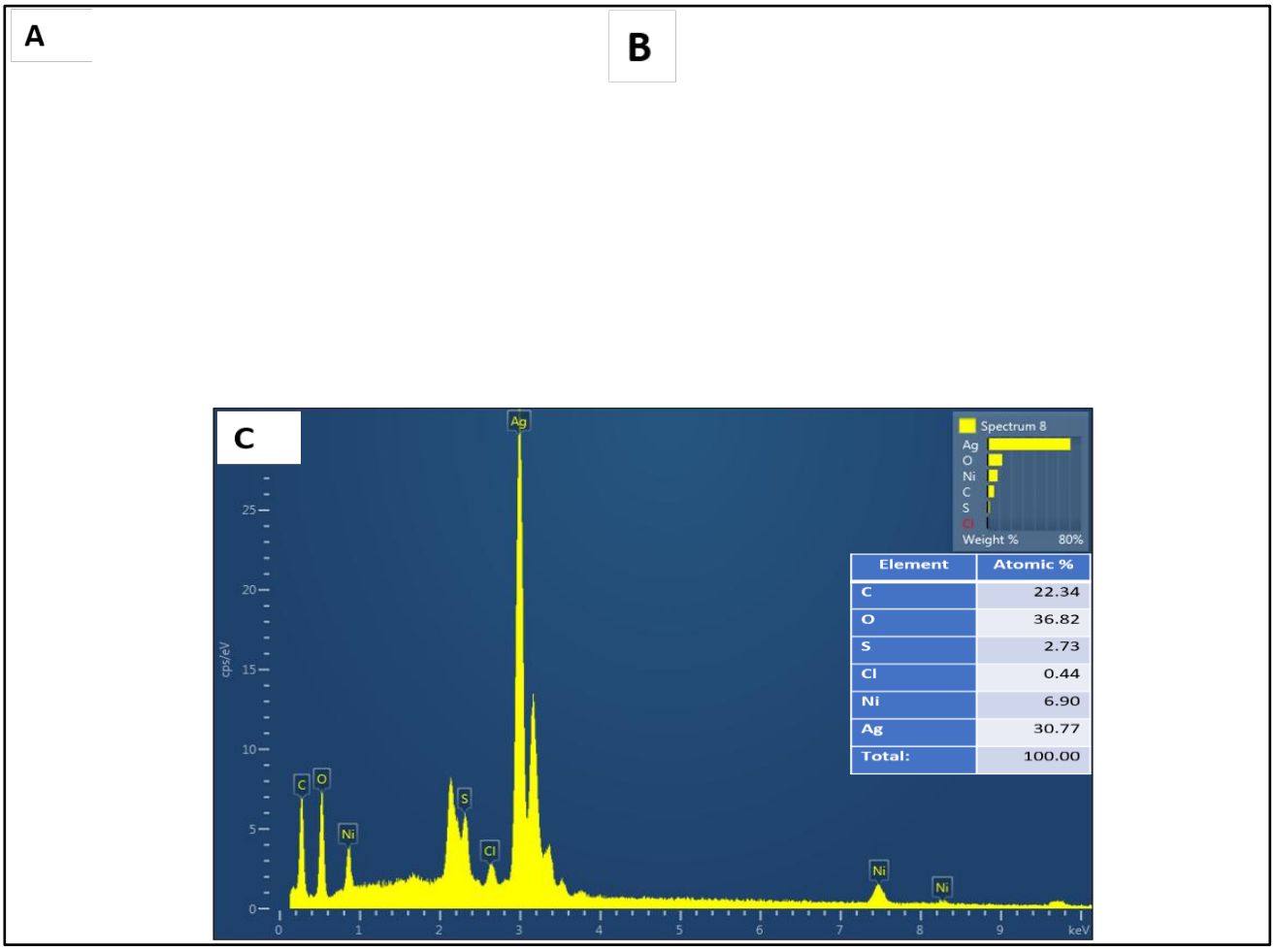

Figure (3-11): FESEM images of the green-synthesized Ag: NiO BNPs 1:1 (A) At 200 nm and (B) at 500 nm (C) EDX spectroscopy of Ag: NiO 1:1 BNPs

Figure (3-12 A, B) corresponds to the nanoparticles prepared in a 3:1 ratio, which are also uniformly spherical with an average size of 38.94 nm and contain clearly. As for figure (3-12 C), it clearly shows the very high percentage of silver compared to nickel, which confirms the formation of a bimetallic nanomaterial of Ag and Ni in a ratio of 3:1 [188].

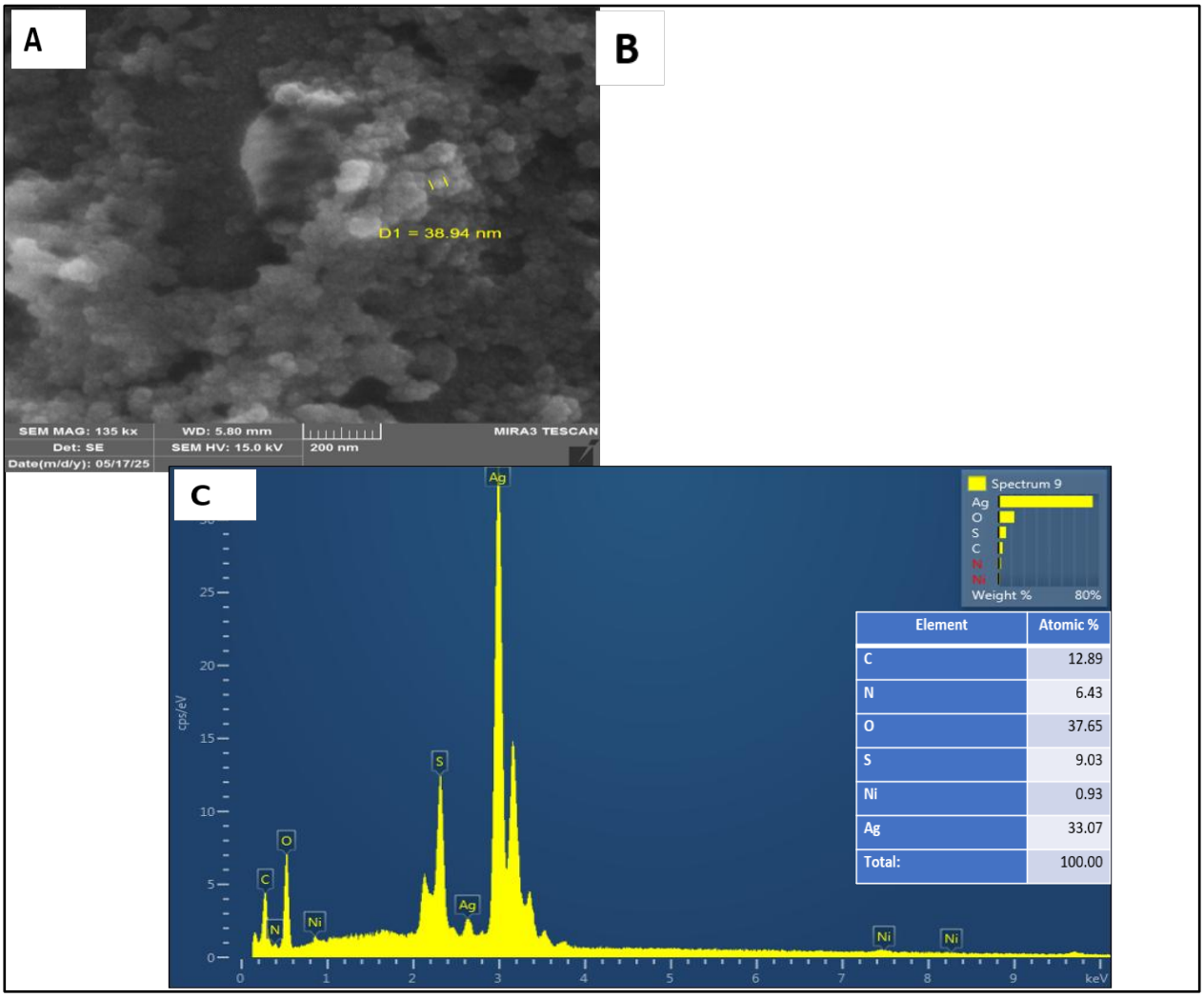

Figure (3-12): FESEM images of the green-synthesized Ag: NiO BNPs 3:1 (A) At 200 nm and (B) at 500 nm (C) EDX spectroscopy of Ag: NiO 3:1 BNPs.

Figure (3-13 A, B) represents an FESEM image showing Cu NPs particles prepared in a spherical shape with some agglomeration, which enhances interactions with other materials [189]. It is also clear from the figure that the particles are approximately spherical in shape with an average size of D=72.71 nm, where the dimensions were measured at a magnification of 200 nm. Moreover, the figure (3-13 C) represents the EDX spectrum of Cu NPs, and the results show that the percentages of Cu (85.02%) and O (14.98%) are present, with no visible impurities, indicating the very high purity of the sample prepared by the green method. This result matches previous studies [190].

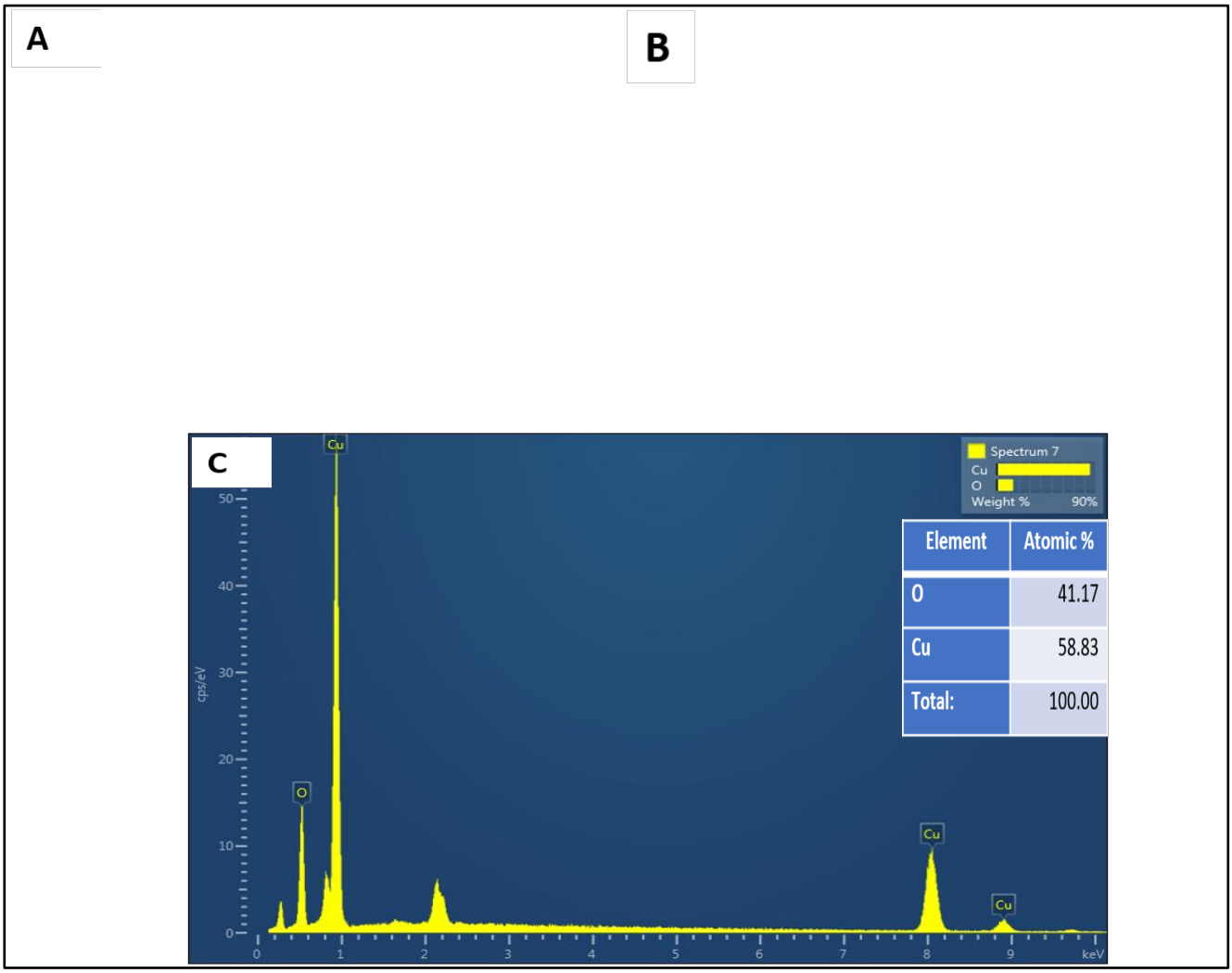

Figure (3-13): FESEM images of the green-synthesized copper nanoparticles (A) at 200 nm and (B) at 500 nm. (C) EDX spectroscopy of copper nanoparticles.

The figure (3-14A, B) depicts the cobalt oxide nanoparticles and shows that the particles are spherical in the form of nanoparticles with a size of 28.04 nm. As for the EDX map shown in figure (3-14C), it was used to examine the elemental composition of cobalt oxide at energies ranging from 0 to 10 kV. Based on weight and atomic ratios, Figure (3-14C) confirms the formation of cobalt oxide at a very high percentage of 42.80%, with a small percentage of carbon at 21.55%, which can be attributed to the plant extract. The appearance of 0.06% Na and 0.05% Al, which are considered very small compared to the percentage of cobalt oxide, was also noted; these results are very close to what was mentioned [191].

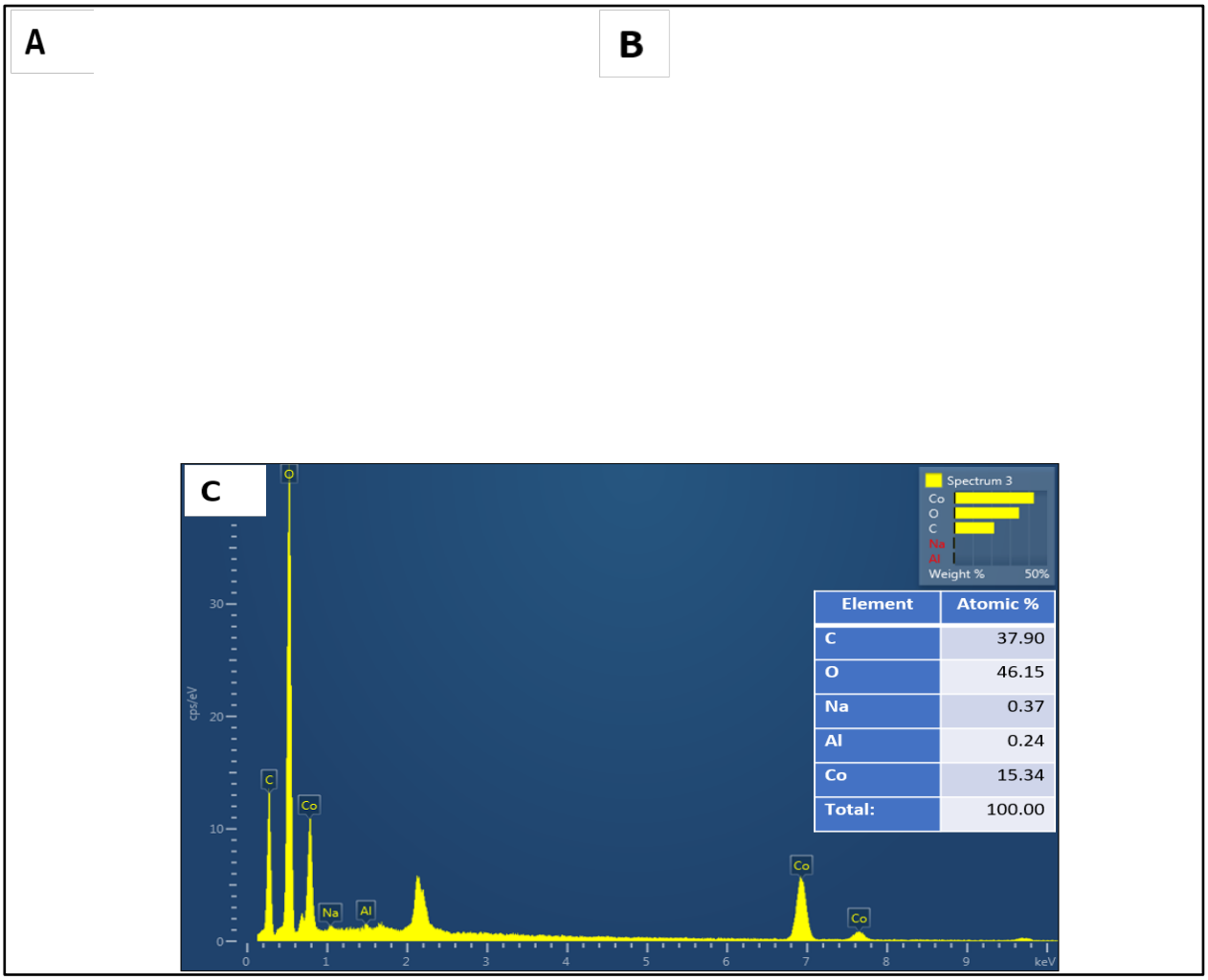

Figure (3-14): FESEM images of the green-synthesized cobalt oxide nanoparticles (A) at 200 nm and (B) at 500 nm. (C) EDX spectroscopy of cobalt oxide nanoparticles.

Figure (3-15 A, B) shows an FESEM image of Cu:CoO bimetallic particles prepared in a 1:1 ratio, clearly displaying spherical particles with slight agglomeration. The average size measured was 43.38 nm. Also, figure (3-15) shows the EDX spectrum of Cu:CoO BNPs prepared by the green method at a ratio of 1:1. We observe high peaks for Cu, Co, and O with very low percentages of S resulting from the plant extract.

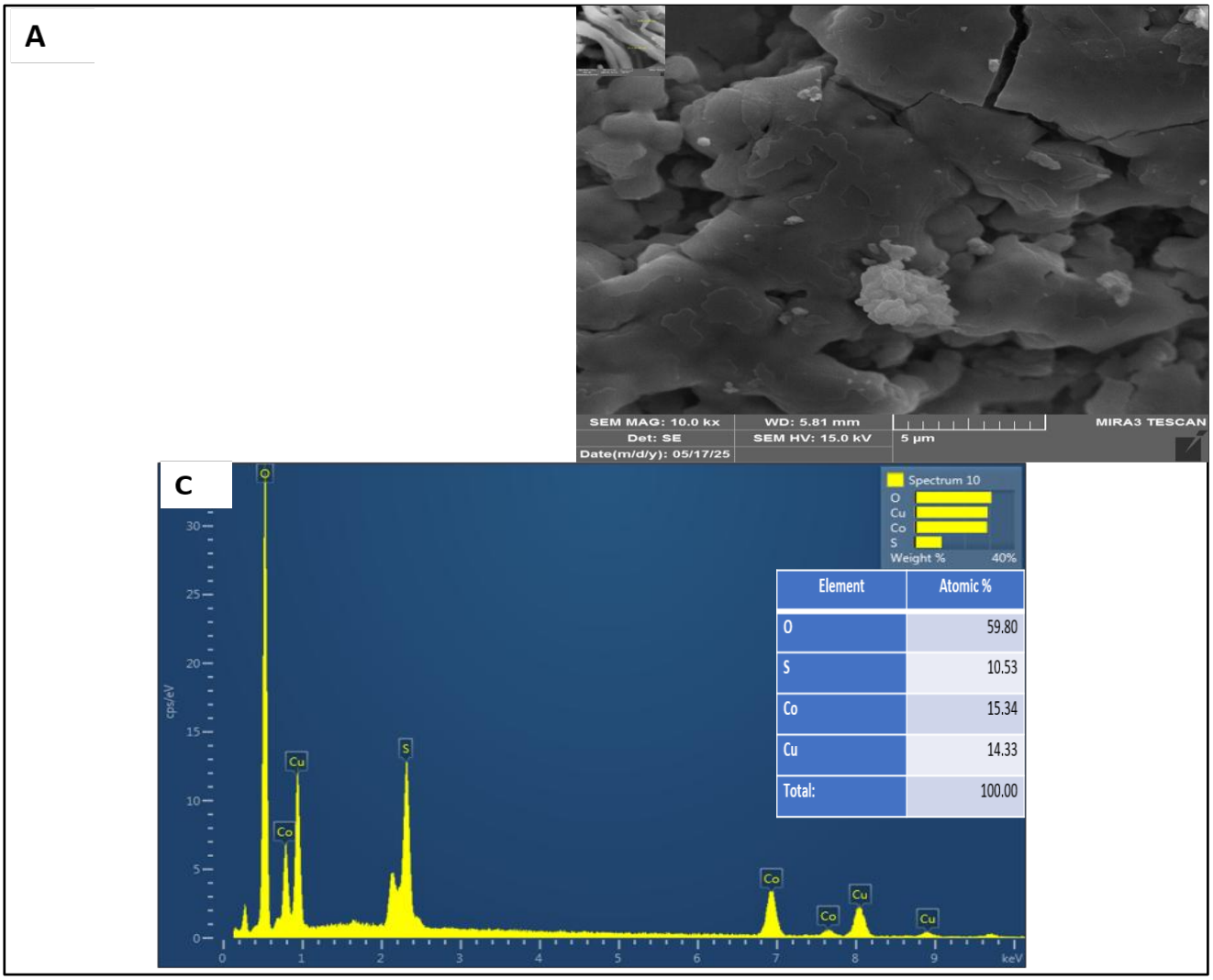

Figure (3-15): FESEM images of the green-synthesized Cu: CoO BNps1:1 (A) At 200 nm and (B) at 500 nm (C) EDX spectroscopy of Cu:CoO BNPs 1:1.

Figure (3-16 A, B) represents the particles prepared in a 3:1 ratio, showing uniformly spherical particles with an average size of 41.49 nm. As for the bimetallic particles prepared at a ratio of Cu:CoO 3:1, they are clearly shown in figure (3-16 C). The high peak corresponds to Cu, with peaks for Co and O and very low percentages of S due to the use of the plant extract. The particles are considered pure, as they do not contain significant impurities.

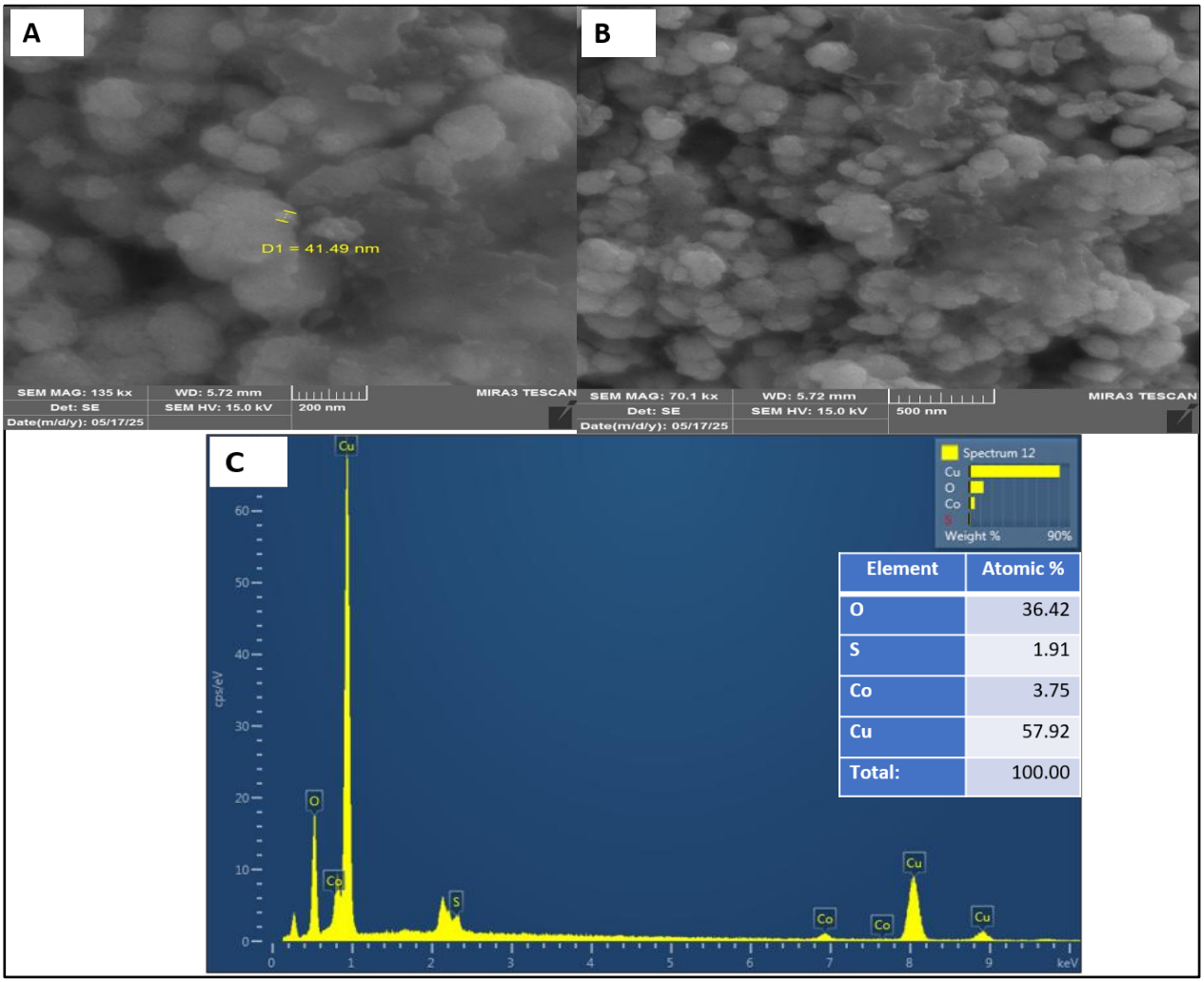

Figure (3-16): FESEM images of the green-synthesized Cu:CoO BNPs 3:1 (A) At 200 nm and (B) at 500 nm (C) EDX spectroscopy of Cu:CoO BNPs 3:1.

Figure (3-17A,B) shows FESEM images of Cu:NiO BNPs bimetallic nanoparticles prepared by the green method in a 1:1 ratio. It is clear from the image that the particles have irregular crystalline shapes with an average size of 24.06 nm, with no agglomeration observed and Figure (3-17C) shows the EDX spectrum of Cu:NiO BNPs prepared by the green method at a ratio of 1:1. We observe high peaks for Cu, Ni, and O with very low percentages of S and N resulting from the plant extract.

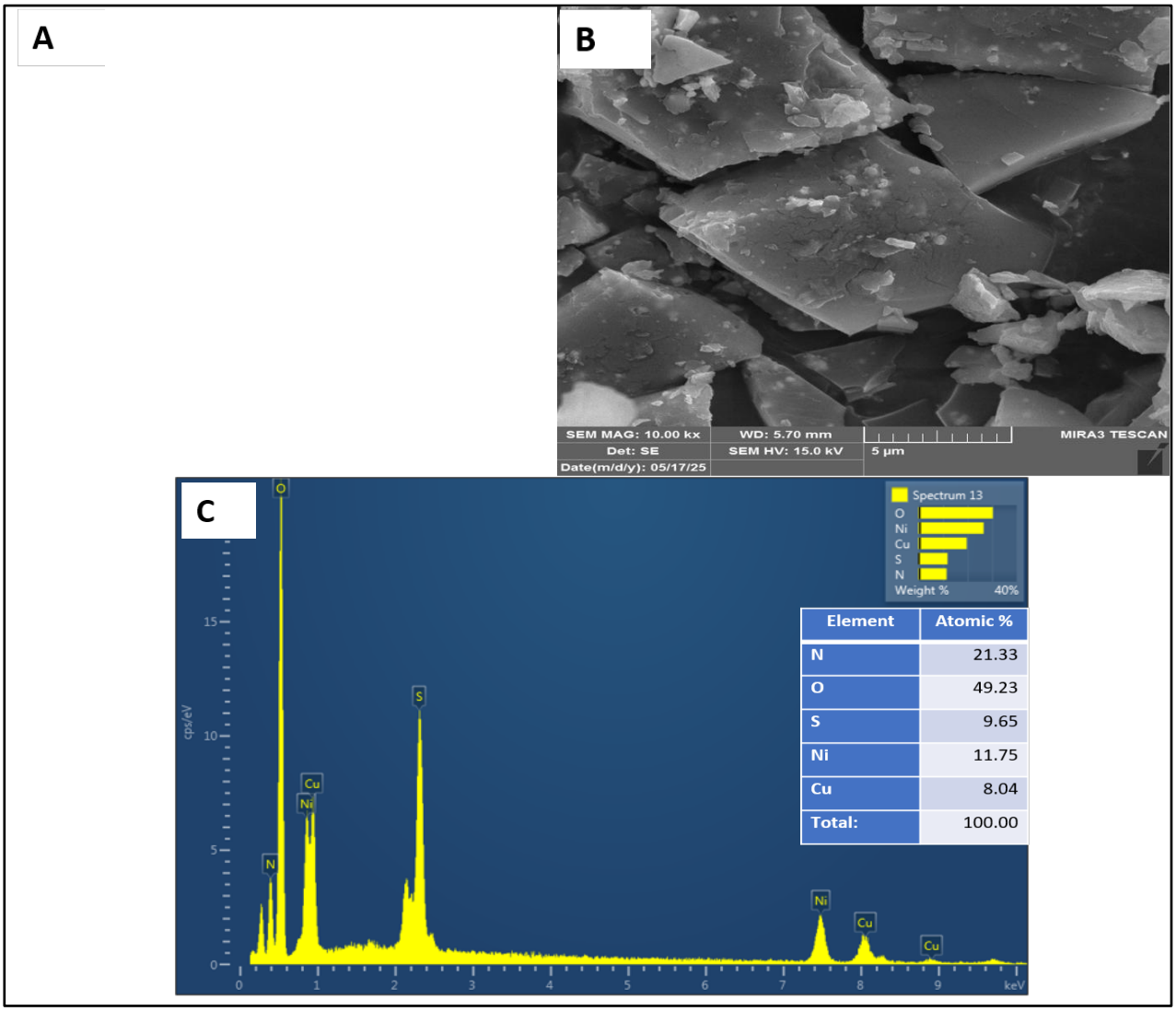

Figure (3-17): FESEM images of the green-synthesized Cu: NiO BNPs 1:1 (A) At 200 nm and (B) at 5 µm (C) EDX spectroscopy of Cu: NiO BNPs 1:1.

Figure (3-18A, B) represents the bimetallic particles Cu: NiO BNPs in a 3:1 ratio. From the figure, it was observed that the particles are uniformly spherical with an average size of 46.72 nm, with the size measured at a magnification of 200 nm. the bimetallic particles prepared at a ratio of 3:1 is clearly shown in Figure (3-18C). The high peak corresponds to Cu, with peaks for Co and O and very low percentages of S due to the use of the plant extract. The particles are considered pure, as they do not contain significant impurities.

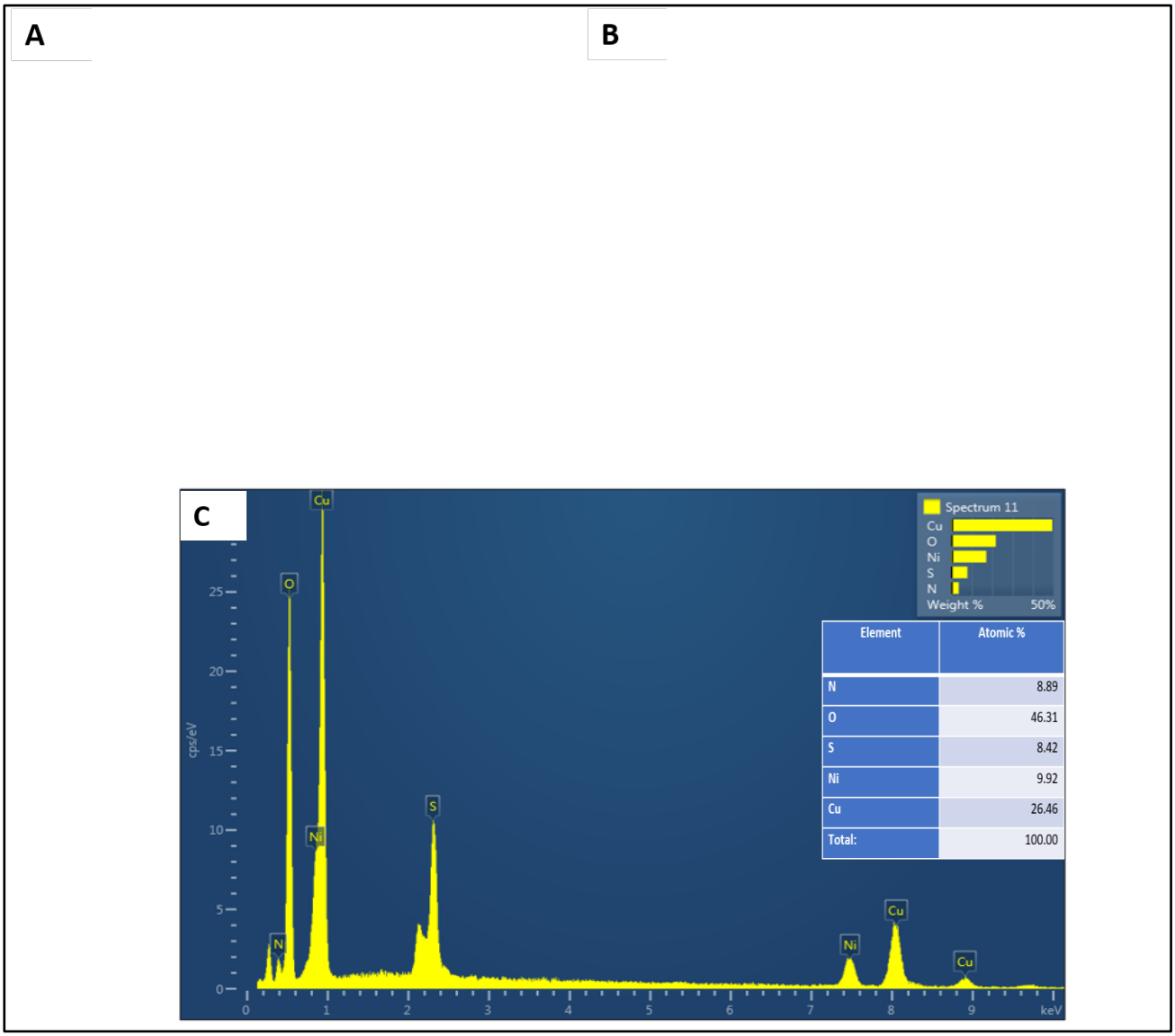

Figure (3-18): FESEM images of the green-synthesized Cu:NiO BNPs 3:1 (A) At 200 nm and (B) at 500 nm (C) EDX spectroscopy of Cu:NiO BNPs 3:1.

Through the FESEM analysis of the nanostructured zinc oxide and presenting the results as shown in figure (3-19 A, B), nearly spherical particles were observed with an average size of D=28.29 nm. This result is very close to the previous study [192]. The figure (3-19 C) shows the EDX spectrum of ZnO NPs, and it is observed that there is a very high percentage of zinc and a peak for oxygen, indicating the formation of ZnO NPs. Very small percentages of Na and N are also observed.

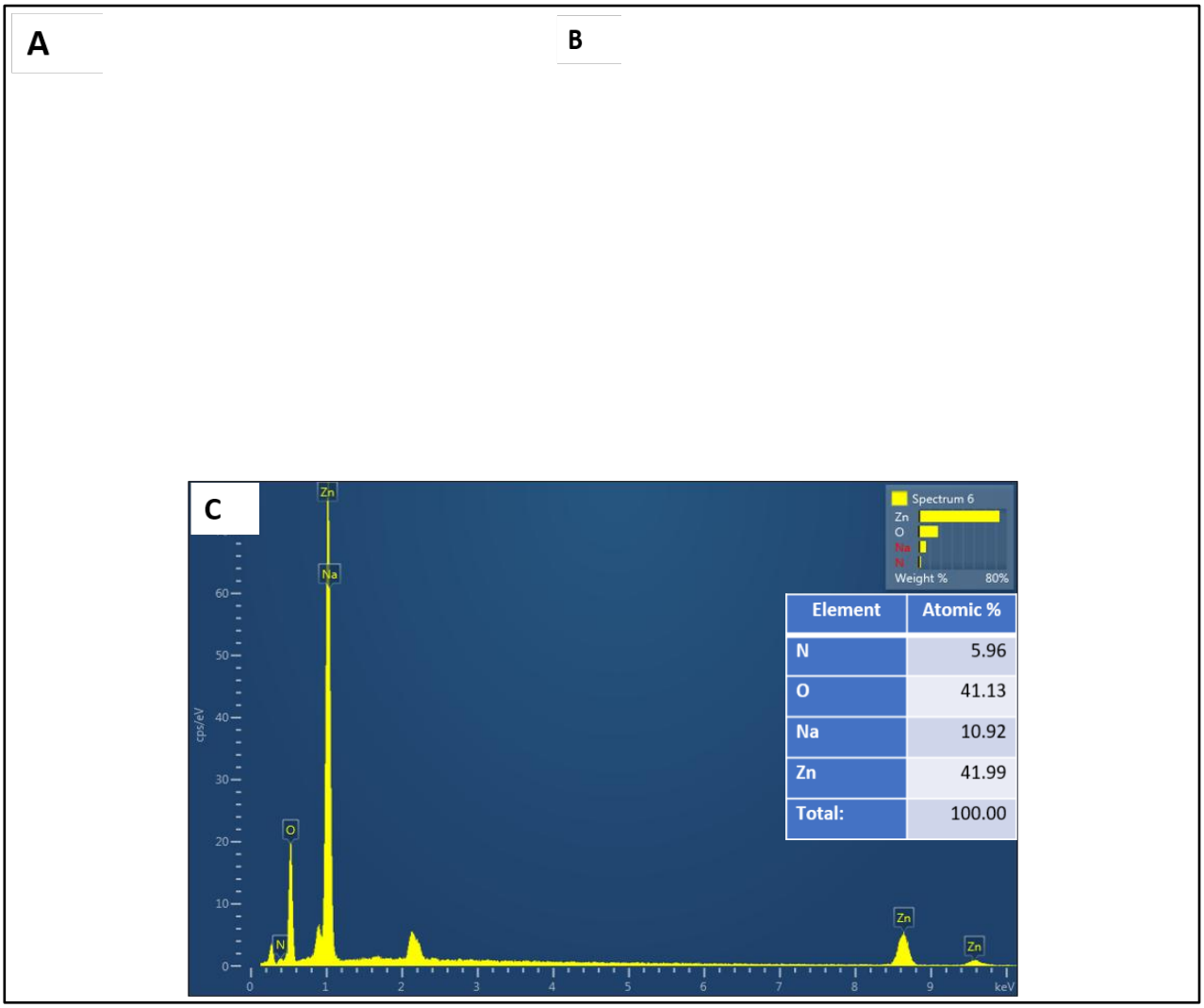

Figure (3-19): FESEM images of the green-synthesized zinc oxide nanoparticles (A) at 200 nm and (B) at 500 nm. (C) EDX spectroscopy of zinc oxide nanoparticles.

Figure (3-20) shows an FESEM image of Cu:ZnO bimetallic particles prepared in a 1:1 ratio, where the image clearly shows nearly spherical, uniform particles with an average size of 33.18 nm. The figure (3-20 C) illustrates the EDX spectrum of Cu: ZnO. In the figure with a 1:1 ratio, we observe high peaks for oxygen, zinc, and copper, in addition to small amounts of Au, S, N, and Na. These impurities could be a result of the synthesis process or remnants of the plant extract.

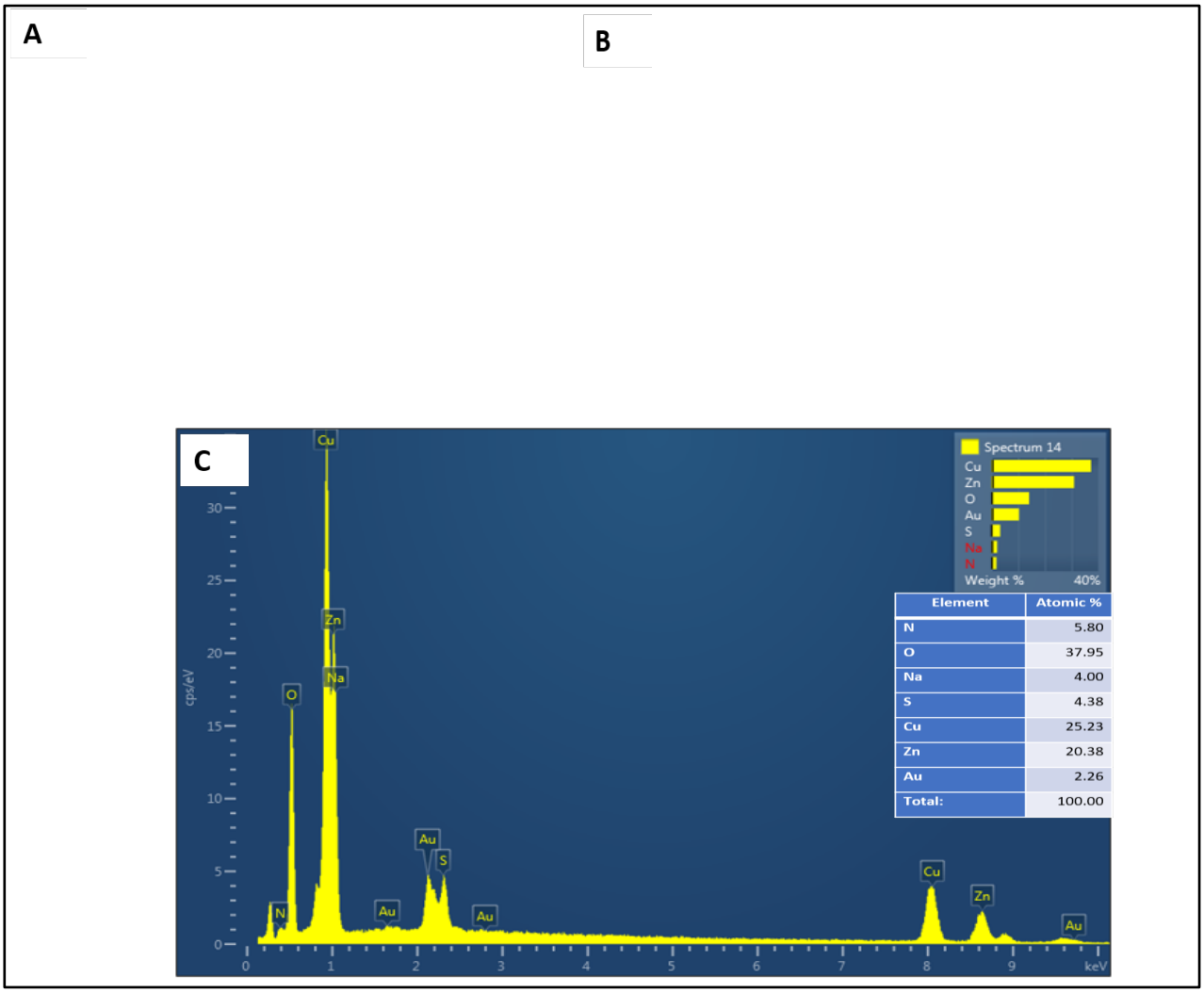

Figure (3-20): FESEM images of the green-synthesized Cu:ZnO BNPs 1:1 (A) at 200 nm and (B) at 500 nm. (C) EDX spectroscopy of Cu:ZnO BNPs 1:1.

Figure (3-21A, B) shows the particles prepared in a 3:1 ratio, which are clearly seen as uniform, homogeneous spherical particles with an average size of 35.17 nm in the figure (C). With a 3:1 ratio, we notice a significant increase in purity due to the high ratios of Cu, Zn, and O, with very little sulfur content because of the use of the plant extract. The high copper ratio in this model did not show the impurities present in the previous 1:1 model.

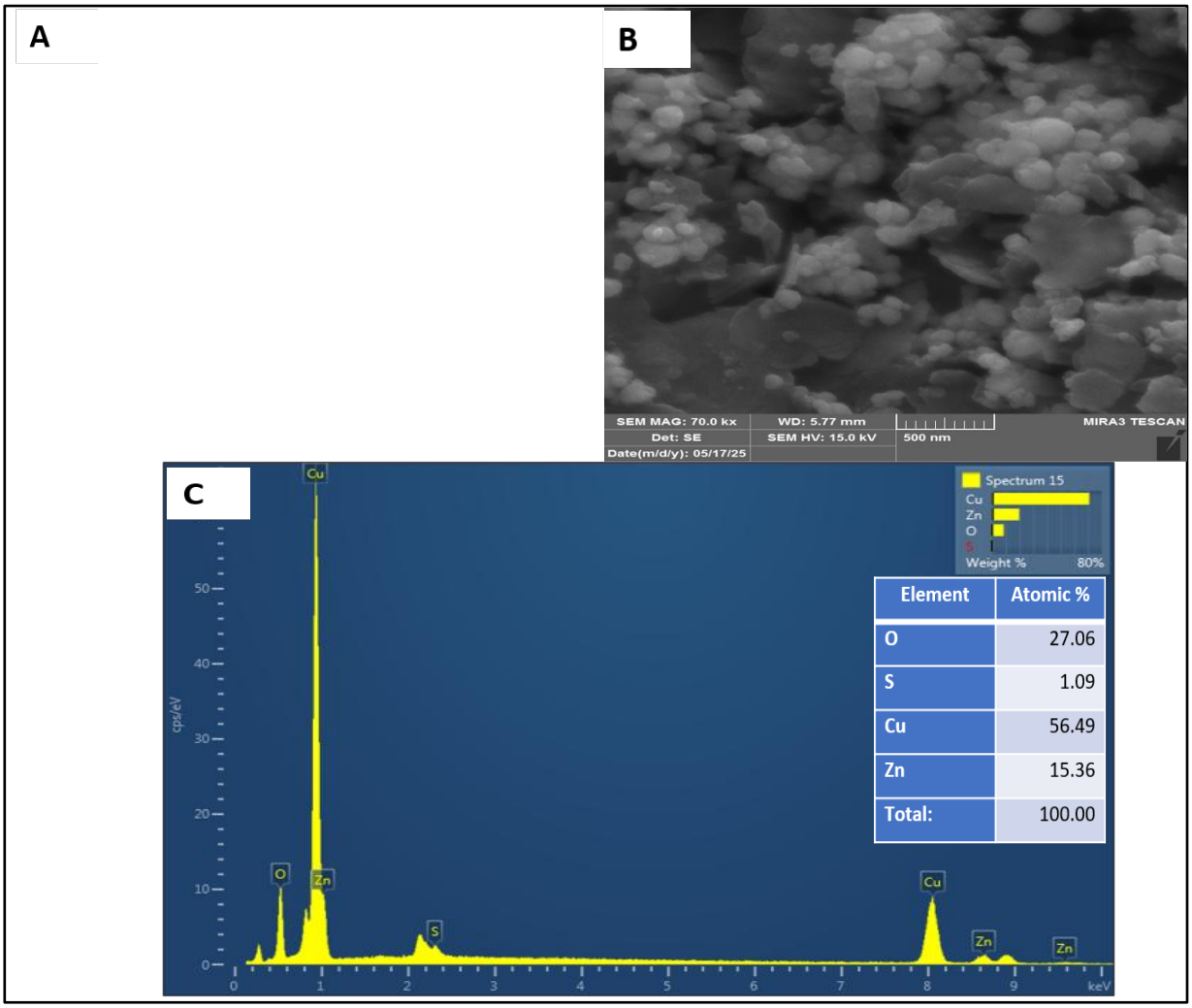

Figure (3-21): FESEM images of the green-synthesized Cu:ZnO BNPs 3:1 (A) at 200 nm and (B) at 500 nm (C) EDX spectroscopy of Cu: ZnO BNPs 3:1.

The figure (3-22A, B) represents an FESEM image showing the nanostructured iron oxide particles prepared by the green synthesis method. The image reveals irregular crystalline shapes with an average size of D=52.54 nm measured at a magnification of 200 nm. The shape of the synthesized particles is similar to previous studies [193]. Also, (C) represents the EDX spectrum of nanostructured iron oxide. As shown in the figure, there is a peak for iron constituting 51.78%, as well as varying percentages of K, C, Na, O, Mn, Mg, Cl, and Si. The appearance of Na and Cl is attributed to the precursors NaOH and Fe Cl_2 used in the preparation, while the presence of C is mainly due to the polyphenol group in

green tea extracts [194]. Other materials are present in very small amounts and are considered impurities resulting from the plant extract.

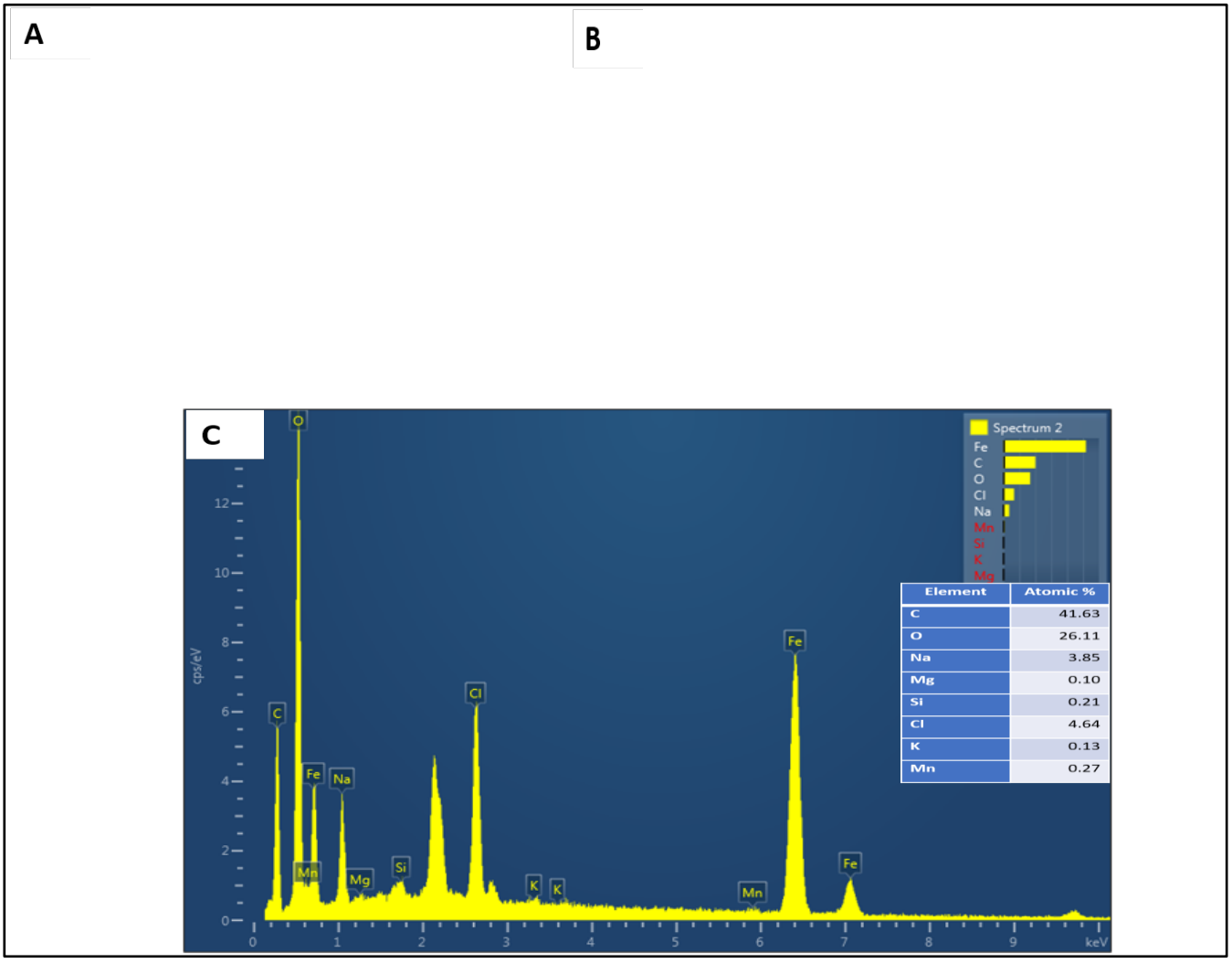

Figure (3-22): FESEM images of the green-synthesized iron oxide nanoparticles (A) at 200 nm and (B) at 500 nm. (C) EDX spectroscopy of iron oxide nanoparticles.

3.1.4 Transmission Electron Microscope Results

The TEM device was used to obtain clear images of particle sizes and shapes. Figure (3-23A) depicts the nanoparticles of Ag NPs, and the image shows a clear dispersion of the silver nanoparticles, with their size distributed in figure (3-23B) in the range (27-65) nm as calculated in the ImageJ program, with the majority concentrated in the region of (37-43) nm.

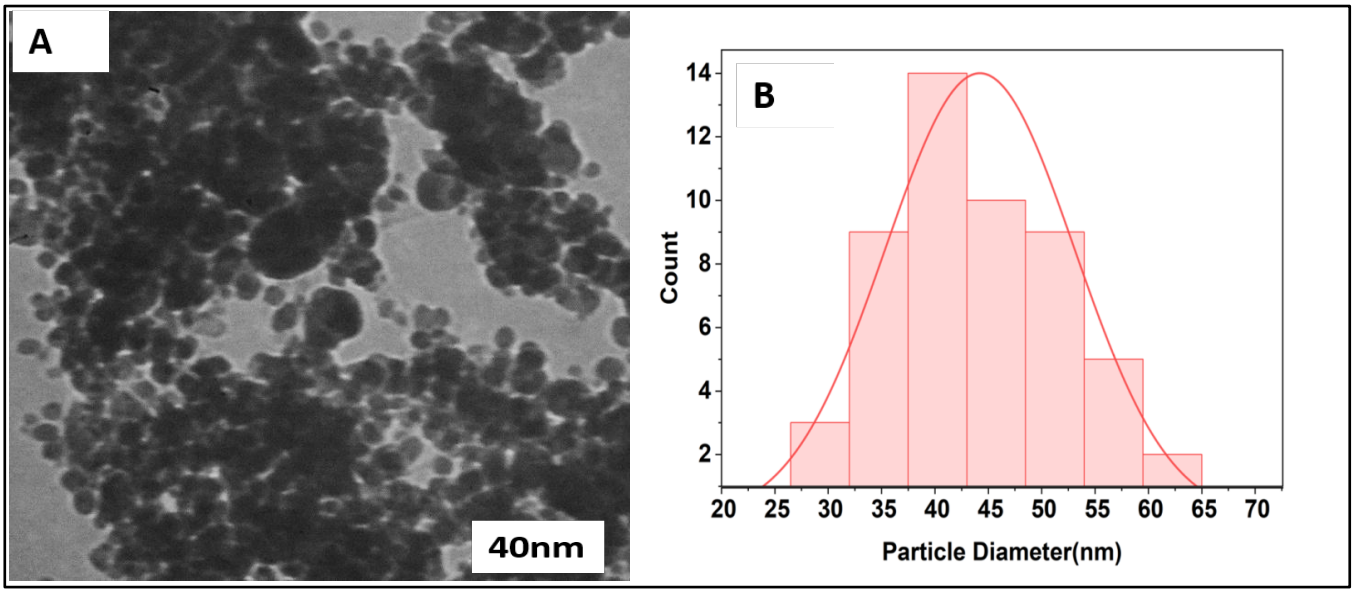

Figure (3-23): TEM measurement of the green-synthesized silver nanoparticles (A) and size distribution (B).

When conducting the microscopic analysis for NiO NPs using the TEM technique, it is shown in figure (3-24 A) that most of the particles have nearly spherical structures. After taking a sample and calculating the size using the ImageJ program, it was found that the particle sizes fall within the range of (10-45) nm, with the majority concentrated in the region of (24-31) nm, as shown in the distribution in figure (3-24 B).

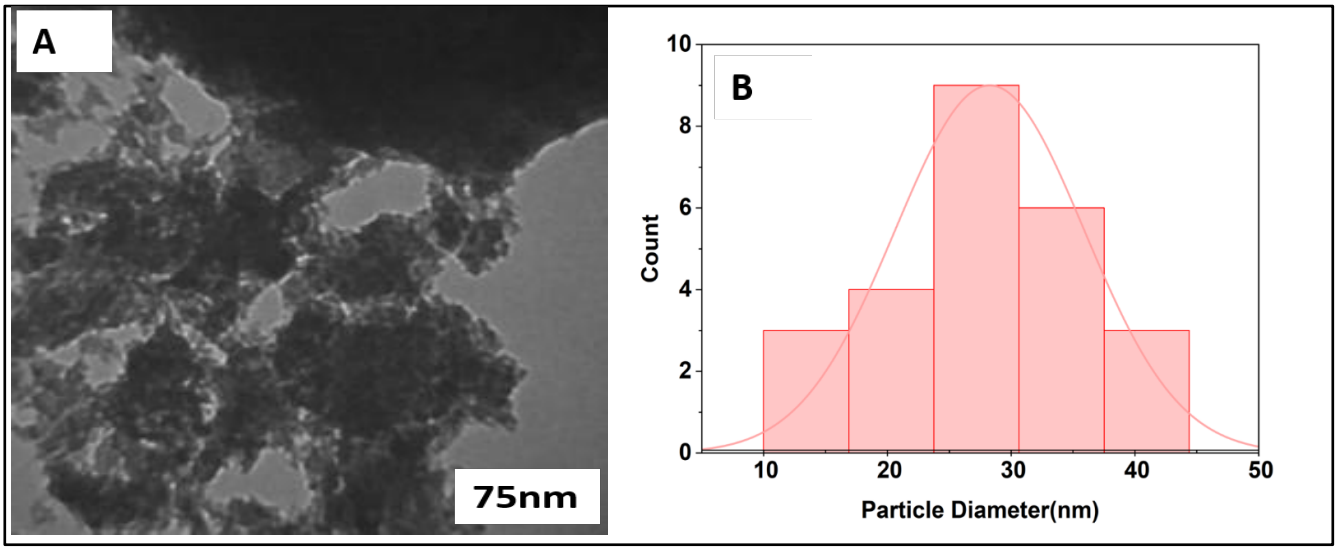

Figure (3-24): TEM measurement of the green-synthesized nickel oxide nanoparticles (A) and size distribution (B).

Through the TEM image of the bimetallic Ag: NiO BNPs nanoparticles prepared by the green method, the clear image in figure (3-25 A) shows the bimetallic nanoparticles prepared in a 1:1 ratio, which appear spherical, After taking a sample of these nanoparticles and calculating their average size using the ImageJ program, it was found that the highest percentage of the nanoparticles are concentrated in the range of 28-30.5 nm, as shown in figure (3-25B).

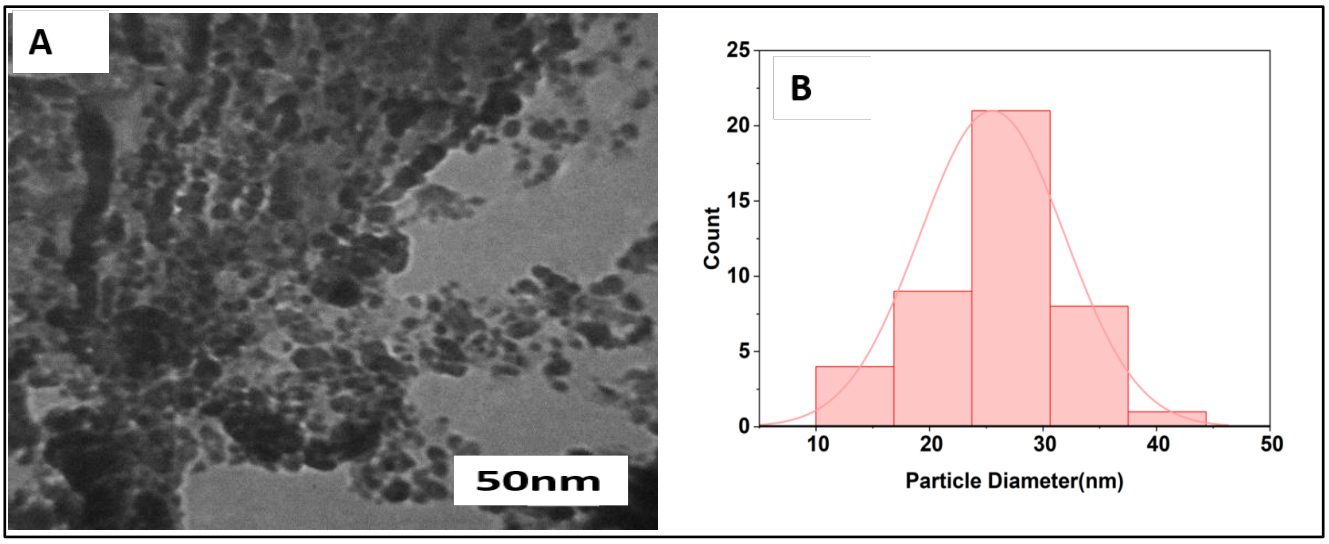

Figure (3-25): TEM measurement of the green-synthesized Ag: NiO BNPs 1:1 (A) and size distribution (B).

Figure (3-26A) shows that Ag nanoparticles appeared as dark cores with a NiO shell that is lighter in color than the core. The rare shell model [195] appears more clearly in the 3:1 ratio due to the increased silver content, making the core a dark black color surrounded by a shell of nickel. The average size of Ag: NiO BNPs 3:1 is 35-45 nm, as shown in Figure (3-26 B) .

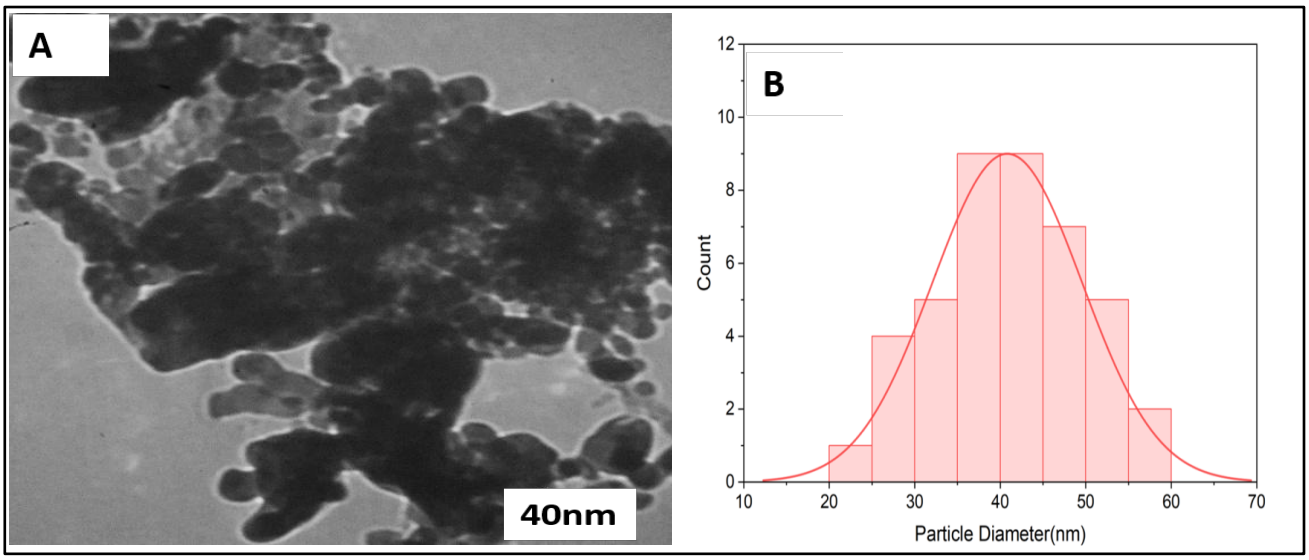

Figure (3-26): TEM measurement of the green-synthesized Ag:NiO BNPs 3:1 (A) and size distribution (B).

Figure (3-27A) shows the TEM measurement of Cu NPs. The high precision indicates the crystalline nature of the model. Through the random field of the TEM image, the average diameter of Cu NPs was calculated by taking approximately 40 particles and measuring their diameters using the ImageJ program. The distribution shown in figure (3-27B) represents particle size distribution within the range (5-27) nm, and the majority are concentrated at (14-18) nm.

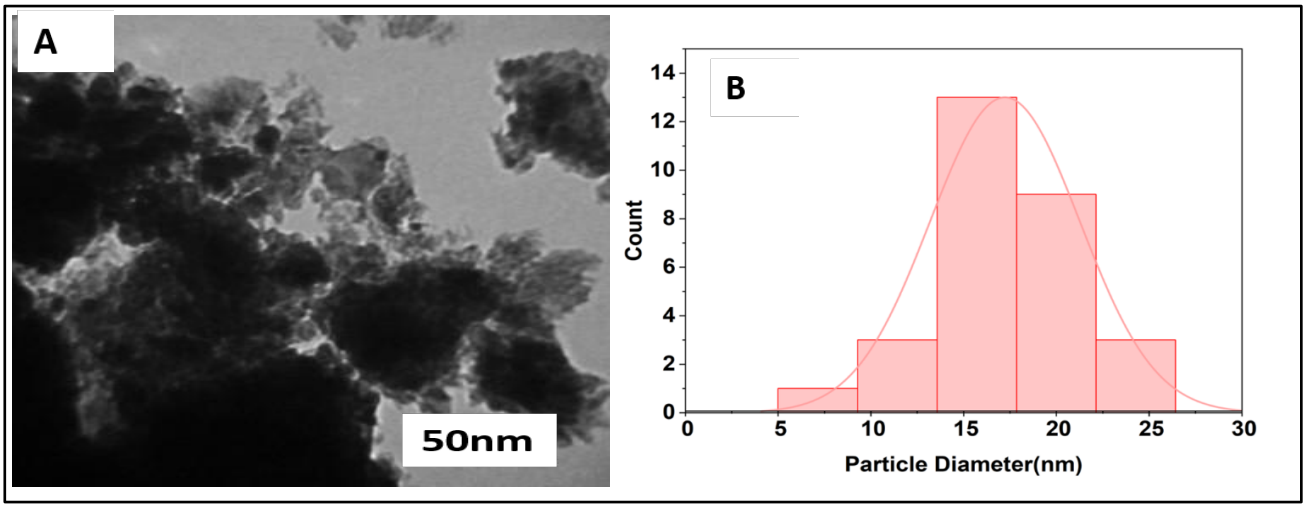

Figure (3-27): TEM measurement of the green-synthesized copper nanoparticles (A) and size distribution (B).

As for the TEM measurement shown in figure (3-28A) for Cu: NiO BNPs at a 1:1 ratio, the particles appear in irregular shapes consisting of opaque and less opaque regions. When a specific group of particles was selected and their volume was calculated using the ImageJ program, it was found that the particles are distributed within the range of 16-44 nm and the majority are concentrated at 21-27 nm. As shown in figure (3-28B).

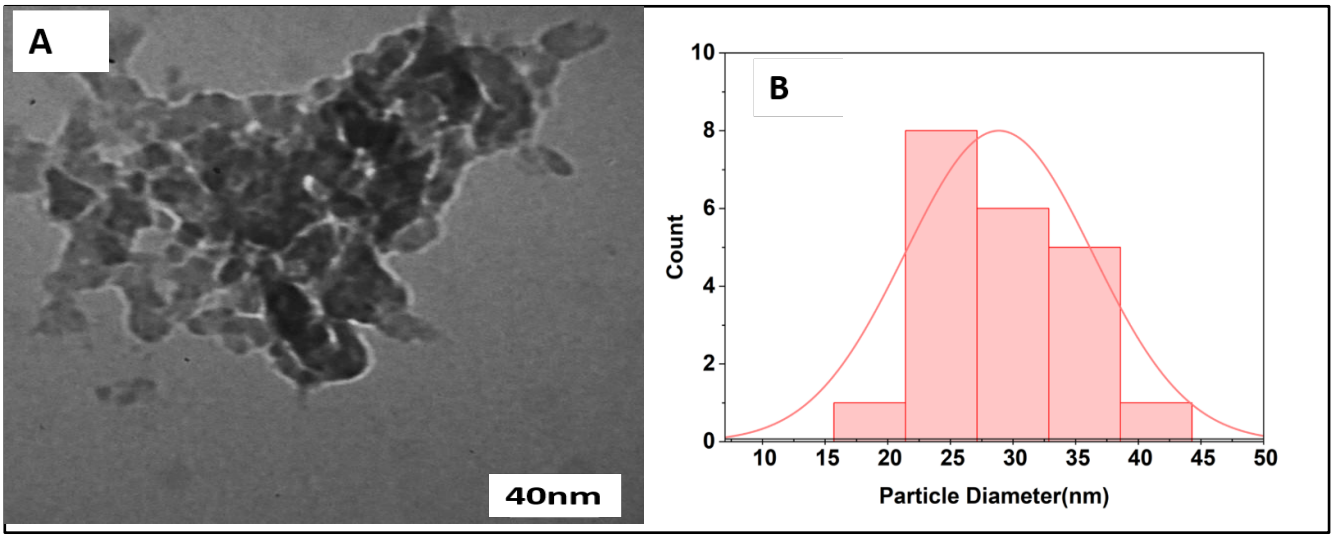

Figure (3-28): TEM measurement of the green-synthesized Cu:NiO BNPs 1:1 (A) and size distribution (B).

Figure (3-29A) shows the TEM measurement of the bimetallic nanoparticles of Cu: NiO prepared in a 3:1 ratio. The figure illustrates the uniform distribution of the nanoparticles and the slight dispersion as shown in the figure. After calculating the particle size range, it was found that they fall within the required nanoscale range, meaning the particle sizes are within the range (29-70) nm, and the majority are concentrated at (46-57) nm, as shown in figure (3-29B).

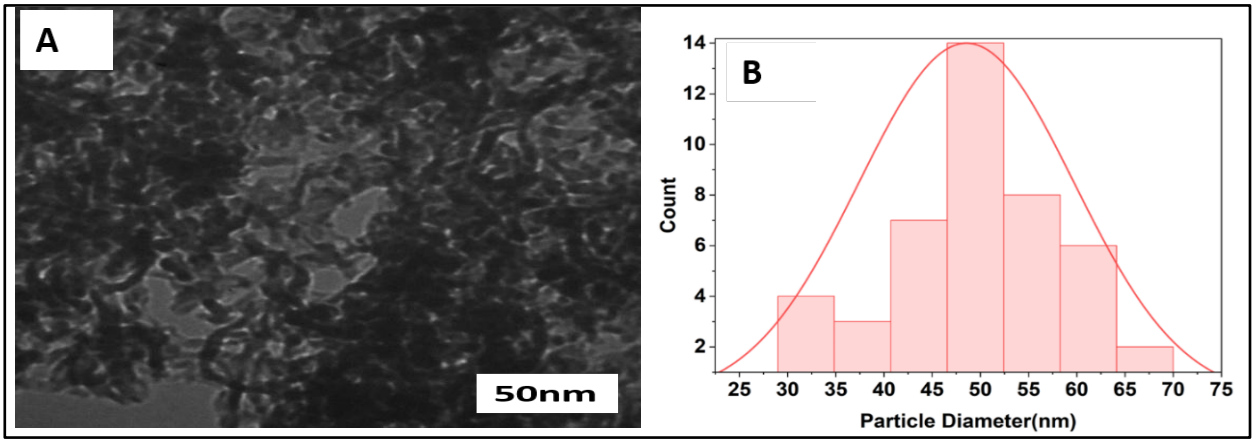

Figure (3-29): TEM measurement of the green-synthesized Cu:NiO BNPs 3:1 (A) and size distribution (B).

Figure (3-30A) shows uniformly distributed nanoparticles, which are cobalt nanoparticles After calculating the size of these particles using the ImageJ program, it was found that they fall within the range (24-65) nm, meaning they are within the nanoscale size, and the majority are concentrated at (38-45) nm as shown in figure (3-30 B).

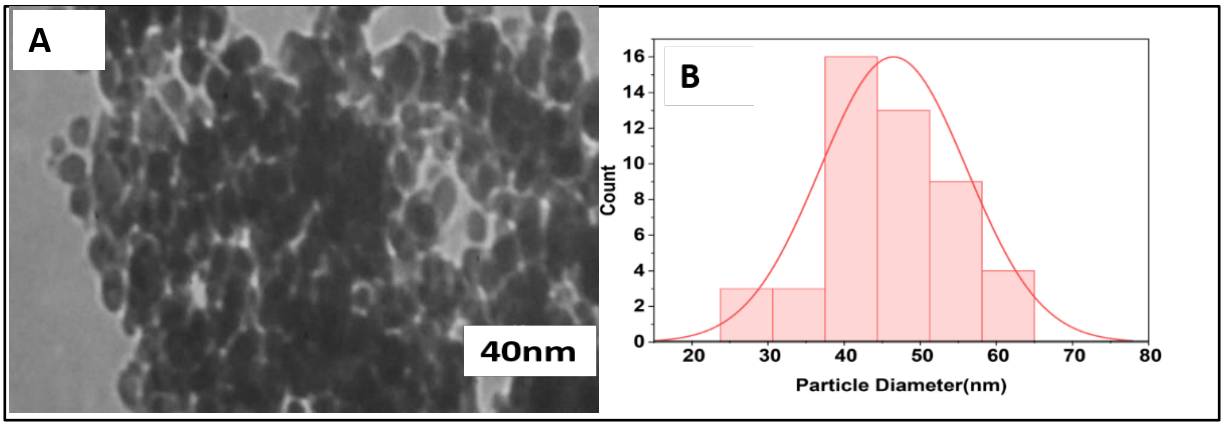

Figure(3-30):TEM measurement of the green-synthesized cobalt oxide nanoparticles (A) and size distribution (B).

TEM measurement of Cu:CoO BNPs particles prepared in a 1:1 ratio, as shown in figure (3-31 A), reveals that the particles are homogeneous and non-agglomerated. When calculating the size by selecting a group of particles and determining their dimensions using the ImageJ program, it was found that the size of the bimetallic particles falls within the range of 20-65 nm, with the majority of the particles concentrated in the 35-40 nm region, as shown in figure (3-31B).

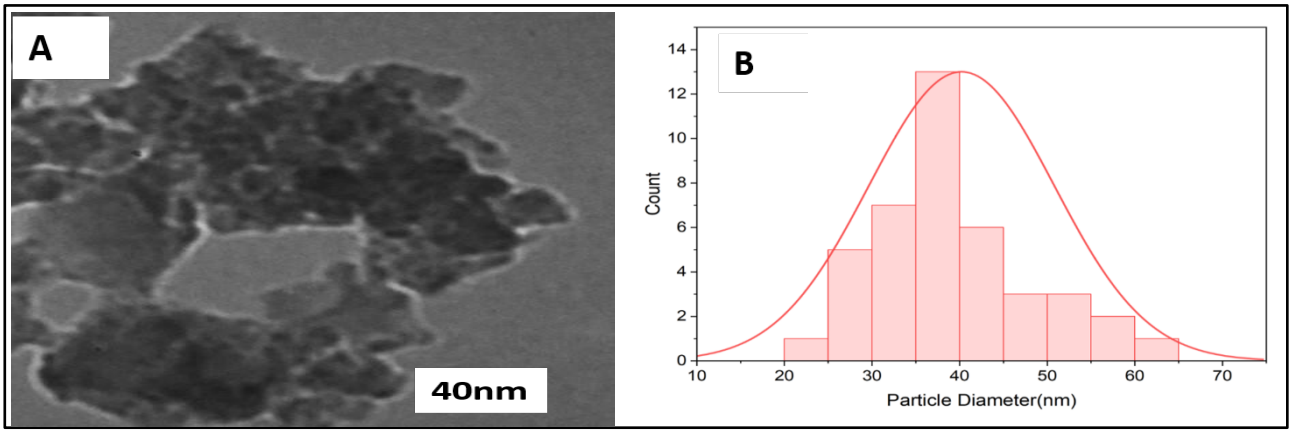

Figure (3-31): TEM measurement of the green-synthesized Cu: CoO BNPs 1:1 nanoparticles (A) and size distribution (B).

Figure (3-32 A) for Cu: CoO BNPs prepared in a 3:1 ratio, it is clear from the TEM image that they are homogeneous spherical particles. After measuring their volumetric distribution, it was found to be within the range of 10-45 nm, with the majority of the particles concentrated in the 25-30.5 nm range, as shown in figure (3-32 B).

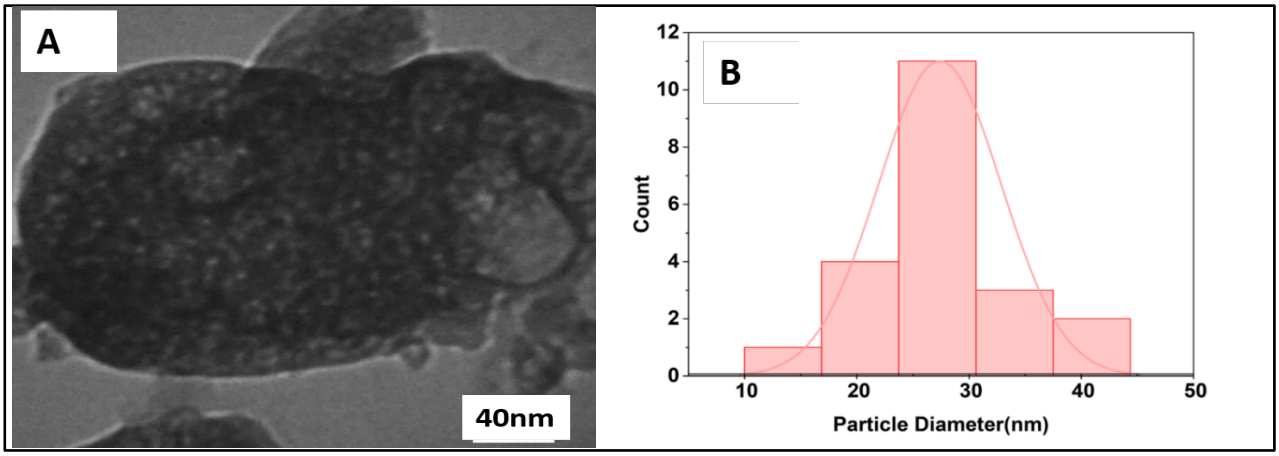

Figure (3-32): TEM measurement of the green-synthesized Cu:CoO BNPs 3:1 nanoparticles (A) and size distribution (B).

Figure (3-33A) represents the TEM microscopic result of zinc oxide nanoparticles, where they appear as homogeneous spherical aggregates. After selecting a specific area consisting of approximately 40 particles and using the ImageJ program to calculate the size, it was found that the sizes of the zinc oxide nanoparticles fall within the range of 31-87 nm, with the majority concentrated around the size of (45-52)nm, as shown in figure (3-33B).

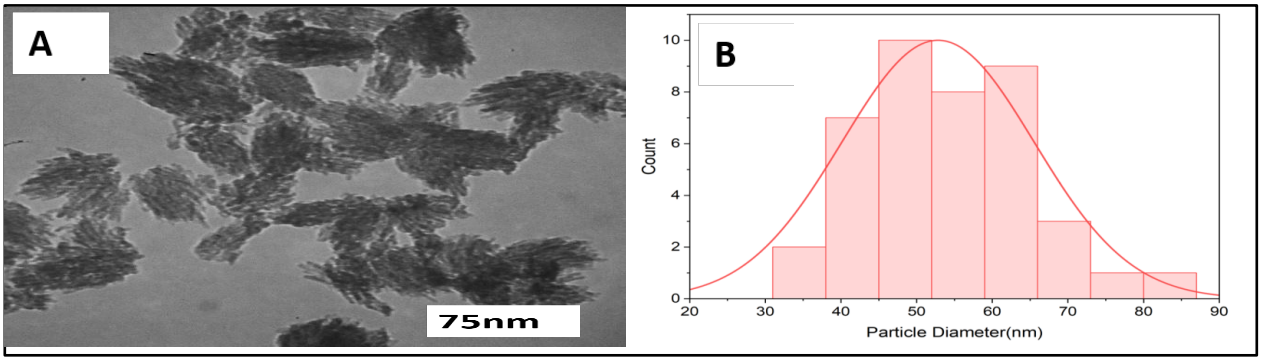

Figure (3-33): TEM measurement of the green-synthesized ZnO NPs nanoparticles (A) and size distribution (B).

Figure (3-34A) illustrates the measurement of Cu: ZnO BNPs particles prepared in a 1:1 ratio, revealing that the particles are homogeneous, non-agglomerated, and spherical, appearing in dark and semi-transparent regions. When calculating the size by selecting a group of particles and determining their dimensions using the ImageJ program, it was found that the size of the bimetallic particles falls within the range of 13-27 nm, with the majority of the particles concentrated in the 19-21.5 nm region, as shown in figure (3-34B).

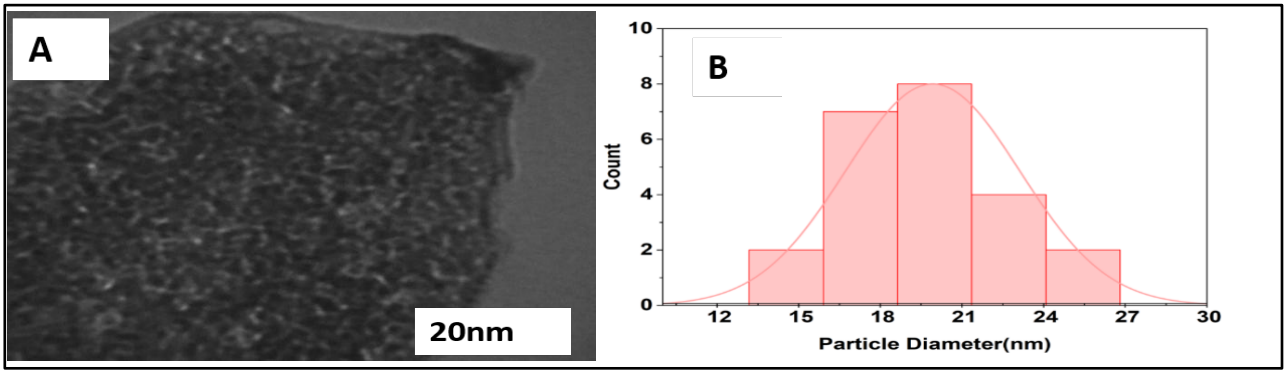

Figure (3-34): TEM measurement of the green-synthesized Cu: ZnO BNPs 1:1 nanoparticles (A) and size distribution (B).

Figure (3-35A) shows Cu: ZnO prepared in a 3:1 ratio, it is clear from the TEM image that they are more uniformly spherical After measuring their volumetric distribution, it was found to be within the range of 25-51 nm, with the majority of the particles concentrated in the range of 33-37 nm, as shown in figure (3-35B).

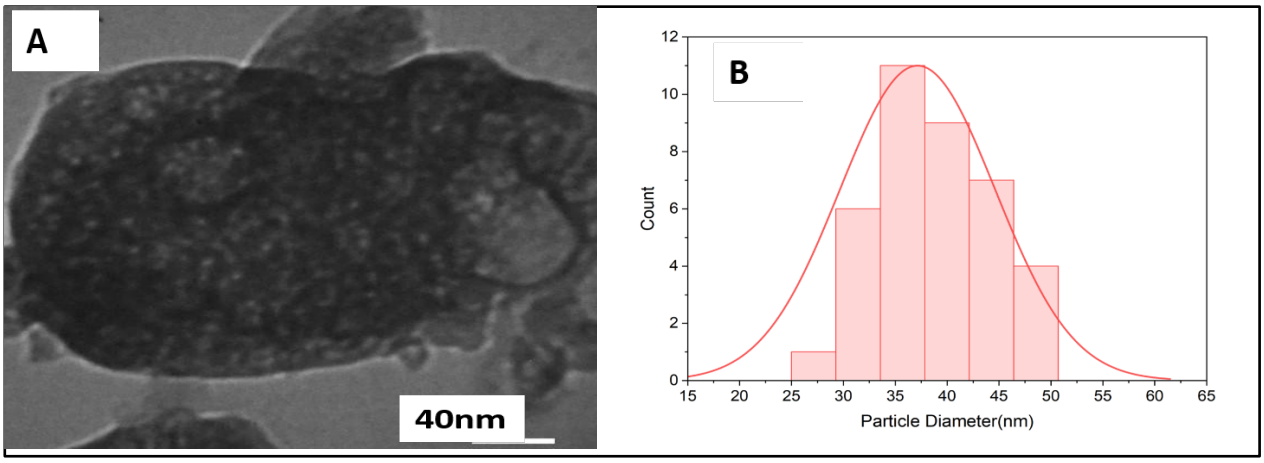

Figure (3-35): TEM measurement of the green-synthesized Cu:ZnO BNPs 3:1 nanoparticles (A) and size distribution (B).

Figure (3-36A) represents an image for TEM analysis to assess the shape and size of the iron oxide nanoparticles [196]. The figure consists of irregular crystals, and after taking a number of them and calculating the average size using the ImageJ program, it was found that the size distribution falls between 10 and 45 nm, as shown in figure (3-36 B); the particles are concentrated in the range of (25-30.5) nm.

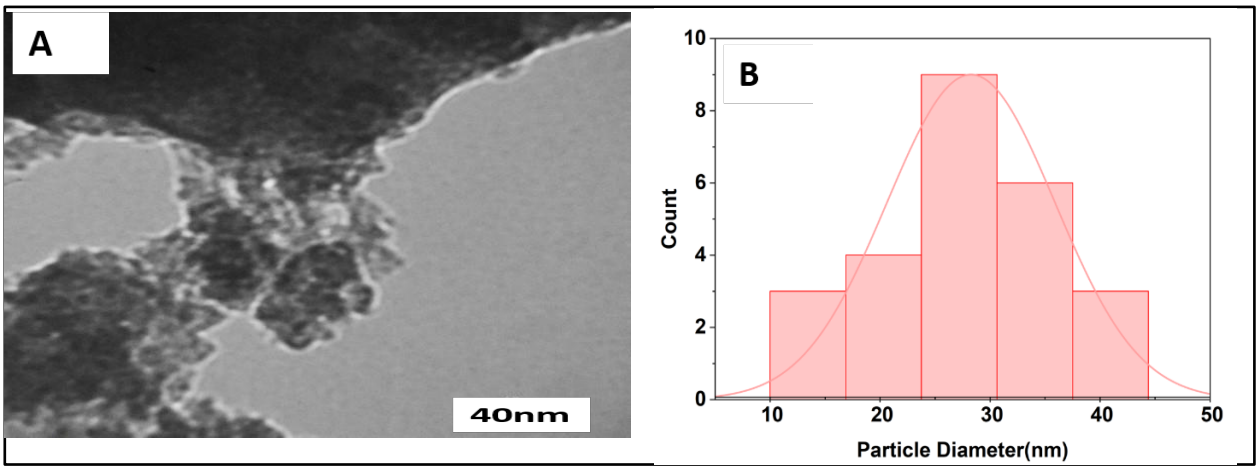

Figure (3-36): TEM measurement of the green-synthesized iron oxide nanoparticles (A) and size distribution (B).

3.1.5 Zeta potential and DLS Analysis

The dynamic light scattering (DLS) technique is used to check the size and measure the zeta potential of the prepared nanoparticles to evaluate how stable these materials are. The figure (3-37A) represents the zeta potential of silver nanoparticles, where the zeta potential reached 93.8 mV. As shown in figure (3-37B), the PI value of the silver nanoparticles is 0.0494.

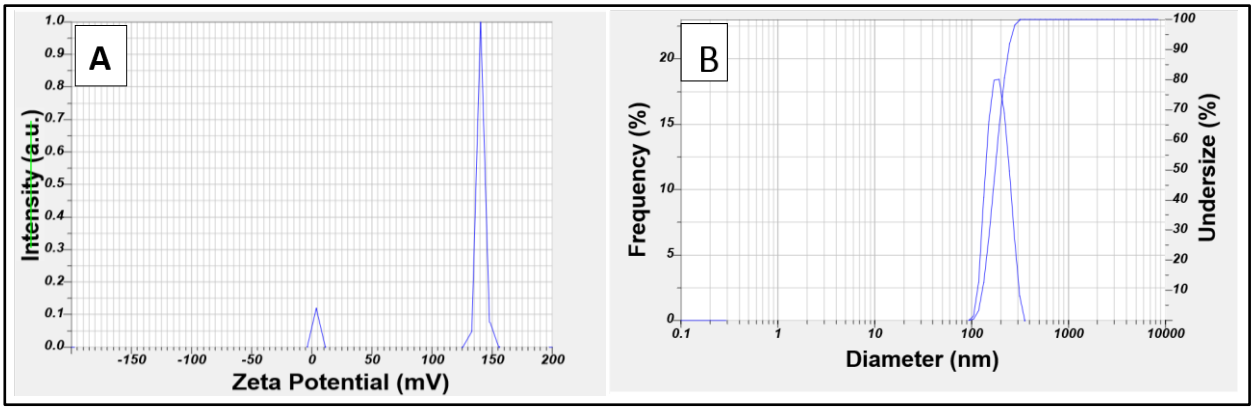

Figure (3-37): (A) zeta potential analysis of silver nanoparticles (B) dynamic light scattering of silver nanoparticles.

The measured zeta potential for the nickel oxide nanoparticles in figure (3-38A) was found to be -11.5, and the expected result for the zeta potential indicates that the NiO particles have high stability, which is almost consistent with the previous study [197]. Dynamic Light Scattering (DLS) technology to verify the hydrodynamic size and, thus, the apparent PI value in figure (3-38B) for the NiO nanoparticle 0.00002 .

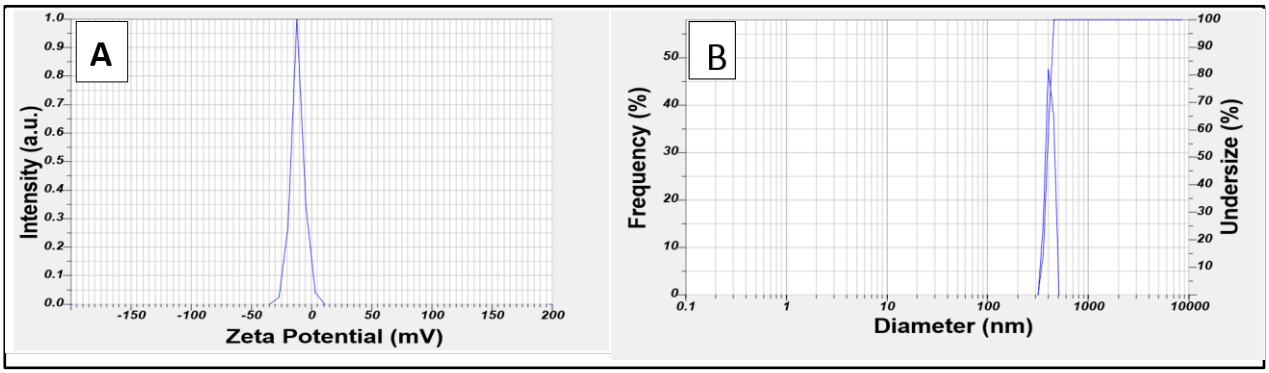

Figure (3-38): (A) zeta potential analysis of nickel oxide nanoparticles (B) dynamic light scattering of nickel oxide.

For the bimetallic nanoparticles Ag:NiO BNPs, the zeta potential, as shown in figure (3-39A), carries a positive charge at a ratio of 1:1, meaning the zeta potential is 0.1 mV, which explains the surface balance between nickel and silver due to the formation of the shell model. As for the hydrodynamic size of Ag: NiO BNPs, it is clear from the figure (3-39B) that pl = 0.044 .

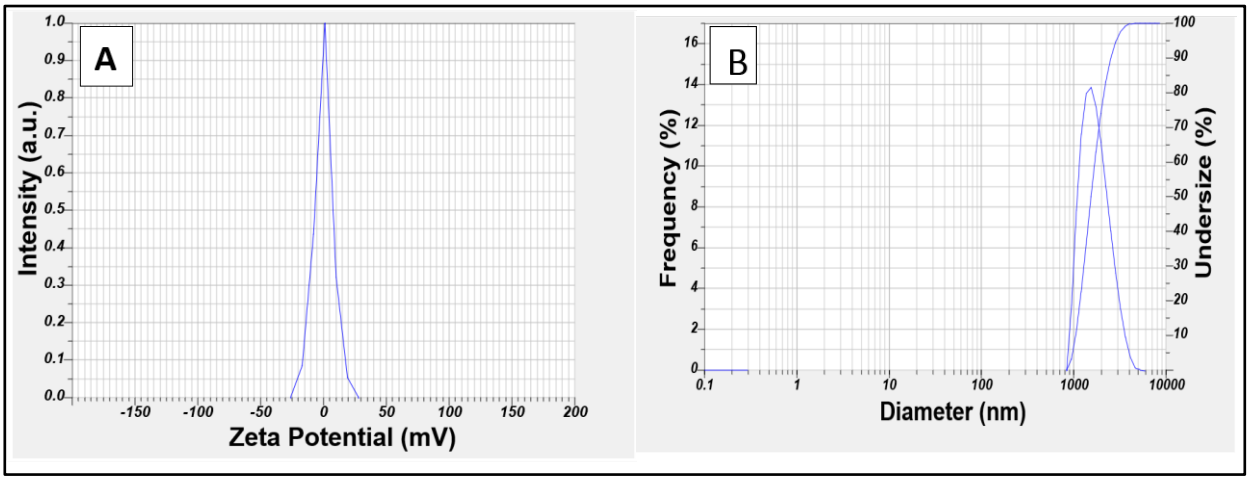

Figure (3-39): (A) zeta potential analysis of Ag: NiO BNPs 1:1 (B) dynamic light scattering of Ag: NiO BNPs 1:1.

Figure (3-40 A) clearly shows the negative charge of zeta potential at a ratio of 3:1 Ag:NiO BNPs, -9.4 mV, and the negative charge is due to the nickel oxide particles being surrounded by a layer of silver in addition to the stabilizers from the used plant extract. hydrodynamic size is pl=0.018, as shown in figure (3-40B).

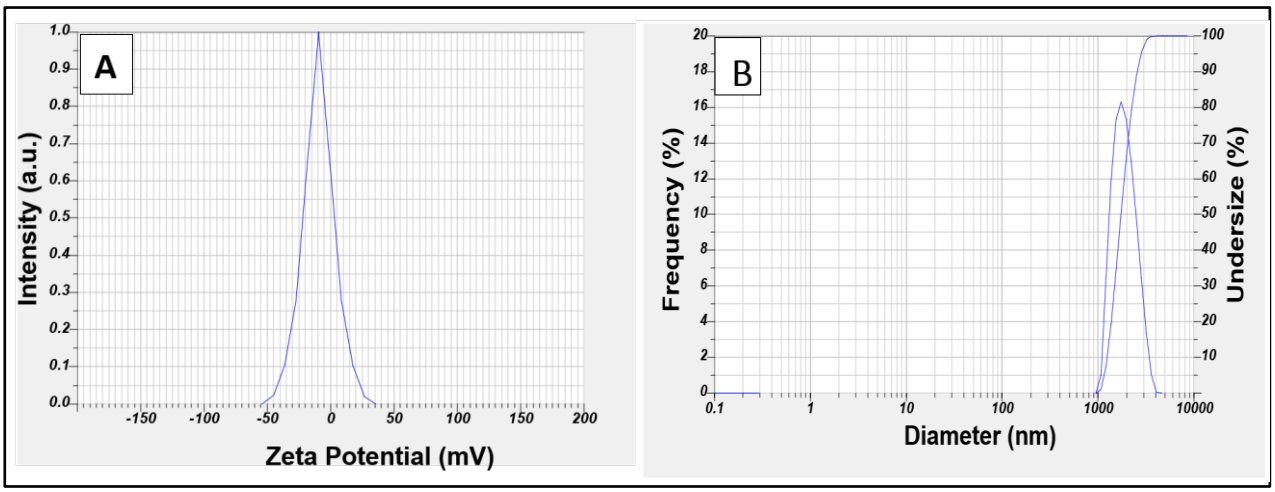

Figure (3-40): (A) zeta potential analysis of Ag: NiO BNPs 3:1 (B) dynamic light scattering of Ag: NiO BNPs 3:1.

Figure (3-41A) shows zeta potential value for Cu NPs measured at an electrode Voltage of 3.9 V, which was found to be -27.0 mV. The negative charge indicates that the manufactured particles possess electrostatic repulsion and thus have good stability. Consequently, the high negative zeta potential leads to strong repulsion between the particles, causing an amplification or enhancement of their stability [198]. The hydrodynamic size is pl=0.0028, as shown in figure (3-41B).

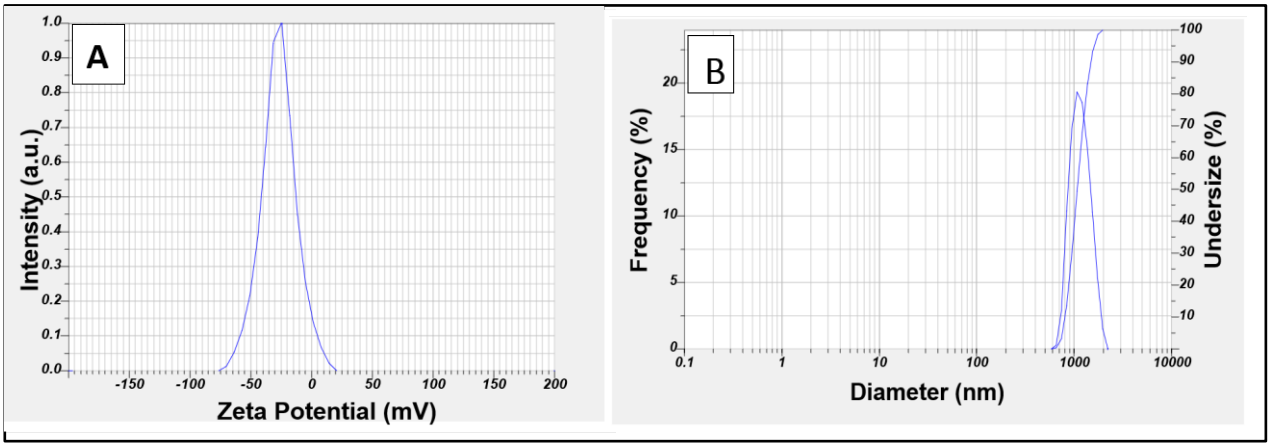

Figure (3-41): (A) zeta potential analysis of copper nanoparticles (B) dynamic light scattering of copper nanoparticles.

Figure (3-42 A) shows the zeta potential of CoO NPs prepared by green synthesis, where it is clear from the figure that there is a peak at -18.7 mV. This result reveals that the particles have a negative charge and are widely dispersed throughout the medium, The hydrodynamic size is pl=0.070, as shown in figure(3-42 B).

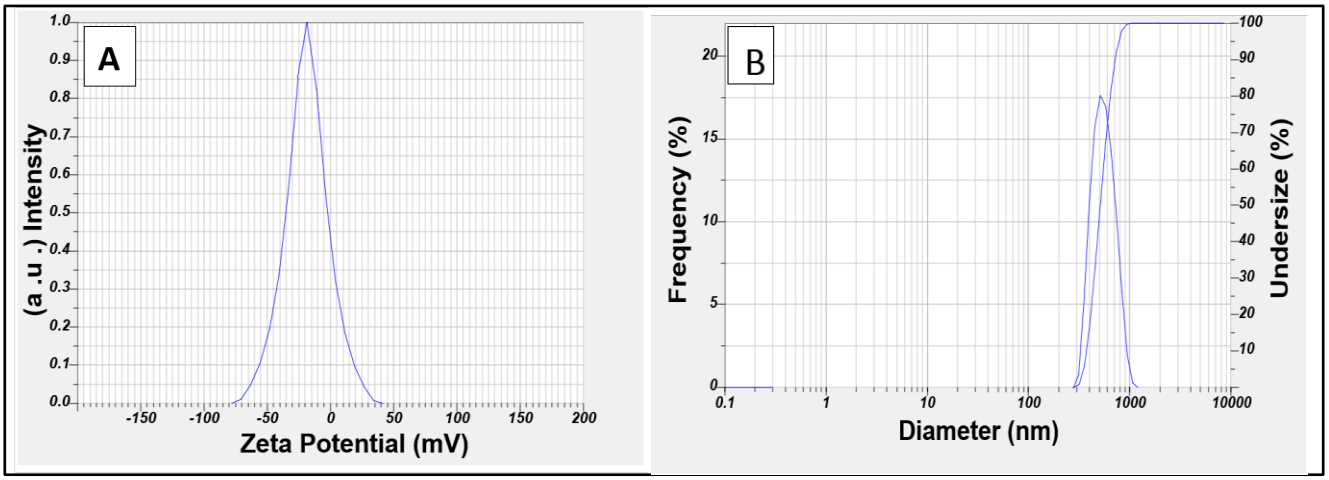

Figure (3-42): (A) zeta potential analysis of cobalt oxide nanoparticles (B) dynamic light scattering of cobalt oxide nanoparticles.

The bimetallic nanoparticles Cu: NiO BNPs are illustrated in figure (3-43A). The positive zeta potential at the ratio of 1:1 is 1.4 mV, indicating that the particles are chemically stable due to the equal proportion of the constituent metals. The hydrodynamic size as shown in figure (3-43B) is PI=0.000035.

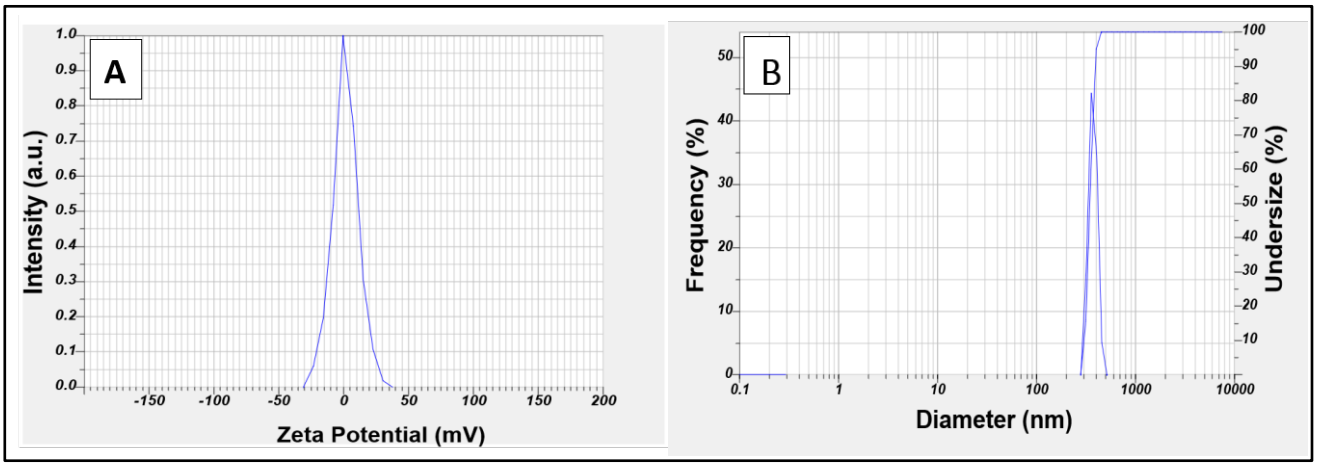

Figure (3-43): (A) zeta potential analysis of Cu: NiO BNPs 1:1 (B) dynamic light scattering of Cu: NiO BNPs 1:1.

Figure (3-44A) shows the negative zeta potential of Cu:NiO 3:1 when the copper ratio is increased threefold compared to the nickel oxide ratio, making the nickel oxide atom a core covered with copper. The surface zeta potential is -8.9 mV, and the hydrodynamic size is pl = 0.000038 in figure (3-44 B).

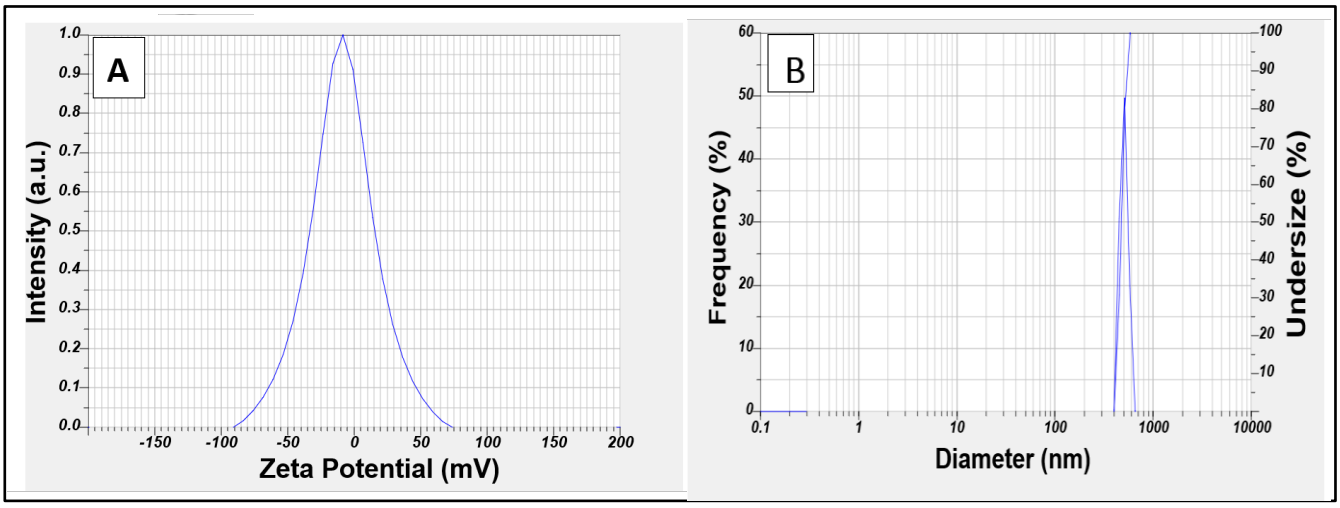

Figure (3-44): (A) zeta potential analysis of Cu: NiO BNPs 3:1 (B) dynamic light scattering of Cu: NiO BNPs 3:1.

Figure (3-45A) shows the zeta potential of Cu: CoO BNPs at a 1:1 ratio, which gives a value of -1.6 mV and a hydrodynamic size of pl = 0.098 in figure (3-45B).

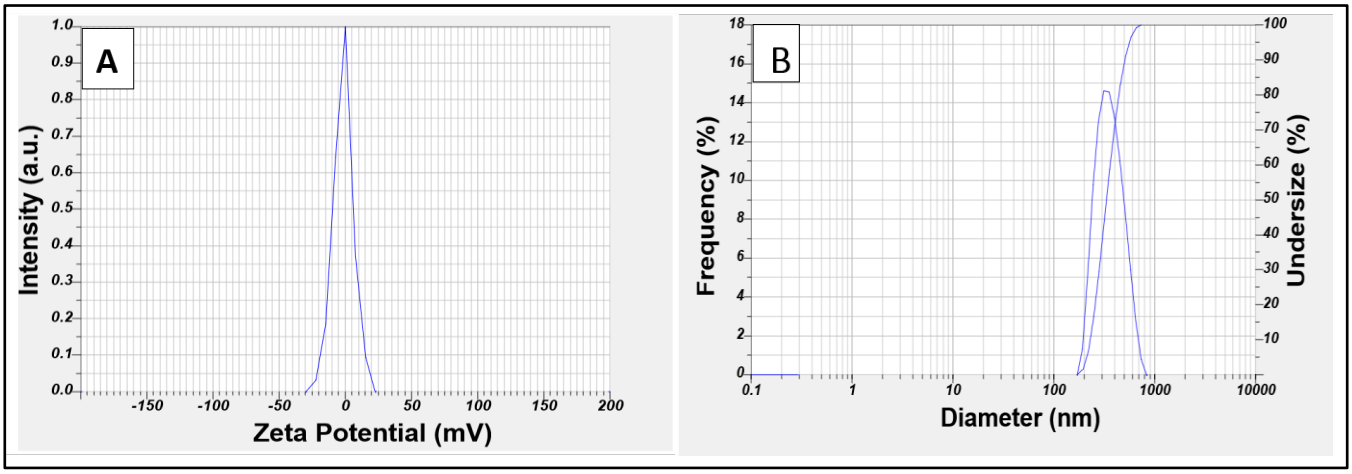

Figure (3-45): (A) zeta potential analysis of Cu: CoO BNPs 1:1 (B) dynamic light scattering of Cu: Co O BNPs 1:1.

Figure (3-46A) shows the zeta potential of Cu:CoO BNPs at a 3:1 ratio, which equals -6.2 mV, and the hydrodynamic size is 0.0001, shown as figure (3-46B). The reason the particles maintain a negative charge even with an increased ratio is that copper, when present in bimetallic compositions, forms oxides on the surface that exhibit negative behavior, facilitating the electrostatic attraction of Co O, thereby enhancing the negative charge [199].

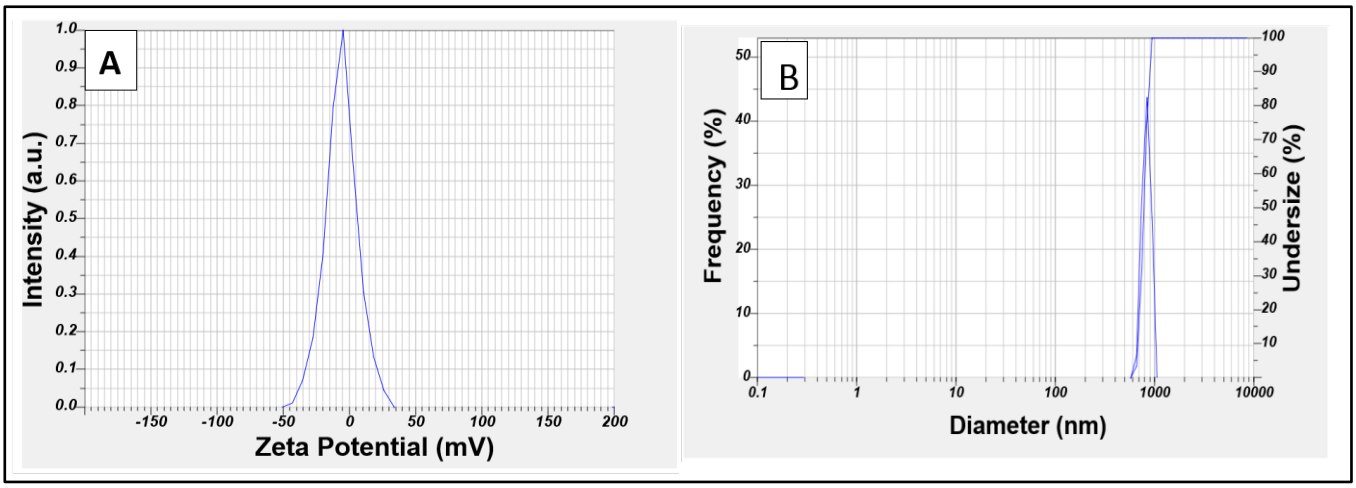

Figure (3-46): (A) zeta potential analysis of Cu: CoO BNPs 3:1 (B) dynamic light scattering of Cu: Co O BNPs 3:1.

The figure (3-47A) shows the zeta potential measurement of zinc oxide nanoparticles, where the potential peak of -22.3 mV indicates that the dispersed ZnO NPs are oriented with negative groups, proving their stability [200].Also, dynamic light scattering (DLS) technology to verify the hydrodynamic size and thus the apparent PI value in figure (3-47 B) for ZnO nanoparticle 0.055.

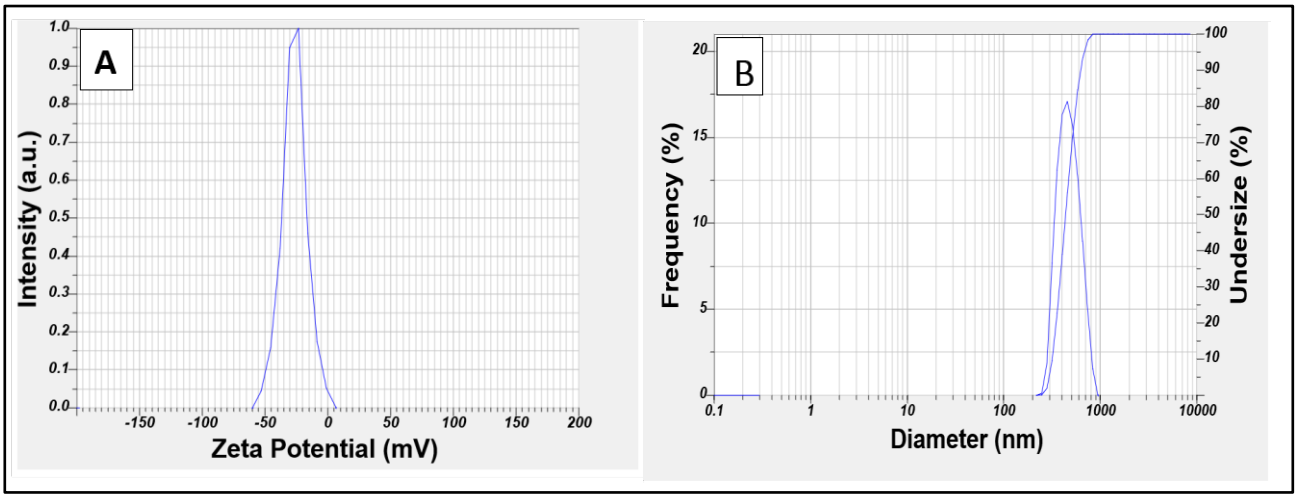

Figure (3-47): (A) zeta potential analysis of zinc oxide nanoparticles; (B) dynamic light scattering of zinc oxide nanoparticles.

The figure (3-48 A) shows the zeta potential of Cu: ZnO BNPs at a ratio of 1:1, where it was found to be -5.9 mV according to the figure, and the hydrodynamic size in the figure (3-48 B) . .

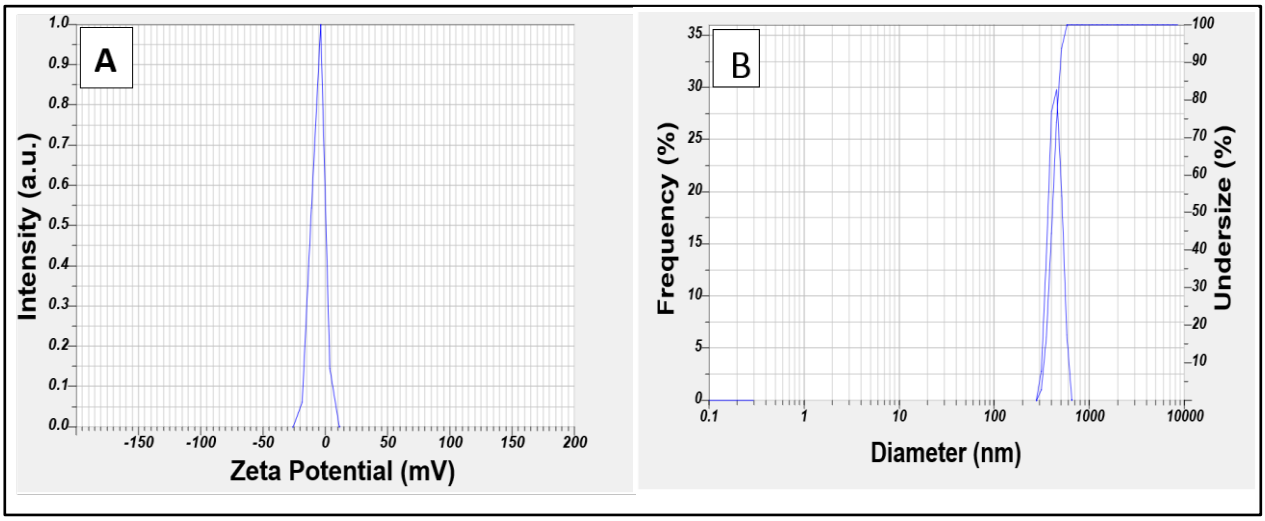

Figure (3-48): (A) zeta potential analysis of Cu: ZnO BNPs 1:1 (B) dynamic light scattering of Cu: ZnO BNPs 1:1.

Figure (3-49A) represents the zeta potential of Cu: ZnO BNPs at a ratio of 3:1; a zeta value of -3.7 mV was found, and the hydrodynamic size in figure (3-49 B).The negative charge was confirmed by increasing the copper ratio because zinc oxide has an isoelectric point around pH 9, and when it rises above 9, the bimetallic particle carries a net negative charge [199] .

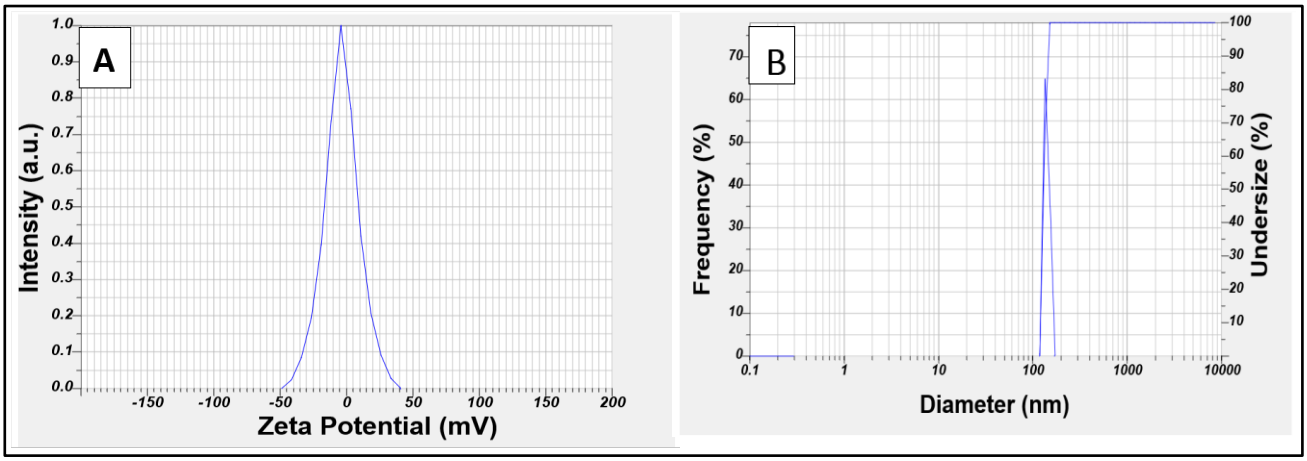

Figure (3-49): (A) zeta potential analysis of Cu: Zn O BNPs 3:1 (B) dynamic light scattering of Cu: Zn O BNPs 3:1.

Figure (3-50 A) shows the zeta potential of the measured iron oxide nanoparticles at an electrode voltage. 3.3 V was found to equal -11.1 mV, the negative charge indicating the high stability of Fe O NPs, and figure (3-50 B) illustrates the use of Dynamic Light Scattering (DLS) technology to verify the hydrodynamic size and thus the apparent PI value in the figure for the iron oxide nanoparticle 0.055.

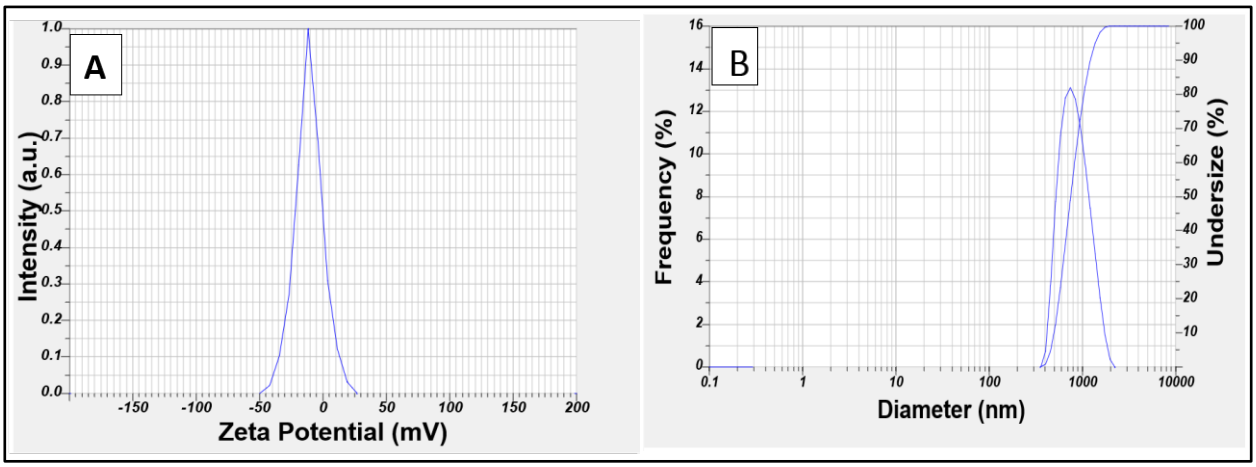

Figure (3-50): (A) zeta potential analysis of iron oxide nanoparticles (B) dynamic light scattering of iron oxide nanoparticles.

Table (3-1): values of each Zeta potential, Mobility, S.D, Z- Average and PI) of the prepared nanoparticles materials.

Nanomaterial	Zeta potential(mV)	Mobility (cm^2/Vs)	S.D (nm)	Z-Average (nm)	PI
Ag NPs	93.8	0.000686	42.4	190.8	0.0493
Zn O NPs	-22.3	-0.000214	117.0	498.5	0.055
Cu NPs	-27	-0.000209	256.3	4842.4	0.0028
Fe O NPs	-11.1	-0.000101	283.6	1208.1	0.055
Ni O NPs	-11.5	-0.000106	32.3	7941.2	0.00002
Co O NPs	-18.7	-0.000155	531.7	505.3	0.070
Ag: NiOBNPs1:1	+0.1	+0.000001	594.2	2834.9	0.044
Ag: NiO BNPs3:1	-9.4	-0.000073	507.3	3806.2	0.018
Cu: NiO BNPs 1:1	+1.4	0.000011	33.7	5664.2	0.000035
Cu: NiO BNPs 3:1	-8.9	-0.000069	41.2	6713.5	0.000038
Cu: ZnO BNPs1:1	-5.9	-0.000046	60.7	0	0
Cu: ZnO BNPs3:1	-3.7	-0.000029	7.8	0	0
Cu: CoO BNPs1:1	-1.6	-0.000012	106.8	340.9	0.098
Cu: CoO BNPs3:1	-6.2	-0.000048	76.5	7516.2	0.0001

Where the value of PI was calculated from the relationship

$$PI = (SD / Z\text{-Average (nm)})^2$$

3.1.6 Fourier Transform Infrared Spectroscopic Analysis

For the purpose of identifying functional groups, FTIR was used. It is observed from the results obtained for measuring the infrared spectrum of the nanomaterials prepared by the green method that there are common or similar vibration peaks, which confirms the effectiveness of the plant extracts used. The vibration peaks have been summarized in Table (3-2).

Table (3-2): Wavelength, the chemical bond and interpretation of the prepared nanomaterials.

Wavelength(cm^{-1})	Chemical bond	Interpretation	References
(3600) (3473.81) (3352.49) (3358.80) (2899)	O-H	stretching vibrations indicating the presence of hydroxyl groups.	[201]
(1324.01)	C=C	stretching vibrations bonds present in aromatic compounds.	[202]
(2923.80) (760.84) (2100)	C-H	stretching vibrations bending vibrations represent aromatic vibrations.	[203]
(1600.22) (1618.92)	C=O	stretching vibrations the presence of sugars or carbohydrate compounds in the plant extract (aldehyde groups).	[203]

(1884.2) (1564.80) (1592.80) (1601.40) (1496.61) (1583.6) (1577.51) (1594.29) (1599.49) (1604.28)	N-H	stretching vibrations bending vibrations represent (amines, amides) bonds from plant extract.	[204]

Through the study and analysis of the infrared spectra of the prepared nanomaterials, it was found that green synthesis of metal nanoparticles uses a variety of chemical functional groups that act as reducing, capping, and stabilizing agents. Hydroxyl groups (O-H) can donate electrons to metal ions, reducing them to their elemental forms, and may act as both a reducing and stabilizing agent at the same time (hydrogen bonding). Amino groups (N-H) facilitate electron transfer during the reduction of metal ions, making them effective reducing agents in the synthesis of nanoparticles, and they also provide stability to the surface of the nanoparticles. Aldehyde or ketone groups can effectively reduce metal ions and help stabilize the formed nanoparticles by creating a protective layer around them. The carbonyl groups (C=O) present in ketones and aldehydes, which are found in various organic compounds and proteins, can facilitate the formation of complexes with metal ions, which is essential for controlling the size and shape of nanoparticles during synthesis [30]. Since the appearance of these links indicates the effectiveness of the plant extracts used in synthesis (green tea and Boswellia sacra). The following figures show the infrared spectrum of the prepared nanomaterials:

Figure (3-51) shows The FTIR spectrum of Ag NPs prepared by the green method reveals clear absorption bands. The peak obtained at 498.26 cm^{-1} is due to Ag vibrations [205].

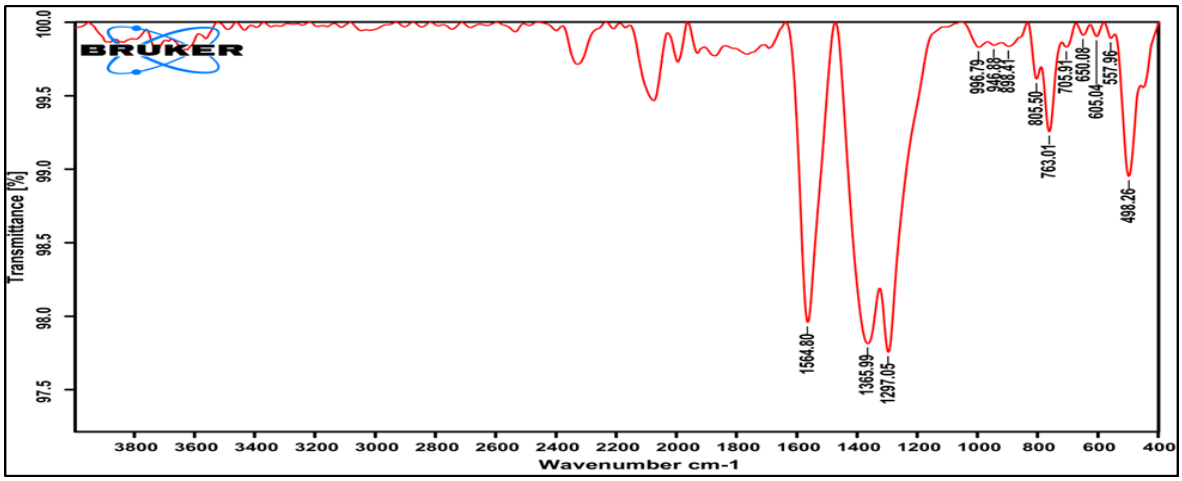

Figure (3-51): FTIR spectrum of Ag NPs prepared by green tea.

Figure (3-52) represents the FTIR spectrum of NiO NPs. The peak obtained at 454.85 cm^{-1} is due to Ni-O vibrations, clearly indicating that the plant extract acts as a reducing agent during the formation of the nanoparticles [201, 206].

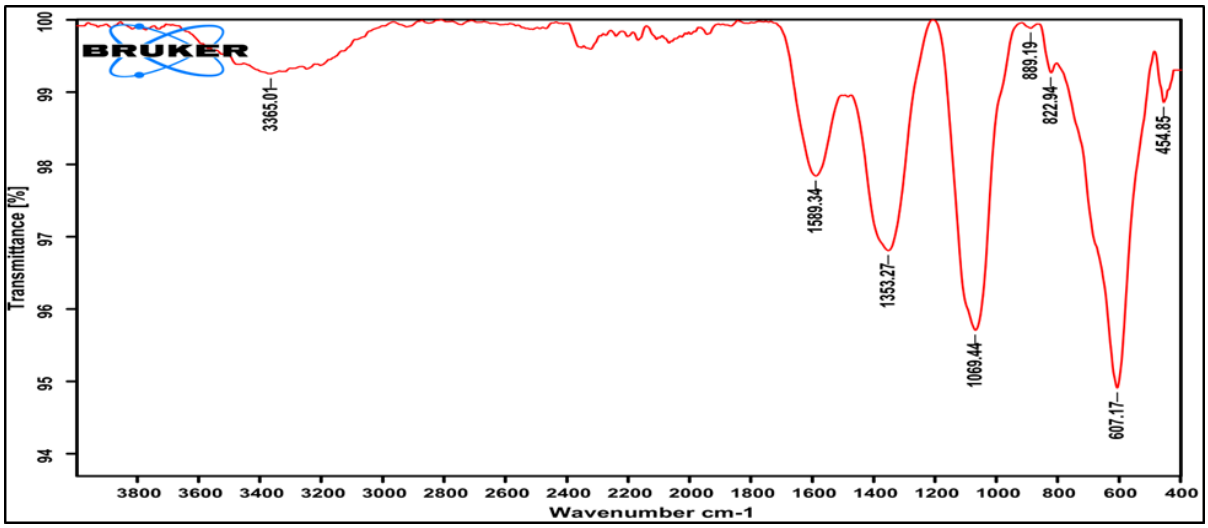

Figure (3-52): FTIR spectrum of NiO NPs prepared by green tea.

The FTIR spectrum of the Ag: NiO 1:1bimetallic nanoparticles are clear in figure (3-53). where the peak is at 595.51 cm^{-1}represents the metal oxides Ni-O or Ag O [207].

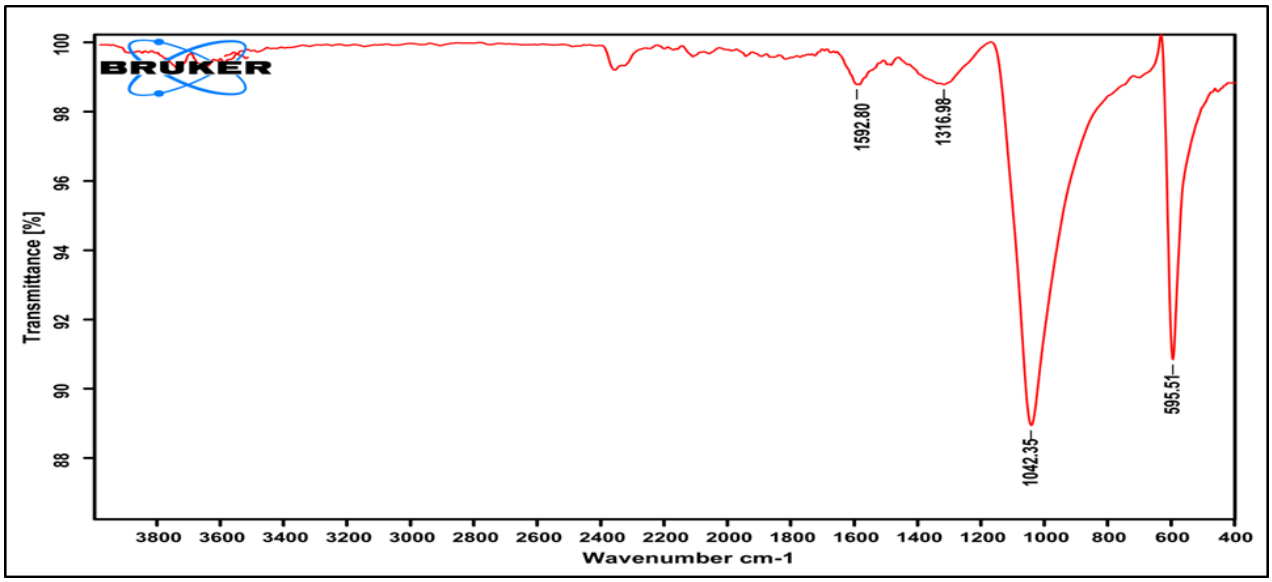

Figure (3-53): FTIR spectrum of Ag: NiO BNPs 1:1 prepared by green tea.

The FTIR spectrum of the Ag: NiO 3:1bimetallic nanoparticles are clear in figure (3-54) where the peak is at 592.87 cm^{-1}represents the metal oxides Ni-O or Ag-O [207].

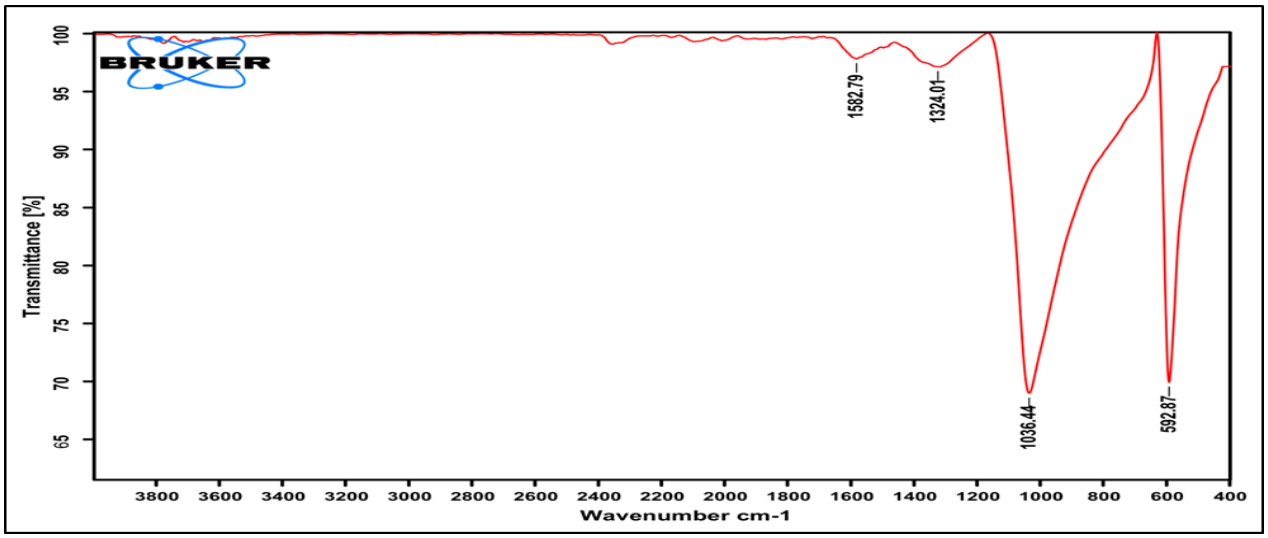

Figure (3-54): FTIR spectrum of Ag: NiO B NPs 3:1 prepared by green tea.

The figure (3-55) represents the FTIR spectrum of Cu NPs. The peaks at 587.96 cm^{-1} and 690.67 cm^{-1} often represent the Cu-O vibration, which is the metal with oxygen, while the peaks at 479.19 cm^{-1} and 422.69 cm^{-1} represent the Cu vibration

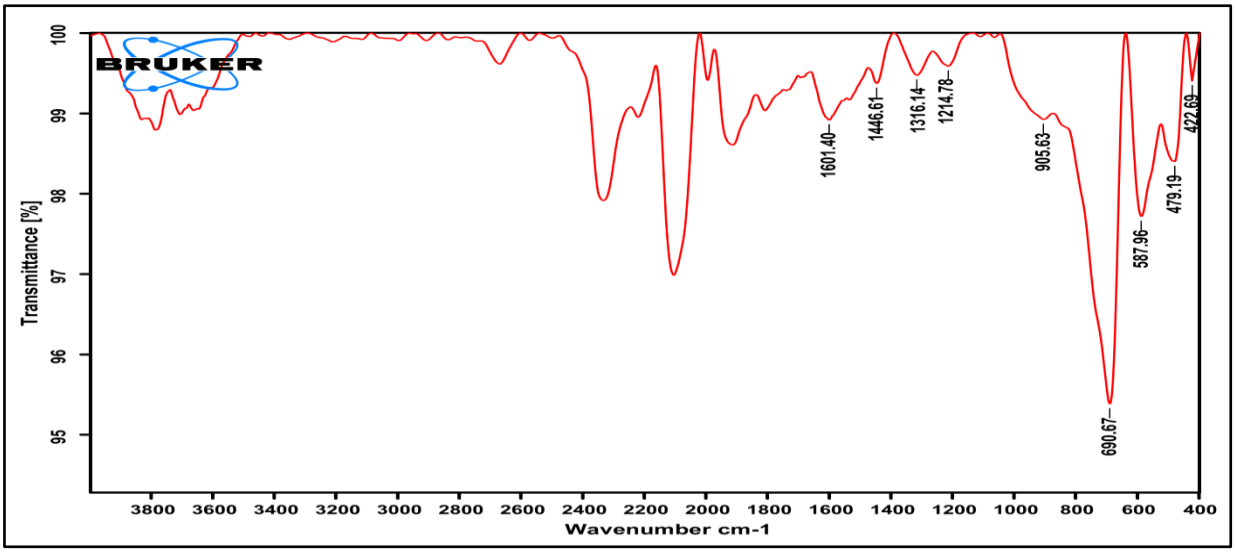

Figure (3-55): FTIR spectrum of Cu NPs prepared by *Boswell sacra*.

The figure (3-56) represents FTIR spectra of CoO nanoparticles prepared with green tea extract in the range of 400-4000 cm^{-1}. The peaks at 517.13 cm^{-1} and 591.70 cm^{-1} indicate Co-O vibrations characteristic of cobalt oxide [208].

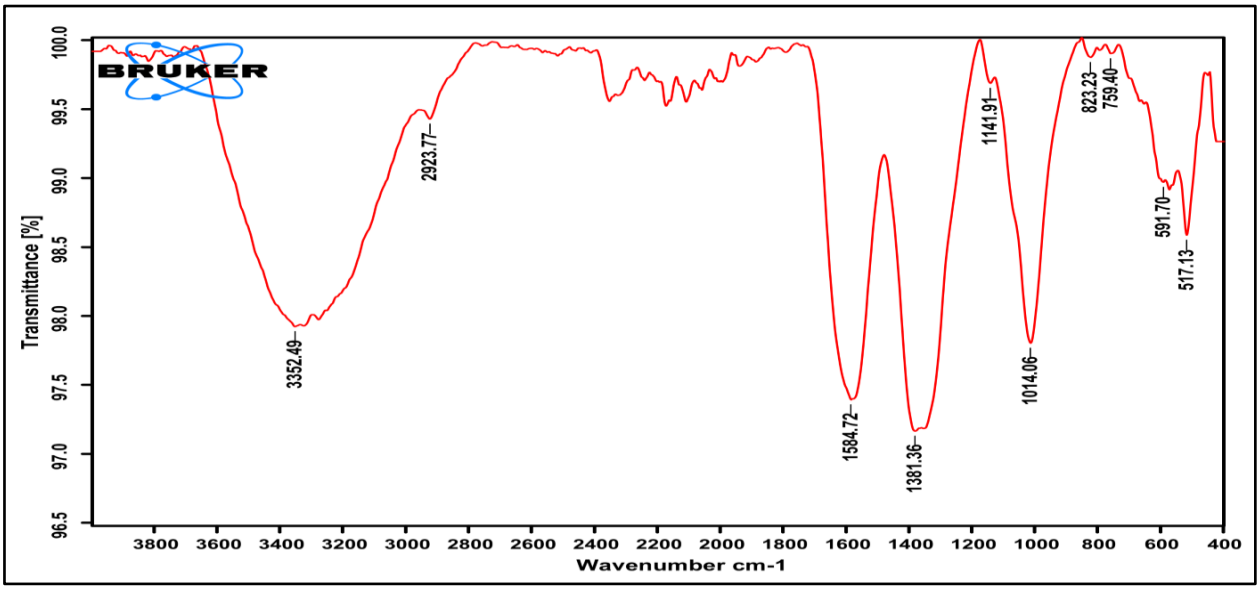

Figure (3-56): FTIR spectrum of CoO NPs prepared by green tea.

The figure (3-57) shows the FTIR spectrum of the bimetallic Cu: CoO BNPs and indicates through the figure the similarity in the active sites for the ratio 1:1. The peaks at 469.80 represent the Cu-O or Co-O .

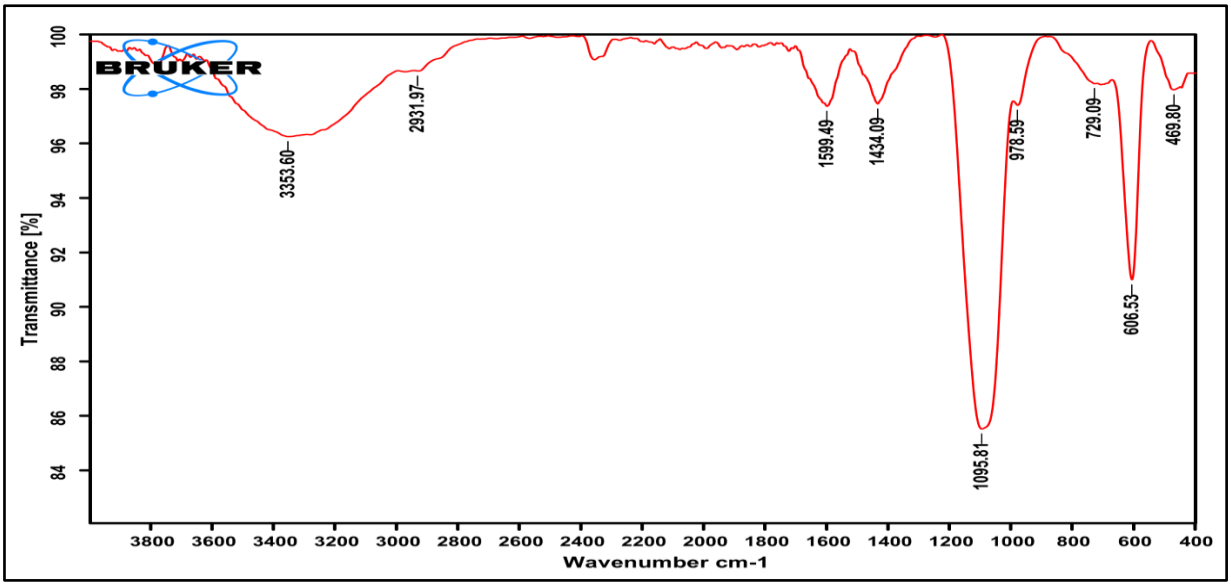

Figure (3-57): FTIR spectrum of Cu:CoO BNPs1:1 prepared by *Boswell sacra*.

The figure (3-58) shows the FTIR spectrum of the bimetallic Cu:CoO BNPs 3:1 and indicates through the figure the similarity in the active sites for the ratio 3:1. The peaks at 444.55 represent the Cu-O or Co-O .

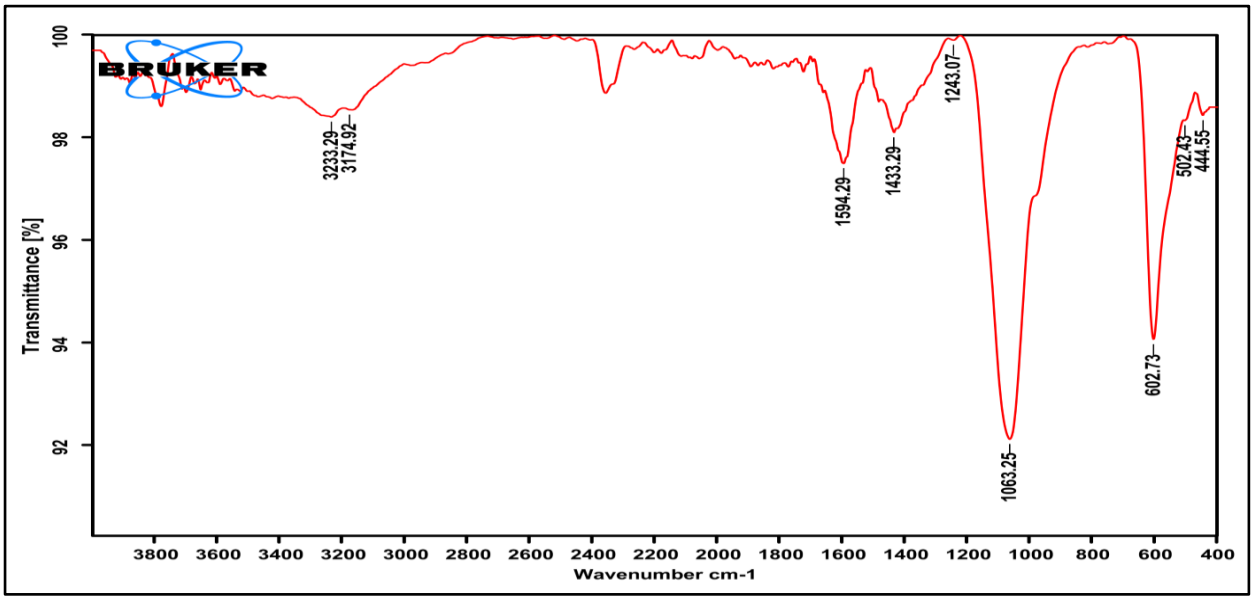

Figure (3-58): FTIR spectrum of Cu:CoO BNPs3:1 prepared by *Boswell sacra*.

Figure (3-59) shows FTIR spectra of the Cu: NiO bimetallic1:1 particle prepared using *Boswell sacra* extract: the sharp peak at 612.92 cm^{-1} is associated with the vibrations of the Ni-O bond, and since nickel, according to previous XRD studies, is present as an oxide, this peak represents nickel oxide. The other small peaks

within the 800 cm^{-1} range are due to the interference of Cu and NiO in the crystalline structure. .

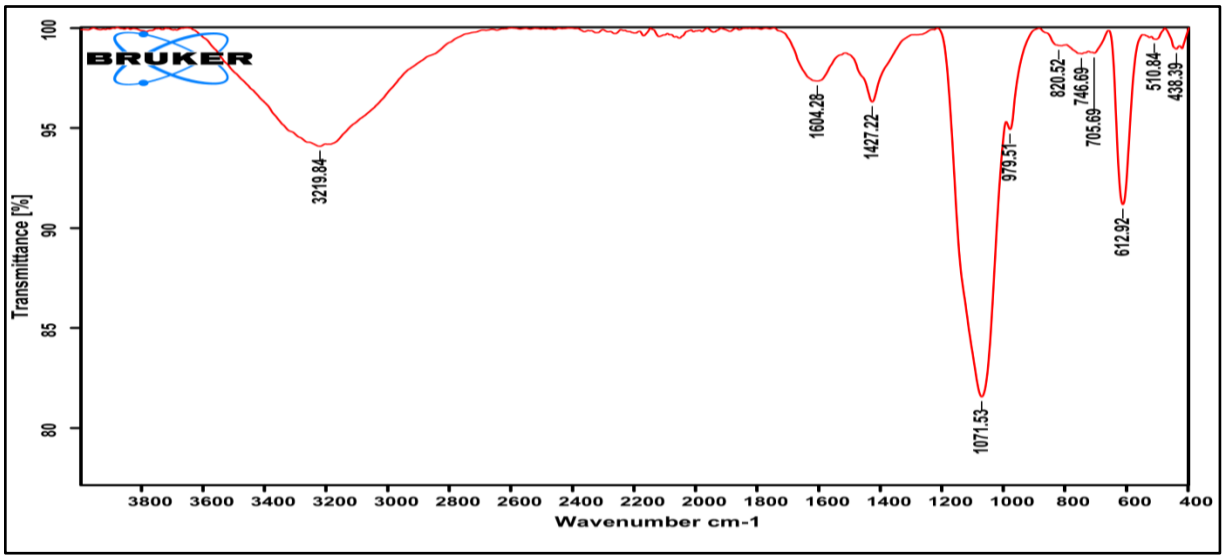

Figure (3-59): FTIR spectrum of Cu: NiO BNPs1:1 prepared by *Boswell sacra*.

Figure (3-60) shows FTIR spectra of the Cu: NiO bimetallic 3:1 particle prepared using frankincense extract: the sharp peak at 612.72 cm^{-1} is associated with the vibrations of the Ni-O bond, and since nickel, according to previous XRD studies, is present as an oxide, this peak represents nickel oxide The other small peaks within the 800 cm^{-1} range are due to the interference of Cu and Ni in the crystalline structure .

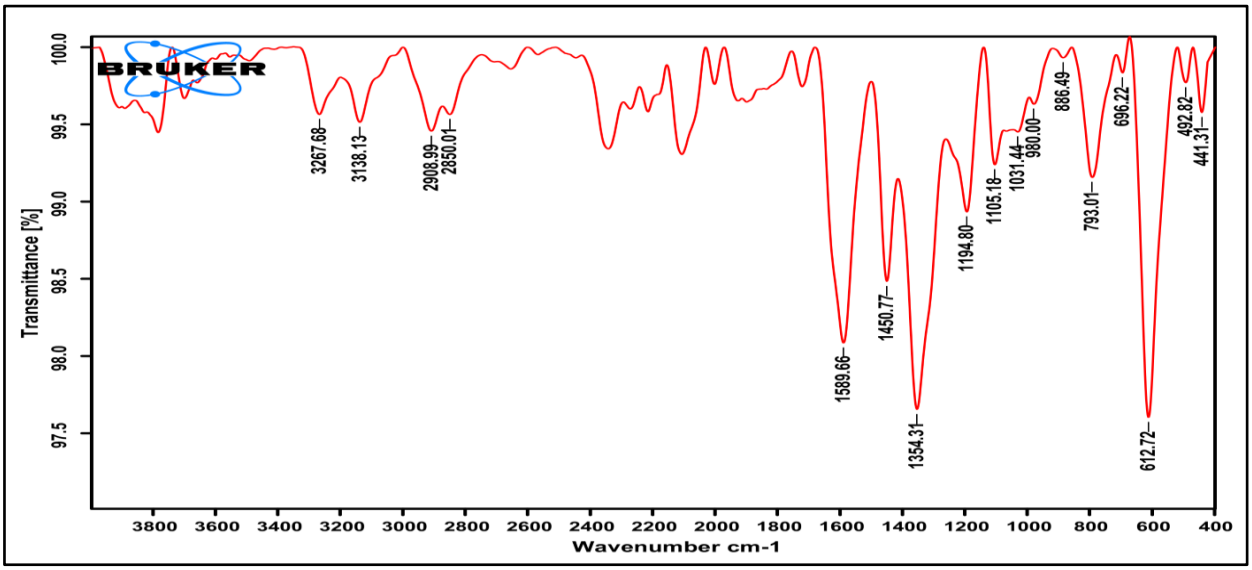

Figure (3-60): FTIR spectrum of Cu: NiO BNPs3:1 prepared by *Boswell sacra*.

The figure (3-61) represents the FTIR spectrum of ZnO NPs prepared by green synthesis. The biomolecules present in the plant extracts are responsible for reducing the nanoparticles, which show metal oxide absorption in the region below 1000 cm^{-1} with peaks at 531.21 cm^{-1}, 628.07 cm^{-1}, and 661.44 cm^{-1}, corresponding to zinc oxide nanoparticles.

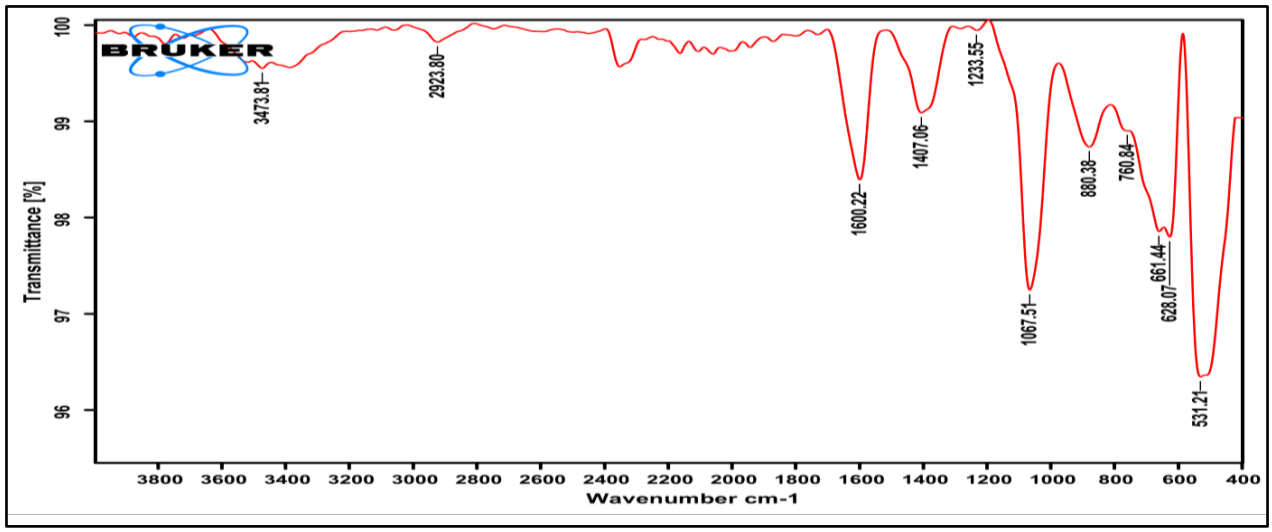

Figure (3-61): FTIR spectrum of ZnO Prepared by *Boswell sacra*.

Figure (3-62) represents the FTIR spectrum of Cu: ZnO BNPs 1:1 prepared by green synthesis The sharp peak at 454.26 cm^{-1} represents the vibration of Cu-Np ZnO and Zn-NPs.

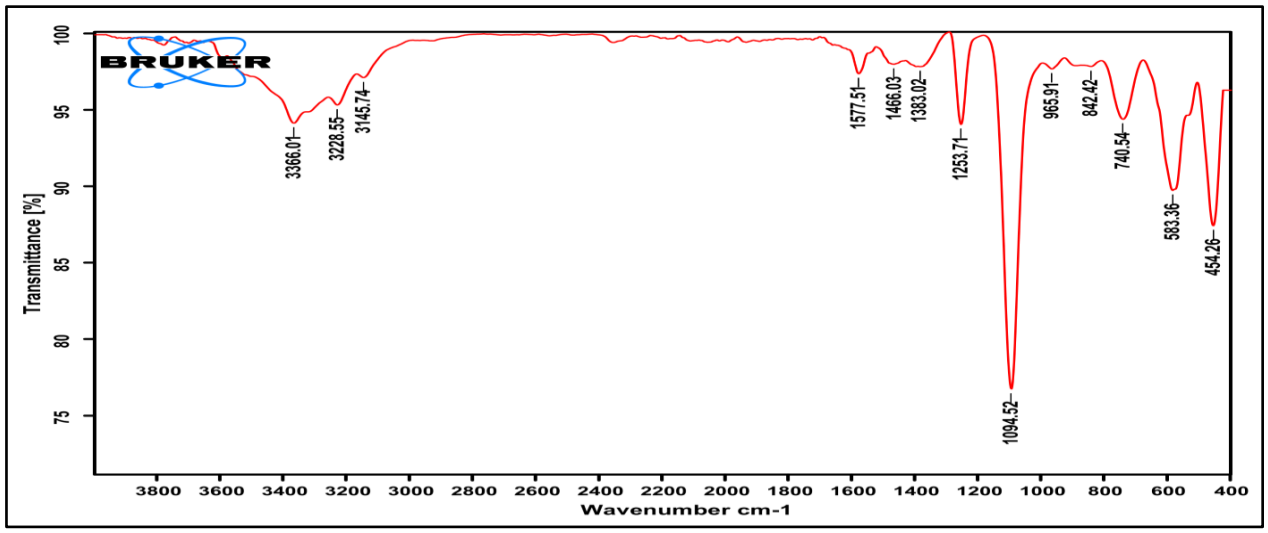

Figure (3-62): FTIR spectrum of Cu: Zn O BNPs 1:1Prepared by *Boswell sacra*.

Figure (3-63) represents the FTIR spectrum of Cu:ZnO BNPs 3:1 prepared by green synthesis; the sharp peak at 447.05 cm^{-1} represents the vibration of Cu-Np or Zn-O, Zn-NPs .

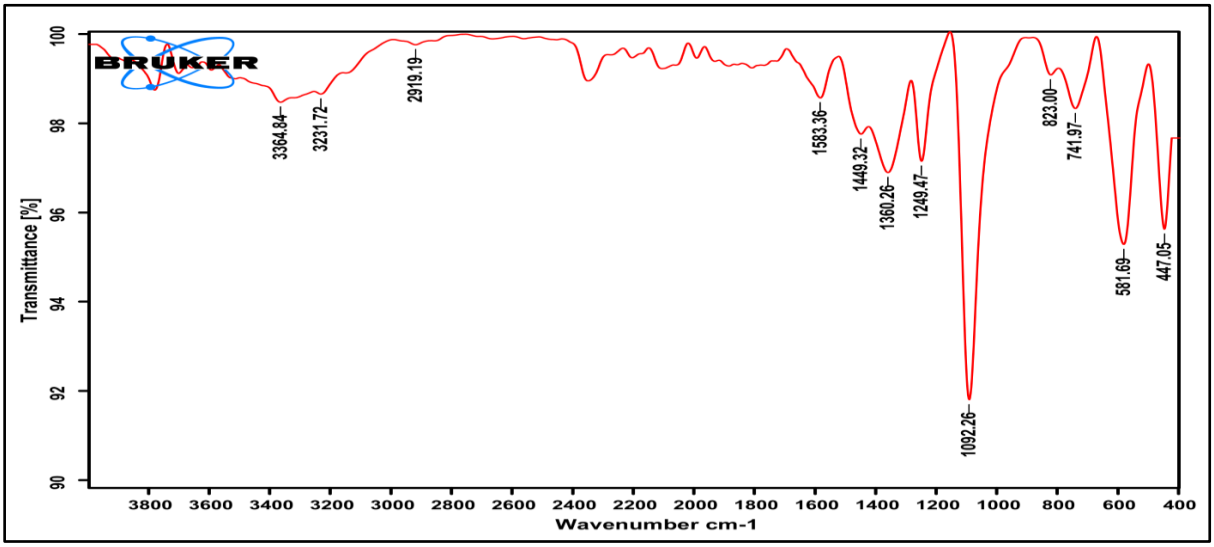

Figure (3-63): FTIR spectrum of Cu: ZnO BNPs 3:1Prepared by *Boswell sacra*.

The figure (3-64) represents the FTIR spectrum of iron oxide nanoparticles. The peak at 499.41 cm^{-1} indicates the Fe-O bond, which corresponds to the vibration of the crystal lattice.

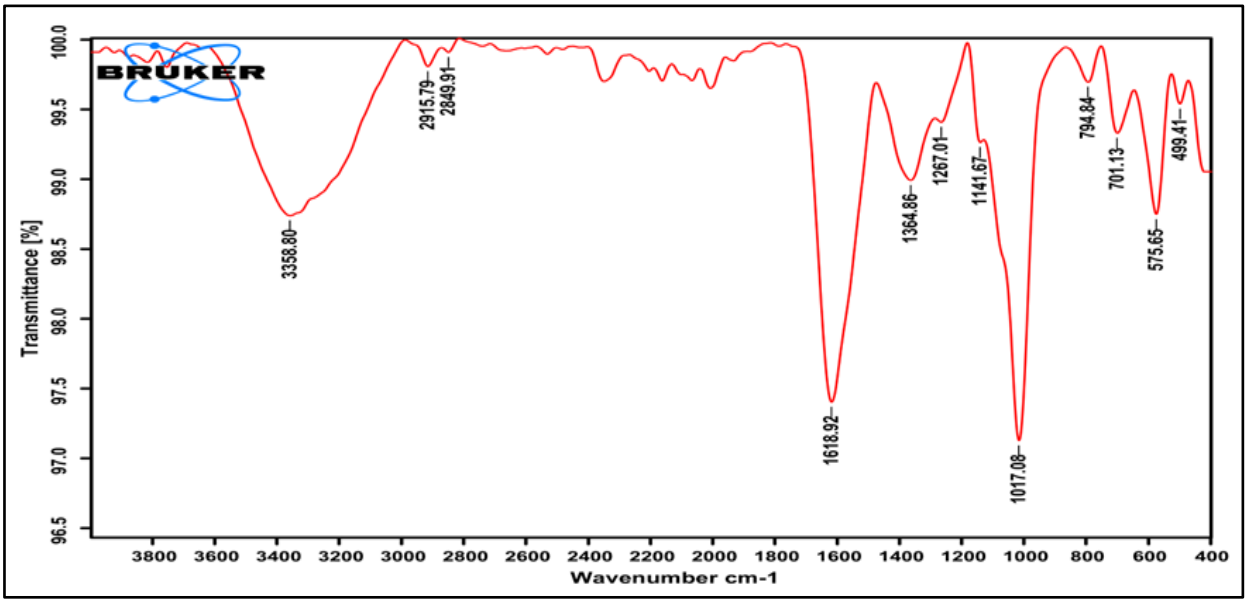

Figure (3-64): FTIR spectrum of iron oxide NPs Prepared by green tea.

3.2 Analysis of nanomaterial reagents for pharmaceutical substances

The solutions resulting from the detection after the color change were analyzed and studied.

3.2.1 Design and printing Microfluidic device

The device was made using previously disclosed procedures and had a total size of 60 x 40 × 1.5 mm and another dual device with two channels of 30 × 13 × 10 mm [157] [209].Briefly, the microfluidic device was drawn and designed using the SolidWorks 2022 design software and then printed using the Object Eden 260VS 3D printer, resulting in a 3D model with four channels as shown in figure (3-65A) and two channels in figure (3-65B). To prepare the microfluidic device for use, we soak the device in distilled water for two hours, then place it in an ultrasonic device for 10 minutes at 92% power and 40 kHz frequency. Finally, it is placed in a 0.1 M sodium hydroxide solution for 40 minutes, washed with water, and left to dry completely to be ready for use .

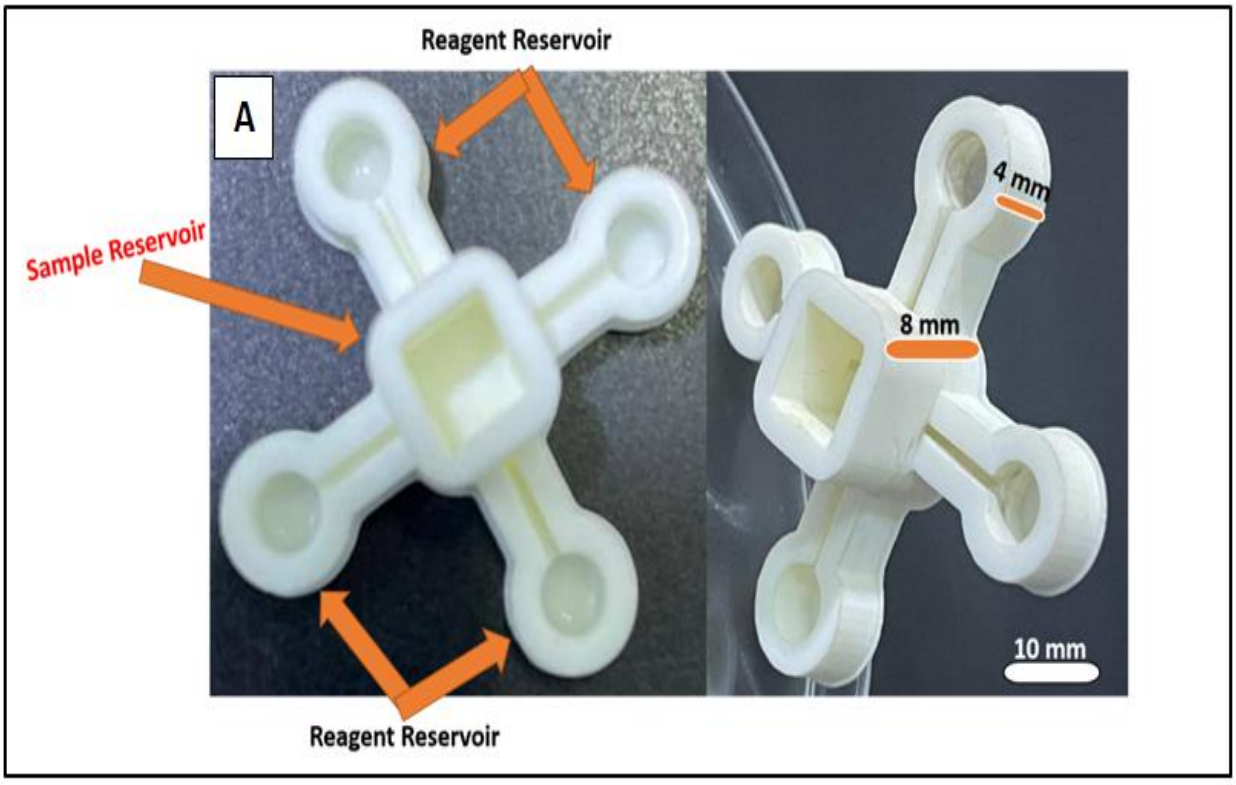

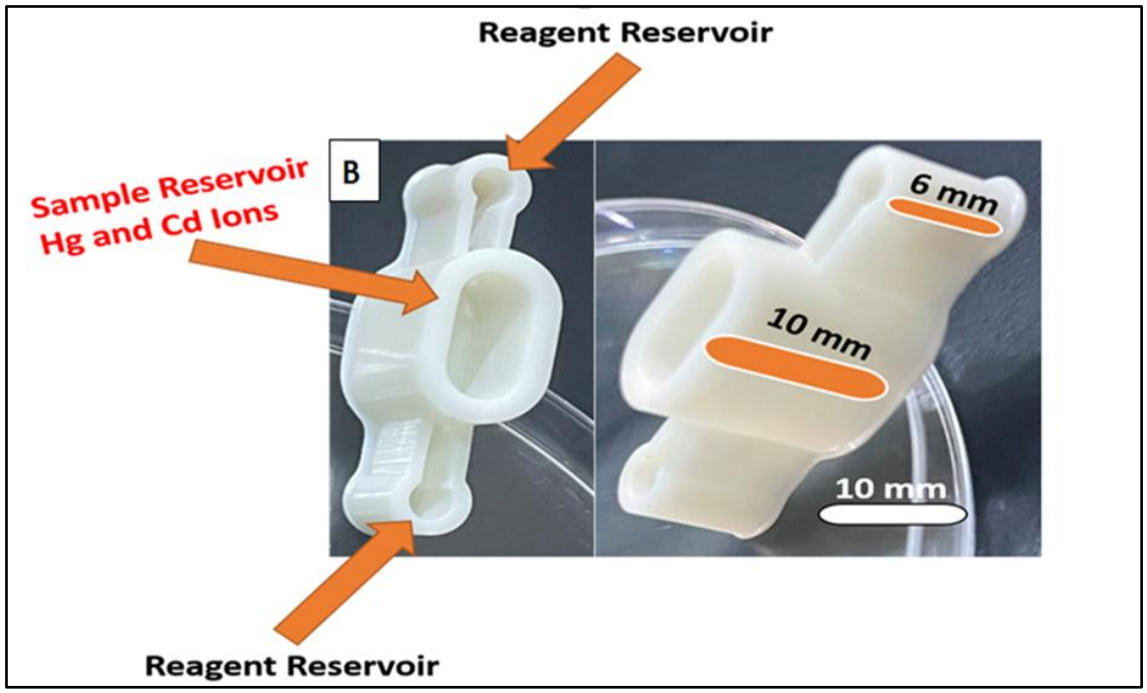

Figure (3-65): Photograph image of the 3D printed microfluidic device (A) square design consists of a main channel in the center and four channels using for the sensors, (B) dual device with a main channel in the center and two channels. The two image with Scale bar = 10mm.

3.2.2 Ultraviolet-Visible Spectrophotometry for Drug

Figure (3-66) represents the visible spectrum of ultraviolet rays. (figure 3-66A) (red line) shows the maximum absorption peak of silver nanoparticles at 420 nm, measured within the wavelength range of 200-1000 nm, as reported [176]. (figure 3-66 B) (orange line) shows the absorption spectrum of fentanyl citrate added to the silver nanoparticle reagent, and (figure 3-66 C) (green line) shows the absorption spectrum of fentanyl citrate.

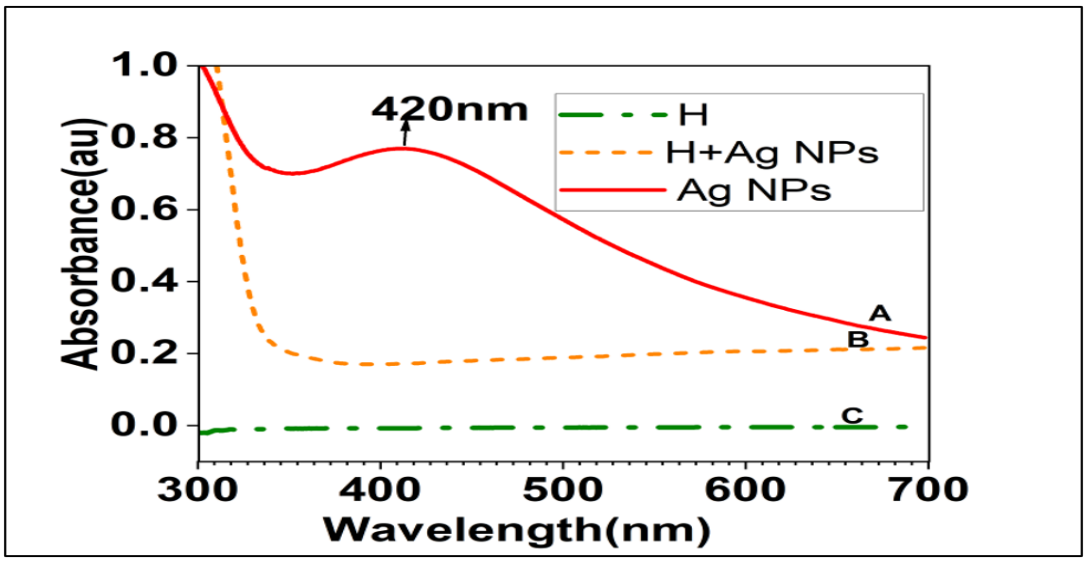

Figure (3-66): UV-Visible spectra of (A) Ag NPs, (B) fentanyl citrate (H) added to Ag NPs, and (C) fentanyl citrate (H) only.

Figure (3-67 A) shows the UV-visible spectrum of cobalt nanoparticles prepared by the green synthesis method The maximum absorption peak appears at 306.5 nm, as mentioned in [210], with slight variation. Additionally, a small peak is observed at the wavelength (529.5 nm), representing the absorption peak of the cobalt oxide nanoparticles, which is close to what was reported in [211]. (figure 3-67B) represents the addition of cobalt nanoparticles to tramadol hydrochloride, while (figure 3-67C) represents the absorption curve of the drug.

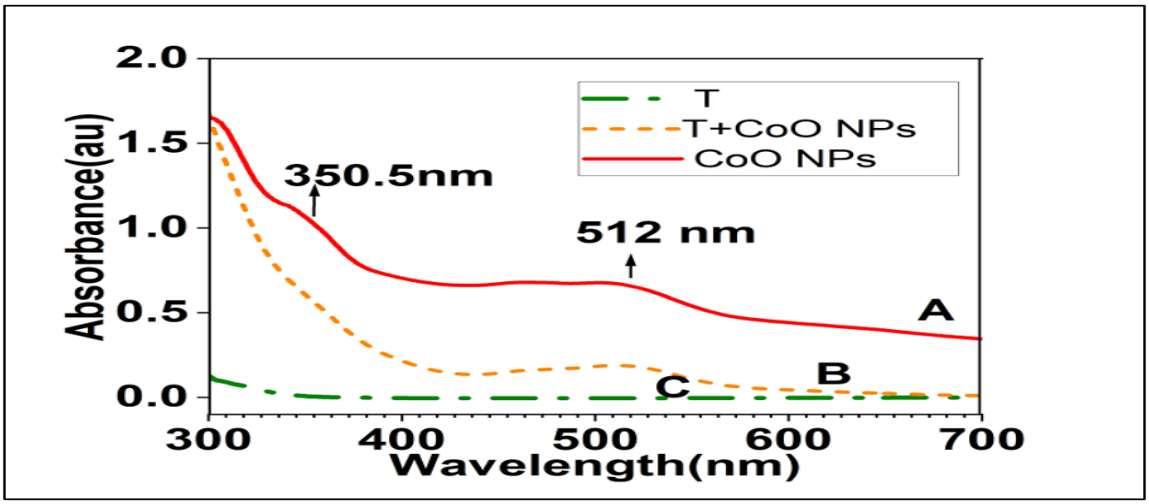

Figure (3-67): UV-Visible spectra of (A) cobalt oxide nanoparticles prepared by the green synthesis method, (B) addition of cobalt nanoparticles to tramadol hydrochloride (T), and (C) tramadol hydrochloride (T) only.

Figure (3-68) shows the visible spectrum of ultraviolet rays for the Cu:NiO bimetallic nanoparticles. It is observed that the peak absorption wavelength is approximately 700 nm, indicating a shift from NiO absorption peak at approximately 330 nm [212]and the Cu NPs absorption peak at around 576 nm [213]. (figure 3-68B) shows the absorption spectrum after adding Cu:NiO BNPs to the anesthetic material (Aldine), while (3-68C) is the absorption spectrum of the anesthetic material (Aldine) .

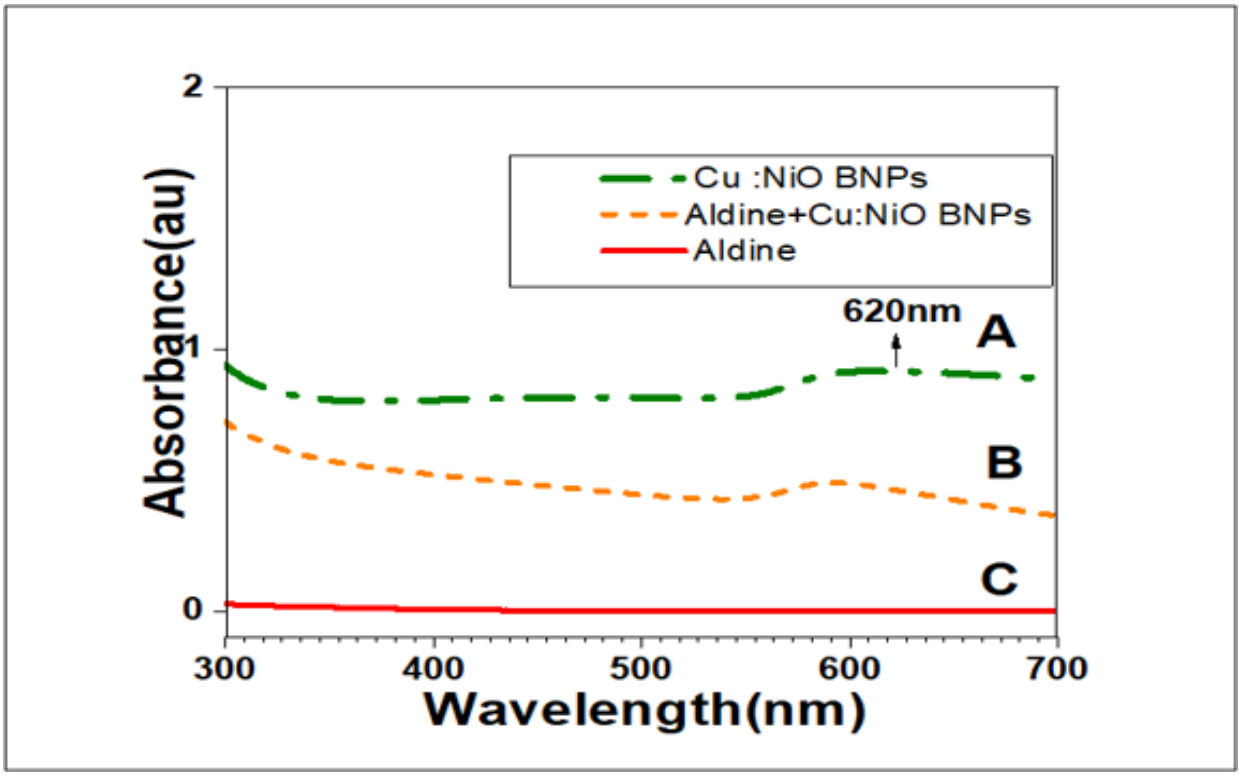

Figure (3-68): UV-Visible spectra of (A) Cu:NiO bimetallic nanoparticles, (B)absorption spectrum after adding Cu:NiO BNPs to the anesthetic material (Aldine), and (C) anesthetic material (Aldine) only.

Figure (3-69) represents the UV spectrum of ZnO, where it is observed from the figure that the clear peak of zinc oxide disappears upon adding the toxic element cd solution. As shown, curve A corresponds to ZnO, while the straight-line B is the detector with the cadmium solution.

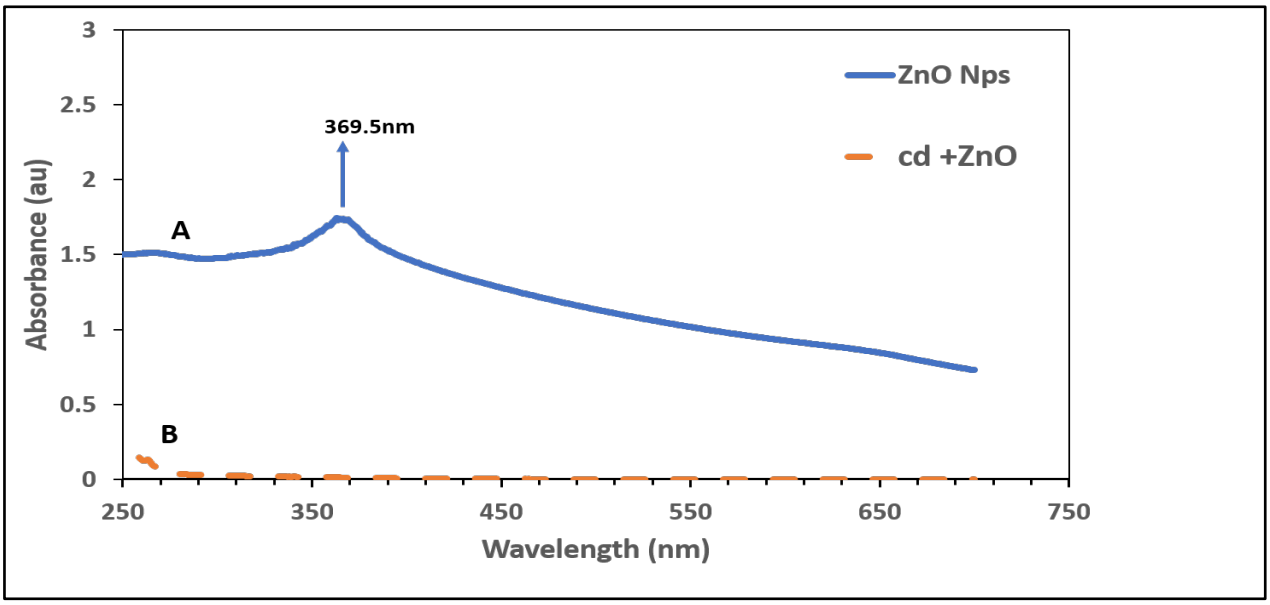

Figure (3-69): UV-Visible spectra of A (blue line) ZnO nanoparticles, B (orange line) absorption spectrum after adding ZnO to the cadmium solution.

The figure (3-70) represents the UV spectrum of Cu, where it is observed that the clear peak of copper disappears upon the addition of the toxic element Hg solution. As shown, curve A corresponds to Cu, while the straight-line B is the reagent with the mercury solution.

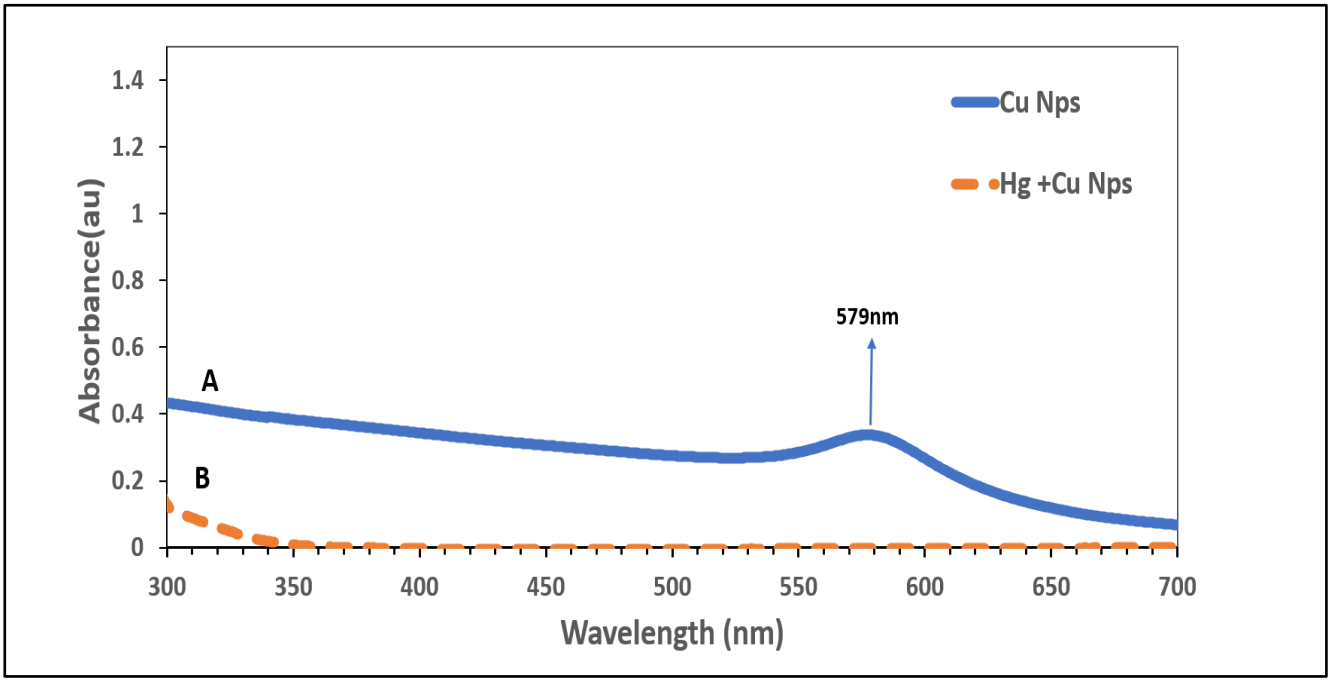

Figure (3-70): UV-Visible spectra of A (blue line) Cu nanoparticles, B (orange line) absorption spectrum after adding Cu NPs to the mercury solution.

3.3 Factors effecting the sensing process

3.3.1 Effect of Time

3.3.1.1 The effect of time on the detection of narcotic drug

For a predefined period of time, the intensity of the grey color was continuously monitored using the microfluidic device after the synthesized nanoparticles were added to their target solutions (tramadol hydrochloride, fentanyl citrate, and Aldine). In less than five minutes, the intensity of the color shift reached around 98% of its maximum value, and after five minutes, it remained constant (Figure 3-72). Because it was predictable enough to allow for the conduct of the measurements, five minutes was selected as the response time duration for the subsequent tests. Lab-on-a-chip (LOC) system color stability was generally suitable for every metric .

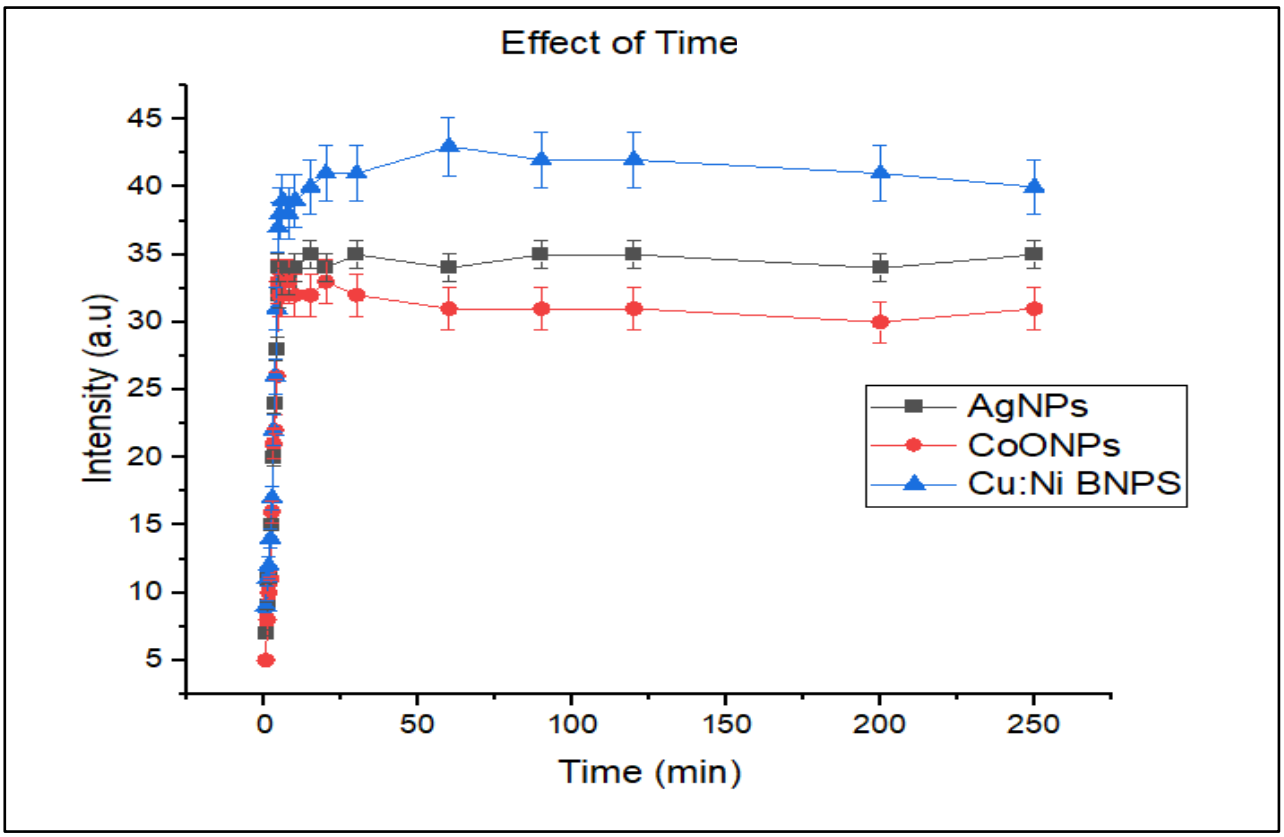

Figure (3-71): Effect of time on the detection of tramadol hydrochloride by Co O NPs, Aldine by Cu: NiO BNPs and fentanyl citrate by Ag NPs.

3.3.1.2 The effect time on the detection of mercury and cadmium

The effect of time on the detection of mercury and cadmium ions was studied starting from the moment the sample was added until 5 min had passed. A noticeable color change was observed during the first few seconds, indicating a rapid initial reaction between the surface of the detector and the ions. The change continued to increase gradually until it stabilized after approximately 5 minutes (Figure 3-72). Based on this, 5 min is considered the ideal time to achieve maximum detection efficiency under the experimental conditions used.

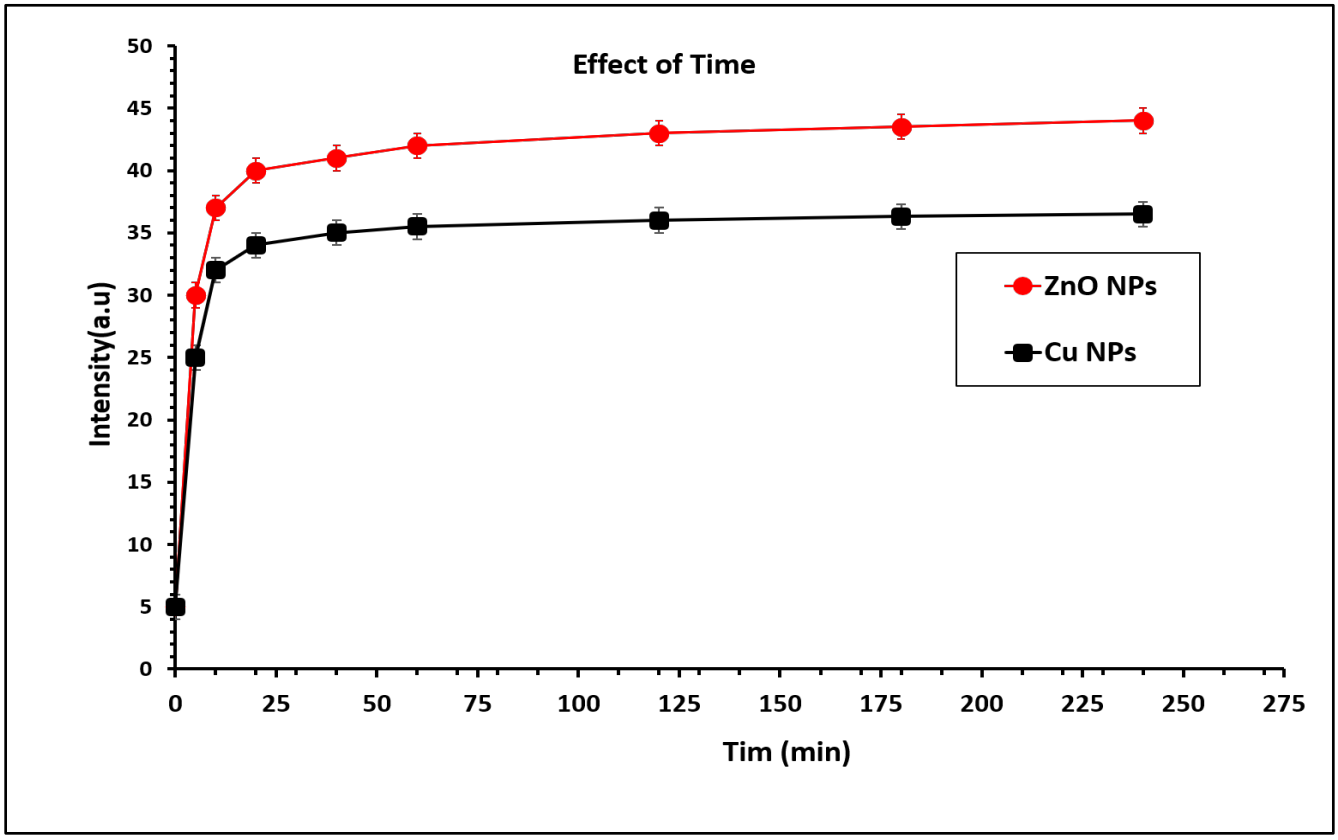

Figure (3-72): Effect of time on the detection of mercury and cadmium by Zn O NPs and Cu NPs.

3.3.2 Effect of Interferences

They are ions or other substances present in the sample that may affect the accuracy of the analysis either by interacting with the reagent itself or by forming competing complexes that affect the color or absorption.

3.3.2.1 Effect of interfering ions on the detection of tramadol hydrochloride, Aldine, and fentanyl citrate

The ability of the synthesized sensors to detect their targets preferentially even when various cations, anions, and nitrogenous substances like urea, creatinine, and uric acid are present was investigated. In this investigation, a number of foreign compounds were evaluated along with a specific dosage of some medications (10 μ g/mL). An optimized procedure created to examine the effects of different interferences on the accurate identification of these medications was used for this evaluation. It was surprising to find that common ions like Ca^{2+}, Mg^{2+}, PO_4^{3-}, K^+, Na^+, SO_4^{2-}, CO_3^{2-}, Cl^-, and NO_3^-, as well as nitrogenous compounds like urea, creatinine, and uric acid, did not change the color or intensity of the solution in less than five minutes, even at concentrations 250 times higher than those of some drugs.

3.3.2.2 Effect of Interfering ions on the detection of Hg^{+2} and Cd^{2+}

The effect of the interferences was evaluated to verify the selectivity of the detector by studying the impact of the presence of other metal ions such as Ca^{2+}, Mg^{2+}, PO_4^{3-}, K^+, Na^+, SO_4^{2-}, CO_3^{2-}, Cl^-, and NO_3^-, as well as nitrogenous compounds like urea, creatinine, and uric acid at concentrations comparable to or higher than the target ion (Hg^{+2} and Cd^{2+}) concentration. The results showed that these ions did not significantly affect the detection signal, indicating high selectivity of the system.

3.4 Performance of Nano sensors

3.4.1 The detection of narcotic drugs (tramadol hydrochloride, Aldine and fentanyl citrate) in blood plasma

After modifying the experimental settings, the procedure's validity was evaluated. Within the concentration range of 0.5 to 2.5 mg/L, a strong linear relationship was seen (Figure3-73). The correlation coefficient (R^2) revealed a substantial relationship between the measured absorption and medication concentrations. For fentanyl citrate, tramadol hydrochloride, and pethidine hydrochloride, the limit of detection (LOD) was found to be 0.143 mg/L, 0.241 mg/L, and 0.347 mg/L, respectively, using the 3σ/slope technique. Furthermore, the 2 mg/L tramadol hydrochloride result was found to have a 4% relative standard deviation (RSD%) (n = 3), indicating high precision .

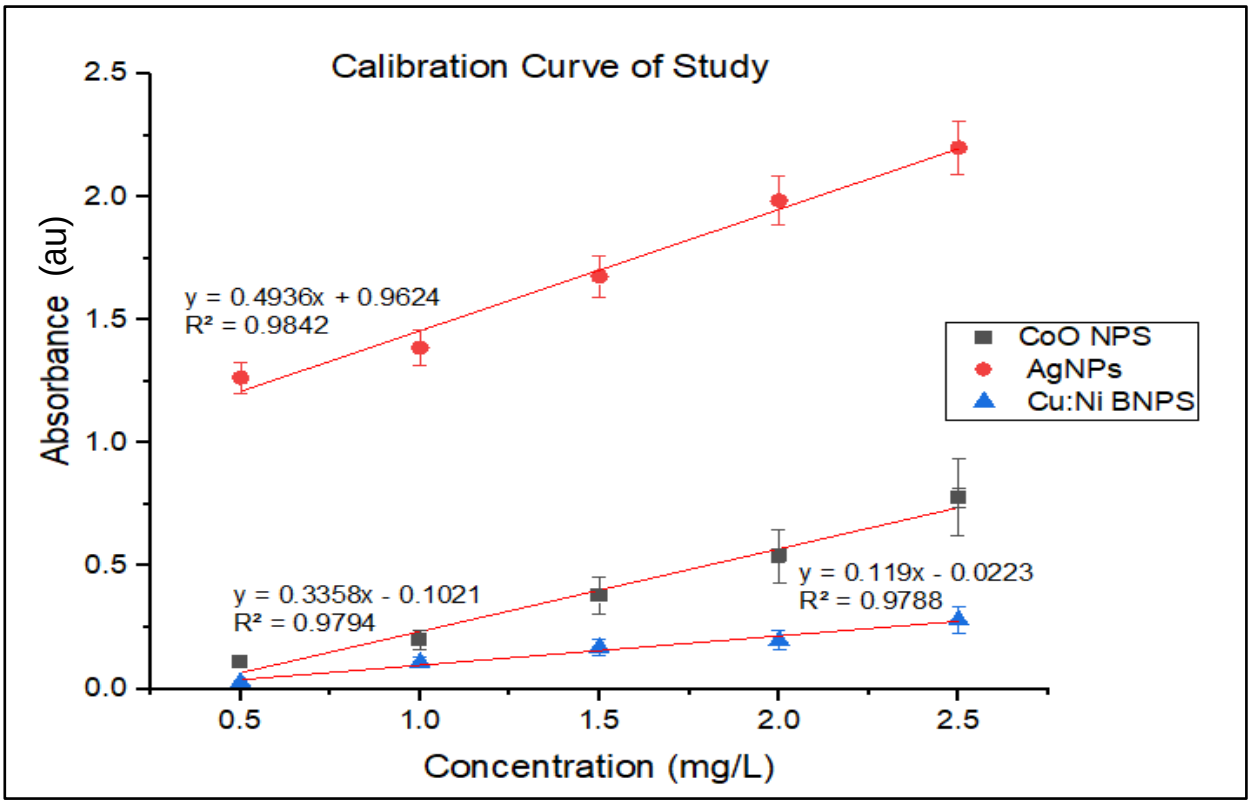

Figure (3-73): The calibration curve for detection of tramadol hydrochloride by CoO NPs, Aldine by Cu:NiO BNPs and fentanyl citrate by Ag NPs, figure illustrates the relationship between intensity and element concentration.

The 3D-printed microfluidic device with a square design for the simultaneous detection of narcotic drugs in blood plasma samples, as shown in Figure 3-74, consists of a main channel in the center dedicated to blood plasma, extending from which are four arms designated for the three sensors and blank. After injecting plasma into the central channel in a specific amount and adding the substances to be detected, and upon their arrival at the sensors injected in the specific channels, the resulting color is captured using an iPhone 12 Pro Max camera and a regular camera. After processing the data, the quantitative measurement is performed using the ImageJ program. Figure (3-74) illustrates the detection steps.

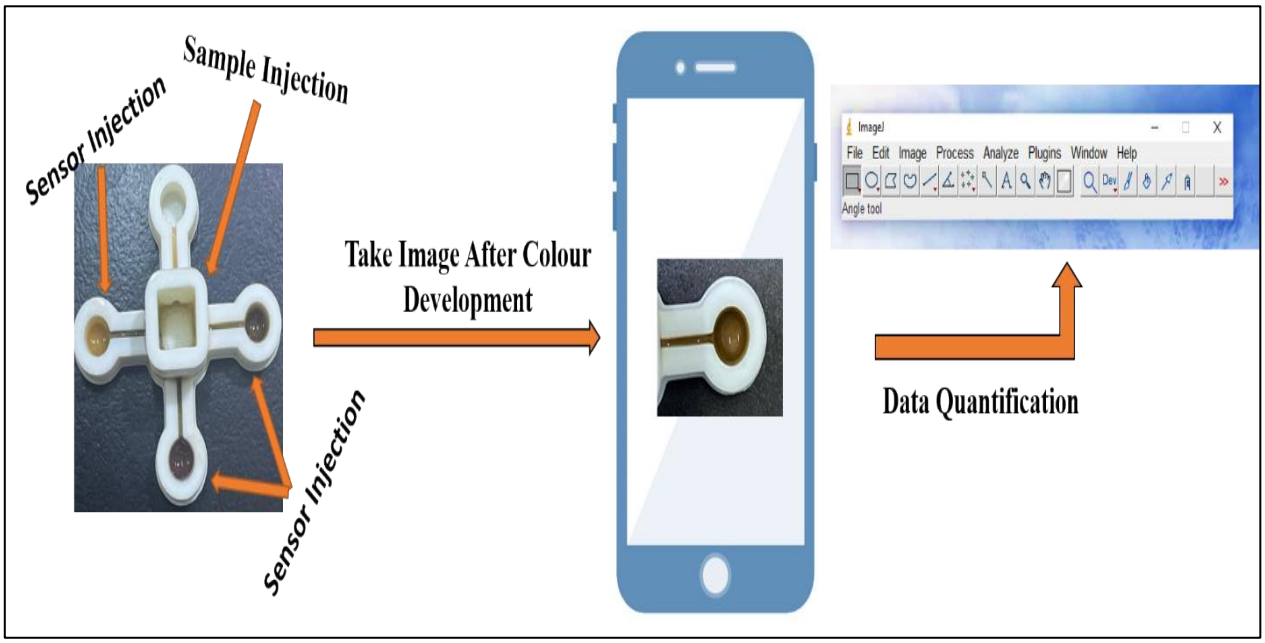

Figure (3-74): Injection, color development, and quantification procedures for the colorimetric naked-eye sensors based on 3D printed microfluidic devices that detect narcotic drugs.

3.4.2 The detection of heavy metal (mercury and cadmium) in blood

The calibration curve was plotted in figure (3-75) using the absorbance measured at five concentrations (0.5, 1 ,1.5 ,2 ,2.5) mg/L. To illustrate the relationship between the concentration of heavy metals (Hg^{+2} and Cd^{+2}) and absorbance. The results showed two linear curves represented by two equations, where the correlation coefficient reached (0.9987), indicating a satisfactory linear

relationship between the concentration of Hg^{+2} and absorption. Similarly, the R^2 for Cd^{+2} indicated (0.9826) an excellent fit with the linear model.

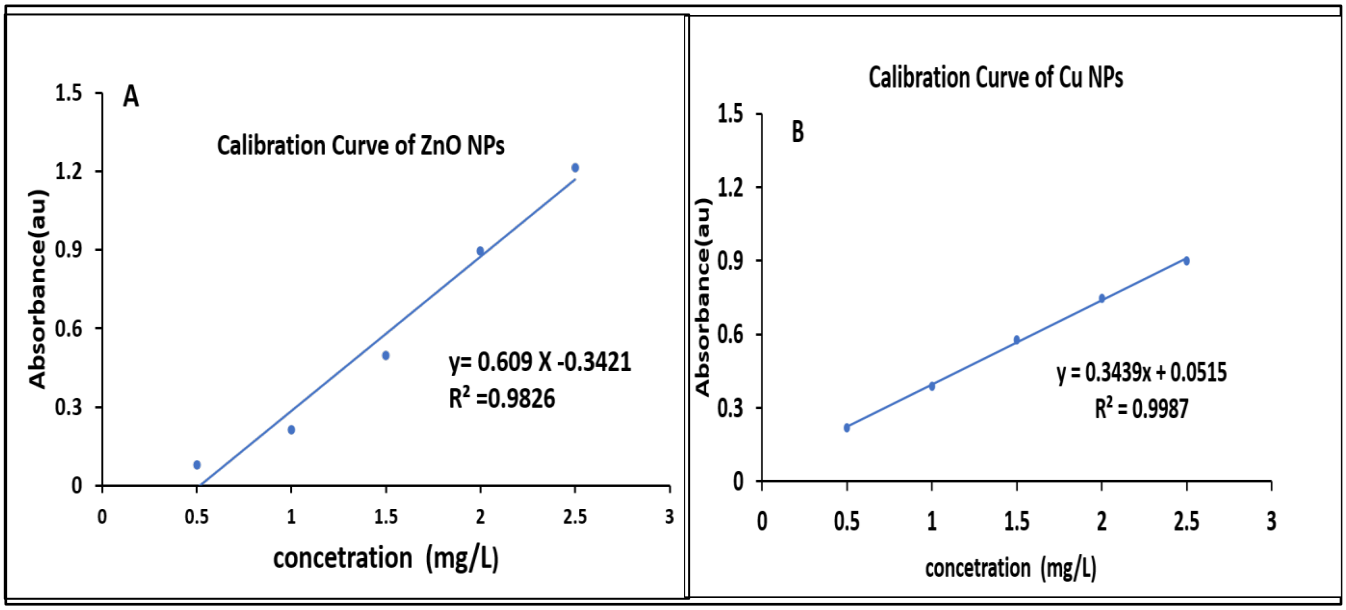

Figure (3-75): The calibration curve for detecting(A) Cd^{+2} by ZnO NPs and (B) Hg^{+2} by Cu NPs, Figure illustrates the relationship between intensity and element concentration.

The microfluidic device printed using 3D printing technology with a dual design for the simultaneous detection of heavy metals (Hg, Cd) in blood plasma samples, as shown in Figure 3-76, consists of a main channel in the center dedicated to blood plasma, from which two arms extend dedicated to sensors (Cu NPs, ZnO NPs). After injecting the plasma into the central channel in a specific amount and adding the substances to be detected, and when they reach the sensors injected in the specified channels, the resulting color is captured using an iPhone 12 Pro Max and a regular camera. After processing the data, quantitative measurement is performed using the ImageJ software. Figure (3-76) illustrates the detection steps.

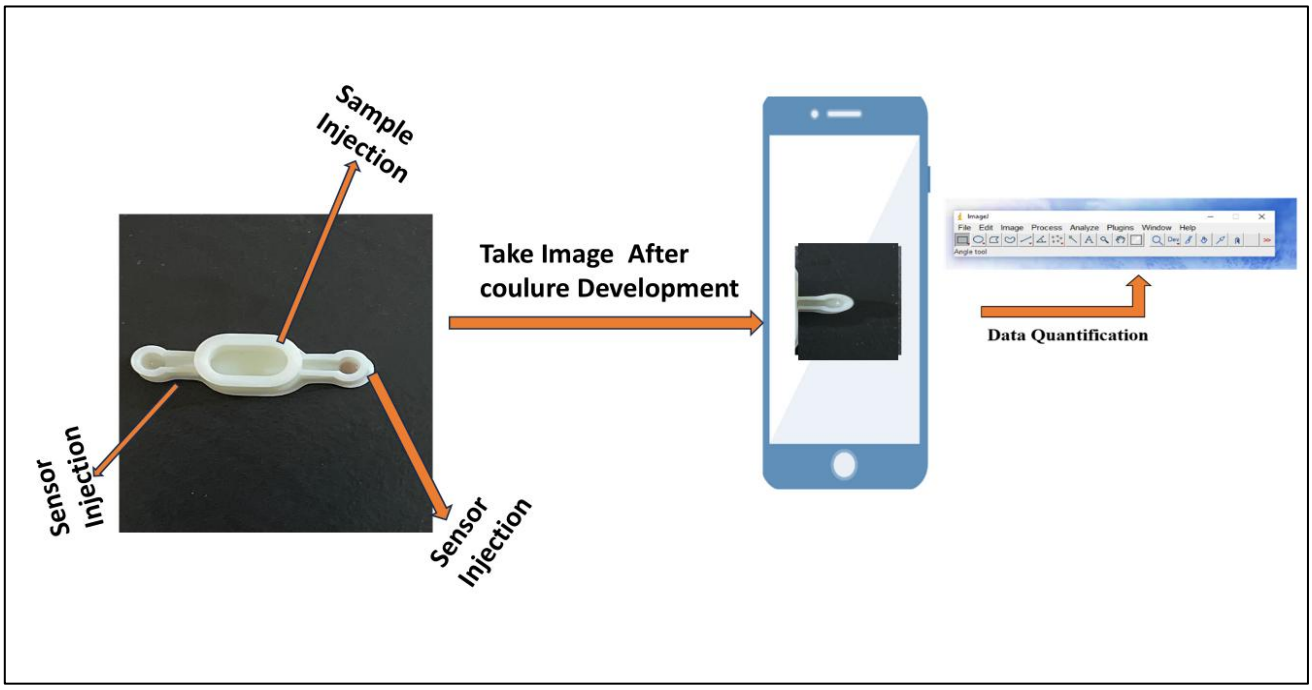

Figure (3-76): Injection, color development, and quantification procedures for the colorimetric naked-eye sensors based on 3D-printed microfluidic devices that detect heavy metals (Hg, Cd).

The new device's purpose is to quantify and detect pharmaceuticals in a selective manner. The detection of the three narcotic drugs fentanyl citrate, tramadol hydrochloride, and pethidine hydrochloride after spiking with blood plasma from a healthy volunteer showed how applicable our novel device is for accomplishing this. For all three drugs, the device exhibits remarkable recovery efficiency (fentanyl citrate 94%, tramadol hydrochloride 97%, and pethidine hydrochloride 98%) as shown in Table (3-3).

Table (3-3): Accuracy of drug and heavy metals quantification at our new microchip in blood plasma samples

Drug Analyte	Spiked Concentration (mg/L)	Found Conc. (mg/L) [a] Mean ± SD	RSD %
fentanyl citrate	0.5	0.47 ± 0.015	3 %
Tramadol	0.5	0.485 ± 0.02	4 %
pethidine hydrochloride	0.5	0.49 ± 0.035	7 %
cadmium	0.5	0.59 ± 0.053	9%
mercury	0.5	0.39 ±0.0021	5%

[a] Mean ± standard deviation (n = 3)

To evaluate the effectiveness of the newly created nano sensor, a comparison was made with current methods for detecting drugs and heavy metals (Table 3-4). Several recent studies that used drug detection as well as heavy metal detection were included in the comparison table. Although some methods result in low detection limits, the obtained data conclusively show that the nanoparticle-based colorimetric sensor we proposed performs better than some previously published sensors because these methods are less portable and therefore more difficult to use on-site.

Our approach significantly simplifies current processes by using a smartphone for estimation and integrated reagents for colorimetric detection. One of the main advantages of our nano sensors is their ability to quickly detect drugs and heavy metals and induce a color change. This rapid response demonstrates the high activity of the catalyst surface. These results demonstrate the success of the produced Nano sensor in integrating high activity, cost-effectiveness, and environmental friendliness in conducting the measurements.

Table (3-4): The efficiency of the synthesized nanoparticles as a colorimetric drug and heavy metal detection sensor in comparison to previously published research.

Detection Methodology	Analyte	LOD	Detection Time	Reference
Capillary electrophoresis	Tramadol	3.012×10^{-8} mol·L^{-1}	300 s	[214]
HPLC	Tramadol	0.010 µg/mL	2.5 min	[215]
Biosensor	Tramadol	0.52 µg/L	-	[216]
Paper-based SERS substrate	fentanyl citrate	0.59 µ g/mL	-	[217]
LC-MS/MS	fentanyl citrate	5 p g/mL	2.2 min	[218]
Raman spectroscopy based on silver aggregates	pethidine hydrochloride	0.1 µ g mL^{-1}	-	[219]
Voltammetry	pethidine hydrochloride	19.3 n M	-	[220]
Chemiluminescence	pethidine hydrochloride	7.1×10-8 mol L^{-1}	-	[221]
Ag NPs in Microfluidic Device	fentanyl citrate	0.143 mg/L	2 min	This Work
CoO NPs in Microfluidic Device	Tramadol	0.241 mg/L	2 min	This Work
Cu: NiO BNPs in Microfluidic Device	pethidine hydrochloride	0.347 mg/L	2 min	This Work
bismuth-modified pre-anodized screen-printed carbon electrode (SPCE)	Cd^{+2}	3.55 µ g/L	3 min	[222]
Differential Pulse Anodic Stripping Voltammetry (DPASV)	Cd^{+2}	0.001 µ mol/L	180 s	[223]

Paper-based colorimetric device (PCD)	Hg^{+2}	0.01 u M	5 min	[224]
fluorescent distance-based Paper device	Hg^{+2}	5 mg L^{-1}	-	[225]
Cu NPs in Microfluidic Device	Hg^{+2}	0.217 mg/L	1 min	This Work
ZnO NPs in Microfluidic Device	Cd^{+2}	0.073 mg/L	1 min	This Work

Chapter four

Conclusions and Recommendations

4.1 Conclusions

In this research, a series of mono and bimetallic nanomaterials were successfully synthesized using green and environmentally friendly methods based on plant extracts. The use of green tea and *Boswellia sacra* extracts proved to be effective not only as reducing agents but also as stabilizing agents, enabling the formation of stable nanoparticles with nanoscale dimensions.

Comprehensive characterization confirmed the successful preparation of the nanomaterials. FESEM and TEM analyses demonstrated that the synthesized nanoparticles possessed well-defined morphologies and sizes within the nanoscale range. EDX analysis verified the elemental composition and high purity of the prepared materials, while FTIR results confirmed the active role of plant extracts through characteristic functional groups responsible for reduction and stabilization.

X-ray diffraction analysis revealed that all prepared nanomaterials exhibited crystalline structures consistent with standard reference data. In addition, zeta potential measurements indicated good surface stability, with bimetallic nanoparticles showing enhanced stability compared to their monometallic counterparts, particularly in the case of Ag:NiO BNPs.

The sensing performance of the prepared nanomaterials was systematically evaluated for the detection of narcotic pharmaceutical substances and heavy metals. Ag NPs, CoO NPs, and Cu:NiO bimetallic nanoparticles demonstrated high sensitivity and rapid colorimetric response toward fentanyl citrate, tramadol hydrochloride, and pethidine hydrochloride. Meanwhile, ZnO NPs and Cu NPs exhibited excellent sensitivity toward cadmium and mercury ions in blood plasma, even at very low concentrations. The detection process was characterized by rapid response times and clear visual color changes, confirming the suitability of these nanomaterials for colorimetric sensing applications.

To enhance detection speed and accuracy, microfluidic devices were successfully designed using SOLIDWORKS and fabricated via 3D printing. The quad-device with four channels and dimensions (60 x 40 × 1.5) mm and dual-device with two channels (30 x 13× 10) mm microfluidic configurations enabled efficient interaction between the nanomaterials and analytes, leading to improved sensitivity, reduced sample volume, and faster detection. The integration of green-synthesized nanomaterials with microfluidic platforms demonstrated a highly efficient system for rapid and reliable colorimetric detection. The optimized geometry of the quad-channel configuration maximized the surface-area-to-volume ratio, ensuring a more homogenous mixing between the green-synthesized nanoparticles and the target analytes. This architectural advantage significantly reduced the diffusion path, which was the key driver behind the achieved sub-minute response times.

The systematic evaluation of the sensing performance revealed that the architectural optimization of the microfluidic platforms was instrumental in achieving superior results. By utilizing the quad-channel and dual-channel configurations, the system facilitated an enhanced collision frequency between the green-synthesized nanomaterials and target analytes. Specifically, the integration of Ag NPs, CoO NPs, and Cu:NiO bimetallic nanoparticles within these micro-environments yielded a synergistic effect that significantly amplified the colorimetric signal intensity for fentanyl citrate, tramadol hydrochloride, and pethidine hydrochloride. Furthermore, the microfluidic control allowed ZnO NPs and Cu NPs to maintain high sensitivity in complex matrices like blood plasma, detecting cadmium and mercury ions at ultra-low concentrations with unprecedented precision. This study confirms that the marriage between precision-designed 3D-printed microfluidics and sustainable nanotechnology creates a robust, high-throughput diagnostic tool characterized by rapid response and clear visual validation.

4.2 Recommendations

1. Preparation of ternary or quaternary nanomaterials
2. Designing microfluidic devices in different shapes and sizes, as well as their use in broader fields.
3. Creating precise channels with the same specifications as the manufactured microfluidics but using other materials such as PDMS.
4. The use of nanomaterials in detecting other compounds in blood plasma and the medical field more broadly.
5. Innovating precise channels with dimensions and designs that reduce response time and increase the efficiency of mixing and transferring the detector and sample.
6. Using bio-compatible and low-cost manufacturing materials, considering ease of large-scale production.
7. Integrating nanomaterials directly into the channels or on the surfaces of microfluidics to ensure their stability and improve real-time sensing.
8. Developing low-energy and environmentally friendly microfluidic systems using recyclable or biodegradable materials.

References

References

[1] Altammar, K.A., *A review on nanoparticles: characteristics, synthesis, applications, and challenges.* Frontiers in microbiology, 2023. **14**: p. 1155622.

[2] Naganthran, G.V., Farah Eryssa Khalid , Mas Jaffri Masarudin 2 ,, N.M.N. Azham Zulkharnain, Murni Karim , Che Azurahanim Che Abdullah 8,9, and and Siti Aqlima Ahmad, *Synthesis, Characterization and Biomedical Application of*

Silver Nanoparticles. 2022

[3] Findik, F., *Nanomaterials and their applications.* Period. Eng. Nat. Sci, 2021. **9**(3): p. 62-75.

[4] Xaba, T., et al., *The effect of temperature on the growth of Ag2O nanoparticles and thin films from bis (2-hydroxy-1-naphthaldehydato) silver (I) complex by the thermal decomposition of spin–coated films.* Materials Science in Semiconductor Processing, 2017. **71**: p. 109-115.

[5] Bayda, S., et al., *The history of nanoscience and nanotechnology: from chemical–physical applications to nanomedicine.* Molecules, 2019. **25**(1): p. 112.

[6] Jalilian, *Green synthesized silver nanoparticle from Allium ampeloprasum aqueous extract: Characterization, antioxidant activities, antibacterial and cytotoxicity effects.* Advanced Powder Technology, 2020. **31**(3): p. 1323-1332.

[7] Bouafia, A., et al., *The recent progress on silver nanoparticles: synthesis and electronic applications.* Nanomaterials, 2021. **11**(9): p. 2318.

[8] Liu, Q., et al., *Current research trends of nanomedicines.* Acta Pharmaceutica Sinica B, 2023. **13**(11): p. 4391-4416.

[9] Barhoum, *Review on natural, incidental, bioinspired, and engineered nanomaterials: history, definitions, classifications, synthesis, properties,*

market, toxicities, risks, and regulations. Nanomaterials, 2022. **12**(2): p. 177.

[10] Salem, S.S., *A comprehensive review of nanomaterials: Types, synthesis, characterization, and applications.* Biointerface Res. Appl. Chem, 2022. **13**(1): p. 41.

[11] Baek, J.W., et al., *Cobalt-doped ceria sensitizer effects on metal oxide nanofibers: Heightened surface reactivity for high-performing chemiresistive sensors.* ACS nano, 2024. **18**(30): p. 19568-19580.

[12] Ji, Z., et al., *Nanomaterial databases: data sources for promoting design and risk assessment of nanomaterials.* Nanomaterials, 2021. **11**(6): p. 1599.

[13] Kumari, S., et al., *A comprehensive review on various techniques used for synthesizing nanoparticles.* Journal of Materials Research and Technology, 2023. **27**: p. 1739-1763.

[14] Genchi, G., et al., *Prevalence of cobalt in the environment and its role in biological processes.* Biology, 2023. **12**(10): p. 1335.

[15] Al-Harbi, N. and N.K. Abd-Elrahman, *Physical methods for preparation of nanomaterials, their characterization and applications: a review.* Journal of Umm Al-Qura University for Applied Sciences, 2024: p. 1-22.

[16] Dhand, C., et al., *Methods and strategies for the synthesis of diverse nanoparticles and their applications: a comprehensive overview.* Rsc Advances, 2015. **5**(127): p. 105003-105037.

[17] Ayuk, E., M. Ugwu, and S.B. Aronimo, *A review on synthetic methods of nanostructured materials.* Chemistry Research Journal, 2017. **2**(5): p. 97-123.

[18] Wei, L.K., et al., *Producing metal powder from machining chips using ball milling process: A review.* Materials, 2023. **16**(13): p. 4635.

[19] Salah, N., et al., *High-energy ball milling technique for ZnO nanoparticles as antibacterial material.* International journal of nanomedicine, 2011: p. 863-869.

[20] Yogesh, G.K., et al., *Progress in pulsed laser ablation in liquid (PLAL) technique for the synthesis of carbon nanomaterials: a review.* Applied Physics A, 2021. **127**(11): p. 810.

[21] Jiang, Z., et al., *Progress in laser ablation and biological synthesis processes:"Top-Down" and "Bottom-Up" approaches for the green synthesis of Au/Ag nanoparticles.* International Journal of Molecular Sciences, 2022. **23**(23): p. 14658.

[22] Alamro, F.S., et al., *Synthesis of Ag nanoparticles-decorated CNTs via laser ablation method for the enhancement the photocatalytic removal of naphthalene from water.* Nanomaterials, 2021. **11**(8): p. 2142.

[23] Kim, M., et al., *Synthesis of nanoparticles by laser ablation: A review.* KONA Powder and Particle Journal, 2017. **34**: p. 80-90.

[24] Vorobyova, M., et al., *PVD for decorative applications: a review.* Materials, 2023. **16**(14): p. 4919.

[25] Saad, K.S.K., T. Saba, and A.B. Rashid, *Application of PVD coatings in medical implantology for enhanced performance, biocompatibility, and quality of life.* Heliyon, 2024. **10**(16).

[26] Xu, W., et al., *Insights into the Synthesis, types and application of iron Nanoparticles: The overlooked significance of environmental effects.* Environment International, 2022. **158**: p. 106980.

[27] Guo, Y., et al., *Ultrafast laser reconstructed PS-PVD thermal barrier coatings with superior silicophobic triple-scale micro/nano structure.* Materials & Design, 2023. **228**: p. 111846.

[28] Kerasidou, A., et al., *Growth of ZnO nanowires on seeding layers deposited by ALD: The influence of process parameters.* Microelectronic Engineering, 2019. **217**: p. 111091.

[29] Santos, N., et al., *Electrochemical and photoluminescence response of laser-induced graphene/electrodeposited ZnO composites.* Scientific Reports, 2021. **11**(1): p. 17154.

[30] Silva, L., et al., *Research Article Synthesis of Fe Nanoparticles Functionalized with Oleic Acid Synthesized by Inert Gas Condensation. Journal of Nanomaterials 2014 Vol. 2014 Issue 1 P 643967.*

[31] Sharma, P., *Colloidal synthesis and characterizations of metal, metal-oxide, and semiconductor nanoparticles by inductive heating method*. 2021: KANSAS STATE UNIVERSITY Manhattan, Kansas 2021 .

[32] Hemben, A., I. Chianella, and G. Leighton, *Surface Engineered Iron Oxide Nanoparticles Generated by Inert Gas Condensation for Biomedical Applications. Bioengineering 2021, 8, 38*. 2021, s Note: MDPI stays neutral with regard to jurisdictional claims in published ….2021

[33] Panchal, V., et al., *Controlling magnetic properties of iron oxide nanoparticles using post-synthesis thermal treatment.* Applied Physics A, 2014. **114**(2): p. 537-544.

[34] Krishna, A.G., et al., *Green synthesis of copper nanoparticles: a promising solution for drug resistance and cancer therapy challenges.* Journal of the Egyptian National Cancer Institute, 2024. **36**(1): p. 44.

[35] Khosravi, N., et al., *Biomedical applications of copper nanoparticles: an up-to-date overview.* Journal of Composites and Compounds, 2024. **6**(21).

[36] Hachem, K., et al., *Methods of chemical synthesis in the synthesis of nanomaterial and nanoparticles by the chemical deposition method: a review.* BioNanoScience, 2022. **12**(3): p. 1032-1057.

[37] Harish, V., et al., *Nanoparticle and nanostructure synthesis and controlled growth methods.* Nanomaterials, 2022. **12**(18): p. 3226.

[38] Szczyglewska, P., A. Feliczak-Guzik, and I. Nowak, *Nanotechnology–general aspects: A chemical reduction approach to the synthesis of nanoparticles.* Molecules, 2023. **28**(13): p. 4932.

[39] Pricop, A., et al., *Copper Nanoparticles Synthesized by Chemical Reduction with Medical Applications.* International Journal of Molecular Sciences, 2025. **26**(4): p. 1628.

[40] Logutenko, O., et al., *A novel method to prepare copper microspheres via chemical reduction route.* Journal of Materials Research and Technology, 2021. **13**: p. 1254-1265.

[41] Landage, S., A. Wasif, and P. Dhuppe, *Synthesis of nanosilver using chemical reduction methods.* International Journal of Advanced Research in Engineering and Applied Sciences, 2014. **3**(5): p. 14-22.

[42] Navas, D., et al., *Review on sol-gel synthesis of perovskite and oxide nanomaterials.* Gels, 2021. **7**(4): p. 275.

[43] Nadeem Baig, a.I.K.d.a.W.F., *Nanomaterials: a review of synthesis methods, properties, recent progress, and challenges.* the Royal Society of Chemistry,2021,2, 1821: p. 1871.

[44] Rajput, N., *Methods of preparation of nanoparticles-a review.* International Journal of Advances in Engineering & Technology, 2015. **7**(6): p. 1806.

[45]Abdurakhmanov, E., et al., *Template Synthesis of Nanomaterials based on Titanium and Cadmium Oxides by the Sol-Gel Method, Study of their Possibility of Application As A Carbon Monoxide Sensor (II).* Journal of Pharmaceutical Negative Results, 2022. **13**: p. 1343-1350.

[46] Meng, Y.Q., et al., *Recent trends in preparation and biomedical applications of iron oxide nanoparticles.* Journal of Nanobiotechnology, 2024. **22**(1): p. 24.

[47] Yusefi, M., K. Shameli, and A.F. Jumaat, *Preparation and properties of magnetic iron oxide nanoparticles for biomedical applications: A brief review.* Journal of Advanced Research in Materials Science, 2020. **75**(1): p. 10-18.

[48] Sarkar, N., R.S. Sharma, and M. Kaushik, Green synthesis and physiochemical characterization of nickel oxide nanoparticles: Interaction studies with Calf thymus DNA. Luminescence, 2020. **35**(2): p. 178-186.

[49] Vinukonda, A., et al., *Synthesis of nanoparticles using advanced techniques.* Next Nanotechnology, 2025. **8**: p. 100169.

[50] Ali, *Review on recent progress in magnetic nanoparticles: Synthesis, characterization, and diverse applications.* Frontiers in chemistry, 2021. **9**: p. 629054.

[51] Anik, M.I., *Recent progress of magnetic nanoparticles in biomedical applications: A review.* Nano Select, 2021. **2**(6): p. 1146-1186.

[52] Nandihalli, N., D.H. Gregory, and T. Mori, *Energy-saving pathways for thermoelectric nanomaterial synthesis: hydrothermal/solvothermal, microwave-assisted, solution-based, and powder processing.* Advanced science, 2022. **9**(25): p. 2106052.

[53] Ndlwana, L., et al., *Sustainable hydrothermal and solvothermal synthesis of advanced carbon materials in multidimensional applications: a review.* Materials, 2021. **14**(17): p. 5094.

[45] Adeyemi, J.O., et al., *Plant extracts mediated metal-based nanoparticles: synthesis and biological applications.* Biomolecules, 2022. **12**(5): p. 627.

[55] Xaba, T., et al., *The influences of the concentrations of "green capping agents" as stabilizers and of ammonia as an activator in the synthesis of ZnS nanoparticles and their polymer nanocomposites.* Green Processing and Synthesis, 2017. **6**(2): p. 173-182.

[56] Sa¨ıd Kinania, S.B.a., Nathalie Milanb, Ivan Ricordelb, *A sensitive and selective method for the detection of diazepam and its main metabolites in urine by gas chromatography–tandem mass spectrometry* Journal of Chromatography A, 1141 (2007) 131–137, 2006.

[57] Mughal, B., *Biogenic nanoparticles: Synthesis, characterisation and applications.* Applied Sciences, 2021. **11**(6): p. 2598.

[58] Velusamy, P., *Bio-inspired green nanoparticles: synthesis, mechanism, and antibacterial application.* Toxicological research, 2016. **32**(2): p. 95-102.

[59] Kulkarni, D., et al., *Biofabrication of nanoparticles: sources, synthesis, and biomedical applications.* Frontiers in bioengineering and biotechnology, 2023. **11**: p. 1159193.

[60] Álvarez-Chimal, R. and J.Á. Arenas-Alatorre, *Green synthesis of nanoparticles: A biological approach*, in *Green chemistry for environmental sustainability-prevention-assurance-sustainability (PAS) approach*. 2023, IntechOpen.

[61] Singh, A., et al., *Green synthesis of metallic nanoparticles as effective alternatives to treat antibiotics resistant bacterial infections: A review.* Biotechnology Reports, 2020. **25**: p. e00427.

[62] Niego, A.G.T., et al., *The contribution of fungi to the global economy.* Fungal Diversity, 2023. **121**(1): p. 95-137.

[63] Khan, S., et al., *The impact of silver nanoparticles on the growth of plants: The agriculture applications.* Heliyon, 2023. **9**(6).

[64] Salem, S.S., *A mini review on green nanotechnology and its development in biological effects.* Archives of Microbiology, 2023. **205**(4): p. 128.

[65] Hosseingholian, A., *Recent advances in green synthesized nanoparticles: from production to application.* Materials Today Sustainability, 2023. **24**: p. 100500.

[66] Ying, S., et al., *Green synthesis of nanoparticles: Current developments and limitations.* Environmental technology & innovation, 2022. **26**: p. 102336.

[67] Agarwal, H., S.V. Kumar, and S. Rajeshkumar, *A review on green synthesis of zinc oxide nanoparticles–An eco-friendly approach.* Resource-Efficient Technologies, 2017. **3**(4): p. 406-413.

[68] Mohammed, A.M., W. Saud, and M. Ali, *Green synthesis of Fe2O3 nanoparticles using Olea europaea leaf extract and their antibacterial activity.* Dig. J. Nanomater. Biostructures, 2020. **15**(1): p. 175-183.

[69] Remya, V., *Silver nanoparticles green synthesis: a mini review.* Chem. Int, 2017. **3**(2): p. 165-171.

[70] Abubakar, A.R. and M. Haque, *Preparation of medicinal plants: Basic extraction and fractionation procedures for experimental purposes.* Journal of Pharmacy and Bioallied Sciences, 2020. **12**(1): p. 1-10.

[71] Alsaiari, N.S., et al., *Plant and microbial approaches as green methods for the synthesis of nanomaterials: synthesis, applications, and future perspectives.* Molecules, 2023. **28**(1): p. 463.

[72] Alprol, A.E., et al., *Advances in green synthesis of metal oxide nanoparticles by marine algae for wastewater treatment by adsorption and photocatalysis techniques.* Catalysts, 2023. **13**(5): p. 888.

[73] Zeebaree, S.Y.S., et al., *Sustainable fabrication, optical properties and rapid performance of bio-engineered copper nanoparticles in removal of toxic methylene blue dye in an aqueous medium.* Current Research in Green and Sustainable Chemistry, 2021. **4**: p. 100103.

[74] Mukherjee, A., D. Sarkar, and S. Sasmal, *A review of green synthesis of metal nanoparticles using algae.* Frontiers in Microbiology, 2021. **12**: p. 693899.

[75] Ahmed, S.F., *Green approaches in synthesising nanomaterials for environmental nanobioremediation: Technological advancements, applications, benefits and challenges.* Environmental Research, 2022. **204**: p. 111967.

[76] Sharma, G., et al., *Novel development of nanoparticles to bimetallic nanoparticles and their composites: A review.* Journal of King Saud University-Science, 2019. **31**(2): p. 257-269.

[77] Dong, Z.-Z., et al., *Tumor microenvironment-responsive Zn/Cu nanoparticles for enhanced chemodynamic therapy.* Smart Materials in Medicine, 2023. **4**: p. 286-293.

[78] Loza, K., M. Heggen, and M. Epple, *Synthesis, structure, properties, and applications of bimetallic nanoparticles of noble metals.* Advanced functional materials, 2020. **30**(21): p. 1909260.

[79] Eom, N., et al., *General trends in core–shell preferences for bimetallic nanoparticles.* ACS nano, 2021. **15**(5): p. 8883-8895.

[80] Chatterjee, K., et al., *Core/shell nanoparticles in biomedical applications.* Advances in colloid and interface science, 2014. **209**: p. 8-39.

[81] Idris, D.S. and A. Roy, *Synthesis of bimetallic nanoparticles and applications—an updated review.* Crystals, 2023. **13**(4): p. 637.

[82] Savina, K., et al., *Dealloying in Pt-based nanoalloys as a way to synthesize bimetallic nanoparticles: Atomistic simulations.* Nano-Structures & Nano-Objects, 2023. **34**: p. 100977.

[83] Dlamini, N.G., A.K. Basson, and V.S.R. Pullabhotla, *Synthesis and characterization of various bimetallic nanoparticles and their application.* Applied Nano, 2023. **4**(1): p. 1-24.

[84] Phinjaroenphan, R., K. Boonserm, and S. Rattanasuporn, *Preparation and characterization of bimetallic Cu-Ni and/or Ni-Cu core-shell nanoparticles with high photocatalytic activity.* Asian Health, Science and Technology Reports, 2021. **29**(2): p. 54-63.

[85] Hosny, M., M. Fawzy, and A.S. Eltaweil, *Green synthesis of bimetallic Ag/ZnO@ Biohar nanocomposite for photocatalytic degradation of tetracycline, antibacterial and antioxidant activities.* Scientific Reports, 2022. **12**(1): p. 7316.

[86] Pan, C.-J., L.S. Sarma, and B.-J. Hwang, *Formation and characterization of bimetallic nanoparticles in electrochemistry*, in *Handbook of Nanoelectrochemistry*. 2016, Springer. p. 169-239.

[87] Feng, Y., *Depletion sphere: Explaining the number of Ag islands on Au nanoparticles.* Chemical science, 2017. **8**(1): p. 430-436.

[88] Idris, D. and A. Roy, *Synthesis of Bimetallic Nanoparticles and Applications-An Updated Review. Crystals 2023, 13, 637*. 2023.

[89] Srinoi, P., et al., *Bimetallic nanoparticles: enhanced magnetic and optical properties for emerging biological applications.* Applied Sciences, 2018. **8**(7): p. 1106.

[90] Vodyashkin, A.A., et al., *Current methods for synthesis and potential applications of cobalt nanoparticles: a review.* Crystals, 2022. **12**(2): p. 272.

[91] Spoială, A., et al., *The development of alginate/Ag NPs/Caffeic acid composite membranes as adsorbents for water purification.* Membranes, 2023. **13**(6): p. 591.

[92] Tunç, T., *Synthesis and characterization of silver nanoparticles loaded with carboplatin as a potential antimicrobial and cancer therapy.* Cancer Nanotechnology, 2024. **15**(1): p. 2.

[93] Anjum, S., et al., *Recent advances in zinc oxide nanoparticles (ZnO NPs) for cancer diagnosis, target drug delivery, and treatment.* Cancers, 2021. **13**(18): p. 4570.

[94] Moussa, N., et al., *Chromium doped ZnO nanoparticles for energy storage, gas and humidity sensing and spin based electronic devices applications.* Optical and Quantum Electronics, 2022. **54**(11): p. 683.

[95] Hegde, V.N., *Study on structural, morphological, elastic and electrical properties of ZnO nanoparticles for electronic device applications.* Journal of Science: Advanced Materials and Devices, 2024. **9**(3): p. 100733.

[96] Al-Aoh, H.A., *Adsorption performances of nickel oxide nanoparticles (NiO NPs) towards bromophenol blue dye (BB).* Desalination and Water Treatment, 2018. **110**: p. 229-238.

[97] Zarenezhad, E., et al., *Nickel nanoparticles: applications and antimicrobial role against methicillin-resistant Staphylococcus aureus infections.* Antibiotics, 2022. **11**(9): p. 1208.

[98] Lu, R., et al., *Self-Assembled CuCo2S4 Nanoparticles for Efficient Chemo-Photothermal Therapy of Arterial Inflammation.* Molecules, 2022. **27**(23): p. 8134.

[99] Kumar, S., et al., *A historical perspective on paper microfluidic based point-of-care diagnostics*, in *Paper Microfluidics: Theory and Applications*. 2019, Springer. p. 1-5.

[100] Lisowski, P. and P.K. Zarzycki, *Microfluidic paper-based analytical devices (μPADs) and micro total analysis systems (μTAS): Development, applications and future trends.* Chromatographia, 2013. **76**(19): p. 1201-1214.

[101] Singh, P.K., et al., *Critical review on toxic contaminants in surface water ecosystem: sources, monitoring, and its impact on human health.* Environmental Science and Pollution Research, 2024. **31**(45): p. 56428-56462.

[102] Niculescu, A.-G., et al., *Fabrication and applications of microfluidic devices: A review.* International journal of molecular sciences, 2021. **22**(4): p. 2011.

[103] Alavi, S.E., *Microfluidics for personalized drug delivery.* Drug Discovery Today, 2024. **29**(4): p. 103936.

[104] Gale, B.K., et al., *A review of current methods in microfluidic device fabrication and future commercialization prospects.* Inventions, 2018. **3**(3): p. 60.

[105] Sackmann, E.K., A.L. Fulton, and D.J. Beebe, *The present and future role of microfluidics in biomedical research.* Nature, 2014. **507**(7491): p. 181-189.

[106] Munyan, J.W., et al., *Electrically actuated, pressure-driven microfluidic pumps.* Lab on a Chip, 2003. **3**(4): p. 217-220.

[107] Cummins, B.M., et al., *Modular pumps as programmable hydraulic batteries for microfluidic devices.* Technology, 2017. **5**(01): p. 21-30.

[108] Lake, J.R., K.C. Heyde, and W.C. Ruder, *Low-cost feedback-controlled syringe pressure pumps for microfluidics applications.* PLoS One, 2017. **12**(4): p. e0175089.

[109] Wang, X., *A hydrostatic pressure-driven passive micropump enhanced with siphon-based autofill function.* Lab on a Chip, 2018. **18**(15): p. 2167-2177.

[110] Zhao, Q., et al., *Mechanical strain-enabled reconstitution of dynamic environment in organ-on-a-chip platforms: a review.* Micromachines, 2021. **12**(7): p. 765.

[111] Alizadeh, A., et al., *Electroosmotic flow: From microfluidics to nanofluidics.* Electrophoresis, 2021. **42**(7-8): p. 834-868.

[112] Qiu, Y. and L. Ma, *Influences of electroosmotic flow on ionic current through nanopores: A comprehensive understanding.* Physics of Fluids, 2022. **34**(11).

[113] Li, D., H. Li, and J. Liu, *Pulse electroosmotic flow of Newtonian fluids in parallel plate microchannels under triangular and half-sinusoidal pulse electric fields.* Journal of Applied Physics, 2024. **136**(18).

[114] Miller, S., et al., *Electroosmotic flow driven microfluidic device for bacteria isolation using magnetic microbeads.* Scientific reports, 2019. **9**(1): p. 14228.

[115] Cai, S., et al., *Micromixing within microfluidic devices: Fundamentals, design, and fabrication.* Biomicrofluidics, 2023. **17**(6).

[116] Prabhakaran, R.A., et al., *Induced charge effects on electrokinetic entry flow.* Physics of Fluids, 2017. **29**(6).

[117] Azizian, P., *Capillary-driven microfluidics: impacts of 3D manufacturing on bioanalytical devices.* Analyst, 2023. **148**(12): p. 2657-2675.

[118] Songok, J. and M. Toivakka, *Enhancing capillary-driven flow for paper-based microfluidic channels.* ACS Applied Materials & Interfaces, 2016. **8**(44): p. 30523-30530.

[119] Wang, S., *A review of capillary pressure control valves in microfluidics.* Biosensors, 2021. **11**(10): p. 405.

[120] Khanjani, E., et al., *Capillary microfluidics for diagnostic applications: fundamentals, mechanisms, and capillarics.* Frontiers in Lab on a Chip Technologies, 2025. **4**: p. 1502127.

[121] Al-Aqbi, Z.T., et al., *Integrated microfluidic devices fabricated in poly (methyl methacrylate)(PMMA) for on-site therapeutic drug monitoring of aminoglycosides in whole blood.* Biosensors, 2019. **9**(1): p. 19.

[122] Gerlero, G.S., et al., *Comprehensive numerical prototyping of paper-based microfluidic devices using open-source tools.* Talanta Open, 2024. **10**: p. 100350.

[123] Olanrewaju, A., et al., *Capillary microfluidics in microchannels: from microfluidic networks to capillaric circuits.* Lab on a Chip, 2018. **18**(16): p. 2323-2347.

[124] Peng, C., Z. Zhang, and Y.S. Ju, *EWOD (electrowetting on dielectric) digital microfluidics powered by finger actuation.* Lab on a Chip, 2014. **14**(6): p. 1117-1122.

[125] Su, K., et al., *Emerging trends in integrated digital microfluidic platforms for next-generation immunoassays.* Micromachines, 2024. **15**(11): p. 1358.

[126] Jia, Z., et al., *Artificial intelligence-enabled multipurpose smart detection in active-matrix electrowetting-on-dielectric digital microfluidics.* Microsystems & Nanoengineering, 2024. **10**(1): p. 139.

[127] Liu, Y. and I. Papautsky, *Heterogeneous immunoassay using channels and droplets in a digital microfluidic platform.* Micromachines, 2019. **10**(2): p. 107.

[128] Fujiwara, M., *Diamond quantum sensors in microfluidics technology.* Biomicrofluidics, 2023. **17**(5).

[129] Xu, X., et al., *Digital microfluidics for biological analysis and applications.* Lab on a Chip, 2023. **23**(5): p. 1169-1191.

[130] Zhao, Y., et al., *A programmable magnetic digital microfluidic platform integrated with electrochemical detection system.* Microsystems & Nanoengineering, 2025. **11**(1): p. 82.

[131] Geng, H. and S.K. Cho, *Hybrid electrodes effective for both electrowetting- and dielectrowetting-driven digital microfluidics.* Droplet, 2023. **2**(3): p. e58.

[132] Zhai, J., et al., *Drug screening on digital microfluidics for cancer precision medicine.* Nature Communications, 2024. **15**(1): p. 4363.

[133] Cioe, K., et al., *A systematic review of patients' and providers' perspectives of medications for treatment of opioid use disorder.* Journal of substance abuse treatment, 2020. **119**: p. 108146.

[134] Xie, Y., L. Dai, and Y. Yang, *Microfluidic technology and its application in the point-of-care testing field.* Biosensors and Bioelectronics: X, 2022. **10**: p. 100109.

[135] Boun, S.S., O. Omonaiye, and S. Yaya, *Prevalence and health consequences of nonmedical use of tramadol in Africa: A systematic scoping review.* PLOS Global Public Health, 2024. **4**(1): p. e0002784.

[136] Lasong, J., Y. Salifu, and J.A.w.M. Kakungu, *Prevalence and factors associated with tramadol use among university students in Ghana: a cross-sectional survey.* BMC psychiatry, 2024. **24**(1): p. 853.

[137] Tobin, D.G., et al., *Opioids for chronic pain management in patients with dialysis-dependent kidney failure.* Nature Reviews Nephrology, 2022. **18**(2): p. 113-128.

[138] Bazazi, A.R., et al., *Illicit use of buprenorphine/naloxone among injecting and noninjecting opioid users.* Journal of addiction medicine, 2011. **5**(3): p. 175-180.

[139] Bio-Sya, A., et al., *Nonmedical use of tramadol among secondary school students in Benin, Africa.* The American Journal of Drug and Alcohol Abuse, 2021. **47**(6): p. 746-752.

[140] Khorasani, M.E., et al., *Sonochemical synthesis of graphene oxide-Ag2O nanozyme as an oxidize-like mimic for the highly sensitive detection of lithium in blood serum.* Ultrasonics Sonochemistry, 2024. **108**: p. 106960.

[141] Fakude, C.T., et al., *Advances in the application of nanomaterials for the electrocatalytic detection of drugs of abuse.* Advanced Sensor and Energy Materials, 2023. **2**(2): p. 100056.

[142] Balali-Mood, M., et al., *Toxic mechanisms of five heavy metals: mercury, lead, chromium, cadmium, and arsenic.* Frontiers in pharmacology, 2021. **12**: p. 643972.

[143] Min, J.-y. and K.-b. Min, *Blood cadmium levels and Alzheimer's disease mortality risk in older US adults.* Environmental Health, 2016. **15**(1): p. 69.

[144] Kim, Y.-M., et al., *Biomonitoring of lead, cadmium, total mercury, and methylmercury levels in maternal blood and in umbilical cord blood at birth in South Korea.* International journal of environmental research and public health, 2015. **12**(10): p. 13482-13493.

[145] Yao, S. and D. Xu, *Relationships between blood concentrations of cadmium, lead, mercury, selenium, and manganese and the risk of chronic kidney disease: a cross-sectional study based on NHANES 2011–2018.* Archives of Medical Science: AMS, 2024. **20**(6): p. 1822.

[146] Chiappini, S., et al., *Misuse of prescription and over-the-counter drugs to obtain illicit highs: How pharmacists can prevent abuse.* The Pharmaceutical Journal, 2020. **305**(7943): p. 1-27.

[147] Ali, M.M., et al., *Environmental pollution with heavy metals: A public health concern*, in *Heavy metals-their environmental impacts and mitigation*. 2021, IntechOpen.

[148] Hadjesfandiari, N., et al., *Measurement of lead, mercury, and cadmium in blood donors in Canada.* Transfusion, 2024. **64**(7): p. 1243-1253.

[149] Jyothi, N.R., *Heavy metal sources and their effects on human health*, in *Heavy metals-their environmental impacts and mitigation*. 2020, IntechOpen.

[150] Nordberg, M. and G.F. Nordberg, *Metallothionein and cadmium toxicology—Historical review and commentary.* Biomolecules, 2022. **12**(3): p. 360.

[151] La-Scalea, M.A., L.D. Chiavassa, and C. de Lima Brito, *The Electrochemistry of Nitro Compounds from a Bibliometric Approach.* Journal of The Electrochemical Society, 2024. **171**(9): p. 096510.

[152] Viegas, S., C. Martins, and R. Assunção, *Human biomonitoring (HBM) as a tool to support policy and regulatory action to prevent chemicals exposure*. 2024, Frontiers Media SA. p. 1376890.

[153] Hussein, Z.A., *Radiation detection and heavy metals measurements in powdered blood sample of leukemia patients.* aro-the scientific journal of koya university, 2023. **11**(1): p. 121-125.

[154] Ma, L., et al., *A new thiacalix [4] arene-based metal-organic framework as an efficient electrochemical sensor for trace detection of Cd2+ and Pb2+*. Food Chemistry, 2024. **441**: p. 138352.

[155] Wang, Y., et al., *Detection of Ultra-Trace Heavy metals in Aerosols with pg^ m3 Sensitivity Using Filament-Induced Fluorescence Spectroscopy.* arXiv preprint arXiv:2506.09295, 2025.

[156] Wang, G., et al., *Portable microfluidic device with thermometer-like display for real-time visual quantitation of Cadmium (II) contamination in drinking water.* Analytica Chimica Acta, 2021. **1160**: p. 338444.

[157] Al-aqbi, Z.T., H.T. Abdulsahib, and F.A. Al-Doghachi, *A portable microfluidic device-based colorimetric naked-eye sensors for determination of mercury and arsenic ions in river water samples.* Plasmonics, 2024. **19**(6): p. 3393-3414.

[158] Andoh, P.K.D., *Development of Novel Electrochemical Sensor to Detect Heavy Metals Cadmium, Lead and Chromium*. 2025, Wright State University.

[159] Fakayode, S.O., et al., *Electrochemical and colorimetric nanosensors for detection of heavy metal ions: a review.* Sensors, 2023. **23**(22): p. 9080.

[160] Sics, P., D. Kalnina, and A. Levina, *Pattern identification in data about unmodified waste eggshell application as an adsorbent for metal ion removal from aqueous media.* Reviews in Chemical Engineering, 2024. **40**(6): p. 683-706.

[161] Sarkar, N., R.S. Sharma, and M. Kaushik, *Green synthesis and physiochemical characterization of nickel oxide nanoparticles: Interaction studies with Calf thymus DNA.* Luminescence, 2020. **35**(2): p. 178-186.

[162] Al-darwesh, M.Y., S.S. Ibrahim, and M.A. Mohammed, *A review on plant extract mediated green synthesis of zinc oxide nanoparticles and their biomedical applications.* Results in chemistry, 2024. **7**: p. 101368.

[163] Giri, A.K., et al., *Green synthesis and characterization of silver nanoparticles using Eugenia roxburghii DC. extract and activity against biofilm-producing bacteria.* Scientific Reports, 2022. **12**(1): p. 8383.

[164] Shashiraj, K.N., et al., *Exploring the antimicrobial, anticancer, and apoptosis inducing ability of biofabricated silver nanoparticles using Lagerstroemia speciosa flower buds against the Human Osteosarcoma (MG-63) cell line via flow cytometry.* Bioengineering, 2023. **10**(7): p. 821.

[165] Cinar, G., et al., *Nanoparticle sizing in the field of nanomedicine: Power of an analytical ultracentrifuge.* Analytica Chimica Acta, 2022. **1205**: p. 339741.

[166] Khorrami, S., et al., *Selective cytotoxicity of green synthesized silver nanoparticles against the MCF-7 tumor cell line and their enhanced antioxidant and antimicrobial properties.* International journal of nanomedicine, 2018: p. 8013-8024.

[167] Gharari, Z., et al., *Eco-friendly green synthesis and characterization of silver nanoparticles by Scutellaria multicaulis leaf extract and its biological activities.* Pharmaceuticals, 2023. **16**(7): p. 992.

[168] Albishri, A., Al-aqbi, Z. T., Moker, M. H., Jebur, N. Q., & Murad, D. M. (2025). 3D Printed Microfluidic Device-Based Highly Sensitive and Selective Sensor for Detection of Human Albumin in Urine Samples. BioNanoScience, 15(4), 556.

[169] Fujioka, K., et al., *Edible green solvent for optimized catechins extraction from green tea leaves: Anti-Hypercholesterolemia.* Journal of pharmacy and pharmacology research, 2022. **6**(2): p. 80.

[170] Khorrami, S., et al., *Selective cytotoxicity of green synthesized silver nanoparticles against the MCF-7 tumor cell line and their enhanced antioxidant and antimicrobial properties.* Int J Nanomedicine, 2018. **13**: p. 8013-8024.

[171] Kalita, C. and P. Saikia, *Magnetically separable tea leaf mediated nickel oxide nanoparticles for excellent photocatalytic activity.* Journal of the Indian Chemical Society, 2021. **98**(11): p. 100213.

[172] Shahwan, T., et al., *Green synthesis of iron nanoparticles and their application as a Fenton-like catalyst for the degradation of aqueous cationic and anionic dyes.* Chemical Engineering Journal, 2011. **172**(1): p. 258-266.

[173] Romanovski, V., et al., *Bimetallic CuNi Nanoparticle Formation: Solution Combustion Synthesis and Molecular Dynamic Approaches.* Inorg Chem, 2024. **63**(52): p. 24844-24854.

[174] Rossi, A., et al., *Silver nanoparticle-based sensor for the selective detection of nickel ions.* Nanomaterials, 2021. **11**(7): p. 1733.

[175] Charkiewicz, A.E., et al., *Cadmium toxicity and health effects—a brief summary.* Molecules, 2023. **28**(18): p. 6620.

[176] Safa, M.A.T. and H. Koohestani, *Green synthesis of silver nanoparticles with green tea extract from silver recycling of radiographic films.* Results in Engineering, 2024. **21**: p. 101808.

[177] Khan, S.A., et al., *Phytomolecules-coated NiO nanoparticles synthesis using abutilon indicum leaf extract: antioxidant, antibacterial, and anticancer activities.* International Journal of Nanomedicine, 2021: p. 1757-1773.

[178] Ani Qomariyah*, A.K.H., *Synthesis of Copper Nanoparticles Using Dragon Fruit (Hylocereus polyrhizus) Extract as a Bio-Reductor and Their Analysis Using a UV-Visible Spectrophotometer.* Indonesian Journal of Chemical Research, 2024.

[179] Zhao, X.L.a.L., *Room-temperature synthesis of air-stable cobalt nanoparticles and their highly efficient adsorption ability for Congo red{*. COMMUNICATION, 2012.

[180] Mojgan Ebadi, a.M.R.Z., a Seyyed Soheil Aghaei,a Mohsen Zargar,a and b.H.S.Z.a.K.A.N. Morvarid Shafiei, *A bio-inspired strategy for the synthesis of zincoxide nanoparticles (ZnO NPs) using the cell extractof cyanobacterium Nostoc sp. EA03: frombiological function to toxicity evaluation.* RSC Advances, 2019.

[181] Potdar, R.P., et al., *Polyvinylpyrrolidone-capped silver nanoparticles for highly sensitive and selective optical fiber-based ammonium sensor.* Nanomaterials, 2022. **12**(19): p. 3373.

[182] Shahzad, A., et al., *Synthesis of nickel nanowires (Ni-NWs) as high ferromagnetic material by electrodeposition technique.* Heliyon, 2023. **9**(1).

[183] Ambati, T., et al., *Efficacy of copper oxide nanoparticles using Piper longum and Piper betle.* Bioinformation, 2023. **19**(9): p. 964.

[184] Almoneef, M.M., et al., *Exploring the multi-faceted potential: Synthesized ZnO nanostructure–Characterization, photocatalysis, and crucial biomedical applications.* Heliyon, 2024. **10**(12).

[185] Padmini, R., et al., *Cytotoxic effect of silver nanoparticles synthesized from ethanolic extract of Allium sativum on A549 lung cancer cell line.* Journal of King Saud University-Science, 2022. **34**(4): p. 102001.

[186] Sudha, M., et al., *Enhancement of corrosive-resistant behavior of Zn and Mg metal plates using biosynthesized nickel oxide nanoparticles.* Journal of Bio-and Tribo-Corrosion, 2021. **7**(2): p. 60.

[187] Al-Saadi, T.M., *Investigating the structural and magnetic properties of nickel oxide nanoparticles prepared by precipitation method.* Ibn Al-Haitham Journal For Pure and Applied Sciences, 2022. **35**(4): p. 94-103.

[188] Gurrala, R., et al., *Biogenic ag-Ni bimetallic nanoparticles from Croton blanpondinum L and their biological applications.* Int. J. Pharm. Sci., 2022. **15**: p. 2.

[189] Ibrahim, F.M., D.A. Najeeb, and H. ThamerSadeq, *Green preparation of Cu nanoparticles of the avocado seed extract as an adsorbent surface.* Materials Science for Energy Technologies, 2023. **6**: p. 130-136.

[190] Godse, J.S., et al., *Synthesis Characterization and Antimicrobial Activity of Copper Oxide Nanoparticles Using Sol-Gel Method.* Clinical Interventions and Clinical Trials, BRS Publishers, 2023. **1**(1): p. 2993-1096.

[191] Govindasamy, R., et al., *Green synthesis and characterization of cobalt oxide nanoparticles using Psidium guajava leaves extracts and their photocatalytic and biological activities.* Molecules, 2022. **27**(17): p. 5646.

[192] Roy, S., R. Priyadarshi, and J.-W. Rhim, *Development of multifunctional pullulan/chitosan-based composite films reinforced with ZnO nanoparticles and propolis for meat packaging applications.* Foods, 2021. **10**(11): p. 2789.

[193] Khashei Siuki, H., P. Ghamari Kargar, and G. Bagherzade, *New Acetamidine Cu (II) Schiff base complex supported on magnetic nanoparticles pectin for the synthesis of triazoles using click chemistry.* Scientific reports, 2022. **12**(1): p. 3771.

[194] Shahwan, T., M. Anjass, and R. Naser, *Discoloration of aqueous methylene blue using bimetallic Fe-Cu NPs in comparison with Fe NPs.* J. Mater. Environ. Sci, 2021. **12**(1): p. 42-54.

[195] Akinsiku, A.A., et al., *Modeling and synthesis of Ag and Ag/Ni allied bimetallic nanoparticles by green method: Optical and biological properties.* International journal of biomaterials, 2018. **2018**(1): p. 9658080.

[196] Jain, R., et al., *Green synthesis of iron nanoparticles using Artocarpus heterophyllus peel extract and their application as a heterogeneous Fenton-like catalyst for the degradation of Fuchsin Basic dye.* Current Research in Green and Sustainable Chemistry, 2021. **4**: p. 100086.

[197] Ga, S. and S. Ra, *Instrumental Elucidation of Nickel oxide nanoparticles obtained via green synthesis of Moringa oleifera leaves.*

[198] Sadia, B.O., J.K. Cherutoi, and C.M. Achisa, *Optimization, characterization, and antibacterial activity of copper nanoparticles synthesized using senna didymobotrya root extract.* Journal of Nanotechnology, 2021. **2021**(1): p. 5611434.

[199] Sultana, M., et al., *Development of a novel and robust CuO-Co3O4@ Biochar nanocomposite using Terminalia chebula leaf extract for reduction of nitro compounds and photodegradation of single and binary mixture of organic contaminants.* Environmental Science and Pollution Research, 2025. **32**(3): p. 1598-1625.

[200] Khan, M., P. Ware, and N. Shimpi, *Synthesis of ZnO nanoparticles using peels of Passiflora foetida and study of its activity as an efficient catalyst*

for the degradation of hazardous organic dye. SN Applied Sciences, 2021. **3**: p. 1-17.

[201] Vijaya Kumar, P., A. Jafar Ahamed, and M. Karthikeyan, *Synthesis and characterization of NiO nanoparticles by chemical as well as green routes and their comparisons with respect to cytotoxic effect and toxicity studies in microbial and MCF-7 cancer cell models.* SN Applied Sciences, 2019. **1**: p. 1-15.

[202] Wong, C.S. and K.H. Badri, *Chemical analyses of palm kernel oil-based polyurethane prepolymer.* Materials Sciences and Applications, 2012. **3**(2): p. 78-86.

[203] Thangeeswari, T., A.T. George, and A.A. Kumar, *Optical properties and FTIR studies of cobalt doped ZnO nanoparticles by simple solution method.* Indian J. Sci. Technol, 2016. **9**(1): p. 1-4.

[204] Pasieczna-Patkowska, S., M. Cichy, and J. Flieger, *Application of Fourier transform infrared (FTIR) spectroscopy in characterization of green synthesized nanoparticles.* Molecules, 2025. **30**(3): p. 684.

[205] Patil, R.B. and A.D. Chougale, *Analytical methods for the identification and characterization of silver nanoparticles: A brief review.* Materials Today: Proceedings, 2021. **47**: p. 5520-5532.

[206] Lingaraju, K., et al., *Biosynthesis of nickel oxide nanoparticles from Euphorbia heterophylla (L.) and their biological application.* Arabian Journal of Chemistry, 2020. **13**(3): p. 4712-4719.

[207] Kamli, M.R., et al., *Combination effect of novel bimetallic Ag-Ni nanoparticles with fluconazole against Candida albicans.* Journal of Fungi, 2022. **8**(7): p. 733.

[208] Al Jahdaly, B.A., et al., *Phytosynthesis of Co3O4 nanoparticles as the high energy storage material of an activated carbon/Co3O4 symmetric supercapacitor device with excellent cyclic stability based on a Na2SO4 aqueous electrolyte*. ACS omega, 2022. **7**(27): p. 23673-23684.

[209] Al-aqbi, Z.T., et al., *A new 3D printing milli-fluidic device with integrated nanojunction for on-site colorimetric analysis of iron in water and soil samples.* Chinese Journal of Analytical Chemistry, 2025. **53**(1): p. 100475.

[210] Liang, X. and L. Zhao, *Room-temperature synthesis of air-stable cobalt nanoparticles and their highly efficient adsorption ability for Congo red.* Rsc Advances, 2012. **2**(13): p. 5485-5487.

[211] Mekhemer, G.A., et al., *Cobalt oxide-catalyzed CO oxidation under steady-state conditions: Influence of the metal oxidation state.* Colloids and Surfaces A: Physicochemical and Engineering Aspects, 2023. **663**: p. 130992.

[212] Niloy Sarkar1, R.S.S.M.K., *Green synthesis and physiochemical characterization of nickel oxide nanoparticles: Interaction studies with Calf thymus DNA.* RESEARCH ARTICLE.

[213] Mohamed, E.A., *Green synthesis of copper & copper oxide nanoparticles using the extract of seedless dates.* Heliyon, 2020. **6**(1).

[214] Zhang, C., et al., *Determination of tramadol in human serum by capillary electrophoresis with the end-column electrochemiluminescence detection.* 2013.

[215] Baconi, D.L., et al., *Determination of Tramadol in human plasma by HPLC with fluorescence detection.* Journal of Mind and Medical Sciences, 2016. **3**(1): p. 55-64.

[216] Čapková, M., E. Hemmerová, and J. Homola, *Surface plasmon resonance biosensor for environmental detection of tramadol.* Analytical and Bioanalytical Chemistry, 2025: p. 1-7.

[217] Han, S., et al., *Sensitive and reliable identification of fentanyl citrate in urine and serum using chloride ion-treated paper-based SERS substrate.* Spectrochimica Acta Part A: Molecular and Biomolecular Spectroscopy, 2021. **251**: p. 119463.

[218] Swaminathan, S.K., J. Fisher, and K.K. Kandimalla, *Sensitive determination of fentanyl in low-volume serum samples by LC-MS/MS.* AAPS PharmSciTech, 2018. **19**(7): p. 2812-2817.

[219] Karimzadeh, Z., et al., *Dual-emission ratiometric fluorescent probe based on N-doped CQDs@ UiO-66/PVA nanocomposite hydrogel for quantification of pethidine in human plasma.* Microchimica Acta, 2023. **190**(4): p. 128.

[220] Khorablou, Z., F. Shahdost-Fard, and H. Razmi, *Voltammetric determination of pethidine in biofluids at a carbon cloth electrode modified by carbon selenide nanofilm.* Talanta, 2022. **239**: p. 123131.

[221] Karimi, M., A. Mokhtari, and A. Dehno Khalaji, *Chemiluminescence determination of pethidine hydrochloride and thebaine alkaloides.* Applied Chemistry Today, 2023. **18**(68): p. 83-106.

[222] Li, Y., et al., *In situ deposition of bismuth on pre-anodized screen-printed electrode for sensitive determination of Cd2+ in water and rice with a portable device.* Scientific Reports, 2024. **14**(1): p. 18433.

[223] Ning, J., et al., *Synergetic sensing effect of sodium carboxymethyl cellulose and bismuth on cadmium detection by differential pulse anodic stripping voltammetry.* Sensors, 2019. **19**(24): p. 5482.

[224] Chen, W., et al., *A simple paper-based colorimetric device for rapid mercury (II) assay.* Scientific reports, 2016. **6**(1): p. 31948.

[225] Ninwong, B., et al., *Sensitive distance-based paper-based quantification of mercury ions using carbon nanodots and heating-based preconcentration.* RSC advances, 2020. **10**(17): p. 9884-9893.

ملخص الرسالة

الزيادة السريعة في الأستخدام غير القانوني للأدوية المخدرة والتعرض المتزايد للمعادن الثقيلة في العينات البيولوجية قد أوجدت حاجة ملحة لطرق كشف سريعة وحساسة وفعالة من حيث التكلفة .تقنيات التحليل التقليدية، على الرغم من دقتها، غالبًا ما تتطلب أجهزة معقدة، وأوقات تحليل طويلة، ومشغلين ماهرين، في هذا السياق ظهرت المواد النانوية التي تم تصنيعها من خلال طرق صديقة للبيئة كبدائل واعدة لتطبيقات الاستشعار اللوني .

في هذا العمل، تم تحضير مواد نانوية مختلفة باستخدام طرق التخليق الأخضر .تم تحضير جسيمات CoO NPs ، وجسيماتAg NPs ، وجسيماتNiO NPs ، وجسيماتFeO NPs باستخدام مستخلص الشاي الأخضر كعامل اختزال، بينما تم تحضير جسيماتCu NPs وجسيماتZnO NPs باستخدام مستخلص *Boswellia sacra*علاوة على ذلك، تم تحضير المواد النانوية الثنائية المعدن باستخدام نفس المستخلصات النباتية بنسب مولارية 1:1 و3:1، حيث تم تحضير Ag:NiO BNPs باستخدام مستخلص الشاي الأخضر، وتحضير Cu:NiO BNPs و Cu:CoO BNPs و Cu:ZnO BNPs باستخدام مستخلص *Boswellia sacra*. تم تشخيص المواد النانوية المحضرة باستخدام FESEM و TEM لتقييم حجم الجسيمات والشكل، مما أكد أن جميع المواد كانت ضمن النطاق النانوي .أكد تحليل EDX التركيب العنصري والنقاء، بينما أكدت مطيافية FTIR الدور الفعال لمستخلصات النباتات من خلال وجود الأطياف الاهتزازية المميزة . تمت دراسة التركيب البلوري باستخدام حيود الأشعة السينية، وتطابقت الأنماط الناتجة مع بيانات المرجع القياسية. تم استخدام مطيافية الأشعة فوق البنفسجية-المرئية لتحديد خصائص الامتصاص البصري.

بالإضافة إلى ذلك، تم تصميم جهاز ميكروفلودنك باستخدام SOLIDWORKS 2022 وتصنيعه عبر طابعة ثلاثية الأبعاد، حصلنا على نموذجين ثلاثيي الأبعاد: الاول رباعي الأضلاع للكشف عن الأدوية المخدرة والاخر ذو ذراعين للكشف عن المعادن الثقيلة في عينات الدم. أظهرت الجسيمات النانوية أحادية وثنائية المعدن التي تم تصنيعها كفاءة عالية في اكتشاف المواد الدوائية المخدرة من خلال تغييرات سريعة ومرئية في اللون .

أظهرت جسيمات الفضة النانوية (Ag NPs) حساسية ممتازة تجاه سترات الفنتانيل ($C_{22}H_{28}N_2O\cdot C_6H_8O_7$)، بينما اكتشفت جسيمات أكسيد الكوبالت النانوية (CoO NPs) هيدروكلوريد الترامادول ($C_{16}H_{25}NO_2\cdot HCl$) بفعالية .كما لعبت المواد النانوية الثنائية المعدن دورًا كبيرًا في الكشف عن هيدروكلوريد البيثيدين .($C_{15}H_{21}NO_2\cdot HCl$) علاوة على ذلك، نجحت جسيمات النحاس النانوية (Cu NPs)في الكشف عن الزئبق بتركيزات منخفضة جداً في بلازما الدم، بينما أظهرت جسيمات الزنك أكسيد النانوية (ZnO NPs) حساسية عالية تجاه الكادميوم .بشكل عام، تؤكد النتائج على إمكانيات المواد

النانوية التي تم تصنيعها بطريقة صديقة للبيئة والمركبة مع اجهزة الميكروفلويديك كنظم استشعار سريعة ومنخفضة التكلفة وفعالة للكشف عن الأدوية والمعادن الثقيلة.

جمهورية العراق
وزارة التعليم العالي والبحث العلمي
جامعة ميسان
كلية العلوم
قسم الفيزياء

أجهزة ميكروفلويدك المعتمدة على المستشعرات النانوية لاكتشاف الأدوية المخدرة والمعادن الثقيلة في بلازما الدم

رسالة مقدمة الى
كلية العلوم / جامعة ميسان كجزء من متطلبات نيل
شهادة الماجستير في علوم الفيزياء

الطالبة

بهية عبد الباقي ضاحي

بكالوريوس علوم فيزياء / جامعة البصرة (2015)

بإشراف

أ.م.د منذر عبد الحسن الشكبان

أ.م.د زيدون طارق العقابي

م ٢٠٢٥

هـ ١٤٤٧